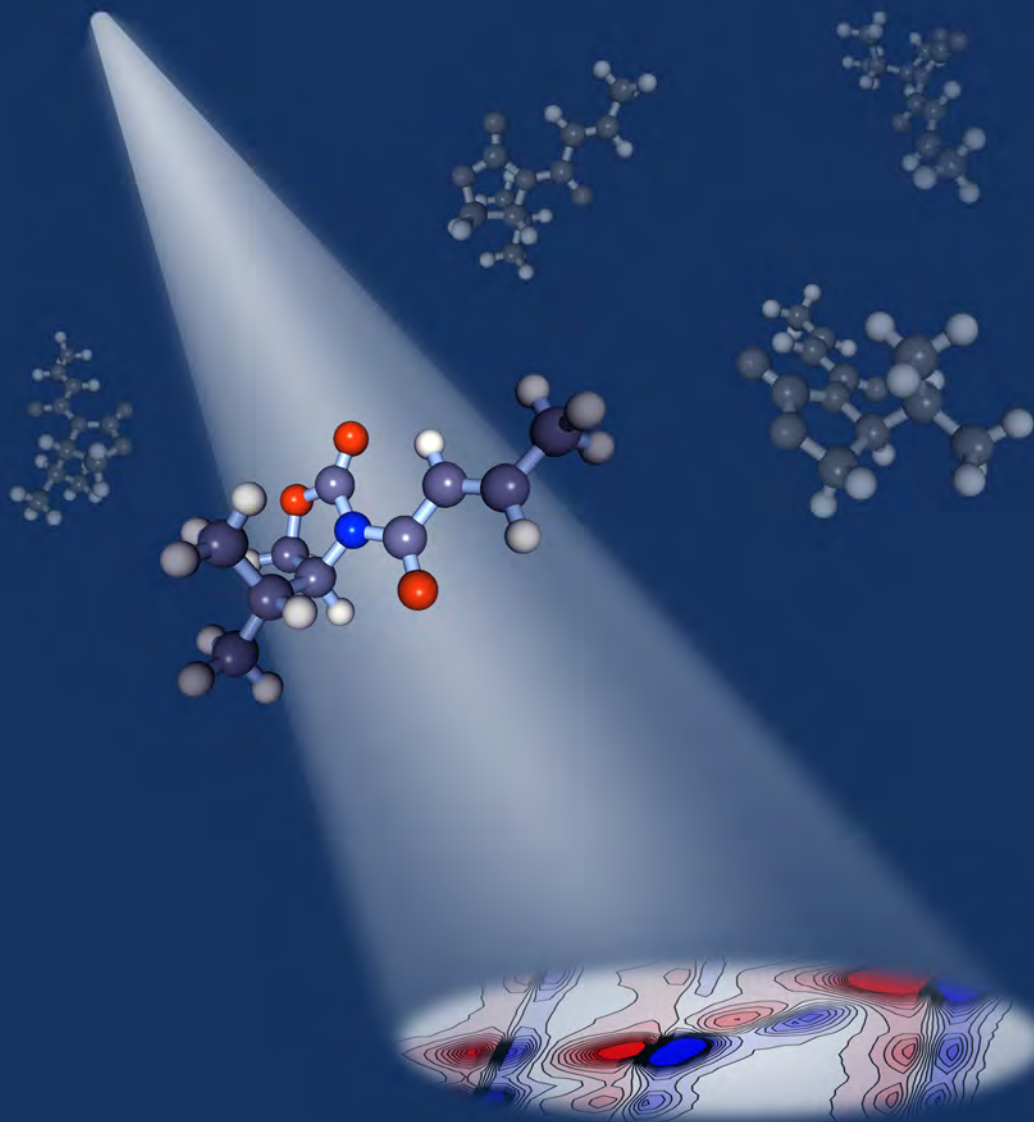# Shedding Light on Reaction Mechanisms

Structure Determination of Reactive Intermediates and Investigation of Protein Structural Dynamics Using 2D-IR Spectroscopy

Dissertation
Andreas T. Messmer

Shedding Light on Reaction Mechanisms

–

Structure Determination of Reactive Intermediates and Investigation of Protein Structural Dynamics Using 2D-IR Spectroscopy

Dissertation
zur Erlangung des Doktorgrades
der Naturwissenschaften

vorgelegt beim Fachbereich Physik
der Johann Wolfgang Goethe-Universität
in Frankfurt am Main

von
Andreas Thomas Messmer
aus Engen/Hegau

Frankfurt 2012
(D 30)

vom Fachbereich Physik der
Johann Wolfgang Goethe-Universität als Dissertation angenommen.

Dekan: Prof. Dr. Michael Huth

Gutachter: Prof. Dr. Jens Bredenbeck

                     Prof. Dr. Josef Wachtveitl

Datum der Disputation:

See first,
think later,
then test.

But always see first.
Otherwise
you will only see
what you were expecting.

Douglas Adams
(1952–2001)

Publications

Published and Submitted Publications

T. Schmid, **A. Messmer**, B.S. Yeo, W.H. Zhang, and R. Zenobi: Towards chemical analysis of nanostructures in biofilms II: tip-enhanced Raman spectroscopy of alginates. *Analytical and Bioanalytical Chemistry* **2008**, *391* (5), 1907–1916.

A. Messmer, A.-M.B. Rodríguez, J. Šebera, P. Hamm, A. Vlček Jr., S. Záliš, and J. Bredenbeck: How do vibrations change their composition upon electronic excitation? – EXSY-T2D-IR measurements challenge DFT calculations. In: P. Corkum, S. De Silvestri, K.A. Nelson E. Riedle, R.W. Schoenlein (Eds.), *Ultrafast Phenomena XVI*, **2009**, pp. 421–424, Berlin/Heidelberg/New York, Springer.

A.T. Messmer, K.M. Lippert, S. Steinwand, E.-B.W. Lerch, K. Hof, D. Ley, D. Gerbig, H.Hausmann, P.R. Schreiner, and J. Bredenbeck: Two-Dimensional Infrared Spectroscopy Reveals the Structure of an Evans Auxiliary Derivative and its $SnCl_4$ Lewis Acid Complex. *Chemisty – A European Journal* **2012**, DOI: 10.1002/chem.201201583.

A.T. Messmer, K.M. Lippert, P.R. Schreiner, and J. Bredenbeck: Structure Analysis of Substrate Catalyst Complexes in Mixtures with Ultrafast Two-Dimensional Infrared Spectroscopy. *Under review at Physical Chemistry Chemical Physics (invited paper).*

A.T. Messmer, S. Steinwand, K.M. Lippert, P.R. Schreiner, and J. Bredenbeck: Ultrafast two-dimensional infrared spectroscopy resolves the conformational change of an Evans auxiliary induced by $Mg(ClO_4)_2$. *Submitted to The Journal of Organic Chemistry.*

Publications in Preparation

A.T. Messmer, K. Nienhaus, Y.L. Li, H.M. Müller-Werkmeister, D. Bigourd, G.U. Nienhaus, and J. Bredenbeck: Investigating the speed limit of functional protein dynamics in equilibrium – a temperature dependent 2D-IR study. *In preparation.*

A.T. Messmer, A.-M.B. Rodríguez, J. Šebera, P. Hamm, A. Vlček Jr., S. Záliš, and J. Bredenbeck: Exchange Transient 2D-IR spectroscopy probes the remixing of vibrational eigenstates upon electronic excitation – a benchmark for DFT calculations. *In preparation.*

L.J.G.W. van Wilderen, **A.T. Messmer**, and J. Bredenbeck: Electronically-enhanced 2D-IR exchange spectroscopy beyond the vibrational T_1 time. *In preparation.*

Conference Contributions

Talks

A.T. Messmer, E.-B.W. Lerch, K. Lippert, K. Hof, P. Schreiner, and J. Bredenbeck: *Multidimensional IR spectroscopy: Towards structure determination of reactive catalyst-substrate complexes.*
Doktorandensemiar des Deutschen Arbeitskreises fuer Angewandte Spektroskopie, July 12th–13th, 2010, Zurich, Switzerland.

A.T. Messmer, Y.L. Li, H.M. Müller-Werkmeister, D. Bigourd, K. Nienhaus, G.U. Nienhaus, and J. Bredenbeck: *Investigating the speed limit of functional protein dynamics in equilibrium.*
Bunsentagung, May 13th–16th, 2010, Bielefeld, Germany.

A.T. Messmer, Y.L. Li, H.M. Müller-Werkmeister, D. Bigourd, K. Nienhaus, G.U. Nienhaus, and J. Bredenbeck: *Investigating the speed limit of functional protein dynamics in equilibrium – a temperature dependent 2D-IR study.*
The 45th Winterseminar, January 09th–23rd, 2010, Klosters, Switzerland.

Posters

A.T. Messmer, K.M. Lippert, S. Steinwand, E.-B.W. Lerch, K. Hof, H.Hausmann, P.R. Schreiner, and J. Bredenbeck (presented by J. Bredenbeck): *Structure determination of reactive catalyst-substrate-complexes by two-dimensional infrared spectroscopy.*
6th International Conference on Coherent Multidimensional Spectroscopy, July 16th–18th, 2012, Berlin, Germany.

L.J.G.W. van Wilderen, **A.T. Messmer**, S. Bauer, R.Berger, and J. Bredenbeck: *IR-Induced Visible Absorption Applications in 2D Infrared Spectroscopy.*
6th International Conference on Coherent Multidimensional Spectroscopy, July 16th–18th, 2012, Berlin, Germany.

A.T. Messmer, S. Steinwand, J. Glatthaar, K.M. Lippert, K. Hof, E.-B.W. Lerch, P.R. Schreiner, and J. Bredenbeck: *Structure determination of reactive catalystsubstrate complexes by polarization-dependent 2D-IR spectroscopy.*
FEMTO10 The Madrid Conference on Femtochemistry, July 11th–15th, 2011, Madrid, Spain.

A.T. Messmer, S. Steinwand, J. Glatthaar, K.M. Lippert, K. Hof, E.-B.W. Lerch, P.R. Schreiner, and J. Bredenbeck: *Structure determination of reactive catalystsubstrate complexes by polarization-dependent 2D-IR spectroscopy.*
Faraday Discussion 150: Frontiers in Spectroscopy, April 6th–8th, 2011, Basel, Switzerland.

A. Messmer, A.-M.B. Rodríguez, J. Šebera, P. Hamm, A. Vlček Jr., S. Záliš, and J. Bredenbeck: *Exchange transient 2D-IR spectroscopy probes the remixing of vibrational eigenstates upon electronic excitation a benchmark for DFT calculations.*
5th International Conference on Coherent Multidimensional Spectroscopy, August 17th–20th, 2010, Minneapolis, USA.

A.T. Messmer, Y.L. Li, H.M. Müller-Werkmeister, D. Bigourd, K. Nienhaus, G.U. Nienhaus, and J. Bredenbeck: *Investigating the speed limit of functional protein dynamics in equilibrium.*
First International Conference on Ultrafast Structural Dynamics, June 7th–10th, 2010, Lausanne, Switzerland.

H.M. Müller-Werkmeister, Y.L. Li, E.-B.W. Lerch, **A.T. Messmer**, D. Bigourd, S. Eger, A. Marx, and J. Bredenbeck: *Investigating the distance dependence of energy transfer times between vibrational modes with two-colour 2D-IR spectroscopy.*
Bunsentagung, May 13th–16th, 2010, Bielefeld, Germany.

A.T. Messmer, Y.L. Li, H.M. Müller-Werkmeister, D. Bigourd, K. Nienhaus, G.U. Nienhaus, and J. Bredenbeck: *Investigating the speed limit of functional protein dynamics in equilibrium.*
International Bunsen Discussion Meeting, September 28th–30th, 2009, Leipzig, Germany.

H.M. Müller-Werkmeister, Y.L. Li, E.-B.W. Lerch, **A.T. Messmer**, D. Bigourd, S. Eger, A. Marx, and J. Bredenbeck: *Distance dependent energy transfer times in azido- and nitrile-labeled amino acids by time-resolved two-colour two-dimensional infrared-spectroscopy (2C2D-IR).*
International Bunsen Discussion Meeting, September 28th–30th, 2009, Leipzig, Germany.

A. Messmer, A.-M.B. Rodríguez, J. Šebera, P. Hamm, A. Vlček Jr., S. Záliš, and J. Bredenbeck: *How do vibrations change their composition upon electronic excitation? – EXSY-T2D-IR measurements challenge DFT calculations.*
16th International Conference on Ultrafast Phenomena, June 9th–13th, 2008, Stresa, Italy.

Contents

III   Conformational Dynamics of Proteins   141

IV   Appendix   175

Zusammenfassung

Die Untersuchung von Reaktionsmechanismen ist von großer Bedeutung für das Verständnis chemischer, biologischer und biochemischer Reaktionen. Sie ist ein klassisches Feld der physikalischen Chemie, insbesondere der Spektroskopie. Es ist aus vielen Gründen wichtig zu verstehen in welchen Einzelschritten eine Reaktion vonstatten geht, welche Intermediate gebildet werden, welche Faktoren die Reaktionsgeschwindigkeit beeinflussen und warum welche (Neben-)Produkte entstehen. Eines der Hauptanliegen der modernen Chemie ist es, neue katalytische Reaktionen zu entwickeln und bestehende zu optimieren. Dafür ist die Kenntnis des Reaktionsmechanismus eine sehr wichtige Grundlage. Das tiefere Verständnis der Reaktion ist nicht nur von wissenschaftlichem Interesse, sondern insbesondere auch von ökonomischer und ökologischer Bedeutung. Die Erhöhung der Ausbeute, eine genaue Kontrolle über die Stereochemie eines Produktes, die Minimierung von Nebenprodukten und somit des Abfalls sowie eine Verringerung des Energiebedarfs führen direkt zu niedrigeren Kosten und gleichzeitig zu geringeren Umweltbelastungen.

Ein essentieller Baustein zur Aufklärung von Reaktionsmechanismen ist die Identifizierung und Charakterisierung von Katalysator-Substrat-Komplexen und Intermediaten. Diese sind jedoch häufig sehr reaktiv und weisen somit nur eine kurze Lebensdauer auf. Als Konsequenz können sie in der Regel nicht isoliert werden und kommen auch in der Reaktionsmischung nur in sehr geringen Konzentrationen vor. Dies führt dazu, dass Methoden, die standardmäßig zur Strukturaufklärung herangezogen werden (wie z.B. Massenspektrometrie, Kristallographie und NMR-Spektroskopie) oft nicht weiterhelfen. In dieser Arbeit wird in einer ausführlichen Untersuchung gezeigt, dass zweidimensionale Infrarotspektroskopie (2D-IR-Spektroskopie) eine hervorragende Ergänzung zu den bestehenden Methoden ist. Sie vereint eine sehr hohe Zeitauflösung (im Pikosekundenbereich) und eine hohe Sensitivität mit struktureller Empfindlichkeit.

Auch in der Biophysik ist die Untersuchung von Reaktionsmechanismen von großer Bedeutung. Besonderes Interesse gilt dabei den Strukturänderungen und Dynamiken in Proteinen. Ziel dieser Untersuchungen ist es zu verstehen, wie die Struktur und die Dynamik eines Proteins mit dessen Funktion zusammenhängen. Dafür ist es auch wichtig zu ergründen, was Proteine und Enzyme so effizient macht und wodurch deren Reaktionsgeschwindigkeit bestimmt wird. Dieses Wissen ist von entscheidender Bedeutung, um die Ursache einiger Krankheiten sowie die Wechselwirkung zwischen Medikamenten und Proteinen aufzuklären. Wie in dieser Arbeit gezeigt wird, kann 2D-IR-Spektroskopie auch auf diesem Gebiet einen bedeutenden Beitrag zum tiefern Verständnis leisten; insbesondere, da diese Methode es ermöglicht, sehr schnelle Prozesse im Gleichgewicht zu untersuchen ohne dabei ebendieses zu stören. Solche Gleichgewichtsprozesse sind zum Beispiel Konformationsänderungen von Proteinen, die eine wichtige Rolle für deren Funktion spielen können.

Die vorliegende Arbeit besteht im Wesentlichen aus drei Teilen: Im ersten Teil werden die Grundlagen der 2D-IR-Spektroskopie erklärt sowie der verwendete Aufbau beschrieben. Der zweite und umfangreichste Teil befasst sich mit der Strukturaufklärung mittels 2D-IR-Spektroskopie am Beispiel eines kleinen organischen Moleküls und dessen Lewis-Säure-Komplexen. Die Temperaturabhängigkeit des Austausches verschiedener Konformationen von Myoglobin ist Gegenstand des dritten Teils dieser Arbeit.

2D-IR-Spektroskopie

2D-IR-Spektroskopie verwendet sehr kurze Laserpulse (im Femtosekundenbereich) um die Interaktionen von Schwingungen zu messen. Es gibt zwei verschiedene Ansätze, ein 2D-IR-Spektrum aufzunehmen – in der Frequenzdomäne oder in der Zeitdomäne. Prinzipiell messen beide Methoden dasselbe, haben jedoch unterschiedliche Vor- und Nachteile. Spektren, die in der Zeitdomäne aufgenommen wurden, haben eine höhere spektrale Auflösung und durch die kürzeren Pulse auch eine höhere Zeitauflösung. Allerdings ist der Aufbau meist komplexer als der Aufbau für das Experiment in der Frequenzdomäne, das im Wesentlichen aus einem abstimmbaren schmalbandigen Anregpuls und einem breitbandigen Abtastpuls besteht. Dadurch können auch einzelne Schnitte durch das Spektrum gemessen werden, ohne das komplette Spektrum messen zu müssen. Dies verkürzt die Messzeit erheblich bzw. verbessert bei gleicher Messzeit die Qualität der Spektren. In der vorliegenden Arbeit wurde ein Frequenzdomänen 2D-IR-Spektrometer verwendet.

Ein 2D-IR-Spektrum wird, analog zu einem zweidimensionalen NMR-Spektrum, von zwei Frequenzachsen aufgespannt und macht die Interaktionen zwischen Schwingungen sichtbar. Es besteht in der Regel aus Diagonalsignalen und Kreuzsignalen. Diagonalsignale spiegeln im Wesentlichen das FTIR-Spektrum wieder, geben aber auch Auskunft über die Anharmonizität einer Schwingung. Aus der Bandenform kann abgelesen werden, ob die Bande homogen oder inhomogen verbreitert ist. Eine inhomogene Verbreiterung weist auf unterschiedliche Strukturen oder unterschiedliche Umgebungen hin. Kreuzsignale können durch verschiedene Prozesse entstehen. Dazu gehören zum Beispiel direkte Kopplungen zwischen Schwingungen, Populationstransfer (in der NMR-Spektroskopie bekannt unter dem Namen Kreuzrelaxation) und intramolekulare Schwingungsrelaxation, die zu einer Erwärmung des Moleküls führt. Die letzten beiden Mechanismen können dazu genutzt werden, um Abstände zwischen Schwingungen zu messen, analog zum Kern-Overhauser-Effekt (NOE) in der NMR-Spektroskopie. Auch chemischer Austausch zwischen zwei Spezies verursacht Kreuzsignale. Da die Schwingungsanregung das Gleichgewicht zwischen den Molekülen (in der Regel) nicht beeinflusst, können die Austauschraten unter Gleichgewichtsbedingungen bestimmt werden. Durch die hohe Zeitauflösung können sehr schnelle Prozesse im Pikosekundenbereich untersucht werden.

Die Intensität der Signale in einem 2D-IR-Spektrum hängt unter anderem von den Übergangsdipolmomenten der involvierten Schwingungen, den Winkeln zwischen diesen und der Polarisation der Laserpulse ab. Aus der Polarisationsabhängigkeit der Signalintensität von Kreuzsignalen lässt sich der Winkel zwischen den Übergangsdipolmomenten exakt bestimmen. Diese Information wird in der polarisationsabhängigen 2D-IR (P2D-IR)-Spektroskopie verwendet, um die dreidimensionale Struktur eines Moleküls abzuleiten.

Im Kapitel 2 werden die unterschiedlichen experimentellen Methoden ausführlich verglichen und die Eigenschaften der Spektren sowie die zugrunde liegenden Prozesse

beschrieben.

Der in dieser Arbeit verwendete experimentelle Aufbau wird in Kapitel 3 vorgestellt. Dabei liegt ein besonderer Schwerpunkt auf dem Aufbau für die polarisationsabhängigen Messungen, der im Rahmen dieser Arbeit entscheidend verbessert wurde. Dieser verbesserte Aufbau erlaubt die präzise und richtige Messung der Winkel zwischen den Übergangsdipolmomenten.

Strukturaufklärung reaktiver Intermediate

Der größte Teil dieser Arbeit befasst sich mit der Strukturaufklärung von *N*-Crotonyl-oxazolidinon (im Folgenden als **1** bezeichnet) und den reaktiven Substrat-Katalysator-Komplexen von **1** mit den Lewis-Säuren $SnCl_4$ und $Mg(ClO_4)_2$. Substituierte, chirale Oxazolidinone werden in der asymmetrischen Synthese häufig als Auxiliar eingesetzt, also als kovalent gebundene Gruppe, die den Verlauf der Reaktion beeinflusst und danach wieder abgespalten wird, um das gewünschte Produkt (in diesem Fall das gewünschte Stereomer) zu erhalten. Die als Evans-Auxiliare bekannten chiralen Oxazolidinone sind auch gerade deshalb so beliebt, weil je nach Reaktionsbedingung mit demselben Auxiliar unterschiedliche Stereoisomere hergestellt werden können. Ein Lehrbuchbeispiel für die Verwendung ist die Lewis-Säuren katalysierte, enantioselektive Diels-Alder-Reaktion. Eine besonders hohe Stereoselektivität wird mit Diethylaluminiumchlorid erzielt. Basierend auf der Stereochemie des Produktes postulierte David Evans einen Reaktionsmechanismus, der ein Chelat als entscheidende, reaktive Zwischenstufe beinhaltet. Dieser Mechanismus ist bis heute akzeptiert. Neuere Dichtefunktional-theorie (DFT)-Rechnungen legen allerdings nahe, dass nicht wie vorgeschlagen ein Ring gebildet wird, sondern ein offenkettiger Komplex. NMR-Messungen dazu wurden in der Vergangenheit gegensätzlich interpretiert.

Die beiden vorgeschlagenen Zwischenstufen unterscheiden sich stark in der Konformation, insbesondere in der Ausrichtung der beiden Carbonylbindungen. Mit Hilfe der P2D-IR-Spektroskopie können die Winkel zwischen den beiden Carbonylschwingungen gemessen und so die beiden Strukturen eindeutig unterschieden werden. Aus experimentellen Gründen wurden in der vorliegenden Arbeit die Lewis-Säuren $SnCl_4$ und $Mg(ClO_4)_2$ verwendet.

Zuerst wurde die Struktur des Substrates in verschiedenen Lösungsmitteln untersucht. Dazu wurde die Polarisationsabhängigkeit (Anisotropie) der verschiedenen Signale im 2D-IR-Spektrum gemessen. Durch die Variation der Zeitabstände zwischen den Laserpulsen konnte die Rotationsdiffusion der Moleküle in Lösung berücksichtigt und deren Einfluss korrigiert werden. Dieses Vorgehen wird im Folgenden als Anisotropiemethode bezeichnet. Die auf 2° bis 3° genau bestimmten Winkel zwischen den Übergangsdipolmomenten der Schwingungen wurden mit DFT-Rechnungen verglichen. In Kapitel 5 wird gezeigt, dass ausschließlich ein Konformer (siehe Abbildung 1) vorliegt. Im Gegensatz zur berechneten Struktur ist die bestimmte Struktur in Lösung jedoch nicht planar, sondern der Oxazolidinonring und der Crotonylrest sind leicht verdreht. Diese Verdrehung ist auch in der Kristallstruktur sichtbar und hat entscheidenden Einfluss auf die Stereoselektivität. Die durch 2D-IR-Messungen bestimmte Struktur kann die NMR-Spektren erklären, insbesondere das [1]H-NOESY-Spektrum, welches keine Kreuzsignale zwischen den Oxazolidinonprotonen und Crotonylprotonen aufweist. Durch das Fehlen dieser Signale ist eine eindeutige Strukturaufklärung mit NMR-Spektroskopie nicht möglich.

Dominierende Strukturen

>95%   >80%   >75%
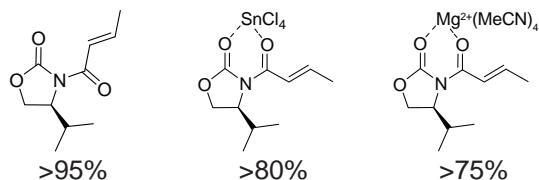
zusätzlich detektierte Komplexe

<15%   <15%   zusammen <15%
Komplex A
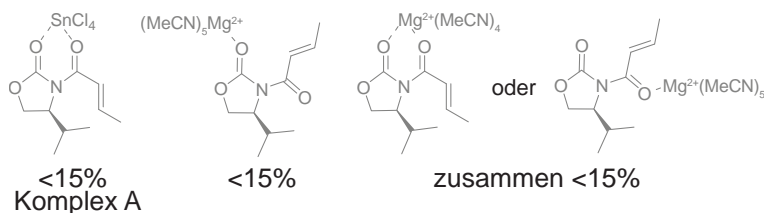
Abbildung 1: *Zugeordnete (oben, schwarz) und vorgeschlagene (unten, grau) Strukturen für die detektierten Spezies.*

Die Sensitivität der 2D-IR-Spektroskopie zeigt sich unter anderem darin, dass die Signale der ^{13}C Isotopologe, deren relative Konzentration nur 1% beträgt, deutlich sichtbar sind. Für **1** wurden keine weiteren Signale detektiert, die von anderen Konformeren stammen könnten.

Durch die Zugabe von SnCl$_4$ ändert sich die Konformation des Substrates und es wird hauptsächlich ($> 80\%$) das von Evans postulierte Chelat gebildet (siehe Abbildung 1). Zur Auswertung der Hauptsignale wurde wieder die Anisotropiemethode verwendet und die bestimmten Winkel mit DFT-Rechnungen verglichen (Kapitel 6). Die ermittelte Struktur stimmt mit der aus dem ^{1}H-NOESY-Spektrum abgeleiteten Struktur überein. Weitere Signale im 2D-IR-Spektrum weisen auf zusätzliche Spezies hin, auf die es zuvor keine Hinweise gab.

Um Mischungen zu analysieren, wird in Kapitel 7 eine alternative Auswertungsmethode eingeführt. Diese beruht darauf, selektiv Signale auszulöschen, indem die Spektren mit paralleler und senkrechter Polarisation gewichtet voneinander abgezogen werden. Das Verhältnis der beiden Spektren, bei dem ein Signal ausgelöscht wird, kann in den Winkeln zwischen den Übergangsdipolmomenten umgerechnet werden. Diese Methode (Aufhebungsmethode) wird am Beispiel einer Mischung aus freiem **1** und dem **1**·SnCl$_4$-Komplex eingeführt und validiert. Aufgrund des endlichen Zeitabstandes zwischen Anreg- und Abtastpuls und der Rotationsdiffusion der Moleküle in diesem Zeitraum entsteht ein kleiner systematischer Fehler. Mit der Aufhebungsmethode sind auch stark überlagernde Banden analysierbar. Im Gegensatz zur Aufhebungsmethode verfälschen überlagernde Banden das Ergebnis der Anisotropiemethode deutlich.

Es wird gezeigt, dass unter den gleichen Bedingungen eine Strukturaufklärung der beiden Spezies mit NMR-Spektroskopie nicht möglich ist, da sich diese zu schnell ineinander umwandeln und mittels NMR-Spektroskopie nicht als einzelne Moleküle detektierbar sind. Es können nur gemittelte Spektren gemessen werden. Der Austausch ist jedoch viel langsamer als die Zeitauflösung der 2D-IR-Spektroskopie (Pikosekunden), so dass das Gleichgewicht in den 2D-IR-Spektren statisch erscheint. Selbst wenn

der Austausch im Bereich der Zeitauflösung der Messung wäre, könnten die Winkel der einzelnen Spezies noch gemessen und so die Struktur bestimmt werden.

Mit Hilfe der Aufhebungsmethode konnten drei weitere **1**·SnCl$_4$-Komplexe detektiert und analysiert werden, deren Existenz bisher noch nicht bekannt war und auf die es in den NMR-Messungen keinen Hinweis gibt (siehe Kapitel 8):

Komplex A, der bis zu 15% populiert ist, ist vermutlich auch ein Chelat (siehe Abbildung 1). Da nur einer der Winkel gemessen werden konnte, ist die Assignierung vorläufig. Diese wird jedoch auch durch die Übereinstimmung von berechneten und gemessenen Schwingungsfequenzen gestützt. Eine Messung mit verbesserter spektraler Auflösung wird voraussichtlich auch die beiden anderen Winkel zugänglich machen und somit eine eindeutige Zuordnung ermöglichen. In einer Reaktion führt die dem Komplex A zugeordnete Struktur zum entgegengesetzten Diastereomer.

Komplex B, der bei Raumtemperatur etwa zu 2% bis 4% populiert ist, konnte bisher nicht zugeordnet werden, da keine der DFT-Rechnungen die experimentellen Winkel reproduziert. Temperaturabhängige FTIR-Messungen deuten an, dass dieser Komplex bei tieferen Temperaturen deutlich stärker populiert ist. Da die Reaktionen typischerweise bei -78 °C durchgeführt werden, kann dieser Komplex wichtig sein, um die experimentellen Selektivitäten zu erklären.

Besonders bei sehr großem SnCl$_4$-Überschuss bildet sich ein weiterer Komplex (Komplex C). Aufgrund der Konzentrationsabhängigkeit wird vermutet, dass es sich um einen Komplex zwischen **1** und einem SnCl$_4$-Cluster handelt.

Bei der Komplexierung von **1** mit Mg(ClO$_4$)$_2$ wird ebenfalls hauptsächlich ($> 75\%$) das von Evans vorgeschlagene Chelat gebildet (siehe Kapitel 9). Zusätzlich zeigen die 2D-IR-Spektren Signale von zwei weiteren Komplexen. Aufgrund der Bandenlage kommen drei der berechneten Komplexen in Frage (siehe Abbildung 1). Für eine eindeutige Assignierung bedarf es weiterer Messungen.

Mit den vorgestellten Untersuchungen wird eindrücklich gezeigt, dass Strukturaufklärung mit P2D-IR-Spektroskopie möglich ist – besonders für Systeme, die aus verschiedenen Gründen nicht mit NMR-Spektroskopie charakterisiert werden können; zum Beispiel wenn sich die Spezies in Mischungen schnell ineinander umwandeln, die Moleküle eine geringe Spindichte besitzen oder nur in sehr geringer Konzentration vorhanden sind. Neben den bevorzugt gebildeten Komplexen konnten noch weitere Komplexe detektiert und teilweise assigniert werden. Die Existenz der zusätzlichen Komplexe war bisher nicht bekannt, sie können aber in der Reaktion eine wichtige Rolle spielen. In Kapitel 10 werden die Ergebnisse nochmals zusammengefasst und die Strukturaufklärung mittels 2D-NMR- und 2D-IR-Spektroskopie verglichen. Durch einen Vergleich der Stärken und Limitierungen der beiden Ansätze wird deutlich, dass sich die beiden Methoden sehr gut ergänzen. Zudem werden Optimierungsmöglichkeiten aufgezeigt, um schnellere Messungen, größere Signale und eine höhere spektrale Auflösung zu erreichen. Mögliche, weiterführende Experimente wie die Untersuchung der Diethylaluminiumkomplexe (mit Hilfe eines Kryostates) oder die Untersuchung wasserstoffverbrückter Komplexe mit chiralen Katalysatoren werden skizziert.

Dynamik der Konformationsänderungen von Proteinen

Eine der offenen Fragen in der Biophysik ist, wie schnell eine enzymkatalysierte Reaktion maximal sein kann und wodurch diese Grenze der Reaktionsgeschwindigkeit bestimmt wird. Damit eng verknüpft ist die Frage, wie schnell Proteine ihre Konformation ändern können und was für diesen Prozess die Rate begrenzt. Myoglobin wird in der Biophysik häufig als Prototyp für ein Protein untersucht. Es existiert in unterschiedlichen Konformationen. Diese führen dazu, dass an Myoglobin gebundenes Kohlenstoffmonoxid je nach Proteinstruktur bei unterschiedlichen Frequenzen absorbiert. Die Absorptionsbanden werden unterschiedlichen Zuständen zugeordnet: A_0, A_1 und A_3. Die Strukturen von A_0 und A_3 sind weitgehend bekannt. Sie unterscheiden sich unter anderem in der Protonierung des distalen Histidins und dessen Orientierung. Die Struktur von A_1 ist bisher nicht bekannt. Frühere Studien legen nahe, dass sie der Struktur von A_3 ähnelt.

2D-IR-Austauschspektroskopie wurde in dieser Studie verwendet, um die Umwandlung von A_1 und A_3 zu untersuchen. Dazu wurde die Myoglobinmutante L29I verwendet (Kapitel 12), die etwa eine gleiche Population von A_1 und A_3 aufweist und deren Absorptionsfrequenzen denen des Wildtyps entsprechen. Durch das Anpassen der Spektren und mit Hilfe eines einfachen Austauschmodells erhält man für die Konformationsänderung von A_1 zu A_3 bei $20\,°C$ eine Zeitkonstante von $79\,ps$; für den entgegengesetzten Prozess beträgt die Zeitkonstante bei derselben Temperatur $87\,ps$.

Durch die Messung der Temperaturabhängigkeit der Austauschrate wird untersucht, welche Faktoren die Dynamik zwischen den Zuständen beeinflussen bzw. dominieren. In dem Temperaturbereich von $0\,°C$ bis $40\,°C$ verändern sich die Raten nur um einen Faktor zwei, von $15\,ns^{-1}$ bei $0\,°C$ bis $31\,ns^{-1}$ bei $40\,°C$. Dies ist weit weniger, als man aus der Extrapolation der Raten bei tiefen Temperaturen erwarten würde. In dieser Studie wird gezeigt, dass die Temperaturabhängigkeit der Proteindynamik der Temperaturabhängigkeit der Lösungsmittelviskosität folgt. Ein Vergleich mit früheren Messungen bei tiefen Temperaturen legt an den Tag, dass diese lineare Abhängigkeit zwischen Zeitkonstante und Viskosität über einen sehr großen Temperaturbereich (von $-100\,°C$ bis $40\,°C$) vorhanden ist. In diesem Bereich variieren die Zeitkonstanten und die Viskosität um 14 Größenordnungen.

Aus der Feststellung, dass die Viskosität der Proteinumgebung die Konformationsdynamik dominiert, folgt, dass für die Konformationsänderung zwischen A_1 und A_3 großräumige Umorientierungen nötig sind. Die Strukturen unterscheiden sich somit nicht nur in der Orientierung einzelner Seitenketten. Da keine zusätzliche, signifikante Temperaturabhängigkeit beobachtet werden konnte, folgt für die inhärente Energiebarriere des Proteins zwischen den Zuständen A_1 und A_3, dass sie im Wesentlichen entropisch ist und ein Enthalpieanteil, falls vorhanden, verschwindend gering ist.

Die qualitative Untersuchung weiterer Myoglobinmutanten sowie des Wildtyps zeigen ebenfalls eine sehr geringe Temperaturabhängigkeit des Austausches (siehe Kapitel 13).

In Kapitel 14 werden die temperaturabhängigen 2D-IR-Experimente an den verschiedenen Myoglobinmutanten diskutiert und zusammengefasst.

Abstract

Detailed knowledge of reaction mechanisms is key to understanding chemical, biological, and biophysical processes. For many reasons, it is desirable to comprehend how a reaction proceeds and what influences the reaction rate and its products.

In biophysics, reaction mechanisms provide insight into enzyme and protein function, the reason why they are so efficient, and what determines their reaction rates. They also reveal the relationship between the function of a protein and its structure and dynamics.

In chemistry, reaction mechanisms are able to explain side products, solvent effects, and the stereochemistry of a product. They are also the basis for potentially optimizing reactions with respect to yield, enhancing the stereoselectivity, or for modifying reactions in order to obtain other related products. Understanding the important steps of reactions in detail is not only of scientific interest, but also desirable for economical and ecological reasons: by using the knowledge of the underlying mechanism, a reaction can be optimized for higher yield, fewer side products, and therefore less waste. Optimizing catalysts may also reduce the energy consumption significantly and thus reduce both costs and environmental impact.

A key step to investigate reaction mechanisms is the identification and characterization of intermediates, which may be reactive, short-lived, and therefore only weakly populated. Nowadays, the structures of those can in most cases only be hypothesized based on products, side products, and isolable intermediates, because intermediates with a life time of less than a few microseconds are not accessible with the commonly used techniques for structure determination such as X-ray crystallography and nuclear magnetic resonance (NMR) spectroscopy.

In this thesis, two-dimensional infrared (2D-IR) spectroscopy is shown to be a powerful complement to the existing techniques for structure determination in solution. 2D-IR spectroscopy uses a femtosecond laser setup to investigate interactions between vibrations – analogous to 2D-NMR, which investigates the interactions between spins. Its ultrafast time resolution makes 2D-IR spectroscopy particularly well suited for the two topics investigated in this thesis: *Structure Determination of Reactive Intermediates* and *Conformational Dynamics of Proteins*.

Structure Determination of Reactive Intermediates

The focus of this thesis is using polarization-dependent 2D-IR (P2D-IR) spectroscopy for structure determination of *N*-crotonyloxazolidinone (referred to as **1**), a small organic compound with a chiral oxazolidinone, known as Evans auxiliary, and its reactive complexes with the Lewis acids $SnCl_4$ and $Mg(ClO_4)_2$. Chiral oxazolidinones in combination with Lewis acids have frequently been used in stereoselective synthesis for over 30 years. Nevertheless, the detailed mechanisms are in many cases

still mere hypotheses and have not yet been experimentally proven. By accurately measuring the angles between the transition dipole moments in the molecules using an optimized P2D-IR setup and comparing the results to density functional theory (DFT) calculations, the conformation of **1** and the conformation and coordination of the main complexes with $SnCl_4$ and $Mg(ClO_4)_2$ are unequivocally identified and analyzed in depth. Structural details, such as a slight twist in the solution structure of **1**, are detected using P2D-IR spectroscopy; these cannot be inferred from NMR spectroscopy or DFT calculations. In addition to the main Lewis acid complexes, complexes in low concentration are detected and tentatively assigned to different conformations and complexation geometries. The knowledge of those structures is essential for rationalizing the observed stereoselectivities. Additionally, a method is introduced that enables structure determination of molecules in complex mixtures and even in the presence of molecules with similar spectral properties and in high concentration. This work sets the stage for future studies of other substrate–catalyst complexes and reaction intermediates for which the structure determination has not been possible to date.

Conformational Dynamics of Proteins

Exchange 2D-IR spectroscopy allows the investigation of fast dynamics without disturbing the equilibrium of the exchanging species. It is therefore well suited to investigate fast dynamics of proteins and to reveal the speed limit of those. The temperature dependence of the conformational dynamics between the myoglobin substates A_1 and A_3 in equilibrium is analyzed. The various substates of myoglobin can be detected with FTIR spectroscopy, if carbon monoxide is bound to the heme. From previous studies it is known that the exchange rates at room temperature are in the picosecond time range, well suited to be investigated by 2D-IR spectroscopy. In the temperature range between $0\,°C$ and $40\,°C$ only a weak temperature dependence of the exchange rate in the myoglobin mutant L29I is observed in the present study. The exchange rate approximately doubles from $15\,ns^{-1}$ at $0\,°C$ to $31\,ns^{-1}$ at $40\,°C$. It turned out that the conformational dynamics correlates linearly with the solvent viscosity, which itself is temperature dependent. Comparing our results to measurements at cryogenic temperatures, the linear relation between exchange time constant for this process and the viscosity is shown for the temperature range between $-100\,°C$ and $40\,°C$ (corresponding to a viscosity change of 14 orders of magnitude). Thus, it is proven that the dynamics of the conformational switching are mainly determined by solvent dynamics, *i.e.*, the protein dynamics are slaved to the solvent dynamics. This is the first time slaving is observed for such fast processes (in the picosecond time range). The observation implies a long-range structural rearrangement between the myoglobin substates A_1 and A_3. In addition, the exchange for other mutants and wild type myoglobin is analyzed qualitatively and found to agree with the conclusions drawn from L29I myoglobin.

Part I

Methodology

Chapter 1

Introduction

The science investigating the energy levels of molecules, or more generally, matter with electromagnetic waves (*e.g.*, light) is called spectroscopy. It is a noninvasive technique that (often) does not destroy the sample. The most common spectroscopic techniques use the absorption of light and include atomic absorption spectroscopy (AAS) as well as nuclear magnetic resonance spectroscopy (NMR), electron paramagnetic resonance spectroscopy (EPR), ultraviolet (UV), visible (VIS), and infrared (IR) spectroscopy. Also, nuclear magnetic resonance spectroscopy (NMR) and electron paramagnetic resonance spectroscopy (EPR) use absorption, however the energies are usually detected *via* coherences. There are also other mechanisms used in spectroscopy such as emission (*e.g.*, fluorescence spectroscopy) and scattering (*e.g.*, Raman spectroscopy). Depending on the frequency used in the specific technique, it is sensitive to a distinct set of energy levels. The energy difference ΔE between two states relates to the frequency ν, the wavenumber $\tilde{\nu}$, or the wavelength λ of the light by

$$\Delta E = h\nu = hc\tilde{\nu} = h\frac{c}{\lambda}, \tag{1}$$

where h is the Planck's constant and c is the speed of light in vacuum. Wavenumbers are commonly used in IR spectroscopy and have the advantage compared to wavelength of being proportional to the energy. Many molecular properties can be derived by analyzing the energy levels, *e.g.*, the molecular structure, the interaction between molecules, and the stability of molecules. The concentration of molecules can also be determined with the help of spectroscopy by evaluating the extinction E of a sample using Lambert-Beer law:

$$E = -\log\frac{I}{I_0} = \epsilon cd. \tag{2}$$

The extinction depends on the extinction coefficient ϵ of the molecule, its concentration c, and the optical path length d. The extinction coefficient depends on the wavelength of the light and the molecule.

In many cases, absorption is used as a synonym for extinction. However, this is only true if no scattering is present. Absorption denotes the amount of light that the molecules absorb while extinction denotes the attenuation of the transmitted light when the sample is in the beam.

1.1   Infrared Spectroscopy

In the work presented in this thesis IR spectroscopy is used to investigate molecules and their dynamics. Light in the mid-IR range (400–$4000\,\text{cm}^{-1}$) is sensitive to the vibrations of a molecule. IR spectroscopy is also often referred to as vibrational spectroscopy, however vibrational spectroscopy is an umbrella term for all spectroscopies investigating vibrations, containing (amongst others) Raman spectroscopy, which is a technique based on inelastic scattering, and infrared spectroscopy, which is based on resonant absorption. Both techniques probe vibrations, however different selection rules apply, *i.e.*, different vibrations can be observed. For Raman spectroscopy it is important that the polarizability of the molecule is changed by the vibration. In IR spectroscopy only vibrations that change the dipole moment of the molecule can be observed. There are also vibrations that change the polarizability and the dipole moment of the molecule at the same time and thus can be observed in both spectroscopies. In the following we focus on IR spectroscopy.

Every nonlinear molecule has $3N - 6$ vibrations where N is the number of atoms it consists of. The simplest theoretical model to describe a vibration is the harmonic oscillator. The energy levels E_v in an harmonic oscillator are quantized and can be calculated as

$$E_v = (v + \frac{1}{2})h\nu, \tag{3}$$

where the transition frequency ν depends on the effective mass μ of the atoms involved in the vibration and the force constant k, a measure for the strength of the bond connecting the atoms

$$\nu = \frac{1}{2\pi}\sqrt{\frac{k}{\mu}}. \tag{4}$$

In reality, vibrations deviate from being harmonic, otherwise a bond would never break. A more realistic model is the anharmonic oscillator, which is described by the so called Morse potential

$$V = D_e(1 - e^{a(r_e - r)})^2, \tag{5}$$

with the energy levels at

$$E_v = h\nu(v + \frac{1}{2}) - \frac{h^2\nu^2}{4D_e}(v + \frac{1}{2})^2, \tag{6}$$

and

$$\nu = \frac{a}{2\pi}\sqrt{\frac{2D_e}{\mu}}. \tag{7}$$

The factor $\frac{h\nu}{4D_e}$ is called the anharmonicity constant. In addition to the fact that the anharmonicity leads to a finite dissociation energy D_e, it has two main additional implications: first, aside from transitions with $\Delta v = \pm 1$ being allowed (as in the case of the harmonic oscillator), additional transitions with $\Delta v = \pm 2, \pm 3, \pm 4, ...$ are possible. This leads to overtones in IR spectra. The eigenmodes of the system also change. As a consequence vibrations can couple, which means that the observed anharmonicity of a vibration depends on the quantum state of the other vibrations. This is particularly important for the two-dimensional IR (2D-IR) spectroscopy introduced in chapter 2.

Even though there are many vibrations present in a molecule, IR spectroscopy is characterized by a high structural sensitivity. Above $1500\,\text{cm}^{-1}$, where the fingerprint region ends, the spectra of small and medium-sized molecules typically are

well resolved and the bands can be assigned to specific vibrations of specific groups in the molecule. Because the vibrational frequencies are sensitive to small changes in the binding energy and the bond length, IR spectroscopy is ideal to investigate interactions between molecules, solvation effects, and conformational changes.

1.2 Time-Resolved Spectroscopies

Time-resolved techniques allow the investigation of dynamic processes in atoms, molecules, and matter. The time resolution of the various techniques is limited by several factors. First and most fundamentally there is the inherent time resolution given by the length of one light cycle of the light used for the investigation. This time limit determines how fast a process can be to be still detected directly. An overview of these limits is given in Fig. 1.1 for selected spectroscopies. For example IR spectroscopy using mid-IR light has an inherent time resolution of $\sim$10 fs (corresponding to $4000\,cm^{-1}$) while the one of NMR spectroscopy is $\sim$1 μs (corresponding to 1 GHz). The inherent time resolution is the theoretical limit. In practice, the time resolution as well as the time range observable is determined by the hardware and design of the experiment. A selection of experiments and their time windows is summarized in Fig. 1.1. Particularly in ultrafast spectroscopy the limit is mostly determined by the pulse length used. For near-IR laser pulses, almost single cycle pulses can be generated. The shortest pulse generated using 720 nm light had a length of 3.3 fs.[1] This pulse was used to generate the shortest light pulse so far which had a pulse length of only $\approx$80 as (in the XUV spectral range).[1]
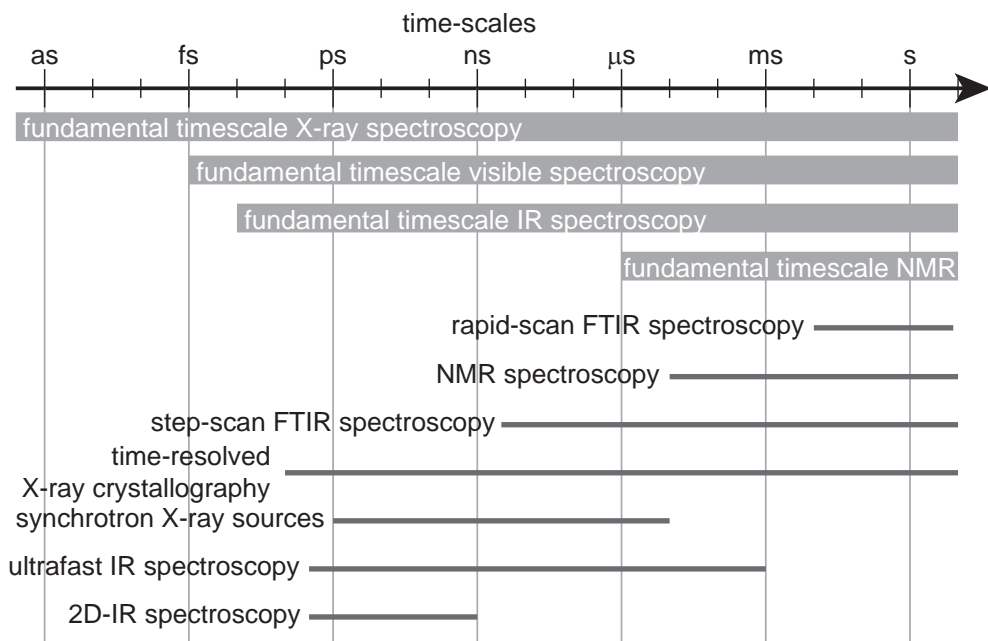

Figure 1.1: *Time resolution of a selection of spectroscopic methods. The gray bars indicate the fundamental time range limited by the inherent time resolution. Adapted with permission from ref. [2].*
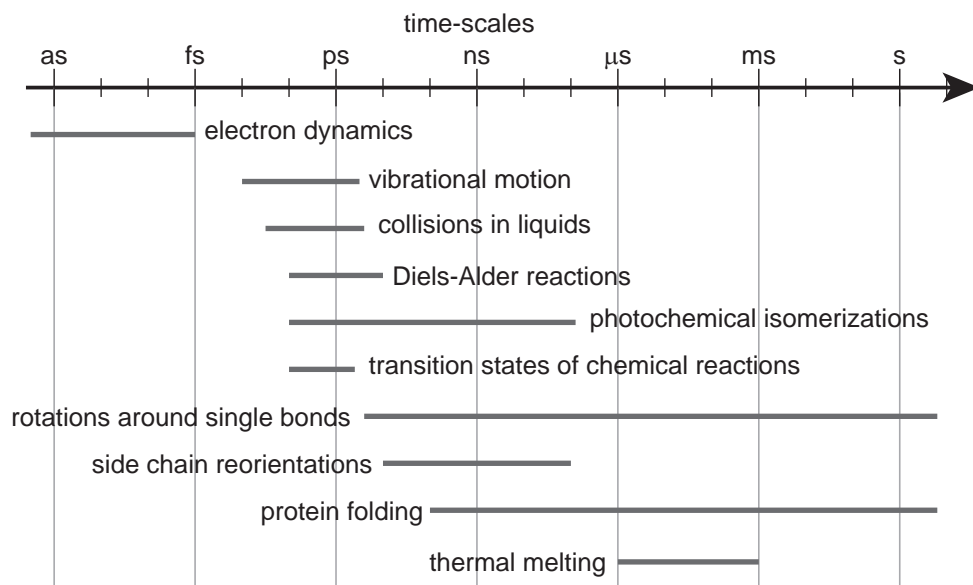
time-scales

Figure 1.2: *Time scales of selected physical, chemical and biochemical processes. Adapted with permission from [2].*

Depending on the time scale accessible by a method, several physical, chemical, and biochemical processes can be investigated. A selection of processes and their time scales is summarized in Fig. 1.2.

The comparison of Fig. 1.1 and Fig. 1.2 visualizes that IR spectroscopy is well suited for the investigation of conformational changes and the detection and distinction of individual species in chemical exchange processes.

1.3 Multidimensional Spectroscopies

Linear spectroscopy investigates the energy levels of molecules and allows for the deduction of molecular characteristics and dynamics. Nonlinear, *i.e.*, multidimensional spectroscopies, additionally provide experimental access to the interactions between vibrations, spins, etc. (*e.g.*, couplings and coherences). For a complete characterization of the states, *e.g.*, their delocalization, the couplings are particularly valuable. They also provide information about the structure of the molecule, which is used heavily in multidimensional NMR spectroscopy (see also chapter 4.1.2). While multidimensional NMR became a standard technique with many applications, *e.g.*, in structure determination, the field of multidimensional optical spectroscopy is still under development and has been rapidly growing over the last two decades. The underlying principle for both techniques is the same, to correlate the energies of the eigenstates. Consequently, the spectra are spanned by two (or more) frequency axes and the signals in these spectra result from the correlations between the vibrations. Several multidimensional optical spectroscopies have been designed including 2D visible (2D-VIS) spectroscopy, 2D THz spectroscopy, and multidimensional IR spectroscopy, the method used in this thesis.[3] Mixed techniques, such as the combination of THz and Raman spectroscopy, have also been developed.[4,5] Depending on

the frequencies used, different properties of the molecules can be investigated.

2D-VIS spectroscopy (also referred to as 2D electronic spectroscopy) investigates the correlations between electronic states. It was introduced first by Brixner *et al.* in 2005.[6] Until now, 2D-VIS spectroscopy has been used to investigate the population relaxation of electronic states, directional excitation transfer, mainly in photosynthetic systems and light harvesting complexes, and the characterization of quantum wells.[7–9]

The first ultrafast 2D-IR spectrum was published by Hamm, Lim, and Hochstrasser in 1998.[10] 2D-IR spectroscopy is sensitive to the interactions between vibrations and can be used to investigate molecules without disturbing the equilibrium they participate in. It has been employed to address questions such as:

- What is the structure of a peptide/protein/DNA molecule in solution? Which parts are stiff; which are flexible?[7,11–17]
- How fast do vibrations relax? What is the relaxation mechanism? How is the energy transported through a molecule/protein?[18–23]
- Is the line width of an IR band predominantly caused by homogeneous or inhomogeneous line broadening?[7,24–26]
- How do the solute and solvent interact?[7,27,28]
- What are the dynamics of hydrogen bonds? How fast do hydrogen bonds form and break?[7,29–34]
- How do vibrations interact?[7,18,35,36]
- How and how fast do molecules rotate or librate?[24]
- Which band is caused by which vibration? To which molecule do the bands belong?[37–39]

Since the first 2D-IR experiments, various methods have been developed. Exchange 2D-IR (EXSY-2D-IR) spectroscopy is used to investigate fast chemical exchange processes in equilibrium. The differentiation between 2D-IR and EXSY-2D-IR spectroscopy is somewhat arbitrary. The method is typically referred to as EXSY-2D-IR if the difference in frequency between the interconverting species is larger than the bandwidth of the absorption bands, *i.e.*, if the signals of the various species can be recognized as individual peaks and do not show up as inhomogeneous line broadening. Typical research fields are:

- How and how fast do molecules or proteins change their conformation in equilibrium?[35,40,41]
- How fast do complex formation and complex dissociation take place in equilibrium?[27,28,42]
- How fast do single bonds rotate? What is the rotation barrier?[43]

Relaxation-assisted 2D-IR (RA-2D-IR) spectroscopy uses intramolecular vibrational relaxation, *i.e.*, the energy transfer within a molecule to determine the distance between vibrational modes.[22,44,45]

Various setups for measuring 2D-IR spectra were also designed. The most common ones are discussed in chapter 2.[7,46] In addition to these setups, which directly detect the infrared light, there are also designs where the signal is upconverted by visible light and detected by a CCD camera.[47] Such a design is also used in a setup

that facilitates the measurement of a 2D-IR spectrum in a single shot. [48] A surface-sensitive version of 2D-IR spectroscopy is SFG-2D-IR spectroscopy, also referred to as 2D-SFG spectroscopy. [49–52]

2D-IR spectroscopy has also been used to investigate non-equilibrium systems. Slow conformational changes such as the unfolding of proteins have been investigated using rapid scanning 2D-IR spectroscopy. [53,54] The combination of the 2D-IR pulse sequence with a preceding light pulse that disturbs the equilibrium or induces a reaction has been used to investigate ultrafast processes including photo-induced conformational changes, energy transfer, the dynamics of intermediates, and the change of the vibrational eigenstates induced by electronic excitation. [38,55–61]

So far, 2D-IR spectroscopy mainly concentrated on proteins, water, solute-solvent interactions and metal carbonyls. Only rarely, organic compounds were investigated. 3D-IR spectroscopy was introduced by Zanni *et al.* and used to study the dynamics of water by Hamm and co-workers. [62,63]

The interaction between vibrations can also be probed by non-resonant transitions, *i.e.*, Raman transitions. Multidimensional spectroscopies involving Raman transitions are electron-vibration-vibration 2D-IR (EVV-2D-IR or DOVE-FWM), [64–68] 2D-Raman spectroscopy, [69,70] and 2D-Raman-THz spectroscopy. [4,5] 2D-Raman-THz spectroscopy is proposed to overcome the experimental limitations of 2D-Raman spectroscopy and 2D-THz spectroscopy, [71] which have only been successfully applied to the solvents CS_2 and formamide, and semiconductor quantum wells, respectively.

The focus of this thesis is 2D-IR spectroscopy on molecules in solution.

Chapter 2

Basics of 2D-IR Spectroscopy

Ultrafast 2D-IR spectroscopy is a nonlinear spectroscopy such as multidimensional NMR and applied to samples in the condensed phase.[i] More precisely it is a third order spectroscopy, meaning that three light matter interactions are needed to generate the signal.[46] Experimentally, the nonlinear response is created by short laser pulses in the spectral region of interest (see chapter 2.1.1 and 2.1.2).

2D-IR spectroscopy has been subject of excellent reviews[3,7,15–18,24,26,42,55,74,75] and only recently a very well written book about the concept and methods of 2D-IR spectroscopy was published.[46] This chapter is mainly based on these publications. There are in principle two different possibilities to record a 2D-IR spectrum – either in the frequency-domain or in the time-domain. Frequency-domain 2D-IR spectroscopy was realized first by Hamm, Lim, and Hochstrasser in 1998.[10] This technique grounds on earlier narrowband pump-probe experiments.[76–80] Two years later, in 2000, Asplund, Zanni, and Hochstrasser published the first 2D-IR spectrum recorded in the time-domain.[81] This technique is more closely related to pulsed 2D-NMR spectroscopy. The similarities between 2D-NMR and 2D-IR spectroscopy have been subject to several publications.[16,82–85] Various experimental setups to measure 2D-IR spectra, their advantages and disadvantages will be discussed first before the general features of a 2D-IR spectrum will be introduced in chapter 2.2. All techniques probe the same 3rd order response function and yield in the same signals in an absorptive 2D-IR spectrum.[74,84]

2.1   Experimental Designs

2.1.1   Frequency-Domain 2D-IR Spectroscopy[3,7,15,46]

Frequency-domain 2D-IR spectroscopy is also referred to as pump-probe 2D-IR spectroscopy, double resonance 2D-IR spectroscopy or dynamic hole burning 2D-IR spectroscopy. From the experimental point of view, it is the most simple 2D-IR setup. A sketch of the setup is shown in Fig. 2.1 left. Like all presented designs, it uses stable, femtosecond, broadband mid-IR laser pulses to start with. These are split into intense pump (dark red) and weak probe pulses (light red). The pump pulses

---

[i]There is also 2D infrared correlation spectroscopy, which is referred to as 2D-IR.[72,73] It investigates time dependent fluctuations of the IR spectrum induced by a perturbation. This method is completely different and will not be discussed.
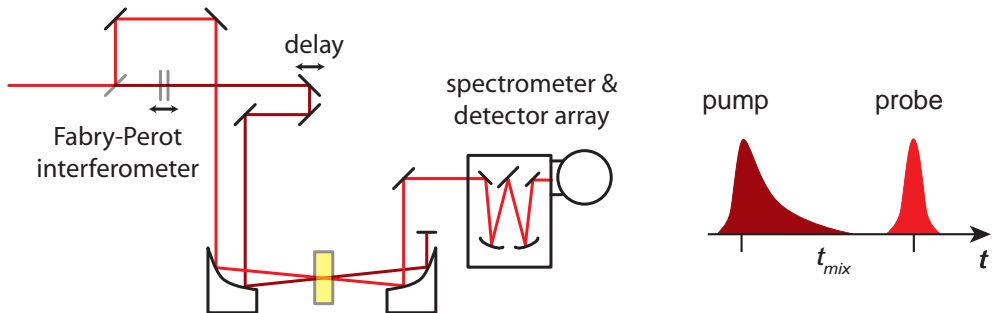
Figure 2.1: *Left: Schematic pump-probe 2D-IR setup using a Fabry–Perot interferometer. Light red: probe beam; dark red: narrowband pump beam; yellow: sample. Right: Pulse sequence of a pump-probe 2D-IR experiment.*

are spectrally narrowed by a computer controlled Fabry–Perot interferometer, which allows the adjustment of the width and central wavenumber of the pump pulse. A mechanical delay line defines the time delay between pump and probe pulses at the sample. The time between the two pulses t_{mix} is referred to as delay time (alternatively, this time is called waiting time or mixing time). The pump pulse hits the sample first, before the probe measures the change in absorption caused by the pump pulse (pulse sequence see Fig. 2.1 right). The probe beam is spectrally dispersed onto a detector array where it is measured.

The 2D-IR spectrum $\Delta\alpha_{2DIR}$ is calculated as difference of the probe absorption with and without pump pulse for each pump wavenumber ω_{pump}, or, in terms of the light intensity I of the probe pulse measured by the detector as:

$$\Delta\alpha_{2DIR}(\omega_{pump},\omega_{probe}) = -\log\frac{I_{pump_{ON}}}{I_{pump_{OFF}}}. \tag{8}$$

The two wavenumber axis (also often referred at frequency axis) are given by the central wavenumber of the pump pulse (ω_{pump}) and by the wavenumber of the probe pulse (ω_{probe}), which is spectrally dispersed on the detector array. The signal size is proportional to the probability that the molecule is excited by the pump pulse. If the pump pulse is resonant with an allowed transition i, the excitation probability depends amongst others on the intensity of the pump pulse $I_{pump}(\omega_{pump})$ at this wavenumber and the transition dipole moment μ_i. In the limit of an infinitely narrow pump pulse, the 2D-IR intensity of the spectrum caused by exciting vibration i is proportional to:

$$\Delta\alpha_{2DIR}(\omega_i,\omega_{probe}) \sim I_{pump}(\omega_i)\,|\mu_i|^2\,. \tag{9}$$

Because the pump pulse is not infinitely narrow but has a finite line width, the spectrum is smeared out along the pump axis – the peaks appear elongated. The spectral width of the pump pulse reduces significantly the resolution along the pump axis, particularly due to the far extending wings of the Lorentzian pulse shape, one main disadvantage of this technique. The intensity of the probe pulse does not affect the signal size.

Another drawback of frequency-domain 2D-IR spectroscopy using a Fabry–Perot interferometer is the time resolution. As indicated in the pulse sequence (see Fig. 2.1 right), the intensity of the pump pulse decays exponentially with time and is pretty long. The pulse length of the pump is typically in the range of 1 ps to 1.5 ps whereas

the probe pulse has a length of ∼150 fs. Thus, the pump pulse limits the minimal delay time measurable.

The big advantage of the frequency-domain approach, beside its experimental simplicity, is that also cuts through the spectrum can be measured without the need of the whole 2D-IR spectrum. The wavenumber of the narrowband pump pulse can be fixed to a desired value and many delay times can be measured subsequently. If one is interested in in the time dependence of single, well separated peaks, this saves a lot of measurement time and consequently enhances the quality of the data.

2.1.2 Time-Domain 2D-IR Spectroscopy[3,7,15,18,26,46,75]

The alternative to frequency-domain 2D-IR spectroscopy is time-domain 2D-IR spectroscopy. It is also called Fourier transform 2D-IR spectroscopy or photon echo 2D-IR spectroscopy. The fundamental difference to the frequency-domain approach is that the narrowband pump pulse is replaced by two broadband pulses. The frequency resolution is then obtained by scanning the delay between these two pulses (τ_1) and subsequent Fourier transformation of the resulting signal.
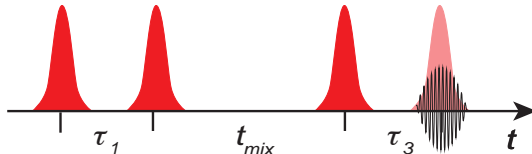

Figure 2.2: *Time-domain 2D-IR pulse sequence. All pulses are spectrally broad and short in time. The three pulses shown in red interact with the sample, which emits a signal (black). the interference between the signal and the local oscillator (light red) is usually detected (heterodyne detection).*

The general pulse sequence of a time-domain 2D-IR measurement is illustrated in Fig. 2.2. The first pulse creates a coherence between the vibrational ground state and the first excited state, which can evolve during τ_1. The next pulse converts this coherence into a population (ground state or excited state). The population may evolve during the delay time t_{mix} (also called waiting time or mixing time) as it is also the case between pump and probe pulses in pump-probe 2D-IR spectroscopy. A third pulse again creates a coherence, either between ground state and first excited state or between first and second excited state. This coherence emits light, the 2D-IR signal (black). Usually, this signal is overlaid and amplified by a mid-IR pulse, the local oscillator (shown in light red), and then detected.[ii] If the first two pulses hit the sample collinearly (pump-probe geometry), the signal is emitted collinearly with the third laser pulse and consequently the third pulse acts as local oscillator. This is also the case in pump probe 2D-IR spectroscopy and any transient absorption experiment. This amplification is called heterodyne detection. There are several possibilities to detect the interference between signal and local oscillator. The most common one is analogous to pump probe 2D-IR spectroscopy: Chopping the signal and using a dispersive spectrometer in combination with a detector array. This has

---

[ii]The very same processes happen in frequency-domain pump-probe 2D-IR spectroscopy, but within pump pulse (first two interactions) and probe pulse (last interaction and interference). However, a different language is typically used for the two experiments. Nevertheless they are equivalent.[84]

the advantage, that the probe frequency is directly given by the spectrometer and only the pump frequency needs to be determined by Fourier transformation. In this case, τ_3 is typically set to zero. [46] Alternative detection techniques involve the detection by a single pixel detector and scanning τ_3, balanced heterodyne detection, or frequency upconversion. [47,48,86] For convenience, these will not be covered in this introduction.

The intensity of the signal S emitted by the sample is proportional to the electric field amplitude of the three pulses and the transition dipole moments the pulses interact with. Additionally, it is scaled by the transition dipole moment of the transition that causes the emission of the signal:

$$S \sim E_1(\omega_i)E_2(\omega_i)E_3(\omega_j)\left|\mu_i\right|^2\left|\mu_j\right|^2. \tag{10}$$

Each absorptive 2D-IR spectrum consists in principle of two different contributions, referred to as rephasing and non-rephasing spectra. The difference between those two spectra is based on the fact that there exist two possible coherences between two states. Between the ground state $|0\rangle$ and the excited state $|1\rangle$ the two coherences $|0\rangle\langle1|$ and $|1\rangle\langle0|$ exist. They are the complex conjugates to each other, *i.e.*, the oscillations have opposite phase. If the coherences during time τ_1 and during τ_3 have the same phase, non-rephasing spectra are generated; if the phases are opposite, rephasing spectra are induced. Rephasing signals create a photon echo. Using the time-domain approach, rephasing and non-rephasing spectra are individually accessible. Due to phase matching conditions, rephasing and non-rephasing signals are emitted into different directions, based on the wave vectors $\vec{k}_x$ of the pulses. The rephasing spectrum is emitted along $-\vec{k}_1 + \vec{k}_2 + \vec{k}_3$ and the non-rephasing along $\vec{k}_1 - \vec{k}_2 + \vec{k}_3$. If the first two pulses are collinear (pump-probe geometry), rephasing and non-rephasing spectra are both emitted along $\vec{k}_3$, collinear with the third pulse, yielding directly in the absorptive 2D-IR spectrum. Rephasing and non-rephasing spectra can still be separated in this geometry *via* phase cycling. There exist several different setups to measure 2D-IR spectra in the time-domain, with their advantages and disadvantages. For all time-domain methods, at least one wavenumber axis is generated by Fourier transformation, and thus always the whole spectrum needs to be measured. It is not possible, to only focus on one (pump) wavenumber. On the other hand, the spectral resolution is determined only by the amount of different time delays measured. Thus, spectra collected in the time-domain have usually a much higher spectral resolution along the pump axis then pump-probe 2D-IR spectra. Another advantage of measuring 2D-IR spectra in the time-domain is that the intensity and polarization of each light interaction can be adjusted individually. Since in time-domain 2D-IR spectroscopy only broadband pulses are used, the maximal pulse length is (depending on the setup) in the range of $\sim 50\,\mathrm{fs}$ to $\sim 150\,\mathrm{fs}$, defining the minimal population delay time. This time is much shorter than in narrowband pump-probe 2D-IR spectroscopy and particularly beneficial, if fast dynamics are the scope of interest or disturbing the measurement.

The different approaches to measure time-domain 2D-IR spectra mainly differ in the beam geometry at the sample and how the pulses are generated. The most common one, the four wave mixing geometry setup and a collinear setup, which is used in the groups of Tokmakoff, Hamm, and Helbing, will be described in the following.
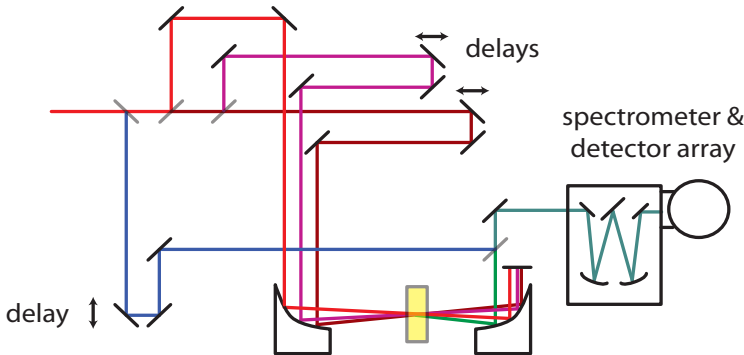
Nondegenerate Four Wave Mixing Geometry [7,15,18,26,46,74,75]

Figure 2.3: *Schematic 2D-IR setup in the four wave mixing geometry. Colors see text.*

The most versatile, however at the same time most complex setup consists of four independent laser beams (see Fig. 2.3), the heterodyned photon echo experiment. The initial beam is split into four beams by three beam splitters. Typically, the three beams interacting with the sample (light red, purple, and dark red) have the same intensity, which is as high as possible. This generates the strongest signal and thus leads to the highest possible sensitivity. These three beams are focused to the same spot. A typical beam geometry, the so called BOXCARS geometry, is illustrated in Fig. 2.4. The three incoming beams are located on the corners of a square. The emitted signal (green) is then positioned at the forth corner of this square. The local oscillator (blue) is much weaker in intensity than the other three pulses. Its intensity is adjusted to the linear range of the detector. After the sample, the created signal is overlaid with the local oscillator using a beam splitter and detected afterwards. In the scheme, the detection by means of a dispersive spectrometer is shown. The detection using a single pixel detector or balanced heterodyne detection are also possible. The time delays between the pulses are adjusted by individual delay lines.
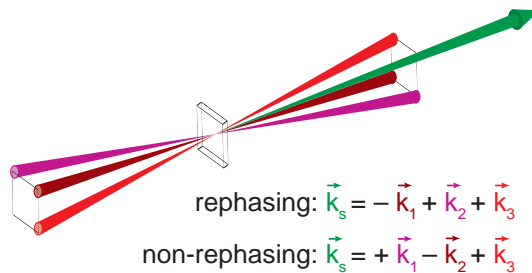

rephasing: $\vec{k}_s = -\vec{k}_1 + \vec{k}_2 + \vec{k}_3$

non-rephasing: $\vec{k}_s = +\vec{k}_1 - \vec{k}_2 + \vec{k}_3$

Figure 2.4: *BOXCARS geometry at the sample.*

As already discussed above, the rephasing and non-rephasing signal are emitted into different directions and thus can be measured individually. Even though they are emitted into different directions, they can be measured with the same experimental setup. To switch between the two signals, just the time order between the first and second pulse needs to be interchanged.

In order to be able to Fourier transform the signal, the delays between the pulses need to be very accurate and the phase between the laser pulses needs to be locked.

This is known as the phase problem and the main drawback of the approach using four individual beams. Several tricks have been developed to lock the phases or to recalculate the phases from the measurements.

Pump-probe Geometry[46,87,88]

The photon echo setup mainly suffers from its experimental complexity and the need to collect two complete 2D-IR spectra (rephasing and non-rephasing) to obtain the absorptive 2D-IR spectrum, the spectrum with the highest spectral resolution.[89] Time-domain experiments in pump-probe geometry are less complex and yield directly in the absorptive 2D-IR spectrum because rephasing and non-rephasing signals are emitted collinearly with the third pulse, which at the same time acts as local oscillator. The experimental setup is very similar to the frequency-domain, narrowband pump-probe setup. Only the Fabry–Perot interferometer is replaced by a Michelson or Mach–Zehnder interferometer, creating two identical pulses with a variable delay τ_1 (see Fig. 2.5).[87,88] Thus, the setup is almost as easy to handle as a narrowband pump-probe setup. The correct phasing can be adjusted by sending a second laser beam, *e.g.*, from a HeNe laser, through the same interferometer as the mid-IR beam and evaluate its interference separately or, in case of the Mach–Zehnder interferometer, by measuring the second output beam.
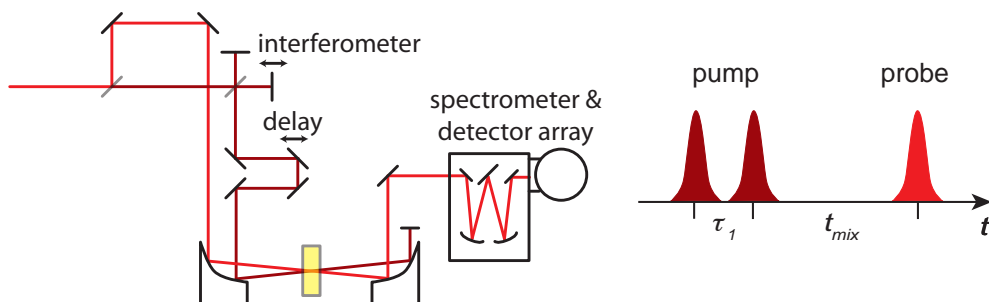

Figure 2.5: *Schematic 2D-IR setup to measure in the time-domain using collinear pump beams. Light red: probe beam; dark red: pump beam; yellow: sample. Right: Pulse sequence of a collinear time-domain 2D-IR experiment. The probe pulse acts simultaneously as local oscillator.*

Compared to the photon echo setup described above, the time-domain setups in pump-probe geometry have two main disadvantages. First, the transmittance through a Michelson interferometer or Mach–Zehnder interferometer is only 50%, reducing the created signal by a factor of 2. Additionally, the probe pulse can only be a low intensity pulse to prevent saturation effects on the detector. This leads to an addinional decrease in the 2D-IR signal and sensitivity.

2.1.3   2D-IR Spectroscopy Using a Pulse Shaper[46,53]

The 2D-IR setup using a pulse shaper in the mid-IR combines frequency-domain 2D-IR spectroscopy and (collinear) time-domain 2D-IR spectroscopy in one setup.[53] Depending on the requirements, the most suitable method can be used. From this point of view, it is the most general approach to measure 2D-IR spectra. However, independent polarization control of all pulses is to date not possible. The general
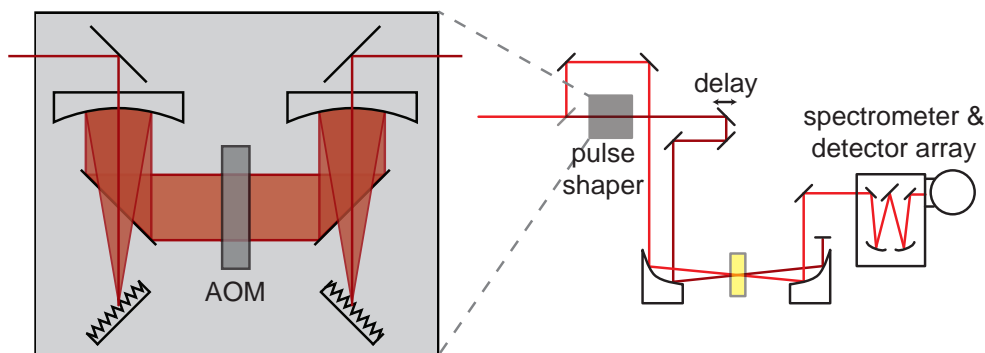
Figure 2.6: *Schematic 2D-IR setup using a pulse shaper. The shaper setup is enlarged on the left. Light red: probe beam; dark red: pump beam; yellow: sample.*

setup is again based on the frequency-domain narrowband pump-probe setup (see Fig. 2.6). In this case, the Fabry–Perot interferometer is replaced by a pulse shaper. The heart of the pulse shaper is a germanium acousto optic modulator (AOM), which is controlled by an arbitrary wave form generator. Using this device, pulse pairs with the desired delay between them or narrowband pump pulses can be generated. If this setup is used to measure 2D-IR spectra in the frequency-domain, the main advantage is that the pump pulses can be Gaussian shaped (in time and frequency-domain). This enhances the temporal resolution compared to the use of a Fabry–Perot significantly. At the same time, also the spectral resolution is enhanced because Gaussian shaped pulses are spectrally more refined than Lorentzian shaped pulses (Gaussian pulses have smaller wings). If the pulse shaper is used to generate pulse pairs, the phase between the two pulses is actively set. Thus phasing the spectra or measuring the phase between the pulses separately becomes obsolete. In both applications, the measurement conditions, *i.e.*, the delay between the pulse pair or the central wavenumber of the pump pulse, can be changed on a shot to shot basis without moving optics. This reduces the measurement time of one single 2D-IR spectrum to less than 1 s. Rapid scanning 2D-IR spectroscopy uses this advantage to study structural dynamics on the minute time scale such as folding and unfolding of proteins.[53,90] The main experimental drawback is the low efficiency of the shaper. Only approximately 30% of the incident intensiy are maximally transmitted, reducing the signal by a factor of > 3. Since also a weak probe pulse is used, this again reduces the signal intensity and therefore sensitivity.

2.1.4 Comparison

As outlined before, the various methods have all their advantages and disadvantages. The choice of the method depends on the scope of interest and the available resources. All described methods have in common that femtosecond broadband mid-IR laser pulses are used as light source. In principle, all methods can be used as two color experiments by using two OPA setups to generate light in different spectral regions. The differences between the methods are summarized in Table 2.1.

In this thesis, the frequency-domain approach was used, mainly because of its experimental simplicity and the compatibility with additional, visible pulses. The last aspect was not used in the presented experiments and will not be discussed.

Table 2.1: *Comparison of various 2D-IR setups highlighting their drawbacks and capabilities.*

Frequency-domain setup	Shaper setup	Collinear time-domain setup	Photon echo setup
most simple setup with only two beams	collinear setup with two beams, shaper alignment complex	simple collinear setup with only two beams	complex setup with four independent beams
standard optics (cheap)	gratings and AOM needed	standard optics (cheap)	standard optics (cheap)
very efficient pump pulse generation (~100%)	efficiency of the pump pulse or pulse pair generation ≤30%	efficiency of the pulse pair generation ≤50%	very efficient pump pulse generation (~100%)
weak probe pulse (reduced signal intensity)	weak probe pulse (reduced signal intensity)	weak probe pulse (reduced signal intensity)	intense third pulse and weak local oscillator (maximal signal intensity)
single cuts through a 2D-IR spectrum measurable	single cuts through a 2D-IR spectrum measurable[i]	only complete 2D-IR spectra measurable	only complete 2D-IR spectra measurable
direct measurement of the absorptive 2D-IR spectrum	direct measurement of the absorptive 2D-IR spectrum	direct measurement of the absorptive 2D-IR spectrum	absorptive 2D-IR spectrum calculated from rephasing and non-rephasing signals
no access to rephasing and non-rephasing signals	rephasing and non-rephasing signals accessible *via* phase cycling[ii]	rephasing and non-rephasing signals accessible *via* phase cycling	direct measurement of rephasing and non-rephasing signals
reduced spectral resolution (pump axis)	improved[i] or maximal[ii] spectral resolution (pump axis)	maximal spectral resolution (pump axis)	maximal spectral resolution (pump and probe axis)
limited time resolution	improved[i] or maximal[ii] time resolution	maximal time resolution	maximal time resolution
easy data analysis	easy data analysis[i]	FT required	FT required
no phase information needed	relative phase between pump pulses known	relative phase between pump pulses measured simultaneously *via* their interferogram[iii]	relative phase between the pulses of the pulse pairs must be determined independently
one polarization degree of freedom	one polarization degree of freedom[iv]	three polarization degrees of freedom	three polarization degrees of freedom

[i] Frequency-domain experiment. [ii] Time-domain experiment. [iii] If a Mach-Zehnder interferometer is used. [iv] To date, no polarization pulse shaping has been demonstrated in the IR.

2.2 Features of 2D-IR Spectra

The frequency-domain approach, also used in this thesis, is more intuitively to understand and used to explain the absorptive spectra in the following. A narrow-band, intense IR pump pulse is scanned through the spectral region of interest. For each pump position, a broadband IR probe pulse measures afterwards the absorption change induced by the pump pulse, *i.e.*, the difference between the absorption of the probe pulse with and without pump pulse. The final 2D-IR spectrum, a difference spectrum, is plotted as a function of the pump wavenumber (where the sample was excited) and the probe wavenumber (where the absorption changed). Thus it is spanned by two wavenumber axes (also often termed frequency axes). Unfortunately, there is no uniform convention about which axis resembles which wavenumber. A group of researchers assign the wavenumber corresponding to the pump pulse (pump or ω_1) to the x-axis and the directly detected wavenumber (probe or ω_3) to the y-axis. The other group of scientists plot the spectra the other way around: pump wavenumber along the y-axis and probe wavenumber along the x-axis (analogous to 2D-NMR). This is the convention also used throughout this thesis. The two different conventions lead to spectra that look fairly different at first glance even if they show the response of the same molecule.
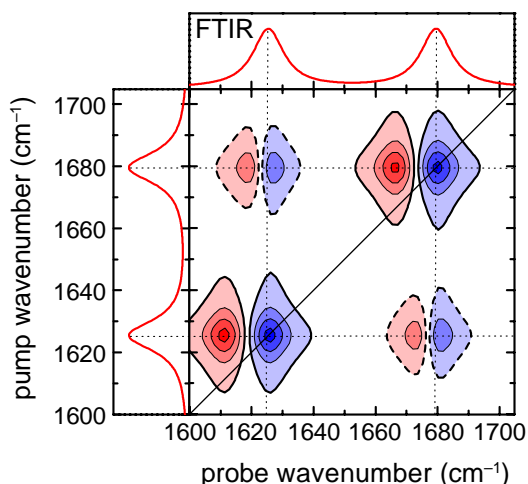

Figure 2.7: *Simulated 2D-IR spectrum of a molecule with two vibrations, e.g., two carbonyl groups. Two types of peaks appear in a 2D-IR spectrum: diagonal peaks (straight edging) and cross peaks (dashed edging). Positive signals are colored red, negative signals are colored blue. The FTIR spectrum of the molecule is shown for reference in the top and side panel.*

A simulated 2D-IR spectrum is shown in Fig. 2.7 for a hypothetical molecule with two IR active, anharmonic vibrations absorbing at $\approx 1625 \, \text{cm}^{-1}$ and $\approx 1679 \, \text{cm}^{-1}$, *e.g.*, two carbonyl groups. The FTIR spectrum of the molecule is shown for reference in the top and side panel. In the 2D-IR spectrum two types of peaks appear. One type is located on the diagonal (straight edging) and thus called diagonal peak. Both, pump and probe wavenumber are equal and correspond to the wavenumber of one absorption band. The other peak type is located off diagonal (dashed edging), *i.e.*, pump and probe wavenumber differ. The peak is located at the crossing of the pump wavenumber of one vibration and the probe wavenumber of an other vibration.

Accordingly these peaks are named cross peaks. Each peak (diagonal and cross peak) consists of two parts with positive (red) and negative (blue) sign, respectively. The origin of the various peaks as well as their information content will be discussed in the following sections.

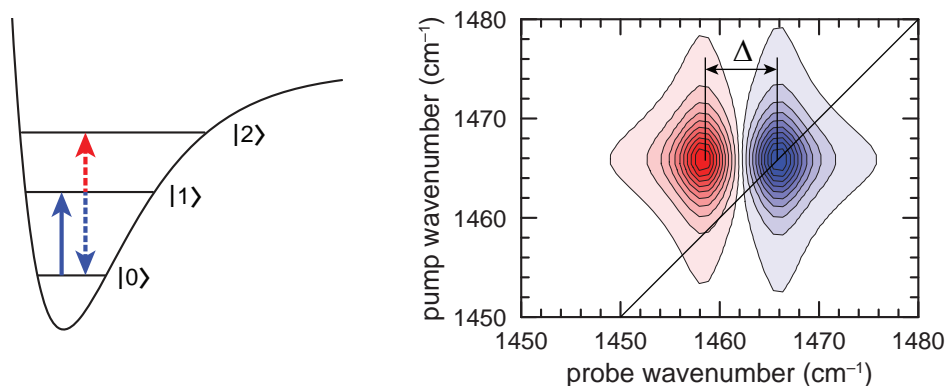## 2.2.1   Diagonal Peaks[7,15,17,24,26,46,55,74,75]

Figure 2.8: *Left: Level scheme of an anharmonic oscillator. The solid blue arrow indicates the pump excitation. The dashed arrows highlight the probe response – excited state absorption from $|1\rangle$ to $|2\rangle$ and stimulated emission from $|1\rangle$ to $|0\rangle$. Right: Simulated 2D-IR diagonal peak. Positive signals (red) are caused by excited state absorption, negative signals are caused by stimulated emission and bleach. If the anharmonicity is large compared to the line width of the bands, the two signals are separated by the anharmonicity Δ.*

As already mentioned, a diagonal peak is composed of two parts, a positive (red) and a negative (blue) one (Fig. 2.8 right). The appearance of these two parts can be easiest rationalized in the double resonance picture. Lets consider an anharmonic oscillator in its ground state $|0\rangle$ (see Fig. 2.8 left). If the pump pulse is resonant with a vibration, it excites the vibration and populates the first excited state $|1\rangle$ (straight blue arrow), which is not populated at room temperature. Since the ground state is depleted, the subsequent probe pulse is absorbed less by the ground state (bleach), causing a negative signal (blue). The bleach is at the same probe and pump wavenumber, *i.e.*, exactly on the diagonal. The probe pulse also interacts with the molecules in the first excited vibrational state. It can stimulate the emission of light, which leads to a relaxation of the excited vibration (stimulated emission, dashed blue arrow). Emission appears in the spectrum as if there would be less absorption and thus causes a negative signal (blue) at the wavenumber corresponding to the transition between $|0\rangle$ and $|1\rangle$. This is exactly the same transition that was excited by the pump pulse and thus this signal also appears exactly on the diagonal, on top of the bleach signal. The probe pulse can also be absorbed by the first excited state (excited state absorption, dashed red arrow). This additional absorption leads to a positive signal (red) in the 2D-IR spectrum at the wavenumber corresponding to the energy gap between the levels $|1\rangle$ and $|2\rangle$. Since vibrations are anharmonic, the energy gap between $|1\rangle$ and $|2\rangle$ is smaller than between $|0\rangle$ and $|1\rangle$. This implies that the positive signal is redshifted compared to the diagonal. In cases where the anharmonicity is large compared to the line width of the bands, the spacing between

the maxima of the positive and negative signal is a direct measure of the vibrational anharmonicity Δ. If the anharmonicity is smaller or of similar magnitude as the line width, the spacing appears larger than the actual anharmonicity due to cancellation effects and the bleach signal appears to be shifted in the 2D-IR spectrum. In case of an harmonic oscillator, the energy levels would be spaced equidistantly, and positive and negative signal would sit exactly on top of each other and cancel.

The diagonal peak intensity decreases with increasing delay time between pump and probe pulse because vibrational relaxation takes place. Typically, the relaxation times are in the range of several ps.
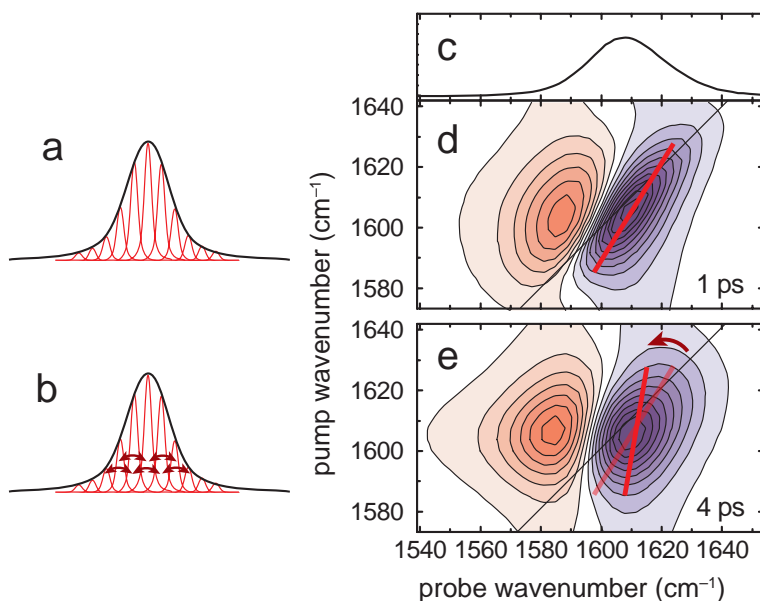
Figure 2.9: *Simulated 2D-IR diagonal peak of an inhomogeneously broadened IR band for different delay times (d: 1 ps, e: 4 ps). The absorption spectrum is shown on top (c) for reference. An inhomogeneously broadened band consists of many narrow bands at different frequencies (a). With increasing delay time, the molecules leading to the single bands exchange (b) and the tilt of the diagonal peak decreases as indicated in (e). The absorption and 2D-IR spectra were adapted with permission from ref. [15], copyright 2002, IOP Publishing.*

For many systems, particularly for proteins, the diagonal peaks are tilted towards the diagonal for short delay times between pump and probe pulse, as shown in Fig. 2.9 d. In this case, the IR absorption is inhomogeneously broadened. In other words, the absorption band, which appears to be one, broad band consists of many much narrower, strongly overlapping bands, as illustrated in Fig. 2.9 a. Thus, also the diagonal peak consists of many, overlapping diagonal peaks, each at a slightly different position, leading to a broad, tilted peak. Such a inhomogeneity can be caused by a distribution of conformations or solvent effects such as strong and weak hydrogen bonding.[25,29–34,91,92] The tilt of the diagonal peak depends on the delay time between the pump and probe pulse. For short delay time, the excited molecule is still in the same surrounding when the probe pulse arrives as when it was hit by the pump pulse – leading to a strong tilt (Fig. 2.9 d). For long delay times, thermal fluctuations change the environment and the memory of the initial surrounding and thus transition wavenumber is lost (Fig. 2.9 b). The line shape of the diagonal peak

does not depend on the initial pump wavenumber anymore. Thus, the tilt decreases (Fig. 2.9 e) and finally disappears. This process is called spectral diffusion and can be used to investigate the dynamics of hydrogen bonds, solute solvent interactions, or how flexible molecular structures such as the backbone conformation in a protein are. [15,25,26,32,41,91–93]

2.2.2   Cross Peaks

Several mechanisms lead to the emergence of cross peaks, showing the interaction between vibrations or the presence of dynamical processes in equilibrium. Some of these mechanisms are coupling between vibrations, population transfer, intramolecular vibrational energy redistribution (IVR), and chemical exchange. These mechanisms and their impact will be discussed in the following sections. In addition, Fermi resonances may lead to cross peaks in a 2D-IR spectrum. [46] However, this process, which leads to a different cross peak shape, will not be discussed here. Information on the molecular properties obtained by analyzing cross peaks are usually not accessible by linear IR spectroscopy.

Molecular Coupling [7,15–18,46,55,74]

Vibrations within a molecule can couple to each other, *e.g.*, *via* mechanical coupling, vibrationally induced electron movements, or transition dipole coupling. For transition dipole coupling, the coupling strength depends on the relative orientation of the transition dipoles to each other and on the distance between them. The coupling is strongest, if the transition dipoles are close and aligned parallel and negligible, if they are far apart. Mechanical coupling works similar as known from a classical experiment where, *e.g.*, balls are connected with springs. If one ball is displaced from its equilibrium position, also the other balls start to wiggle.
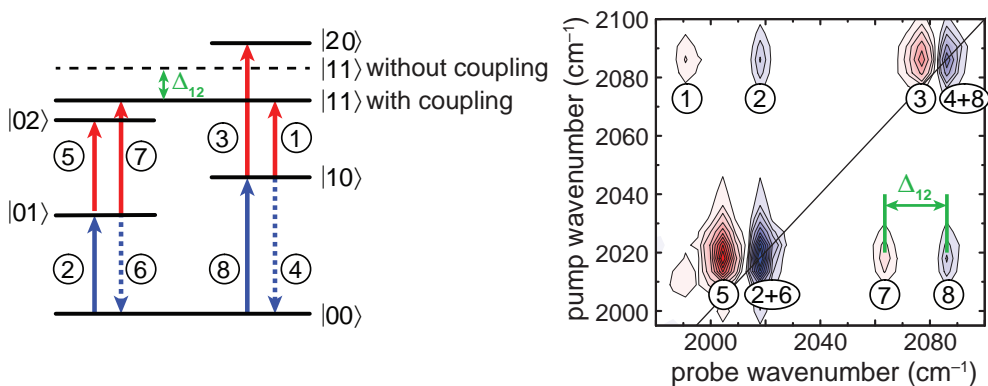

Figure 2.10: *Left: Level scheme of two coupled oscillators like the two carbonyl vibrations in RDC. The transitions that lead to signals in the 2D-IR spectrum are marked by the colored arrows. Blue arrows lead to negative signals, red arrows to positive signals. The dashed line indicates the energy of the state $|11\rangle$ without coupling. The shift of this level due to coupling is the off-diagonal anharmonicity Δ_{12}. Right: 2D-IR spectrum of RDC for a delay time of 2 ps. Blue: negative signals; red: positive signals. 2D-IR signals and transitions in the level scheme are numbered accordingly. The spectrum was kindly provided by Jens Bredenbeck. [84]*

The spectrum of dicarbonylacetylacetonato rhodium (RDC) is an instructive example of a 2D-IR spectrum of two coupled vibrations (Fig. 2.10).[18,84,94] The corresponding level scheme in a modified normal mode picture[iii] is shown next to the spectrum for explanation. The arrows in the level scheme indicate the transitions that cause the signals observed in the 2D-IR spectrum. Peaks and arrows are numbered accordingly.

The diagonal peaks arise in the very same manner as described before. If the pump pulse is resonant with one transition, *e.g.*, the transition from $|00\rangle$ to $|10\rangle$ (2), excited state absorption (5), stimulated emission (6), and bleach (2) form the diagonal peak. In the case of two oscillators, additionally the transition from $|10\rangle$ to $|11\rangle$ (7) is accessible by the probe pulse leading to excited state absorption (positive signal). Since the ground state $|00\rangle$ is depleted by the pump pulse, also the transition from $|00\rangle$ to $|01\rangle$ (8) is bleached (negative signal). In the case of coupled oscillators, the two cross peak contributions (7 and 8) are separated by the off-diagonal anharmonicity Δ_{12}, which is a function of the energy difference between the coupled vibrations, the coupling constant, and the diagonal anharmonicity of the involved vibrations. The experimental 2D-IR spectrum of RDC clearly shows that the off-diagonal anharmonicity generally differs from the diagonal anharmonicity. If the two modes do not couple with each other, the transitions 7 and 8 are still allowed, however, their contributions cancel each other exactly since they have the same transition frequency.

Cross peaks that are caused by coupling arise instantaneously and show exactly the same time dependence as the corresponding diagonal peak (the diagonal peak with the same pump wavenumber). They provide a sensitive probe for nature of the eigenstates of the molecule. Using the information provided by the cross peaks, their shape, anharmonicity, and intensity, the bands can be assigned and details on the delocalization of the band as well as the structure of the molecule can be retrieved.[95] Additionally, close intermolecular contacts can be detected by couplings.[96,97] In mixtures, cross peaks indicate which vibrations belong to the same molecule.[37,75,98]

Population Transfer[15,18,46]

Not only couplings, but also dynamical processes such as relaxation can induce cross peaks. One special case is population transfer, in NMR spectroscopy also known as cross relaxation.[99,100] It is facilitated by fluctuations of vibrational couplings, modulating the energy levels $|10\rangle$ and $|01\rangle$. These modulations allow that population from $|10\rangle$, where it was originally created by the pump pulse, can be transferred to $|01\rangle$ and *vice versa*. The population can be transferred to a state with lower energy or, if the energy difference between the two states is small compared to $k_B T$, also to a state with higher energy.[101] Population transfer is indicated by the green arrows in the level scheme (Fig. 2.11 left) and leads to additional peaks in the 2D-IR spectrum of RDC measured with a delay of 7 ps (Fig. 2.11 right).[18,84] The green numbers indicate the transitions leading to the additional peaks. If, *e.g.*, the pump is resonant with the transition from $|00\rangle$ to $|10\rangle$ (2), the state $|10\rangle$ becomes populated and the transitions 2, 5, 6, 7, and 8 can be accessed by the probe. Without any relaxation, the transitions 1, 3, and 4 are not accessible, since there is no population in state $|01\rangle$. Population transfer leads to a partial depletion of state $|10\rangle$ and a population of state $|01\rangle$. Accordingly, the transitions 1, 3, and 4 become accessible to the probe

---

[iii]Normal modes exist only in the harmonic approximation and are orthogonal to each other, *i.e.*, cannot couple. In the modified model, anharmonicity is introduced *ad hoc*.
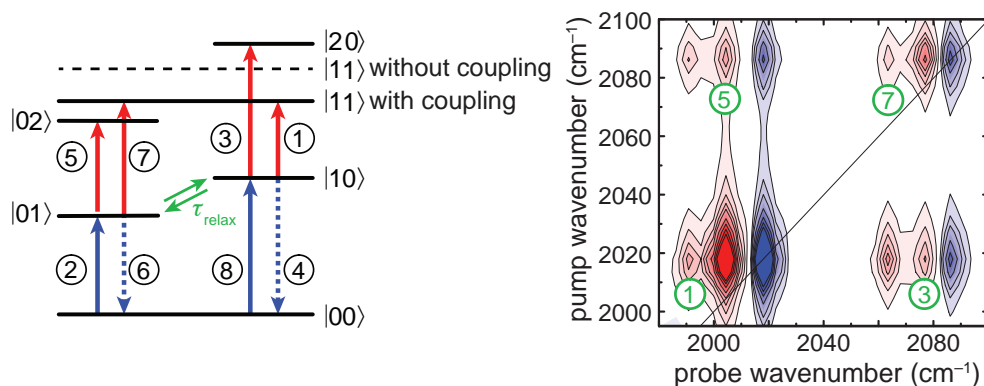
Figure 2.11: *Left: Visualization of population transfer (green arrows) in the level scheme of two coupled oscillators. Right: 2D-IR spectrum of RDC for a delay time of 7 ps. blue: negative signals, red: positive signals. The green numbers highlight the bands created via population transfer (c.f. Fig. 2.10). Additional 2D-IR signals and transitions in the level scheme are numbered accordingly. The spectrum was kindly provided by Jens Bredenbeck.* [84]

and show up in the spectrum as if there would have been a partial direct excitation of transition 8. In that sense, the response of the two pump positions is mixed. The diagonal peak contributions 3 and 4 appear as additional cross peak and the excited state absorption 1 as additional positive feature of the diagonal peak. As already mentioned, population transfer is caused by the fluctuations of the couplings. Hence, population transfer is important if vibrations are strongly coupled, *e.g.*, in metal carbonyls. [21,35,38]

The intensity of a population transfer induced cross peak is zero for a delay time of $t = 0$ ps and raises with increasing delay time as the state is populated. Vibrational relaxation and back population transfer cause a decrease of the signal at longer times. Because population transfer is bidirectional, population transfer cross peaks disappear on a similar time scale as the corresponding diagonal peak, in most cases a little bit earlier as their intensity is smaller.

Population transfer can be used to investigate the fluctuations of the couplings between vibrations. Since the coupling is in many cases related to the structure of the molecule, these fluctuation give insight on the conformational fluctuations within a molecule, *i.e.*, which part of the molecule is flexible and which part is stiff. [101]
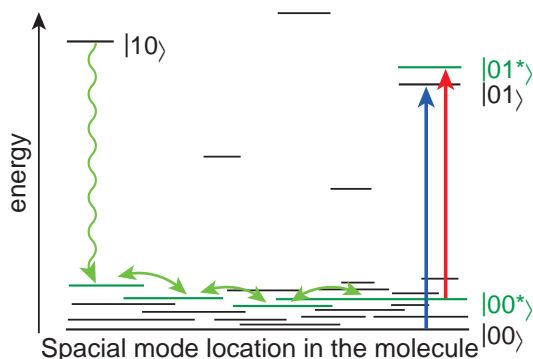
Intramolecular Vibrational Energy Redistribution[22,44,46]

Figure 2.12: *Level scheme to illustrate the mechanism of IVR induced cross peaks. The green arrows show the relaxation from the initially populated vibration (wiggly arrow) and the heat redistribution (straight arrows). The red and blue arrows indicate the transitions leading to the cross peak. Adapted with permission from ref. [22]. Copyright 2009, American Chemical Society.*

Another relaxation process that causes cross peaks is IVR.[22,44] The mechanism is illustrated in Fig. 2.12. The excited high energy mode (here $|10\rangle$) relaxes to modes that are lower in energy (wiggly arrow). These low energy modes are delocalized over a larger area of the molecule and are strongly coupled to other low frequency modes. Mechanisms such as population transfer and other relaxation paths redistribute the energy (straight arrows), originally disposed in one, more or less localized vibration, to a larger part of the molecule and induce a heating of this part. This heating expands with time over the whole molecule and is eventually transfered to the solvent. Some of the excited low energy modes couple themselves to other high energy modes and create *via* the mechanism described in section 2.2.2 cross peaks. The off-diagonal anharmonicity of cross peaks between directly coupled vibrations are usually larger than for those who arise through IVR. The underlying mechanism is exactly the same as for the temperature dependent shift of IR bands. This is also the reason, why heating of the solvent induced by the pump pulse can lead to artifacts in 2D-IR spectra.

Since IVR is an entropy driven mechanism, it is not reversible. This has a main implication for the time dependence of the cross peak in the 2D-IR spectra. The diagonal peak can be completely relaxed before the heat arrives at the position of the other high energy mode. The cross peak arises not before that time point and disappears as the molecule cools down. In other words, this means that this kind of cross peak can in some cases persist much longer than the diagonal peak – a major difference to the cross peaks induced by direct population transfer.[22]

Relaxation-assisted 2D-IR (RA-2D-IR) spectroscopy uses this mechanism to enhance cross peaks.[22,44,45] The delay times when the cross peaks appear are a sensitive measure for the distances in a molecule and for the delocalization of the involved vibrations. This mechanism also gives insight on how energy and heat are transported through a molecule.[11,19,20,102]
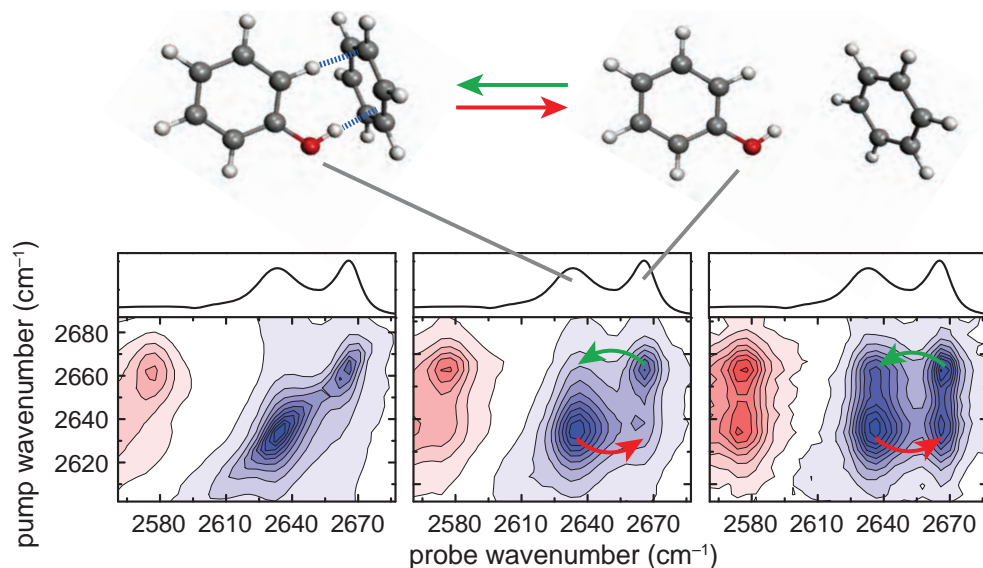
Chemical Exchange[3,7,42,46,74,75]

Figure 2.13: *EXSY-2D-IR spectra of a phenol-benzene mixture for different delays (left: 1 ps, middle: 5 ps, right: 20 ps). The spectra are normalized to the largest signal. The molecular structure of the involved species is schematically illustrated as reference on top. The colored arrows highlight the exchange process (green: complex formation, red: dissociation). The figure was adapted with permission from ref. [103].*

A completely different mechanism leading to cross peaks is chemical exchange. All processes that were discussed so far occurred in one quantum system that did not change (despite small fluctuations causing relaxation). Chemical exchange however means that a molecule changes its properties, *e.g.*, through a conformational change or complex formation and dissociation. In a simplified picture, the excitation induced by the pump stays on the vibration and due to the change of the molecule, the frequency of this vibration changes. Figure 2.13 shows the 2D-IR spectrum of a phenol-benzene mixture in chloroform.[28,103] Phenol and Benzene form hydrogen bonded complexes. The OH stretch vibration is sensitive to complexation and absorbs differently if it belongs to the complex or to the free phenol. So if the OH stretch vibration of the complex is excited by the pump pulse and the complex dissociates before the probe pulse interacts, the probe pulse detects the response of the OH vibrations in the free phenol. This process is highlighted by the red arrows in Fig. 2.13. The opposite process, the complex formation is marked by the green arrows. The cross peaks show exactly the same anharmonicity as the corresponding diagonal peaks (the diagonal peaks at the same probe wavenumber), similar as the peaks induced by population transfer. They are also dynamic, meaning that they are absent for a delay of $t = 0$ ps and increase in intensity as time evolves and exchange takes place. Vibrational relaxation leads to a decrease of the intensity like it is the case for the diagonal peak and thus limits the maximal observation time. Since the two vibrations belong to different quantum systems, there can never be another type of cross peak between them.

Exchange 2D-IR spectroscopy (EXSY-2D-IR) uses this mechanism to investigate structural dynamics and reaction dynamics in a wide variety of systems.[27,28,30,35,40–43]

2.2.3 Polarization Dependence[7,24,46]

The intensity of the signals in 2D-IR spectra depends first of all on the properties of the involved vibrations, *i.e.*, their transition dipole moments and the angle between them. Additionally, it depends on the experimental settings, *i.e.*, the intensity of the laser pulses and their relative polarization. In isotropic samples, there are only three independent polarization conditions. The signal intensities are related by:

$$\langle ZZZZ \rangle = \langle XXZZ \rangle + \langle XZXZ \rangle + \langle ZXXZ \rangle. \tag{11}$$

The notation $\langle XXZZ \rangle$ represents the measured response, *i.e.*, signal, if the light of the first two interactions is polarized along the x-axis and the light of the last two interactions parallel to the z-axis (the direction of the light is along the y-axis). Any spectrum measured with arbitrary polarized pulses $\langle \alpha\beta\gamma\delta \rangle$ can be reconstructed using three of the spectra in eq. 11. In pump-probe spectroscopy, the first two interactions are caused by the pump pulse and the last two by the probe pulse. Thus, only spectra with the polarization condition $\langle \alpha\alpha ZZ \rangle$ can be measured. α describes the angle between pump and probe polarization. In pump-probe spectroscopy, $\langle ZZZZ \rangle$ is often referred to as $\Delta\alpha_\parallel$ and $\langle XXZZ \rangle$ as $\Delta\alpha_\perp$.[iv] The polarization dependence of a signal is a function of the angle θ between the involved transition dipole moments. For a signal measured with the polarization condition $\langle \alpha\alpha ZZ \rangle$, the polarization dependent factor $D(\alpha)$ is given by:

$$D(\alpha) = \cos^2(\alpha)(1 + 2\cos^2(\theta)) + \sin^2(\alpha)(2 - \cos^2(\theta)). \tag{12}$$

Thus, polarization dependent 2D-IR measurements can be used to derive the angle between transition dipole moments. A measure for the polarization dependence of a signal is the anisotropy r, calculated as:

$$r = \frac{\langle ZZZZ \rangle - \langle XXZZ \rangle}{\langle ZZZZ \rangle + 2\langle XXZZ \rangle} = \frac{\Delta\alpha_\parallel - \Delta\alpha_\perp}{\Delta\alpha_\parallel + 2\Delta\alpha_\perp}. \tag{13}$$

For a fixed isotropic distribution of molecules, the anisotropy gives direct access to the angle θ between the transition dipole moments of the vibrations of the molecule *via* the relation:[104]

$$\theta = \cos^{-1}\sqrt{\frac{5r + 1}{3}}. \tag{14}$$

This relationship is illustrated in Fig. 2.14. The curve is fairly steep for small and large anisotropies (around –0.2, corresponding to an angle of 90° and around 0.4, corresponding to 0°) and much flatter in between. This shape has an important consequence for the accuracy of the angle measurement: small errors in the measured anisotropy have a much larger effect on the determined angle, if the real angle is close to 0° or 90° than if it is, *e.g.*, around 45°. Lets assume, the accuracy of the anisotropy measurement is ±0.01, then, for a measured anisotropy of 0.39 the confidence interval around the determined angle of 7.4° is from 0° to 10.5° (see green shaded area in Fig. 2.14). For a measured anisotropy of 0.1, the confidence interval around the determined angle of 45° is only ±1° (see blue shaded area in Fig. 2.14). The measurement is thus much more precise. The angle, for which the signal size is independent from the polarization, *i.e.*, $r = 0$, is called magic angle. It has a value of $\theta \approx 54.74°$.

[iv]Also $I_\parallel$ and $I_\perp$ are commonly used as synonyms.
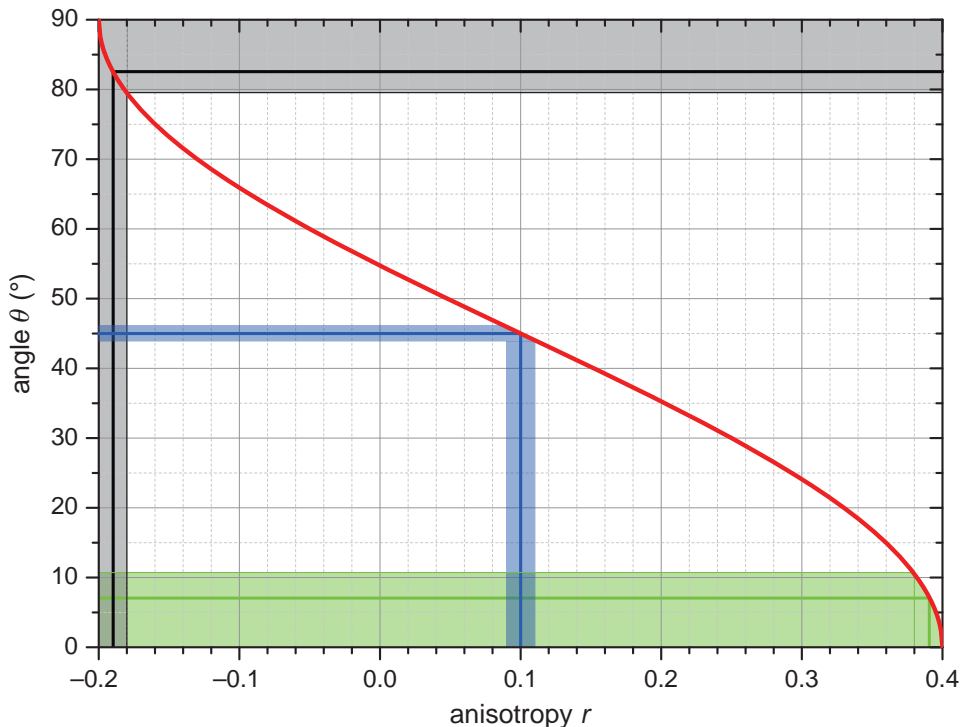
Figure 2.14: *Relation of the peak anisotropy r and the angle θ between the involved transition dipole moments (red curve). The angle determination is illustrated for anisotropy of –0.19 (black line), 0.1 (blue line), and 0.39 (green line). The gray, blue, and green shaded areas illustrate the accuracy of the angle determination for an assumed accuracy of 0.01 for the anisotropy measurement.*

Alternatively, also the ratio $x = \langle ZZZZ \rangle / \langle XXZZ \rangle = \Delta\alpha_\parallel / \Delta\alpha_\perp$ can be used to derive the angle θ *via*:

$$\theta = \cos^{-1} \sqrt{\frac{6x - 4}{3x + 3}}. \tag{15}$$

From the mathematical point of view, eq. 14 and eq. 15 are identical. However, from the experimental point of view it is sometimes more convenient to determine the relative peak intensity x by subtracting one spectrum from the other such that the peak of interest vanishes:

$$\langle ZZZZ \rangle - x\langle XXZZ \rangle = \Delta\alpha_\parallel - x\Delta\alpha_\perp = 0 \tag{16}$$

This procedure can also be used to suppress strong peaks, *e.g.*, diagonal peaks, to reduce overlap with smaller signals and therefore enhance the resolution. With a setup that allows the control of the polarization of all four pulses, distinct signals can be suppressed directly by choosing the proper polarizations. This is used, *e.g.*, in polarization angle scanning 2D-IR (PAS 2D-IR) spectroscopy discussed in chapter 7.3.1.[105–107] The measurement of $\langle \frac{\pi}{3}, -\frac{\pi}{3}, 0, 0 \rangle$ is for example equivalent to $\frac{1}{4}(\langle ZZZZ \rangle - 3\langle XXZZ \rangle)$. In such a measurement, diagonal peaks are suppressed experimentally.[108]

A more detailed analysis of the polarization dependence, including the derivation of the equations and possible experimental pitfalls such as saturation effects can be found in references [18,46,104,108–118].

Rotational Diffusion

So far, only static and isotropic systems have been considered. However, in solutions the molecules are not fixed in space. They move around and rotate. The rotation affects the polarization dependence of the spectra. Thus, the measured anisotropy is not constant, but a function of the delay time t between pump and probe pulse:

$$r(t) = r(0)e^{-6Dt_{mix}} = \frac{3\cos^2\theta - 1}{5}e^{-6Dt_{mix}}, \tag{17}$$

where D is the Debye constant, also known as rotational diffusion constant.[119] The rotational correlation time τ_c is calculated as:

$$\tau_c = \frac{1}{6D}. \tag{18}$$

For small molecules, such as small organic compounds, the rotational correlation times are in the range of several to tens of ps.[120,121] This is in the same order of magnitude as the delay times in a 2D-IR experiment, which leads to the fact that rotational diffusion influences the measured anisotropy significantly. It is therefore necessary, to extrapolate the anisotropy to zero delay time to extract correct angles that are not perturbed by rotational diffusion.[46,122] The bigger the molecule is, the slower it tumbles. Consequently, the correlation time is large for big molecules including proteins; typically in the range of several ns.[119] This is much slower than the delay times in a 2D-IR experiment. Hence, rotational diffusion can be neglected in those cases.

Chapter 3

Experimental Setup

The experimental setup for measuring 2D-IR spectra was built during this thesis and is described in this chapter. The output of a commercial laser system (chapter 3.1) was used generate mid-IR pulses by means of a setup containing optical parametric amplification (OPA) and subsequent difference frequency generation (DFG) (chapter 3.2). The mid-IR pulses were coupled into the 2D-IR setup (chapter 3.3), which was modified and improved for the polarization dependent measurements (chapter 3.3.1) to determine the structure of molecules and complexes (see part II of this thesis). For the study of conformational dynamics of myoglobin (see part III), a high-power OPA setup (chapter 3.2.2) was added for the generation of intense pump pulses.

3.1 Laser Source

For the generation of of short laser pulses (800 nm), the commercial regenerative amplifier system *Spitfire Pro XP* built by Spectra Physics was used.[123–126] It consists of mainly four parts as sketched in Fig. 3.1.[127]
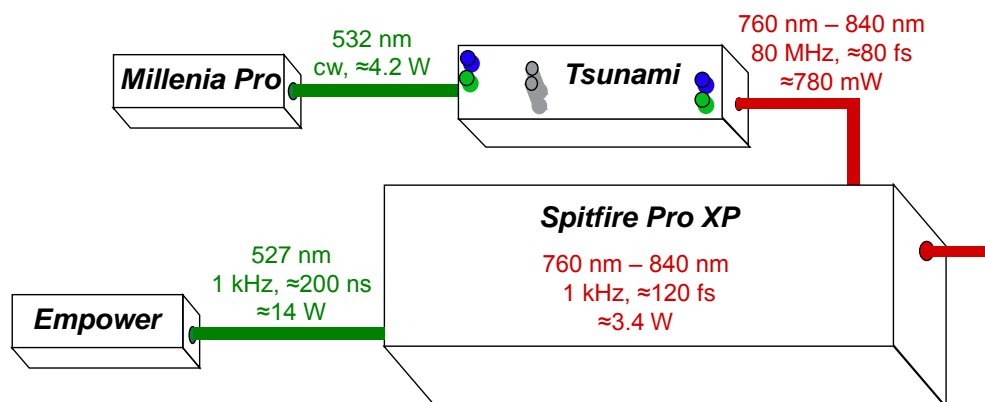
Figure 3.1: *Scheme of the Spitfire Pro XP setup showing the acessible frequency ranges, repetition frequencies, and typical energies of the used system. Adapted with permission from ref. [127].*

In brief, *Millenia Pro 5sJ* is a continuous wave (cw), diode-pumped laser at a wavelength of $\lambda = 532$ nm.[125] As laser medium it uses a neodymium(III) doped yttrium vanadate (Nd:YVO) crystal, where neodymium ions are responsible for lasing and emit light at $\lambda =$1064 nm. After the laser cavity, the output is frequency doubled in a temperature stabilized lithium triborate (LBO) crystal. LBO is a birefringent material that facilitates that two waves add up to generate a new wave with doubled frequency, *i.e.*, 532 nm. The output beam has a power of up to 5 W.

Empower 30 is a diode-pumped, Q-switched neodymium(III) doped lithium yttrium fluoride (Nd:YLF) laser running at a repetition rate of 1 kHz.[124] The neodymium ions in this surrounding emit 1053 nm laser light, which is frequency doubled to 537 nm in a temperature stabilized LBO crystal in the laser cavity. The Q-switching is done by means of an acoustic optical modulator (AOM) yielding in pulses with a pulse length of 100–350 ns and an output energy of up to 20 mJ. The laser is externally triggered by a function generator to adjust the repetition rate slightly in steps of 0.1 Hz to minimize interferences with the measurement electronics.

The laser oscillator *Tsunami* generates a pulse train of $\approx$80 fs long pulses with a repetition rate of around 80 MHz.[126] The laser medium, a temperature controlled titanium(III) doped sapphire (Ti:Sa) crystal, is pumped by the output of Millenia. The in the crystal embedded titanium ions have a very broad emission spectrum and thus can be used in tunable lasers. The frequency of Tsunami can be tuned in the range from 720–850 nm by a combination of four prisms and a slit in the laser cavity. The slit selects the wavelength while the prisms compensate for group velocity dispersion (GVD). The oscillator can be ran either actively mode locked with an AOM or passively mode locked. In our case, it was typically ran passively mode locked. The output power is $\sim$750 mW.

Spitfire XP Pro amplifies the laser pulses generated by Tsunami employing chirped pulse amplification (CPA).[123] The pulses are stretched using gratings before they are guided to the laser cavity of the spitfire. A Pockels cell selects one pulse of the pulse train that can enter the cavity and seed the lasing process in a Ti:Sa crystal. This Pockels cell is triggered by the Empower, which is used to pump the Ti:Sa crystal. The amplified pulse is coupled out of the cavity when it reaches maximal intensity by another Pockels cell. After passing a telescope, the pulse is compressed to $\sim$120 fs. At the output, the amplified pulses have an energy of $\approx$3.4 mJ/pulse with a repetition rate of 1 kHz. The spectral properties of the pulse are determined by the seed pulses. The beam diameter $(1/e^2)$ is $\approx$8 mm.

3.2   Mid-IR Generation

The Spitfire output was used to generate mid-IR light in the OPA setups using the processes of white light generation, optical parametric amplification, and difference frequency generation. These fundamental nonlinear optical processes are explained briefly before the experimental setup of the two OPAs is described. More detailed descriptions of the nonlinear processes can be found in several textbooks and publications, which have been used for the following summary.[128–131]

White Light Generation

Focusing intense, narrowband laser pulses to specific media leads to a significant broadening of the spectrum generating white light, also referred to as supercontinuum. This process has first been described by Alfano and Shapiro for glass[132] and afterwards white light generation was also seen in other media involving solids, liquids, and gases.[133,134] The underlying processes are still under investigation and rather complex; most probably several mechanisms including self-phase modulation, self-focusing, filamentation, GVD and self-steepening are involved.[133–139] The high intensities of focused beams lead to a distortion of the charge distribution in the material, resulting in a time and intensity dependent change of the refractive index. Most importantly, the refractive index determines the speed of light. Changes in the refractive index thus effect how fast the pulse and the different frequencies of the laser pulse travel through the medium. Because the beginning of the laser pulse experiences a different refractive index than the later parts, the time profile (self-phase modulation and self-steepening) and consequently the spectrum of the pulses are altered (GVD). The refractive index changes not only with time, but is also dependent on the spacial intensity profile. Therefore the center of the beam experiences a different refractive index than the outer parts leading to lensing effects (self-focusing). Other effects including multi-photon absorption counteract the focusing. If focusing and defocusing compensate exactly, filamentation occurs. This means that the pulse stays focused over a long range. All the described effects lead to white light generation. Since the refractive index is frequency dependent, the generated pulses are strongly chirped.

Several materials can be implemented in ultrafast laser setups for withe light generation such as sapphire, CaF_2, yttrium vanadate, yttrium aluminum garnet, gadolinium vanadate, and potassium-gadolinium tungstate.[139] In the applied setup a sapphire plate was used.

Frequency Conversion

Several nonlinear processes are known that convert laser pulses of one frequency to pulses with another frequency. These processes are summarized by the term frequency conversion and include second harmonic generation (SHG), sum frequency generation (SFG), difference frequency generation (DFG), and optical parametric amplification (OPA). All mentioned processes depend on the electric field of the light to the power of two; therefore these processes are termed nonlinear. The electric field of the light,

$$\vec{E} = \vec{E_0} \cos(\omega t + \vec{k}\vec{z}), \tag{19}$$

is a function of time t and the position in the direction of travel $\vec{z}$. It also depends on the frequency ω and the wave vector $\vec{k}$. In a crystal or any other material the light induces a polarization,

$$\vec{P}(\vec{E}) = \epsilon_0(\chi^{(1)}\vec{E} + \chi^{(2)}\vec{E}^2 + \chi^{(3)}\vec{E}^3 + ...), \tag{20}$$

where χ^n is the nth order susceptibility of the material. The magnitude of χ^n decreases rapidly with increasing order n. This is the reason why for low light intensities in everyday life only the linear susceptibility is observed. The magnitude of χ^n also depends strongly on the material, *i.e.*, the crystal, and its symmetry (*e.g.*, $\chi^2 = 0$ for media with inversion symmetry). The second order polarization

$$\vec{P}^{(2)}(\vec{E}) = \epsilon_0 \chi^{(2)} \vec{E}^2, \tag{21}$$

is responsible for the nonlinear processes mentioned above. If two waves $\vec{E_1}$ and $\vec{E_2}$ interact simultaneously with the crystal, the second order polarization is given by:

$$
\begin{aligned}
\vec{P}^{(2)}(\vec{E_1} + \vec{E_1}) =\ & \epsilon_0 \chi^{(2)}(\vec{E_{01}}^2 + \vec{E_{02}}^2) \\
& + \epsilon_0 \chi^{(2)}\left[\vec{E_{01}}^2 \cos(2\omega_1 t + 2\vec{k_1}\vec{z}) + \vec{E_{02}}^2 \cos(2\omega_2 t + 2\vec{k_2}\vec{z})\right] \\
& + \epsilon_0 \chi^{(2)}\left[\vec{E_{01}}\vec{E_{02}} \cos\left((\omega_1 + \omega_2)t + (\vec{k_1} + \vec{k_2})\vec{z}\right)\right] \\
& + \epsilon_0 \chi^{(2)}\left[\vec{E_{01}}\vec{E_{02}} \cos\left((\omega_1 - \omega_2)t + (\vec{k_1} - \vec{k_2})\vec{z}\right)\right].
\end{aligned}
\tag{22}
$$

This equation clearly shows that the two waves interact with each other and new waves with different frequencies are generated. The different lines in the equation belong to different processes. The first line without any frequency is referred to as optical rectification, which means that a non-oscillating polarization is induced in the medium. The second term involving the frequencies $2\omega_1$ and $2\omega_2$ describe SHG. The third line depending on $(\omega_1 + \omega_2)$ and the fourth line depending on $(\omega_1 - \omega_2)$ correspond to SFG and DFG, respectively. The processes SHG, SFG, and DFG are also grouped under the umbrella term three-wave-mixing because two waves generate a third one $(2 + 1 = 3)$.

In order to be efficient, the generated wave $\vec{E_3}$ needs to interfere constructively with the polarization by which it is created at every position in the crystal. This requirement is satisfied, if:

$$
\vec{k_3} = \vec{k_1} + \vec{k_2}.
\tag{23}
$$

This condition is called *phase matching* and is equivalent with conservation of momentum. Using the definition of the wave vector,

$$
\vec{k}(\omega) = \frac{n(\omega)}{c}\vec{e_z},
\tag{24}
$$

equation 23 transforms to

$$
n(\omega_3)\omega_3 = n(\omega_1)\omega_1 + n(\omega_2)\omega_2.
\tag{25}
$$

$n(\omega)$ is the diffractive index experienced by a wave with the frequency ω. This equation can be fulfilled in birefringent crystals such as β-barium borate (BBO) or silver thiogallate (AGS) since they differ in the refractive index for light polarized along the ordinary or extraordinary axes. Phase matching can thus be achieved by a proper orientation of the crystal with respect to incoming and generated beams.

The DFG process also leads to OPA. The difference between DFG and OPA is that in DFG the two input waves are of similar intensity while in OPA the high frequency pulse (pump) is much stronger in intensity than the second, low frequency pulse (seed). This configuration leads to a gain in intensity of both low frequency pulses (which are typically called signal and idler). In other words, the seed pulse (signal) is amplified by the pump pulse and an additional pulse (idler) is generated. Usually the process is called OPA if the aim of the process is to amplify the seed and DFG if one is interested in the wave with the difference frequency.

Both, DFG and OPA are used in the setup to generate mid-IR pulses. SHG is used in the laser systems Empower and Millenia to generate green light.

3.2.1   Setup

The setup that was built to generate mid-IR laser pulses consisted of a white light seeded, two stage OPA with subsequent DFG and was based on the concept of Hamm *et al.* [131,140] It is sketched in Fig. 3.2. Approximately $366\,\mu$J/pulse of the Spitfire output (horizontally polarized) were used for the frequency conversion in the low-power setup. A small fraction of the beam was separated by a glass slide (BS1), which had an anti-reflective (ar) coating on the back side. It passed a half-wave plate ($\lambda/2$), which rotated the polarization of the beam by $90°$. The intensity of the vertically polarized beam was fine tuned by an iris to $\approx 1.9\,\mu$J/pulse before the beam was focused with a lens (L1) into a sapphire (Sa) plate, where white light was generated. The divergent withe light was subsequently focused into the BBO crystal using an achromatic lens (L2). Only the part of the white light with a wavelength larger than $665\,$nm was transmitted by the longpass filter (LF) to the BBO crystal.

The residual part of the laser light, which was transmitted by the ar coated glass slide passed over a delay stage (delay1) and was split into pump 1 and pump 2 by another glass slide (BS2, ar coated on the back side). The reflected beam, pump 1 ($\approx 1.6\,\mu$J/pulse), was focused by lens L3 to the BBO crystal. Its intensity was adjusted with neutral density filters to be just below the threshold where parametric fluorescence occurred. The beam was overlaid with the white light seed using a dichroitic mirror (DM1), which reflected the laser fundamental and transmitted the near-IR part of the white light. Pump 1 and the withe light seed entered the BBO crystal colinearly. The time overlap of both was adjusted by a delay stage (delay1). OPA in the BBO crystal led to the amplification of the white light (signal) and the generation of idler. The signal was reflected back to the BBO crystal and collimated by a dichroitic mirror (DM2) and a focusing gold mirror (FM1). The idler of the first stage was blocked directly after the dichroitic mirror (DM2).

For the second stage OPA, the reflected and collimated signal was overlaid co-linearly with pump 2 in the BBO crystal. The pump 2 pulses had an energy of $\approx 290\,\mu$J/pulse and passed a telescope (L4 and L5) to match the beam diameter to the reflected signal. The time overlap was adjusted by a delay stage (delay2). In the second OPA step generated signal and idler pulses had in sum an energy of around 80–$90\,\mu$J/pulse. The the pulse energies depended (slightly) on the wavelength of the generated beams, which could be selected by rotating the BBO crystal.

Both, signal and idler were reflected by a square gold mirror (M2) and sent to a Michelson interferometer. In the Michelson interferometer the two beams were separated with a dichroitic mirror (DM2) and overlaid in space and time with two focusing gold mirrors (FM2), from which one was mounted on a delay stage (delay3). The beams were focused into an AGS crystal leading to DFG. Broadband mid-IR pulses with a pulse length of $\sim 150\,$fs and a spectral width of $\sim 200\,$cm^{-1} were generated. Depending on the wavelength of signal and idler, the wavelength of the mid-IR pulses could be tuned between $\sim 3\,\mu$m and $\sim 10\,\mu$m. The tunability for the generated mid-IR pulses is illustrated in Fig. 3.3, while the dependence of the accessible mid-IR wavelength on signal and idler is shown in fig 3.4. The energy of the created pulses depended on their wavelength ($\approx 2.5\,\mu$J/pulse at $\lambda = 5.8\,\mu$m; $\approx 3.3\,\mu$J/pulse at $\lambda = 3.8\,\mu$m).
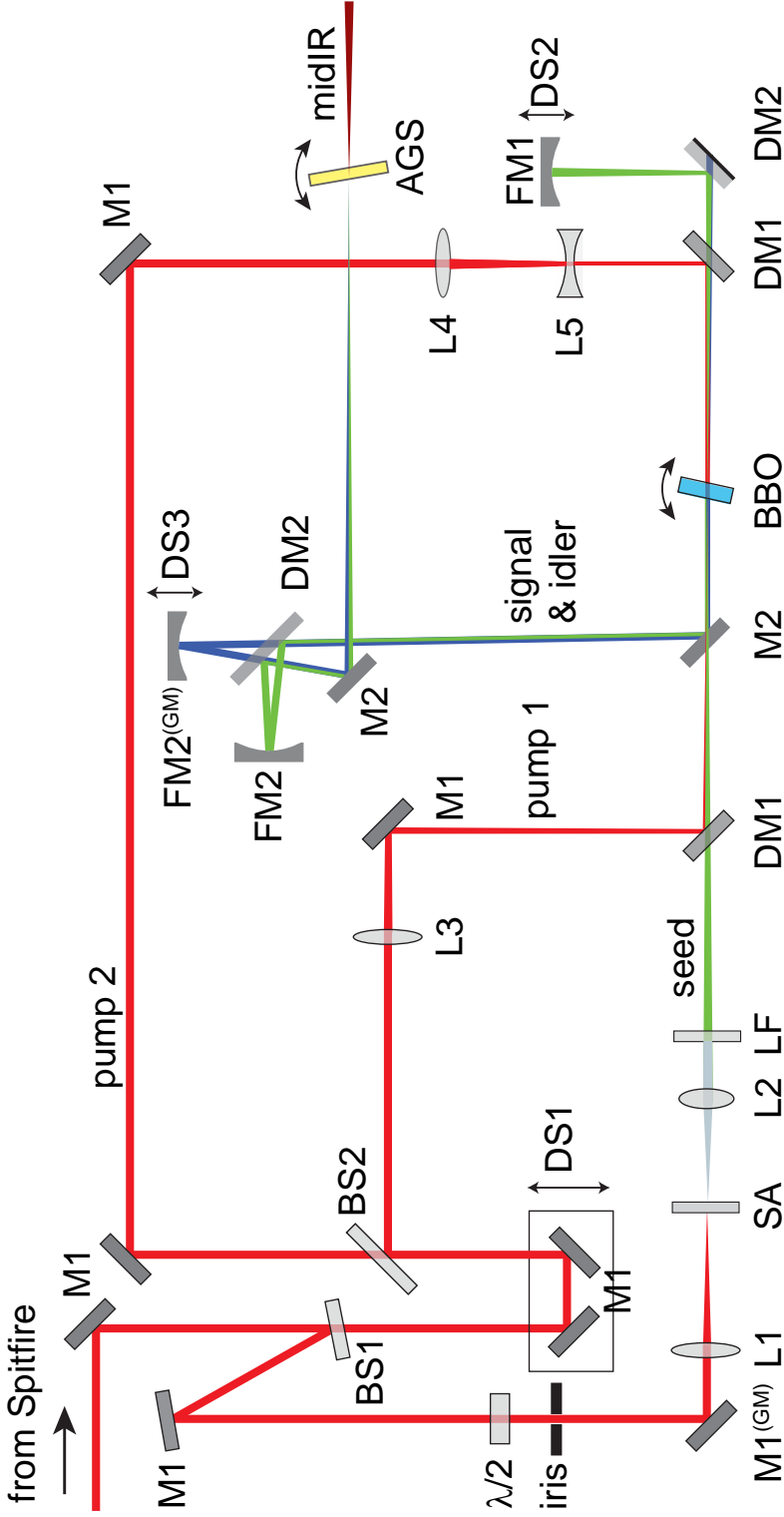
Figure 3.2: Sketch of the OPA setup used to generate mid-IR pulses.[10] The used optics are specified in the part list (see Table 3.1). M – mirror, BS – beamsplitter, DM – dichroitic mirror, FM – focusing mirror, L – lens, and LF – longpass filter. The ND filters and alignment irises are not shown. The color of the beams refer to the frequency of the pulses: red – laser fundamental (800 nm); gray – white light; green – signal (1.25–1.5 µm); blue – idler (1.75–2.3 µm); dark red – mid-IR (3–10 µm).

Table 3.1: *Used optics in the low-power OPA setup.*

	description	manufacturer
plane mirrors		
M1	HRr(45°, 750–850 nm) ≥ 99.9%, GVD ≤ 20fs², Ø 5 mm, d 6.35 mm, fused silica	Layertec (100715)
M1^{GM}	same as M1, mounted on a gimbal mount	Layertec (100715)
M2	square gold mirror, 25.4 × 25.4 × 6.35 mm³, N-BK7, Au and protective (p) coating	Laseroptik (L-03715)
beamsplitters		
BS1	back: ARp(45°, 795±40 nm) ≤ 0.2%, Ø 25.0 mm, d = 3 mm. fused silica	Layertec
BS2	back: ARp(45°, 795±40 nm) ≤ 0.2%, Ø 38.1 mm, d = 3 mm. fused silica	Layertec
dichroitic mirrors		
DM1	front: HRp(45°, 800±40 nm) ≥ 99.7%, Rr(45°, 1200–2700 nm) ≤ 10%, back: ARr (45°, 1200–2700 nm) ≤ 2%, Ø 25 mm, d = 3 mm, Infrasil	Layertec
DM2	front: HRp(45°, 1220–1560 nm) ≥ 99.7%, Rr(45°, 1620–2500 nm) ≤ 10%, Ø 25 mm, d 3 mm, Infrasil	Layertec
focusing mirrors		
FM1	focusing gold mirror, r = 500 mm, Ø 25.4 mm, d = 6.35 mm, N-BK7, Au and p coating	Laseroptik
FM2	focusing gold mirror r = 1000 mm, Ø 25.4 mm, d = 6.35 mm, N-BK7, Au and p coating	Laseroptik
FM2^{GM}	same as FM2, mounted on a gimbal mount	Laseroptik

Used optics in the low-power OPA setup (continued).

	description	manufacturer
lenses		
L1	plano-convex lens, $f = 100\,mm$, Ø 25.4 mm, N-BK7, ar 650–1050 nm	Thorlabs (LA1509-B)
L2	achromatic lens, $f = 30\,mm$, Ø 12.7 mm, N-LAK22/N-SF6HT, ar (1050–1620 nm)	Thorlabs (AC127-030-C)
L3	plano-convex lens, $f = 500\,mm$, Ø 25.4 mm, N-BK7, ar (650–1050 nm)	Thorlabs (LA1908-B)
L4	plano-convex lens, Ø 25.4 mm, N-BK7, $f = 200\,mm$, ar (650–1050 nm)	Thorlabs (LA1708-B)
L5	plano-concave lens, Ø 25.4 mm, $f = -50\,mm$, N-BK7, ar (650–1050 nm)	Thorlabs (LC1715-B)
crystals		
SA	sapphire, Ø 25.4 mm, $d = 2\,mm$, cut along [001]	Topag
BBO	BBO, type II, $\Theta\,27°\ \Phi\,30°$, $5 \times 5 \times 5\,mm^3$, p coating	Döhrer
AGS	AGS, type I, $\Theta\,40°\ \Phi\,45°$, $5 \times 5 \times 1\,mm^3$, front: ar(1200–2200 nm), back: ar(2700–7000 nm)	Döhrer
miscellaneous		
λ/2	zero oder half wave plate, silica, Ø 10 mm, both sides: ar (800 nm)	Döhrer
iris	iris diaphragm, Ø 0.8–15 mm	Thorlabs (ID15/M)
LF	longpass filter, colored glass (RG665), cut on: 665 nm, Ø 25.4 mm, $d = 2\,mm$	Thorlabs (FGL665)
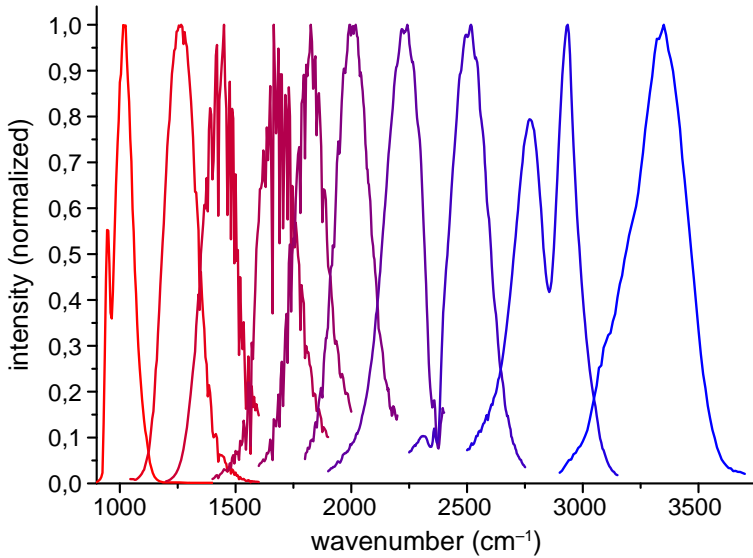
Figure 3.3: *Tunability of the mid-IR spectra. Since the setup was not purged with nitrogen, the IR absorption of water vapor and carbon dioxide modulate in the DFG spectra.*
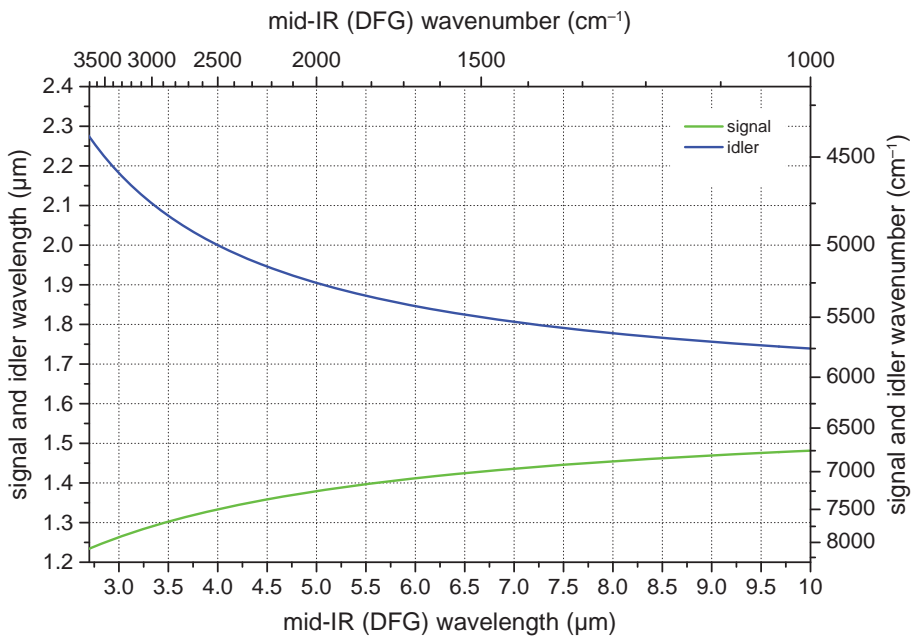
Figure 3.4: *Accessible DFG wavelengths and their dependence on the wavelength of signal and idler in the used setup for a laser fundamental of 800 nm.*

3.2.2   High-Power Setup

The high-power version of the OPA setup differed only very slightly from the setup described before. One difference is that more power from the Spitfire was used (1.6 W) and thus the pump 2 pulses had more energy (730 μJ/pulse). As consequence, the telescope (L4 and L5) was adapted to bring the power density below the damage threshold of the BBO crystal. Additionally, the size of the used crystals varied. The BBO crystal had a larger area (10 mm×10 mm×4 mm) than in the low-power setup and the AGS crystal was thinner (thickness: 0.5 mm). To reduce damage due to the high intensities, the focal lengths of the focusing mirrors in the Michelson interferometer were altered while the distance to the AGS crystal was kept constant. As consequence, the AGS crystal was not in the focus of signal and idler. All differences, including typical pulse energies, are summarized in Table 3.2. The wavelength dependence of the pulse energies was much more pronounced in the high-power setup than in the low-power setup. Typical pulse energies are given in Table 3.3.

Table 3.2: *Comparison of the two OPA setups. The presented energies are typical energies and depend on alignment and wavelength of the generated mid-IR light.*

	low-power setup	high-power setup
input energy (μJ/pulse)	366	1600
seed energy (800 nm, μJ/pulse)	1.9	1.3
pump 1 energy (μJ/pulse)	1.4	0.7
pump 2 energy (μJ/pulse)	290	730
energy of signal + idler (μJ/pulse)	70–80	300–350
mid-IR energy at $\lambda = 3.8\,\mu$m (μJ/pulse)	3.3	19.2
focus length L4 (mm)	200	500
focus length L5 (mm)	–50	–250
focus length FM2 (mm)	500	750
BBO dimensions (mm×mm×mm)	$5 \times 5 \times 4$	$10 \times 10 \times 4$
AGS dimensions (mm×mm×mm)	$5 \times 5 \times 1$	$5 \times 5 \times 0.5$
AGS position	in focus	before focus

Table 3.3: *Wavelength dependence of the energies of the mid-IR pulses generated with the high-power OPA setup.*

wavelength (μm)	pulse energy (μJ/pulse)
3.8	19.2
4.8	10.3
5.8	5.2
6.25	5.6

3.3   2D-IR Setup

The pump-probe 2D-IR setup was based on the concept of Hamm *et al.*[10] and purged with nitrogen. A sketch of the setup built during this thesis is illustrated in Fig. 3.5. The mid-IR beam generated by DFG in the AGS crystal of the OPA setup was collimated using a focusing mirror (FM3). A longpass filter (LP2) separated residual signal and idler generated in the OPA process. The neat mid-IR light, which was polarized horizontally, was guided to a BaF_2 wedge (W1), where two weak reflections ($\sim$50 nJ/pulse each) on the front and backside of the crystal generated probe and reference beam, respectively (colored in light red). The diameter of both beams was enlarged by a telescope (FM4 and FM5). They were then sent on basically the same path to the sample; the beam paths differed only in the height. An off-axis parabolic mirror (PM1) focused both beams to the sample. The focus of the probe beam ($\varnothing \approx 80\,\mu$m (FWHM)) was exactly on the focus point of the mirror (in spacial overlap with the pump beam) while the focus of the reference beam ($\varnothing \approx 90\,\mu$m (FWHM)) was shifted in height, but still in the same plane. Both beams passed the sample solution and were collimated by a second parabolic mirror (PM1). The beams were then focused by a third parabolic mirror (PM2) to an imaging spectrometer (Horiba scientific, TRIAX 180). Before probe and reference beam entered the spectrometer, the beams were made parallel to each other and perpendicular to the entrance slit of the spectrometer by two BaF_2 wedges (7.7°, W2). This allowed that the two beams
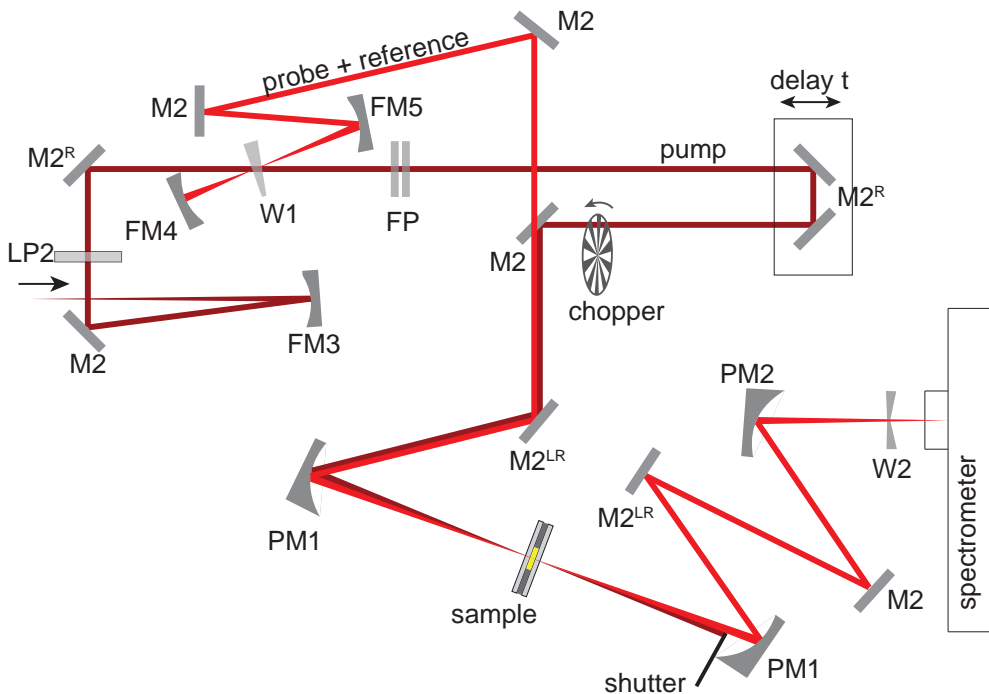
Figure 3.5: *Sketch of the 2D-IR setup. The used optics are specified in the part list (see Table 3.4). M – mirror, FM – focusing mirror, PM – parabolic mirror, LF – longpass filter, W – wedge, and FP – Fabry–Perot interferometer. The ND filters and alignment irises are not shown.*

Table 3.4: Used optics in the 2D-IR and P2D-IR setup.

	description	manufacturer
plane mirrors		
M2	square gold mirror, 25.4 × 25.4 × 6.35 mm³, N-BK7, Au and p coating	Laseroptik (L-03715)
M2R	round gold mirror, Ø 25 mm, d = 6.35 mm, N-BK7, Au and p coating	Laseroptik (L-00093)
M2LR	large gold mirror, Ø 50.8 mm, d = 6.35 mm, N-BK7, Au and p coating	Laseroptik
focusing mirrors		
FM3	focusing gold mirror, r = 750 mm, Ø 25.4 mm, d = 6.35 mm, N-BK7, Au and p coating	Laseroptik
FM4	focusing gold mirror r = 100 mm, Ø 25.4 mm, d = 6.35 mm, N-BK7, Au and p coating	Laseroptik
FM4	focusing gold mirror r = 150 mm, Ø 25.4 mm, d = 6.35 mm, N-BK7, Au and p coating	Laseroptik
parabolic mirrors		
PM1	off-axis parabolic mirror, 30°, f = 101.6 mm, Ø 50.8 mm, Au coating, aluminum	Janos (A8037-256)
PM2	off-axis parabolic mirror, 30°, f = 127.0 mm, Ø 50.8 mm, Au coating, aluminum	Janos (A8037-232)
Fabry–Perot mirrors		
FP	*experiment: structure determination of reaction intermediates* front: 89–92% reflective coating (0°, 5–8μm), back: ar(0°, 5–8μm)≤0.5, Ø 25.4 mm, d = 3 mm, ZnSe	Reynards Corporation
	experiment: conformational dynamics in proteins front: 89–92% reflective coating (0°, 3.8–5.8μm), Ø 25 mm, d = 3 mm, CaF₂	BMV optical
miscellaneous		
LP2	longpass filter, cut on 2.5 μm, transmission 70% average, Ø 25.4 mm	Janos (FXLP 0250)
W1	wedge 2°, Ø 25.4 mm, d = 1.5 mm, BaF₂	crystal
W2	wedge 7.7°, 25 × 12.5 × 4 mm³, BaF₂	crystal
additional parts P2D-IR		
λ/2	zero order half wave plate, 6 μm, free aperture Ø 9.5 mm, MgF₂	B. Halle Nachfl.
polarizer	holographic wire grid polarizer, extinction ratio (6μm): >400:1, Ø 25 mm, d = 2 mm, BaF₂	edmund optics (NT62-770)

focused to different focus points, which were individually frequency dispersed by the spectrometer to a mercury cadmium telluride (MCT) array detector (2x32 pixel). Additionally, the wedges reduced significantly imaging artifacts.

The pump beam was generated from the intense beam that was transmitted by the wedge W1. The pump pulses (colored in dark red) passed a computer controlled Fabry–Perot (FP) interferometer, which transformed the broadband input pulses into narrowband pulses, for which both, the central wavenumber and the spectral width could be chosen by adjusting the distance between the two mirrors. A typical pump pulse spectrum and the corresponding (temporal) pulse shape is shown in Fig. 3.6. For the experiments investigating the structure determination of reactive intermediate presented in part II of this thesis, the FP interferometer was tuned to 6th order, corresponding to a spectral width of $\approx 11\,\mathrm{cm}^{-1}$ and a pulse length of $\approx 1.2\,\mathrm{ps}$ ($1/e^2$). For the myoglobin experiments presented in part III of this thesis, the FP interferometer was adjusted to give a spectral width of $5.4\,\mathrm{cm}^{-1}$ (10th order, $1.5\,\mathrm{ps}$ ($1/e^2$)). The narrowband pump pulse was sent afterwards over a computer controlled, mechanical delay stage, which was used to adjust the time delay t between pump and probe pulses. A mechanical chopper running at $500\,\mathrm{Hz}$ blocked every second pump pulse to facilitate a quasi simultaneous measurement of the absorption difference of the sample induced by the pump pulse – leading to the 2D-IR spectra (see chapter 2). The narrowband pump beam was then focused by the same off-axis parabolic mirror as the other beams (PM1) to the sample, in spacial overlap with the probe beam. The focus had a spot size diameter of $\approx 130\,\mu\mathrm{m}$ (FWHM). During the measurement, the pump beam was blocked directly after the sample by a shutter. To adjust the wavenumber of the pump pulse, the shutter could be moved to block the probe beam instead and the pump beam was guided to the spectrometer, on basically the same beam path as described before for probe and reference beams.
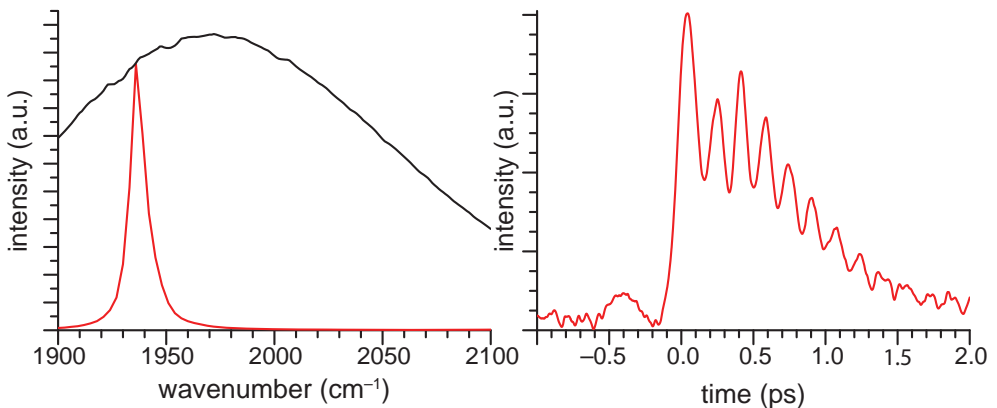
Figure 3.6: *Characterization of the pump pulse. Left: Typical spectrum of the pump pulse after the Fabry–Perot interferometer (red) in comparison to the broadband spectrum generated by the OPA setup (black). Right: Time profile of the pump pulse measured with a GaAs plate.*

The spacial overlap of probe and pump beam was adjusted by a pinhole that was located at the position where the sample cell was during the measurement. A gallium arsenide (GaAs) plate was used at that position afterwards to determine the time overlap of the two pulses. A typical measurement for determining the time overlap, which at the same time gives the (temporal) pulse shape of the pump pulse, is shown

in Fig. 3.6 (right).

For the measurements, the sample solutions were filled into a flow cell described by Bredenbeck *et al.*[141] Briefly, two CaF_2 windows are spaced by a Teflon spacer, which leaves a small channel between them. The sample was filled into this channel *via* tubes that are connected to two small holes in one window. The thickness of the spacer defines the optical pass length and was adjusted individually for each experiment, ranging between $50\,\mu$m and $250\,\mu$m.

3.3.1 P2D-IR Setup

Measuring the polarization dependence of 2D-IR spectra is a very powerful tool. P2D-IR spectra give access to the angle between vibrations and allow to enhance the resolution of 2D-IR spectra by suppressing distinct signals, *e.g.*, diagonal peaks. Many setup designs for measuring P2D-IR spectra, in particular those that measure the spectra in the frequency-domain (pump-probe setup), showed systematic errors in the measurement.[38,85,95,142–144] The errors become most obvious, if the intensities of the diagonal peaks measured under various polarization conditions are compared. If the relative polarization between pump and probe pulses are parallel or perpendicular, the diagonal peak intensities in the two spectra should have a ratio of 3:1 (see chapter 2.2.3). However, in most cases only a ratio of $\sim$2.7:1 is measured.[38,85,95,142–144] This leads to significant errors in the deduced angles between the transitions (see also Table 3.6).

In this thesis an improved frequency-domain P2D-IR setup has been built, based on similar laser setups such as polarization dependent time-resolved infrared spectroscopy.[34,122,145,146] The idea behind the setup is to excite the sample with a pump pulse that is polarized $+45°$ compared to the probe polarization. The signal, heterodyned by the probe beam, is a linear combination of the signals emitted with a polarization parallel to the pump polarization ($+45°$) and with a polarization perpendicular to the pump polarization ($-45°$). These two contributions can be selected by a movable polarizer selecting either the parallel or perpendicular signal. Figure 3.7 shows the optics added to the 2D-IR setup described in chapter 3.5 (*cf.* Fig. 3.5). The 2D-IR setup was upgraded with two fixed polarizers, a half wave plate ($\lambda/2$) and a motorized polarizer. The first polarizer was implemented directly after the longpass filter to clean the polarization of generated mid-IR light. Without polarizer, the polarization ratio between horizontally and vertically polarized light was around 18:1. This ratio was increased by the used polarizer to $\gg$1900:1.

A $\lambda/2$ rotated the polarization of the pump pulse to $+45°$ after the FP interferometer. The polarization of the pump was cleaned by a polarizer positioned as close to the sample as possible, *i.e.*, directly before the parabolic mirror. Cleaning the pump polarization was important because the contrast of the polarization was reduced by the $\lambda/2$ and the mirrors by a factor of > 50.

Directly after the sample, a motorized polarizer (analyzer) was implemented. It could be swapped between $+45°$ (parallel to the pump polarization) and $-45°$ (perpendicular to the polarization) and thus only the signals for parallel relative polarization or perpendicular relative polarization, respectively, were detected. The measurement is in principle the same as if one would directly measure with beams with parallel or crossed polarization. However, only 50% of the probe intensity is sent to the spectrometer. This does usually not pose any problem because the probe intensity is anyway reduced by filters to avoid saturation of the detector. The motorized polarizer swapped every 300 laser shots between $+45°$ and $-45°$ and therefore allowed the
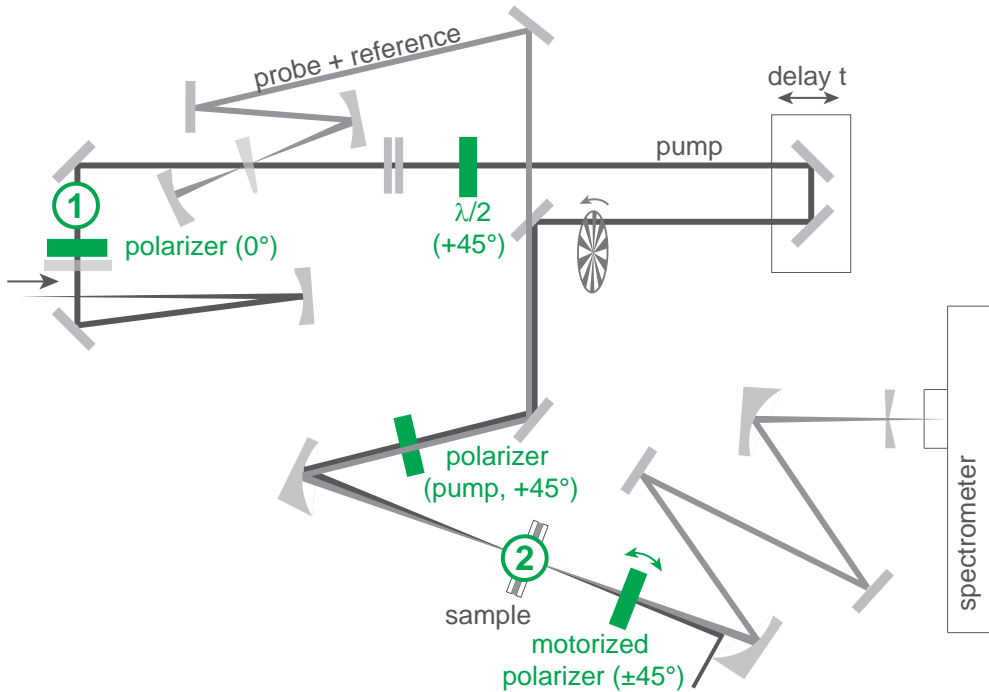
Figure 3.7: *Sketch of the improved P2D-IR setup. The additional optics compared to the 2D-IR setup are highlighted in green. Numbers see text.*

quasi-simultaneous measurement of parallel and perpendicular polarization.

This setup has three main advantages. First, it is characterized by a very high polarization contrast for the pulses at the sample. The polarization contrast for the probe and reference beams was $> 1200{:}1$ ($0°$) and $> 1400{:}1$ ($45°$) for the pump beam (with the FP interferometer built in). The relative polarizations between the two beams were adjusted with an accuracy of $\pm 1°$. Secondly, there are no rotating optics before the sample, thus there are exactly the same measurement conditions for both polarization conditions, *i.e.*, the polarization contrast is the same for both measurements, the excitation energies are identical, and the beam overlap in the sample is constant. Finally, the rotating analyzer has no influence on the measured signal size. This was ensured because the difference between pumped and unpumped signal was measured quasi-simultaneously and, at the same time, the signal was referenced by the reference beam, which also passed the analyzer. This compensates for the polarization selectivity of the optics after the analyzer such as the grating in the spectrometer. Swapping the position of the motorized polarizer every 300 laser shots minimized the influence of long term laser fluctuations.

All P2D-IR spectra shown in part II were measured with this setup.

Comparison to the Previous Design

The previous setups only used a $\lambda/2$ to swap the polarization of the pump beam between horizontally and vertically polarized (see Fig. 3.8).[38,95,142–144] The reduced anisotropies, which were observed in the previous setups as stated before, originate from four dominating error sources.
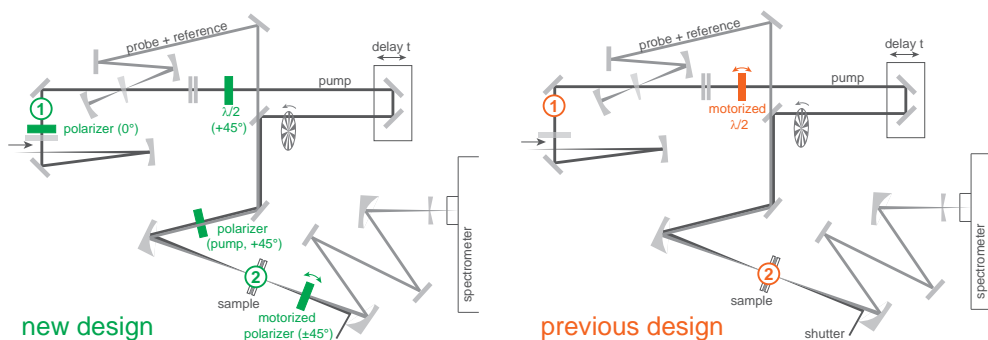
Figure 3.8: *Comparison between the improved (left, green) and the previous (right, orange) P2D-IR setup. Numbers see text.*

First, the $\lambda/2$ works nicely only for exactly the wavelength where it is specified for, *e.g.*, at $1667\,\mathrm{cm}^{-1}$ ($6\,\mu\mathrm{m}$), and already small deviations from the specified value lead to significant errors in the polarization. Figure 3.9 (left) shows the wavenumber dependent polarization error if the $\lambda/2$ is adjusted to rotate the beam by $90°$. Rotating the polarization by using only a $\lambda/2$ leads to significant artifacts, which is revealed in the following (best case) example: Lets assume a mid-IR spectrum with the central wavenumber of $1667\,\mathrm{cm}$, exactly matching to the $\lambda/2$, and a typical bandwidth of $200\,\mathrm{cm}^{-1}$ (FWHM). The $\lambda/2$ is adjusted to rotate the polarization by $90°$ for the specified wavenumber, *i.e.*, the center wavenumber of the pulse. At the spectral positions with half maximum intensity, $100\,\mathrm{cm}^{-1}$ from the center apart (*e.g.*, $1567\,\mathrm{cm}^{-1}$), already 5% of the beam are wrong polarized. For a diagonal peak at this position, the oberserved intensity ratio between parallel and perpendicular polarization would be 2.7:1 instead of 3:1. This ratio corresponds to an angle of $14°$ instead of the true value of $0°$– an error of $14°$. The wavelength dependent change of the intensity ratio for diagonal peaks has been observed experimentally and is visualized in Fig. 3.9 (right)
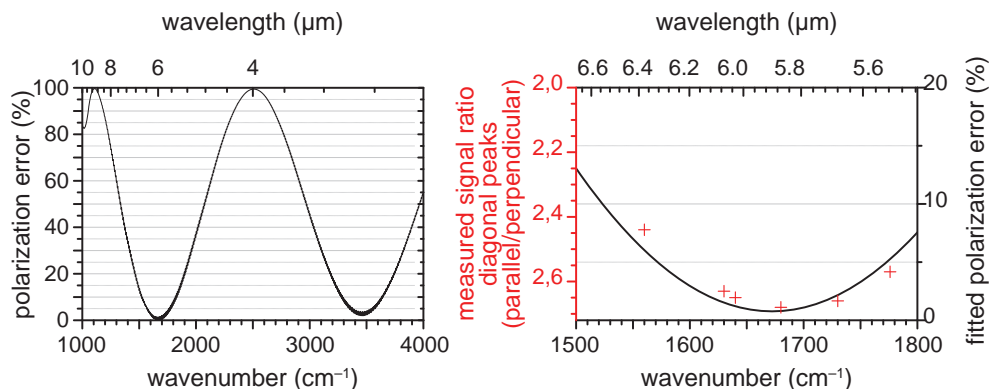
Figure 3.9: *Black curve: Polarization error of a $\lambda/2$ ($6\,\mu\mathrm{m}$) adjusted to rotate the polarization by $90°$ measured with an FTIR spectrometer. The measured polarization error is fitted in the right graph. Red data points: measured signal ratio (parallel/perpendicular) for various diagonal peaks. The ratios do not reach the theoretical value of 3:1 because the polarization contrast of the mid-IR pulses was low.*

by the red data points. The measured signal ratios do not reach the the theoretical value of 3:1 because the polarization contrast of the beams was low. The wavenumber dependent error makes it impossible to deduce the structure of molecules for which the vibrations of interest are splitted by more than $100\,\mathrm{cm^{-1}}$.

The second source for errors is the rotating optic itself. Tiny misalignments of the optic (*e.g.*, mounted under an angle) or if the optic has a tiny wedge will change the beam pointing when the optic is rotated. Thus the overlap of pump and probe beam will change as a function of the polarization and consequently also influence the signal size, even if it would not depend on the polarization itself.

A third important source for errors is caused by the optics in the pump path between the $\lambda/2$ and the sample. The reflectivity of the mirrors depend on the polarization of the light. This leads to a change in pump power depending on the polarization, which again modulates the intensity of the measured signal, even if it would not depend on the polarization itself.

The fourth source for errors is the scrambling of the polarization by the used optics. It turned out that particularly some of the used gold mirrors reduce the polarization contrast significantly. This is the reason why in the improved setup the pump polarization is cleaned so close before the sample, even though the various beams are pretty close to each other there and the alignment of the polarizer is accordingly challenging. The polarization contrast of the beams at the positions 1 and 2 labeled in Fig. 3.8 are compared in Table 3.5.

Table 3.5: *Comparison of the polarization contrast in the previous and the improved P2D-IR setup at the labeled positions in Fig. 3.8. Measured at a central wavelength of $\lambda = 6\mu m$ and without Fabry–Perot interferometer. The angles relate to the relative polarizations between pump and probe pulses.*

	polarization contrast previous setup	polarization contrast improved setup
position 1	18:1 (0°)	≫ 1900:1 (0°)
position 2		
probe beam	13.5:1 (0°)	> 1200:1 (0°)
pump beam	21.6:1 (0°)	> 1600:1 (45°)[i]
	11.6:1(90°)	

[i] With Fabry–Perot interferometer: > 1400:1 (45°).

The angles derived from the P2D-IR spectra measured with the different setups are compared in Table 3.6. Where applicable, the known angles are compared too. The angles can either be derived by evaluating the P2D-IR spectrum for one delay time (ideally as short as possible, italic numbers) or by measuring many delay times and extrapolating the signals to zero delay time (regular numbers, see also, *e.g.*, Fig. 5.6). The first approach neglects rotational diffusion, which is, however important to consider for small molecules. Mainly the length and shape of the pump pulse determines the minimum time delay that can be evaluated without artifacts caused by the time overlap of pump and probe pulses, such as signals from interchanged time orders. This minimum time is the main limitation of the improved setup because rotational diffusion during this time causes a systematic error. For the molecules studied in this thesis, this error is at a delay of $1.5\,\mathrm{ps} \leq \pm 6°$ for angles $>20°$. The use of pump pulses

with a Gaussian or time-reversed Etalon shape [53] could reduce the minimum time delay significantly and thus improving the accuracy of the experiment. Measuring many time delays and extrapolating the time dependent anisotropy to a delay of $t = 0$ also leads to values that are not affected by rotational diffusion, however at the expense of additional measurement time. Using this approach, the estimated statistical error is in the range of $\pm 3°$ for angles $> 20°$. Its accuracy was proven by the comparison of measured angles with known angles. For dicarbonylacetylacetonato rhodium (RDC) both extreme angles, $0°$ and $90°$ were measured precisely (see Table 3.6).

Table 3.6: *Comparison of the angles determined with the previous and the improved P2D-IR for the three molecules dicarbonylacetylacetonato rhodium, oxazolidinone, and the oxazolidinone-SnCl$_4$ complex. The angles written in regular font were determined by extrapolating the anisotropy to $t = 0$ ps, the angles in italics were determined at a delay time of 1.5 ps. As a reference, the exact angles are presented, if they are known.*

	old setup	improved setup	true value
DICARBONYLACETYLACETONATO RHODIUM (RDC)			
ν_1/ν_1	–	$0° \pm 5°$	$0°$
	–	*$18° \pm 3°$*	
ν_1/ν_1	–	$90° \pm 5°$	$90°$
	–	*$79° \pm 3°$*	
OXAZOLIDINONE			
ν_2/ν_2	$14° \pm 5°$	$0° \pm 7°$	$0°$
	$21° \pm 3°$	*$14° \pm 4°$*	
ν_1/ν_2	$62° \pm 2°$	$57° \pm 2°$	–
	$63° \pm 2°$	*$57° \pm 2°$*	
ν_1/ν_3	$32° \pm 3°$	$27° \pm 3°$	–
	$33° \pm 3°$	*$30° \pm 2°$*	
ν_2/ν_3	$49° \pm 3°$	$43° \pm 2°$	–
	$49° \pm 2°$	*$46° \pm 2°$*	
OXAZOLIDINONE-SnCl$_4$ COMPLEX			
ν'_2/ν'_2	$14° \pm 5°$	$0° \pm 7°$	$0°$
	$19° \pm 4°$	*$7° \pm 5°$*	
ν'_1/ν'_2	$26° \pm 3°$	$18° \pm 4°$	–
	$28° \pm 2°$	*$22° \pm 2°$*	
ν'_1/ν'_3	$52° \pm 3°$	$46° \pm 2°$	–
	$53° \pm 2°$	*$47° \pm 2°$*	
ν'_2/ν'_3	$54° \pm 2°$	$49° \pm 2°$	–
	$54° \pm 2°$	*$49° \pm 2°$*	

Part II

Structure Determination of Reactive Intermediates
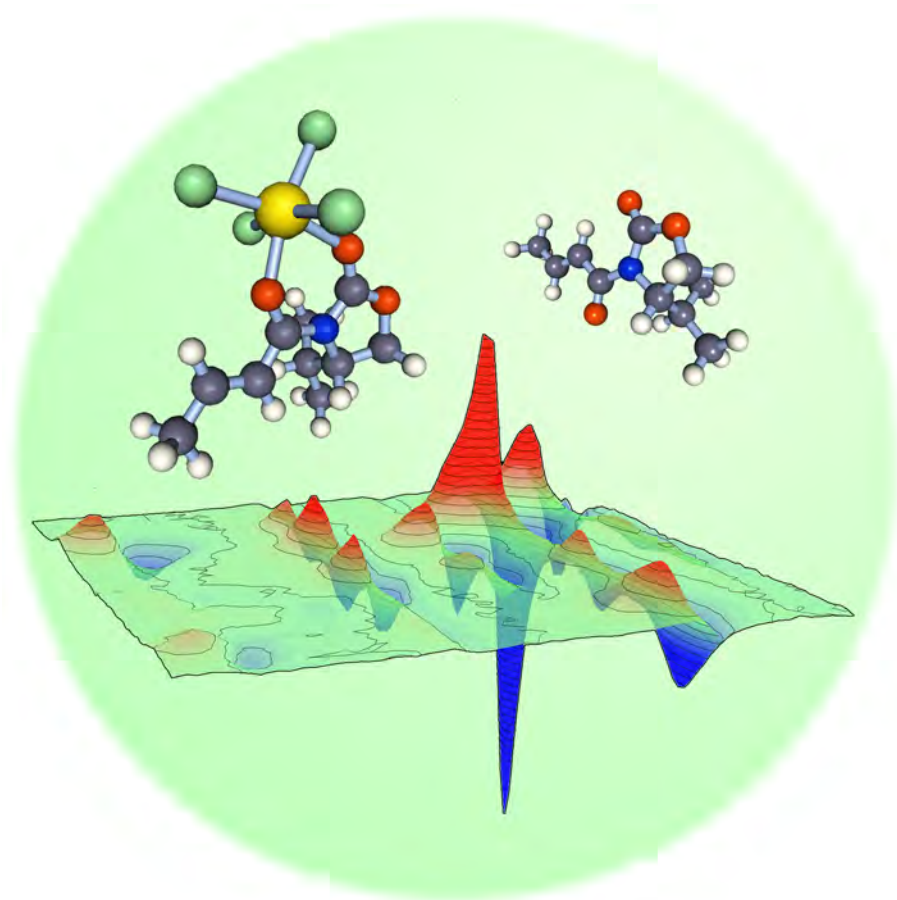
Chapter 4

Motivation

4.1 Investigation of Reaction Mechanisms

The knowledge about reaction mechanisms is without doubt of immense importance to a chemist. The term *reaction mechanism* usually describes a sequence of simple chemical reactions (sometimes even elementary reactions). It can explain the observed products and stoichiometry of the overall reaction, all observed intermediates and the kinetics of the process.[147] The reaction mechanism thus facilitates the understanding of the reaction and the prediction of the products for analogous reactions using other reactants. Additionally it establishes a basis for the optimization of the reaction with respect to yield or side products.[147] Understanding the reaction mechanism is essential when stereochemically pure products shall be obtained in organic reactions or the obtained stereoselectivity shall be rationalized. The entire part II of this thesis only deals with organic reactions in solution.

The elucidation of reaction mechanisms is typically the task of physical organic chemistry. The experimental methods commonly used can roughly be classified in three groups: *preparative methods*, *spectroscopic methods* for detecting intermediates and *methods for structure determination* of products, side products and, in the ideal case, intermediates. All experimental methods are usually complemented by various theoretical methods (*e.g.*, molecular dynamics simulations, DFT) and theories or models (*e.g.*, transition state theory, mechanisms of energy transfer), which are not in the focus of this thesis. Only the DFT calculations that are used to understand and interpret the 2D-IR experiments are briefly described in this thesis (see chapter 15).

The preparative methods comprise approaches such as product analysis, kinetic studies, isotope labeling (for product or kinetic studies), solvent studies and trapping, stabilizing or isolating intermediates.[147] Those methods are most often used to deduce information about the reaction mechanism. Most familiar are probably the kinetic studies to resolve the mechanisms of the S_N1 and S_N2 reaction.[147–149]

The group of spectroscopic methods to detect intermediates (or intermediate products) have in common that they can be used "on the fly", *i.e.*, during the reaction, and are able to detect intermediates. The most common techniques used for that purpose are IR, UV/VIS, NMR, and EPR spectroscopy.[147] Each of those has its advantages and disadvantages leading to different scopes. EPR spectroscopy is the most sensitive of the mentioned methods, however only applicable to paramagnetic compounds and radicals. NMR spectroscopy on the other hand has only a limited sensitivity and is restricted by its inherent time resolution in the millisecond range. It is widely

used due to the high information content of the spectra, its structural selectivity, the easy handling and the variety of available methods. All these qualities make NMR spectroscopy the most powerful analytic technique for organic compounds. Visible spectroscopies feature ultrafast time-resolution and a very high sensitivity. The spectra, however, contain only little structural information. IR spectroscopies combine an inherent ultrafast time resolution with a high sensitivity and structure sensitivity. Compared to NMR spectroscopy, the obtained spectra usually are more congested, contain less information on the atomic level and require the construction of specialized experimental setups. It is noteworthy that for all spectroscopic investigations the intermediates need to exist in measurable concentration while the reaction is proceeding. Therefore only intermediates before the rate determining step can be observed. It is also important to be aware that not all species in solution are reacting. In catalytic reactions there are often so called off-cycle resting states.[147] These are molecules that are in equilibrium with one species in the catalytic cycle, but do not participate in the reaction. The question, which species participate in the reaction and which do not is sometimes quite difficult to answer.

The third group of methods used to investigate reaction mechanisms allows the structure determination of the reactant, product, and in some cases intermediates. Knowing these structures gives the most direct access to the reaction mechanism and a picture on the atomic level. The most prominent representatives of these methods are mass spectrometry, X-ray crystallography, and multi-dimensional NMR. As shown in this thesis, also 2D-IR spectroscopy belongs into this group. In the following the methods facilitating the determination of the configuration and also the conformation of molecules are discussed, *i.e.*, X-ray crystallography, NMR spectroscopy, and 2D-IR spectroscopy. Even though mass spectrometry is a very powerful technique, it is not reviewed here because it only gives access to the constitution of molecules. It is insensitive to configuration and conformation, essential information needed to investigate reactivities and stereoselective reactions.

4.1.1   Structure Analysis with Crystallography

The method of choice for obtaining the 3D structure of a molecule or protein is, if a crystal is available, the determination of its crystal structure. In this section a very short sketch of X-ray crystallography will be given, based on ref. [150]. For simplicity, only single crystal methods will be discussed.

In the experiment, a single crystal is placed in an X-ray beam. This beam is diffracted by the electrons in the crystal forming a diffraction pattern, which can be recorded, *e.g.*, on a photographic film or an electronic area detector such as a CCD camera. In order to collect all reflections, the crystal needs to be rotated and the diffraction pattern for each position is measured. A typical diffraction pattern for one crystal orientation is shown in Fig. 4.1. This diffraction pattern contains the information on the electron density of the crystal and the symmetry of the unit cell. Only those diffractions can be observed that fulfill Braggs law:

$$n\lambda = 2d_{hkl}\sin\theta. \tag{26}$$

Braggs law tells in principle that only these diffractions can be observed, for which the path length difference between reflections from two parallel lattice planes is a multiple of the wavelength λ because only then constructive interference of the two beams will occur. The path length difference depends on the angle θ between the incoming beam
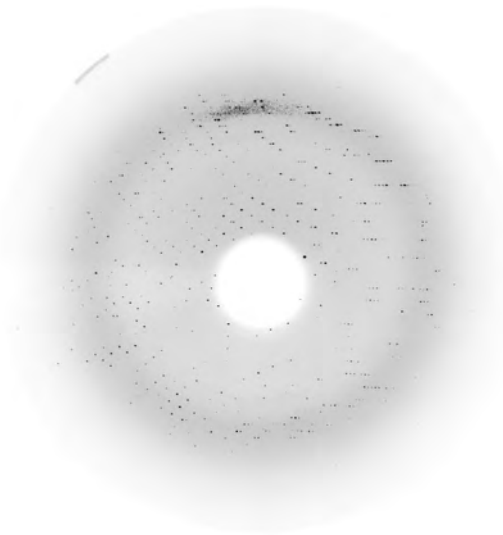
Figure 4.1: *Typical diffraction pattern. This picture was kindly provided by Georg Wille.*

and the lattice plane as well on the distance d_{hkl} between the lattice planes. The indices h, k, and l define the set of lattice planes. Braggs law is illustrated in Fig. 4.2 for two different sets of parallel lattice planes.

The intensity of the spots in the diffraction pattern is determined by the electron density $\rho(xzy)$. The diffraction pattern $F(hkl)$ is the Fourier transform of the electron density:

$$F(hkl) = \int_{cell} \rho(xzy)e^{2\pi i(hz+ky+lz)}dxdydz. \tag{27}$$

However, the available detectors can only measure $|F(hkl)|$; the phase information is lost. If the phase would be known, the electron density and thus the positions of the atoms could be retrieved directly by an inverse Fourier transformation of the diffraction pattern. Without knowing the phase of $F(hkl)$, the inverse FT is not possible, which is known as the *phase problem*. Nevertheless, there are methods available how the electron density can be reconstructed, *e.g.*, Patterson synthesis and
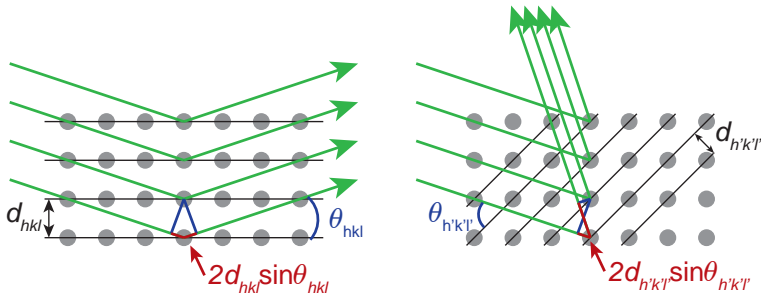
Figure 4.2: *Illustration of the Bragg reflection for two different sets of parallel lattice planes with the same incident beam (green). The additional path length is marked in red. The lattice planes are seen edge on.*

direct methods for small molecules. When the approximate positions for all atoms are found, the structure is refined by varying the positions of the atoms and optimizing the agreement between simulated and measured diffraction pattern.

Xray crystallography has the advantage that the the electron density of the molecule of interest and thus its structure is measured directly, in contrast to spectroscopic techniques including NMR and IR spectroscopy, which measure the energy levels of a molecule and the structure is then deduced from those. Additionally, it is a very precise technique, allowing a resolution of around 0.2 Å. However, crystals of the molecules are needed. While this is normally no problem for small molecules, it can be very tedious or even impossible to obtain a suitable crystal of a protein. The need of a crystal has several implications on the structures that can be analyzed. The molecule or complex of interest must be isolable and, hence, stable and long-lived. As a consequence, short-lived reactive intermediates are usually not accessible. For the investigation of reaction mechanisms, which is the focus in this thesis, one is usually interested in the molecular structure under reaction conditions, *i.e.*, in solution. Hence, it needs to be made sure that packing effects in the crystal do not alter the structure significantly compared to the solution structure, where the solvent will interact with the molecule.

4.1.2   Structure Analysis with NMR Spectroscopy

As already mentioned above, NMR spectroscopy is a very powerful technique to investigate molecular structure. After a very brief general introduction to the basics of NMR based on the references [99,100,151–153], this chapter focuses on a selection of NMR techniques typically used for structure determination, based on the references [99,100,151–154]. The scope of these techniques, their fundamentals and also their limitations will be discussed – mainly on a phenomenological level.

Basics

NMR spectroscopy measures the energy levels of the nuclear spins in a magnetic field. Only nuclei, with a spin quantum number unequal to zero interact with the magnetic field and are detectable by NMR. This is the case for nuclei containing an odd number of protons or neutrons (or both), *e.g.*, the frequently used nuclei ^{1}H, ^{13}C, and ^{14}N, and also ^{19}F, ^{31}P, and ^{119}Sn. The most common carbon isotope ^{12}C is not sensitive to the magnetic field and thus invisible in NMR spectra.

Nuclei with a spin angular momentum align in a magnetic field (so called Zeeman effect). Due to the quantum character of the spins, only discrete alignments are possible. In the case of particles with a spin $I = 1/2$, only two orientations are allowed. Roughly speaking, the magnetic moment can be aligned in the same direction (spin up) as the field or opposite to the field (spin down). The energy difference ΔE between these two states is given by

$$\Delta E = h\nu = \hbar\gamma B \qquad (28)$$

where h is Planck's constant, γ is the gyromagnetic ratio of the nucleus, and B the magnetic field that is experienced by the nucleus. Table 4.1 gives an overview of the gyromagnetic ratios, NMR frequencies ν and natural abundances of selected nuclides.[151] All frequencies are in the MHz range and thus radio frequency.

Since the energy difference between the two states is small compared to $k_B T$, the thermal energy available at a given temperature, the population difference between

Table 4.1: *Gyromagnetic ratios, NMR frequencies (in a 14.1 T field), and natural abundances of selected nuclides. Adapted from ref. [151].*

	$\gamma\ (10^6 T^{-1} s^{-1})$	ν (MHz)	Natural abundance (%)
^{1}H	26.75	600.1	99.99
^{13}C	6.73	150.9	1.11
^{14}N	1.93	43.4	99.63
^{19}F	25.18	564.7	100.0
^{31}P	10.84	242.9	100.0
^{119}Sn	−10.03	223.8	8.59

the two states are very small (in the case of ^{1}H the populations differ by only 0.001% in a 14.1 T field). This means that (in the best case) only approximately one nucleus out of 10^6 active nuclei is detected by NMR and is one reason for the low inherent sensitivity of NMR.

The energy difference ΔE between the two states and thus the frequency ν of the transition between them depends on the magnetic field B that is experienced by the spin (see eq. 28). This field is mainly determined by the external field B_0 applied by the spectrometer. However, this field is altered slightly by the surrounding of the nuclei leading to slightly different frequencies. The frequency differences are typically in the range of few to several ppm and referred to as chemical shift δ with respect to the frequency of a standard molecule, *e.g.*, TMS for ^{1}H NMR. The main reason for the chemical shifts are the electrons around the nuclei. Since also electrons have a spin of $I = 1/2$, they also align to the magnetic field and therefore shield or enhance the external magnetic field. Hence the chemical shift is mainly a measure for the chemical bonds and groups the nuclei participate. In addition, the oxidation state of the atoms and neighboring groups, particularly if they are aromatic, influence the chemical shifts. [155]

For illustration, the ^{1}H NMR and (decoupled) ^{13}C NMR spectrum of ethanol are shown in Fig. 4.3. The decoupled ^{13}C NMR spectrum shows two signals, one for the methylene carbon ($\delta = 57.8$ ppm) and one for the methyl carbon ($\delta = 18.1$ ppm). The ^{1}H NMR spectrum shows three sets of signals. The signal set at $\delta = 3.7$ ppm is caused by the methylene protons, the signal at $\delta = 2.6$ ppm by the hydroxy proton and the methyl protons cause the signals at $\delta = 1.2$ ppm. Chemically equivalent protons, *e.g.*, the three methyl protons, have the same resonance frequency and the peak intensities add up. By integrating the peak areas, the number of chemically equivalent protons causing the signals can be deduced. Coupling between the methyl and methylene protons lead to a splitting of those signals into multiplets.

J-Coupling   The coupling responsible for the splitting of the signals in solution NMR spectra is the so called J-coupling. It is also referred to as spin–spin coupling, scalar coupling, indirect (dipole–dipole) coupling, or through-bond coupling. The mechanism is intuitively explained in Fig. 4.4. [99] Let's consider a chemical bond between two atoms. The electrons forming this bond are paired and due to the Pauli principle one electron is spin–up and the other one spin–down. If the nuclei of the atoms do not have a spin, the two states illustrated in Fig. 4.4 a are degenerate. If now one of the nuclei has a non–zero spin (*e.g.*, $J = 1/2$, positive gyromagnetic ratio), the hyperfine interaction between the nucleus and the electrons splits the degeneracy
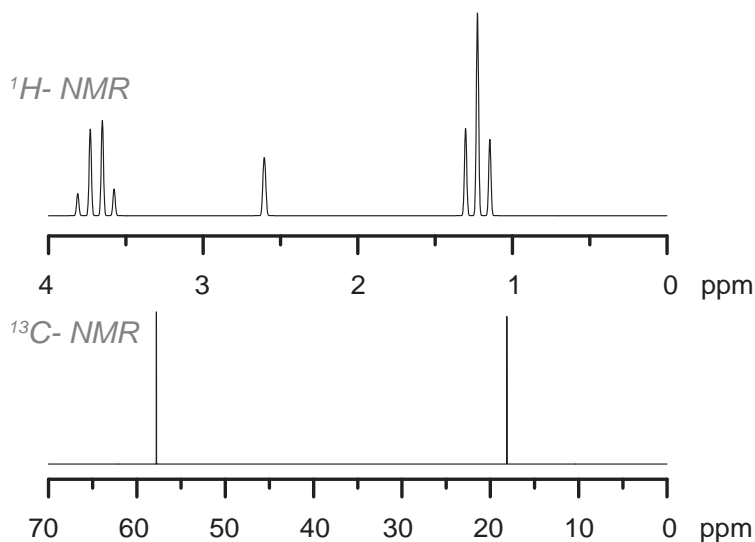
Figure 4.3: *Top: ^{1}H NMR spectrum of ethanol. Bottom: ^{13}C NMR spectrum of ethanol. The spectra are simulated based on the data in the spectral database for organic compounds SDBS, SDBS No. 1300.*

(see Fig. 4.4 b). This can be rationalized if one replaces the spins by small magnets. The situation where the closest electron and the nucleus have the same spin direction is slightly favored because electrons have a negative gyromagnetic ratio. Figure 4.4 c shows the case, where both nuclei involved in the bond have an active spin (both with positive gyromagnetic ratio). Similarly to the case before, the states where the spins of the nucleus and the adjacent electron point into the same direction are slightly lower in energy.

This coupling is also called indirect coupling, because the coupling is not generated by a direct interaction between the nuclear spins, but is caused and mediated by the electrons in the chemical bond. This coupling works only through bonds, but not through space. It also works through several bonds, however gets smaller the more bonds are between the nuclei. How many bonds are involved in the coupling is indicated by the superscript (^{1}J: coupling over one bond, ^{2}J: geminal coupling, ^{3}J - vicinal coupling). The J-coupling between equivalent nuclei is because of symmetry reasons zero. The amount of coupling partners and their spin determine the multiplicity of the band, *i.e.*, into how many bands the signal is split. The methylene protons of ethanol couple to three protons of the methyl group leading to a quartet while the methyl protons couple to two methylene protons leading to a triplet.

The scalar coupling does not depend on the external field, but depends, amongst others, on the angles between the involved bonds and thus can provide information on the structure and conformation of a molecule. The probably most useful coupling with respect to retrieving structural information is the vicinal coupling (^{3}J). The strength of the coupling constant depends on the dihedral angle θ according to the Karplus relation:[156]

$$^{3}J = A + B \cos \theta + C \cos^2 \theta. \tag{29}$$

A typical Karplus curve for the ($^{3}J_{HH}$) coupling is shown in Fig. 4.5 ($A = 2$ Hz, $B = -1$ Hz, $C = 10$ Hz).
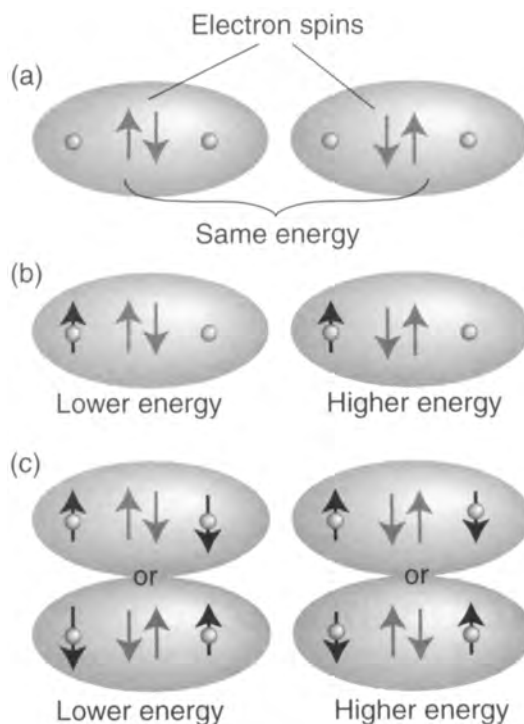
Figure 4.4: *Mechanism of J-coupling through one bond (^1J). Explanation see text. Reproduced with permission from ref. [99], copyright 2001, John Wiley and Sons LTD.*

This dependence has been proven to be very valuable in the conformation analysis of, *e.g.*, substituted cyclohexanes and proteins. Using the ^3J-coupling it is also very easy to distinguish between *cis* and *trans* alkenes; *cis* couplings between protons are typically in the range of 4–12 Hz, while *trans* couplings are around 14–19 Hz.[157] In cases of fast rotation around a bond (*i.e.*, a fast variation of dihedral angle θ) the observed coupling is an averaged coupling. The parametrization of the Karplus relation may be unknown for ions, radicals and metal complexes due to a lack of comparable molecules.

Not only protons couple to each other, but also protons and carbons (^{13}C) couple. The coupling between protons and carbons is typically annihilated in the ^{13}C NMR spectrum experimentally (through broadband decoupling) in order to simplify the spectrum, which is in particular for large molecules and proteins beneficial. At the same time this enhances the sensitivity. In ^{1}H NMR spectra these couplings are (if the molecules are not enriched with ^{13}C) rarely seen due to the low natural abundance of ^{13}C.

Dipolar Coupling In addition to the J coupling there exists the so called dipolar coupling (or alternatively direct (dipole–dipole) coupling or through-space coupling). This coupling can easily been understood if again the spins are thought of as small magnets. Then one magnet experiences the magnetic field of the other one. The
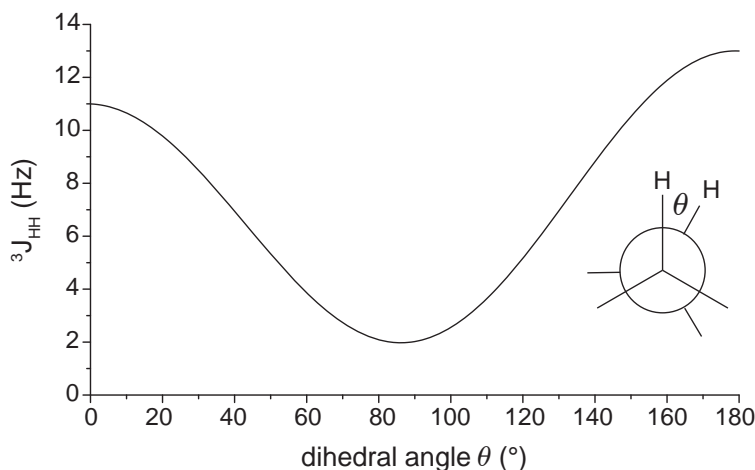
Figure 4.5: *Typical dependence of the* ^3J*-coupling on the dihedral angle (Karplus curve).*

dipole–dipole coupling constant b_{jk} is calculated as:

$$b_{jk} = -\frac{\mu_0}{4\pi}\frac{\gamma_i\gamma_k\hbar}{r_{jk}^3}. \tag{30}$$

The dipole–dipole coupling constant is dependent on the third power of the distance between the two spins. The orientation dependence is expressed with the secular dipole-dipole coupling constant d_{jk}:

$$d_{jk} = b_{jk}\frac{1}{2}(\cos^2\Theta_{jk} - 1). \tag{31}$$

The coupling is dependent on the angle Θ_{jk} between the external field and the vector joining the two interacting spins. In isotropic media such as typical solutions, the intramolecular dipolar couplings average to zero because the molecules are randomly oriented. In addition, short-range intermolecular dipolar couplings vanish due to the fast translational motion in liquids. The long-range intermolecular dipolar couplings can in general be neglected because they are very small. Hoverer, even if the dipolar coupling is not directly observed in solution NMR spectra, it is important for the relaxation of spins, the so called dipolar relaxation, which causes the nuclear Overhauser effect (NOE). The NOE and its application will be discussed in detail in chapter 4.1.2.

In solids and anisotropic liquids such as liquid crystals, the dipolar couplings do not vanish. Here we will limit the discussion to anisotropic liquids. As for any liquid, the intermolecular dipolar coupling vanishes or is negligible. The intramolecular dipolar coupling is not canceled completely. The amount of orientational organization determines the remaining dipolar coupling. This so called residual dipolar coupling (RDC) can be used to determine how the spin pairs of a molecule are aligned on average with respect to the external magnetic field. Combining the direction of all the different spin pairs in the molecule, the (relative) conformation of the molecule can be determined.[158–161]

Inherent Time Resolution If two species or conformations are in a dynamic equilibrium to each other, they can only be distinguished from each other using NMR,

if the rate constant is slower than the difference in the chemical shift. More exactly, the exchange rate k needs to be slower than

$$k = \frac{\pi \Delta \nu}{\sqrt{2}}, \tag{32}$$

the so called coalescence point where the two single peaks merge. Lets assume that two protons exchange for which the chemical shift differs by 5 ppm (which would actually be a pretty large difference for exchanging protons). In a 600 MHz spectrometer one observes two separate lines, if the exchange rate is slower than 6.6 kHz, which corresponds to a life time of 0.15 ms. If it is faster, only one line appears and the properties of the two protons are averaged. In addition to the chemical shifts also all other properties including the couplings are averaged. The properties are weighted in this average by their population p. This leads to the fact that in the fast exchange regime the properties and thus also the structure of the exchanging molecules cannot be uniquely derived by NMR spectroscopy. Figure 4.6 illustrates how the NMR spectra change with increasing exchange rate.[151]
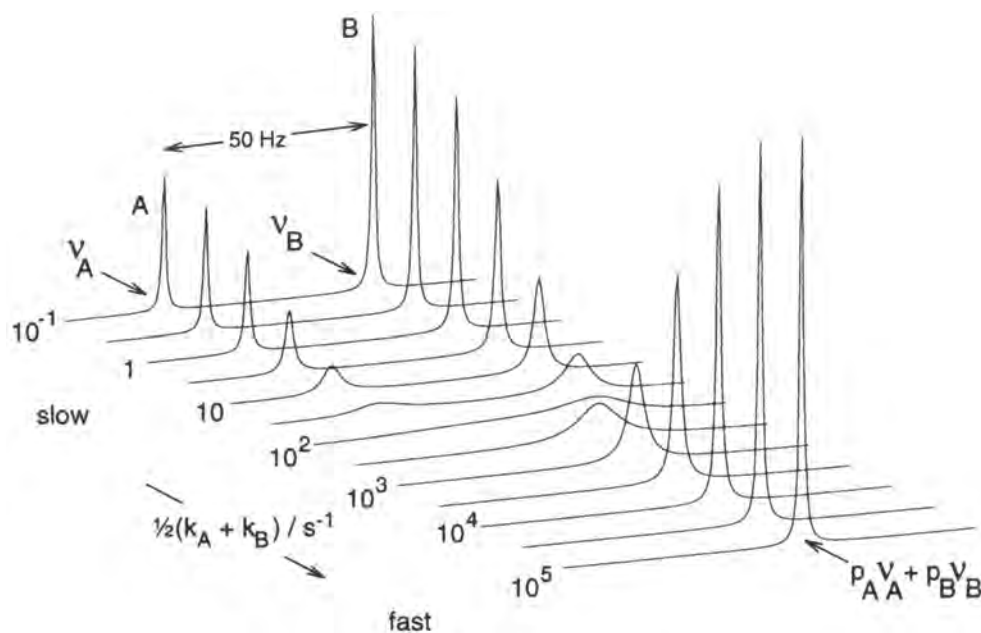
Figure 4.6: *Calculated NMR spectra for a pair of exchanging nuclei as a function of the exchange rate k. For fast exchange between species A and B, the peaks at ν_A and ν_B merge to a single peak located at $p_A \nu_A + p_B \nu_B$, where p_A and p_B are the relative populations of A and B, respectively. Reproduced with permission from ref. [151], copyright 1995, Oxford University Press.*

Multidimensional NMR Spectroscopy   The great breakthrough for NMR spectroscopy came with the invention of FT NMR spectroscopy, which enhanced the signal-to-noise ratio dramatically and allowed the development of multidimensional NMR spectroscopy. Both inventions were awarded with the Nobel prize to Richard Ernst in 1991. The functionality of FT NMR spectroscopy can nicely be illustrated by

the tuning of a bell.[162] One way of tuning the bell would be, to excite the bell with a given frequency and measure the response of the bell with a microphone. Afterwards the frequency is changed and again the response is measured. This procedure would correspond to continuous-wave NMR spectroscopy. The other, much easier and faster method is to excite the bell with a short hammer stroke. Then the bell emits all frequencies it is resonant to. The same can be done in NMR by a short, broadband radio frequency pulse. All spins are excited simultaneously and precess with their resonance frequency in the external magnetic field. During this precession they emit themselves an electromagnetic wave with their resonance frequency, which is detected by the NMR spectrometer. This emission is called free induction decay (FID).

The possibility to excite and manipulate spins by resonant pulses lead to the design of multi pulse experiments and thus multidimensional NMR. Here, only 2D-NMR spectroscopies will be discussed to illustrate the capabilities of these methods. The general scheme of any 2D-NMR experiment is shown in Fig. 4.7 and consists of preparation, evolution time, mixing, and detection. First, a desired spin state (coherence) is prepared by the preparation pulse sequence. Then the coherence can evolve during the evolution time t_1. After this time the coherence is transferred to an other spin in the mixing step. The mixing sequence determines the mechanism of the coherence transfer and thus which information can be obtained by the spectrum. Afterwards, the obtained coherence is detected by measuring the FID as it is done in linear FT NMR spectroscopy. During the experiment, the evolution time t_1 is varied. A Fourier transformation over t_1 gives the second frequency axis of a 2D-NMR spectrum. For a 3D experiment, another evolution time and mixing step are added.

preparation (p)   evolution (e)   mixing (m)   detection (d)

time

Figure 4.7: *General pulse scheme of any 2D-NMR experiment.*

Two groups of 2D-NMR methods are important for structure determination. Methods that use the J-coupling and probe the connectivities in the molecule (some representatives of these are COSY, TOCSY, and HSQC) and methods that use the effect of through space coupling on the relaxation (such as NOESY and ROESY). For large molecules and proteins one also often uses 3D experiments, mainly to enhance the resolution by using one evolution/mixing sequence to select a subset of spins.

COSY and HSQC – Determining the Connectivity between Spins

COSY   The correlation spectroscopy (COSY) is one of the simplest and most often used homonuclear 2D-NMR experiments. Its pulse sequence (Fig. 4.8) consists of only two radio frequency pulses, which flip the overall magnetization by 90° around the x-axis. In the short hand notation, the pulses are referred to as $90°_x$ pulses. The first pulse in the COSY sequence is used to flip the magnetization into the plane perpendicular to the magnetic field (preparation), where they precess during t_1 under the action of the external magnetic field as well as the *J*-coupling. The second pulse flips the spins again and transfers the coherence initially created *via* the
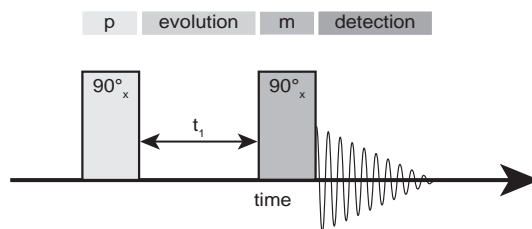
Figure 4.8: *COSY pulse sequence.*

J-coupling to the coupled spins. Unfortunately, the mechanism cannot be illustrated by visual images. The mathematical description, which uses product operators, goes far beyond the scope of this chapter. Interested readers will find it in many NMR textbooks. [99,100] Here, we will focus on how the spectrum looks like and how it can be interpreted. As already mentioned, the coherence transfer is mediated by the *J*-coupling between the spins. So all signals (*i.e.*, cross peaks) observed in the spectrum are caused by through-bond couplings. Typically only the ^2J- and ^3J-couplings are strong enough to form significant cross peaks. Thus, one can conclude from the cross peak in a COSY spectrum that the coupled nuclei are connected to each other with generally less than four bonds. Fig. 4.9 shows as an example the ^{1}H COSY spectrum of methyl nicotinate. [163] As one can nicely see in the spectrum, the COSY spectrum is symmetric to the diagonal.
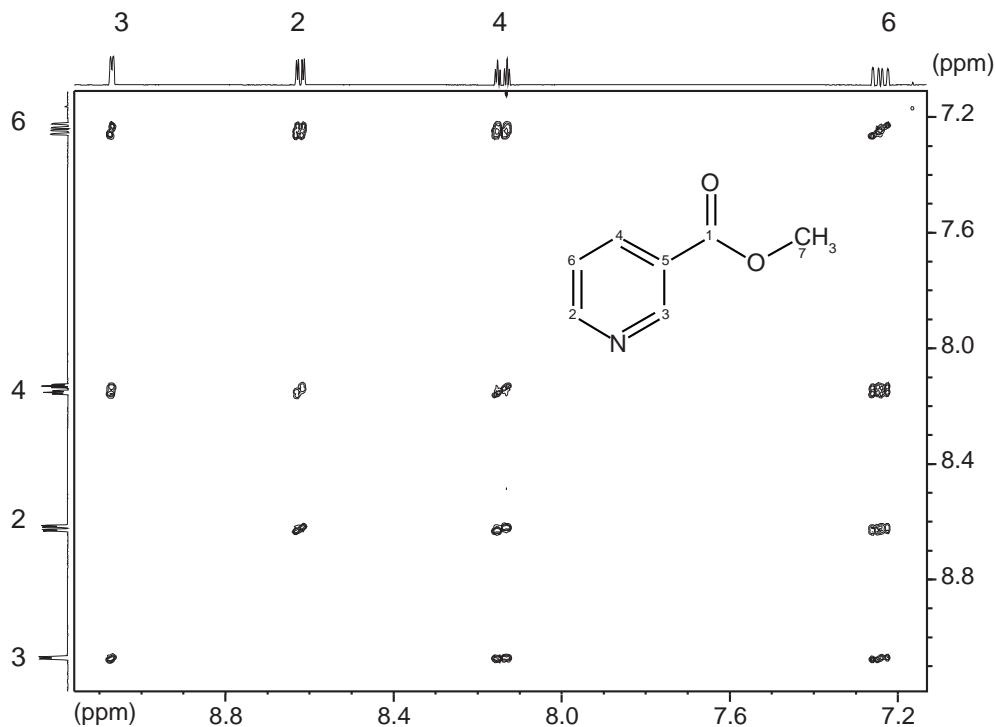
Figure 4.9: *Part of the ^{1}H COSY spectrum of methyl nicotinate (simulation). Adapted with permission from ref. [163].*

While the COSY spectrum only shows the direct coupling partners, an alternative experiment, the total correlation spectroscopy (TOCSY) shows cross peaks between all the spins that are directly or indirectly coupled to each other, *i.e.*, belong to the same spin system. Both spectroscopies are very valuable for assigning the NMR signals and for determining the connectivities within a molecule.

HSQC   The heteronuclear analogon to the COSY spectroscopy is the heteronuclear single quantum correlation spectroscopy (HSQC). It shows the coupling between two heteronuclei, *e.g.*, the coupling between ^{13}C and ^{1}H. Its pulse sequence is more complicated (see Fig. 4.10) and uses two radio frequencies for the pulses, one resonant to the protons and one resonant to the carbons. In the preparation period, the magnetization of the protons is transferred *via* the J-coupling to the coupled carbons, which can precess during the evolution time with respect to the external magnetic field. The 180° pulse during the evolution period effects that the coupling between ^{1}H and ^{13}C is canceled during the evolution time. The last pulses transfer the coherences of the carbons back to the protons (mixing), where it is detected while decoupling. The final spectrum shows which proton is bound to which carbon (see example in Fig. 4.11).[163] The selection of τ_1 determines that only ^1J-couplings are seen in the spectrum.
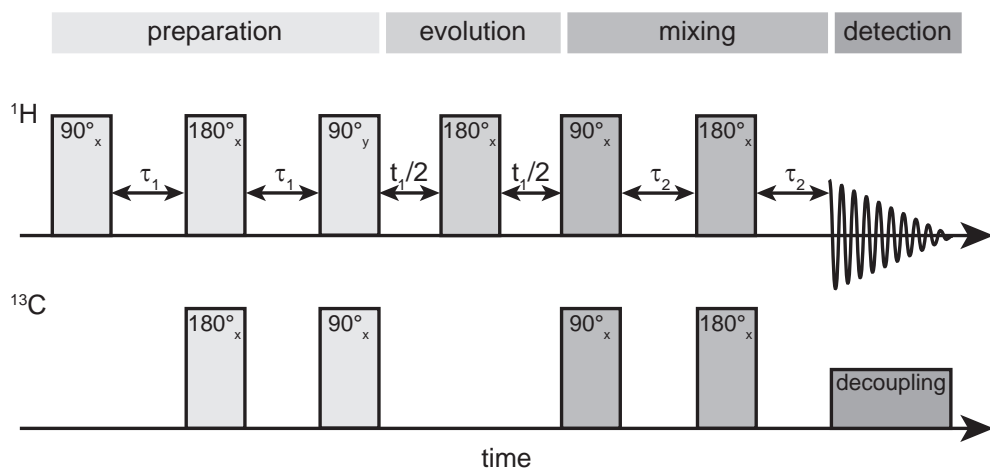
Figure 4.10: ^1H-^{13}C HSQC pulse sequence.

There are two alternatives to HSQC. One is heteronuclear multi quantum correlation spectroscopy (HMQC). In principle the spectrum shows the same. The pulse sequence is shorter and experimentally more robust, however at the expense of less resolution along the ^{13}C axis. The other alternative is heteronuclear multiple bond correlation spectroscopy (HMBC). This is the heteronuclear analogon to TOCSY and shows couplings over multiple bonds.

The aim of both introduced techniques, COSY and HSQC, is to determine the molecular constitution, *i.e.*, the connectivity of the atoms within the molecule. They provide no or only very limited information on the configuration or conformation of the molecule.
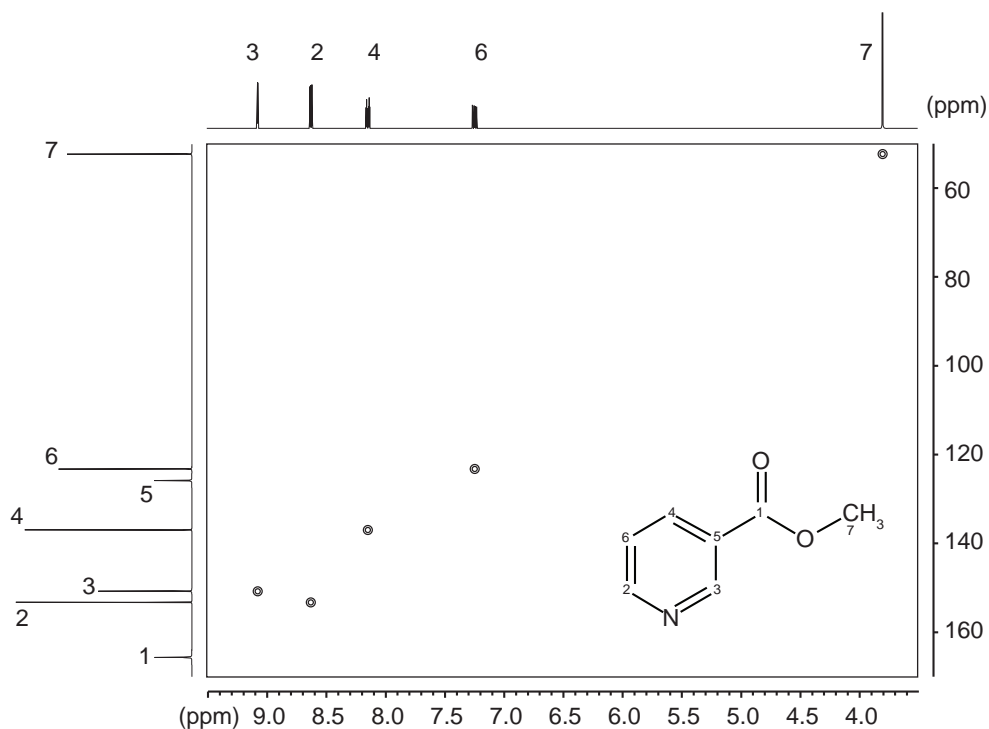
Figure 4.11: ^1H-^{13}C *HSQC spectrum of methyl nicotinate (simulation). Adapted with permission from ref. [163].*

NOESY – Measuring the Distance between Spins

One of the most powerful NMR measurement techniques to deduce the three dimensional structure of a molecule or protein is nuclear Overhauser effect spectroscopy (NOESY). Cross peaks in a NOESY spectrum indicate which spins are close in space to each other. The spectroscopy is based on the NOE, which is the effect that the signal of nucleus i increases (or decreases) if the transition of a nearby spin k is irradiated. The NOE is a direct consequence of the dipolar relaxation. As already induced in chapter 4.1.2, the dipolar coupling depends on the angle between the vector connecting the interacting spins and the external magnetic field. If the molecule rotates or tumbles, the dipolar coupling fluctuates and thus the energy levels of the spins fluctuate too. This fluctuation induces relaxation, if the spectral density of the fluctuations $J(\omega)$ is large at the transition frequency ω. $J(\omega)$ is proportional to:

$$J(\omega) \sim \frac{\tau_c}{1 + \omega^2 \tau_c^2}. \tag{33}$$

Thus for long correlation times τ_c, *i.e.*, slow tumbling, the spectral density function is narrow and for short correlation times τ_c, *i.e.*, fast tumbling, it is broad. This is illustrated in Fig. 4.12.

The for the NOE important relaxation pathways are the so called cross relaxation paths where two spins simultaneously flip their orientation. These pathways are highlighted in Fig. 4.13 by the red arrows. The probability of those transitions is
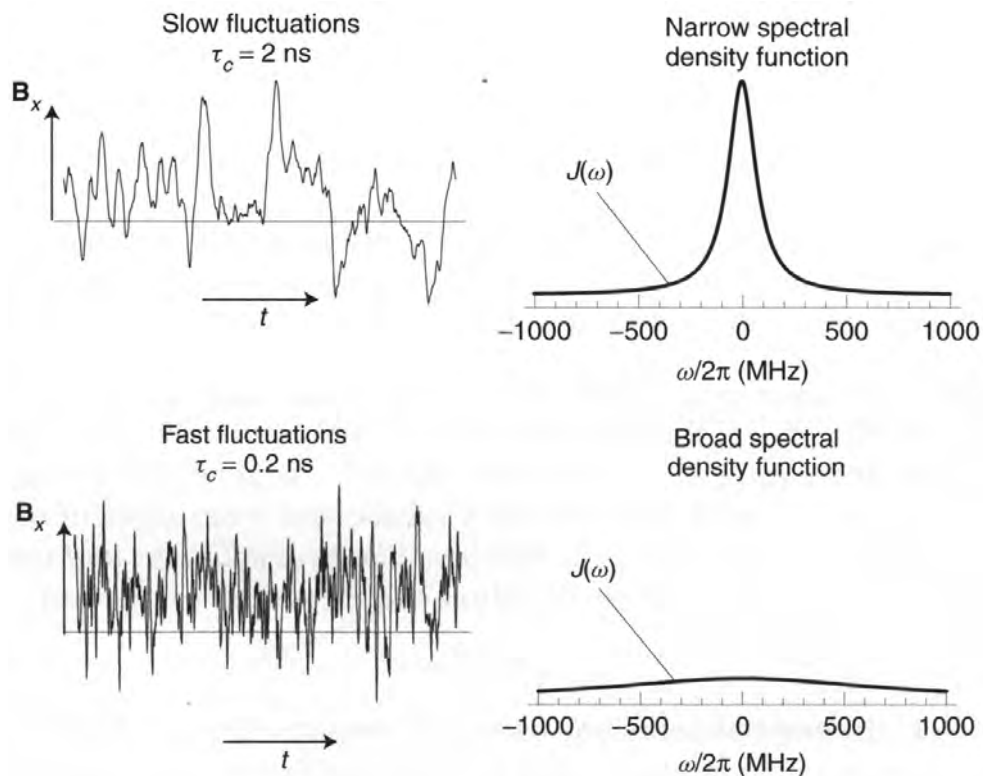
Figure 4.12: *Spectral density function for slow (top) and fast (bottom) tumbling. Adapted with permission from ref [99], copyright 2001, John Wiley and Sons LTD.*

given by:

$$W_2 = \frac{\mu_0^2}{160\pi^2} \frac{\gamma_i^2 \gamma_k^2 \hbar^2}{r_{jk}^6} \cdot 6J(\omega_i + \omega_k \approx 2\omega_0), \tag{34}$$

and

$$W_0 = \frac{\mu_0^2}{160\pi^2} \frac{\gamma_i^2 \gamma_k^2 \hbar^2}{r_{jk}^6} \cdot J(\omega_i - \omega_k \approx 0). \tag{35}$$

For slow tumbling molecules, *i.e.*, large molecules, $J(\approx 0) \gg J(\approx 2\omega_0)$ (see Fig. 4.12). According to the eq. 35 and 34, relaxation *via* the zero quantum transition is therefore dominating ($W_0 > W_2$). If the molecule tumbles fast, *i.e.*, is small, $J(\approx 0) \approx J(\approx 2\omega_0)$ (see Fig. 4.12). Thus, relaxation *via* the double quantum transition is dominating ($W_2 > W_0$). Equations 35 and 34 also show that the dipolar relaxation probability depends on r^{-6} and thus is only effective if the nuclei are very close to each other. Because the dipolar relaxation is the origin for the NOE, also the NOE shows a distance dependence of r^{-6}. Hence the NOE is a very local effect.

The mechanism of the NOE is explained in Fig. 4.13. Lets assume a two spin system in equilibrium (Fig. 4.13 a). The energy levels are populated according to Boltzmann, which is indicated by the black dots. If now all spins of one type (marked in green) are selectively flipped, a population inversion with respect to those transitions is obtained (see Fig. 4.13 b, green transitions). However, the population difference for
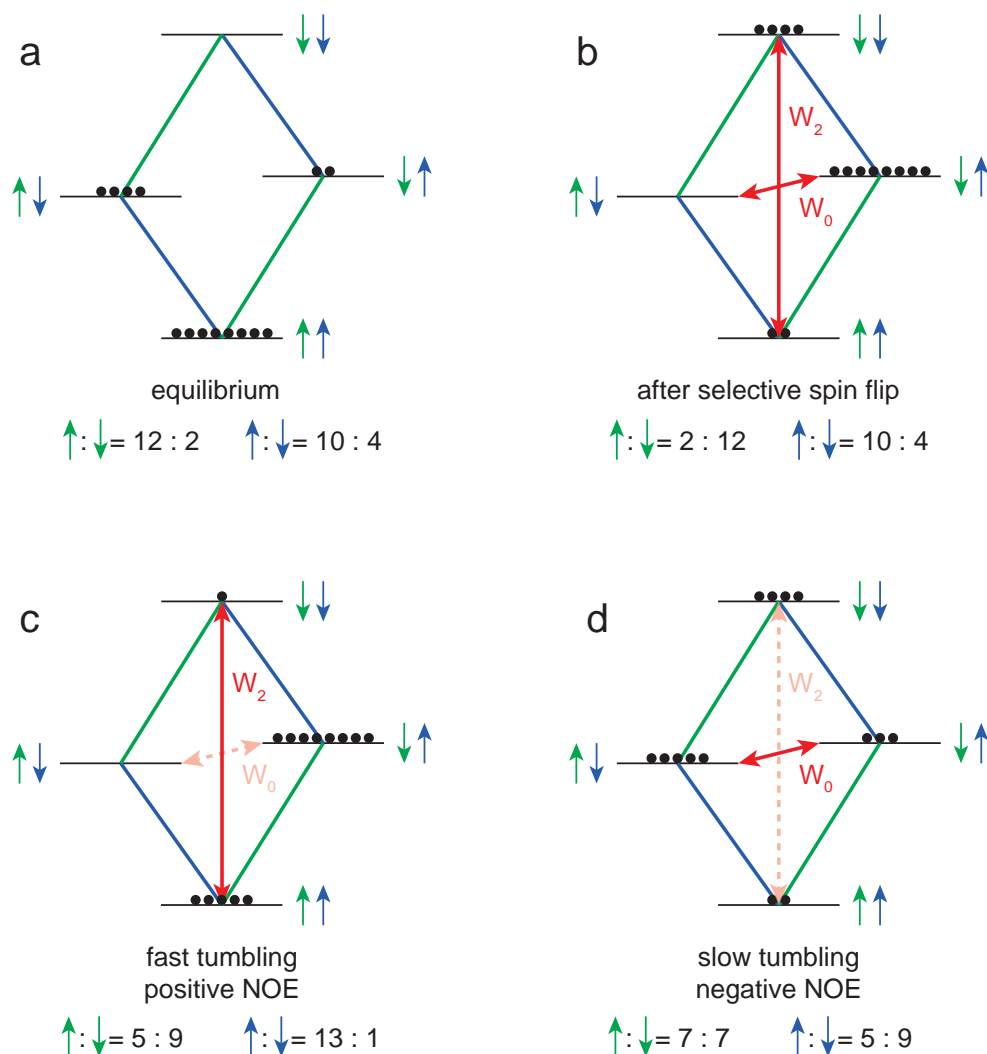
Figure 4.13: *Illustration of the mechanism of the NOE. Explanation see text.*

flipping the other spin (marked in blue) is still constant (Fig. 4.13 b, blue transitions). Because the populations are not in equilibrium anymore, they will relax towards the equilibrium populations (*c.f.* Fig. 4.13 a). Which relaxation path dominates is determined by the spectral density of the fluctuations. If the molecule tumbles fast, the double quantum transition (W_2) is preferred. This relaxation increases the population difference along the blue transitions (Fig. 4.13 c) and thus increases the signal observed for the second spin (blue). This is called a positive NOE – exciting one spin leads to an increased signal of the dipolar coupled spin. If on the other hand the molecule tumbles slowly, the relaxation through the zero quantum transition (W_0) dominates (Fig. 4.13 d). This leads to a reduction of the population difference or even a population inversion for the coupled spin (blue) and thus to a smaller signal. This behavior is called negative NOE. In NOESY spectra, cross peaks caused by a negative NOE have the same sign as the diagonal peaks while cross peaks caused by a
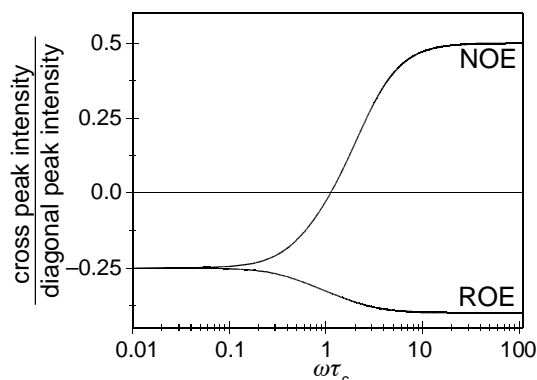
Figure 4.14: *Relative cross peak intensity induced by NOE and ROE as function of the correlation time τ_c. The NOE signal vanishes at $\omega\tau_c = \frac{\sqrt{5}}{2}$. Adapted with permission from ref. [164].*

positive NOE have opposite sign. For intermediate tumbling rates both relaxation pathways become important and positive and negative NOE compete against each other. A schematic plot of the dependence of the NOE cross peak and of its sign on the correlation time τ_c is shown in Fig. 4.14. [164] If the correlation time is

$$\tau_c = \sqrt{\frac{5}{4}}\frac{1}{\omega_0},\tag{36}$$

positive and negative NOE cancel each other and no NOE is observed.

The pulse sequence of a homonuclear NOESY experiment is shown in Fig. 4.15. It consists of three 90° pulses. The first pulse prepares a coherence, which evolves during t_1. The second pulse transforms the coherence into a non-equilibrium population, which relaxes as described above during τ_m. The last pulse induces the FID, which is measured.

Part of the ^{1}H NOESY spectrum of quinine is shown as example in Fig. 4.16. [100] Homonuclear NOESY spectra are symmetric to the diagonal, as it is also the case for COSY spectra. Cross peaks connect spins that are close in space. In proteins (*i.e.*, in the slow tumbling limit) cross peaks normally appear if the spins are closer than 5Å. Because the enhancement is smaller for molecules that tumble faster (see Fig. 4.14), the maximum distance between spins that can be observed is smaller, typically in the range of 3–4 Å.

Since the NOE is a very local effect, it can be used to determine the three dimensional structure, *i.e.*, conformations of molecules and proteins. Especially for
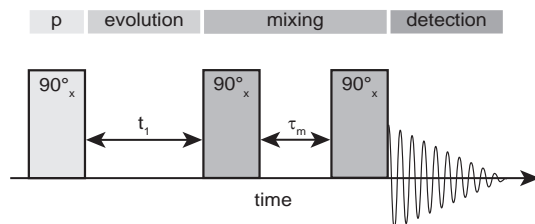
Figure 4.15: *^{1}H NOESY pulse sequence.*
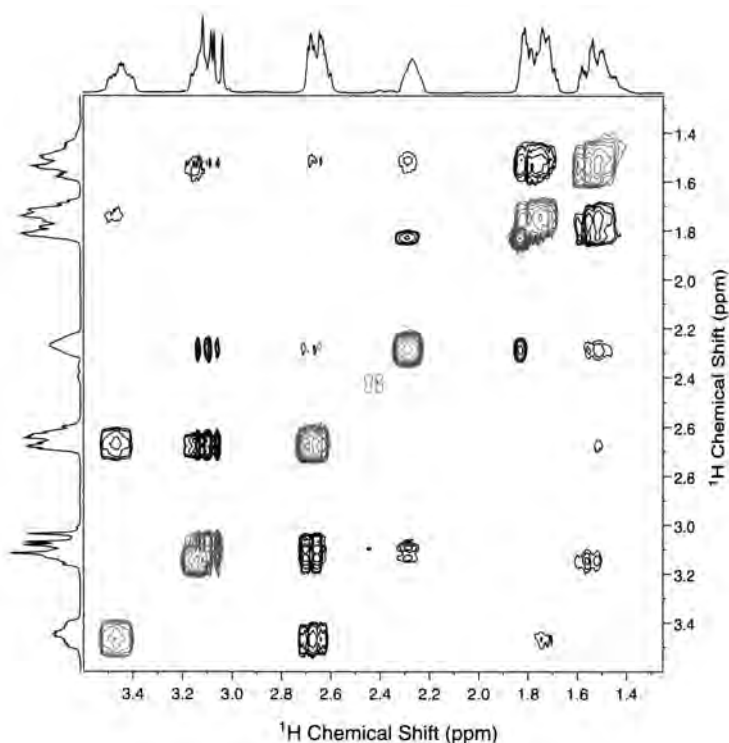
Figure 4.16: *Part of the ^1H NOESY spectrum of quinine. Reproduced with permission from ref. [100], copyright 2005, John Wiley and Sons LTD.*

determining the tertiary structure of proteins in solution NOESY has been proven to be very powerful. One indication for the importance of NOESY in structure determination is the Nobel prize that was awarded 2002 to Kurt Wüthrich for the development of the structure determination of proteins with NOESY. For proteins, NOESY cross peaks are usually classified in strong, medium and weak, which is then used to define a maximal distance between the two spins. With many of those distance restrictions and the knowledge of the connectivity of the nuclei (*e.g.*, determined with COSY) the protein structure can be refined. It is important to note here that usually NOESY cross peaks only give a maximal distance that separates the spins. In standard applications they cannot be used to derive directly the exact distance or a minimal distance. In other words: the presence of a cross peaks proves two spins to be closer than a threshold value. The absence of a cross peak does *not* imply that they are further apart than this threshold distance. However, there are exceptions to this rule. Only recently researchers in the groups of Riek and Butts used NOEs to determine inter proton distances to a high accuracy in proteins and organic molecules, respectively.[165–168] There are several reasons for a cross peak being absent despite only being far, *e.g.*, a "matching" tumbling rate where positive and negative NOE cancel each other. In these cases an alternative pulse sequence could be used, the rotation frame Overhauser effect spectroscopy (ROESY). The underlying principle is basically the same, however there is no zero crossing of the enhancement (see Fig. 4.14). Since ROESY and TOCSY pulse sequence are basically identical the ROESY spectrum also contains TOCSY signals. Also too short (or too long) mixing times and the presence

of paramagnetic ions or oxygen in the solution can lead to an absence of the NOE.

The structure determination of proteins benefits from many spins and thus many spin interaction in them. For small molecules with a sparse set of NMR active nuclei, it regularly happens that there are only few or even no meaningful NOESY cross peaks to refine the structure unambiguously. In these cases alternative approaches are required. Sometimes the J-coupling constants give a deeper insight for organic molecules. In the case of organometallic substances, the exact Karplus relationships are often unknown leading to the fact that the observed couplings cannot be used to deduce geometric information.

It is also noteworthy at this point that the NOESY pulse sequence is exactly the same as for 2D-EXSY, which measures the exchange of spins. This leads to the fact that if there is (slow) exchange present in the sample, it will show up as additional cross peaks. The line and shape will be the same as for a negative NOE cross peak. In the case of fast exchange, where the peaks of the exchanging nuclei collapse to one single peak, the NOESY spectrum shows the cross peaks of both species at the averaged frequencies. It is not possible to distinguish which cross peak belongs to which species and thus a structure determination in fast equilibrium is not possible.

Application Range and Limitations

The great advantage of the presented NMR methods are that they can be applied to molecules in solution, under the typical reaction conditions. From the experimental side, it is very easy to use. In most cases, the NMR spectrometer can be used as a black box and controlled by intuitive computer programs including all the parameters for the established methods. [100] There also exist a broad range of models to evaluate the spectra and to retrieve the structure. This is particularly true for proteins. For small molecules, the models are not that well established. Structure determination of those lacks often on a low density of spins and meaningful interactions (NOEs, couplings) between them. Additionally, only molecules with a lifetime longer than milliseconds, the inherent time resolution of NMR, are accessible. This means that species participating in fast equilibria or short-lived intermediates cannot be analyzed. Especially if they are only populated in low concentrations, they might be completely invisible.

4.2   The Potential of P2D-IR Spectroscopy

P2D-IR spectroscopy gives access to the angles between the transition dipole moments of the vibrations (see chapter 2.2.3) from which information on molecular structure can be deduced. In the ideal case, where the vibrations are localized on specific bonds, these angles directly transform into the geometry of the molecule. However, in most cases, vibrations are delocalized over several bonds and thus the transition dipole moment is not oriented along one bond. [169,170] In order to relate the orientation of the transition dipole moments to the structure of the molecule the exact character of the vibrations, *i.e.*, their delocalization need to be known. Quantum chemical calculations give access to them and allow a comparison of the measured and calculated angles and thus a determination of the structure. [39] Because the calculations are required, one needs to have an idea of the structure. In principle, the delocalization of the vibrations can also be quantified *via* the anharmonicities of diagonal and cross peaks.

However, the direct and detailed analysis of them is to date limited by the spectral resolution of the experiments and not feasible with the current data quality.

The aim of part II of the thesis is to establish P2D-IR spectroscopy in combination with DFT calculations as a method for structure determination of small, highly functionalized molecules as a complement to NMR investigations. In highly functionalized molecules, the low number of active spins makes the conformational analysis with NMR sometimes difficult or even impossible. The ultrafast time resolution makes P2D-IR particularly well suited for investigating short-lived intermediates and molecules participating in fast equilibria. In addition, species in low concentration are detectable, because P2D-IR spectroscopy has the high sensitivity of IR spectroscopy. These are exactly the conditions where NMR is beyond its limits. In chapter 10 the current capabilities and limitations of 2D-IR spectroscopy are reviewed based on the experimental results of the present thesis.

4.3 Oxazolidinones as Chiral Auxiliaries
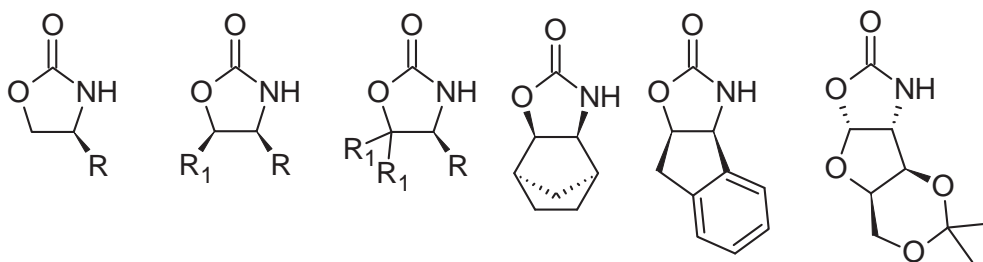
Figure 4.17: *Chiral oxazolidinone based auxiliaries.* [171]

In this thesis the structures of the chiral *N*-crotonyloxazolidinone in solution and as complex with Lewis acids were determined. Chiral oxazolidinones were introduced by Evans *et al.* as auxiliaries for asymmetric organic reactions. [172–176] Nowadays they are widely used in stereoselective synthesis and a great variety of substituted oxazolidinones, commonly called Evans auxiliary, exist. [171,177–186] Some representative structures are shown in Fig. 4.17. All have in common that a bulky group attached to the oxazolidinone moiety shields one side of the reactive group of the substrate and hence forces the catalyst or the reaction partner to approach from the opposite side.

The fact that oxazolidinones have found widespread applications stems from several reasons. They can be easily synthesized from inexpensive, commercially available starting materials. The various derivatives are typically crystalline, which allows uncomplicated purification and handling. [187] Additionally, the attachment to the prochiral substrate is straight forward and usually results in high yields (see Fig. 4.18). [177,187] There also exist a large variety of cleavage protocols, which differ, *e.g.*, in solvent or reagent. [172,177,178,187,188] Thus different functional groups can easily be introduced at the position of the auxiliary and conditions that are tolerated by the rest of the molecule can be chosen for cleavage. Some cleavage reactions that do not alter the induced stereogenic centers are shown in Fig. 4.18.

Moreover very high induced stereoselectivities were observed using the Evans auxiliary in many mechanistically unrelated reactions. [171,177,178,187] Figure 4.19 shows

substrate preparation
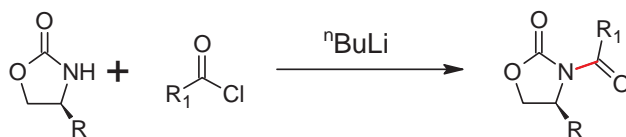
auxiliary cleavage
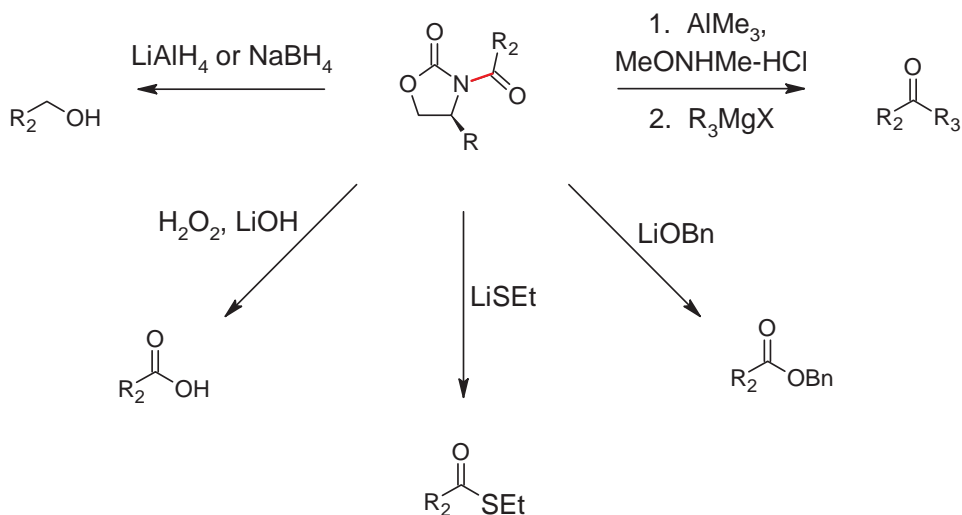
Figure 4.18: *Top: Commonly used reaction for attaching the Evans auxiliary to the substrate.*[187] *The newly formed bond is highlighted in red. Bottom: Some possible reactions for the cleavage of the Oxazolidinones.*[172,173,187]

a very limited selection of reactions using the Evans auxiliary involving aldol reactions,[190] alkylations,[189] and pericyclic reactions.[173,191] It also has been proven to be valuable in heterogeneous catalysis.[192]

Another important factor is that depending on the reaction conditions all four possible diastereomers are accessible in high selectivities.[171,184,193] This is illustrated in Fig. 4.20 for an aldol reaction.[171] The diastereoselectivity for the reaction is determined by the orientation around the oxazolidinone substrate bond (see highlighted bond in Fig. 4.18) as well as the orientation of the aldehyde with respect to the substrate. Which of the possible transition states or intermediates is energetically favored and thus important, is typically rationalized using sterical considerations in combination with the chelating abilities of the Lewis acids.[184,185,194] On an empirical level, the stereoselectivities of the reactions in Fig. 4.20 are understood and can be predicted. However, to our best knowledge, none of the involved intermediate structures have been investigated experimentally. To understand the reaction mechanisms it is of great importance to know which rotamer of **1** is preferred under reaction conditions and which one is the reacting intermediate. In organic chemistry, two models are usually used to rationalize the conformation leading to the observed product: chelation and dipole minimization.[171,184,187] Chelation is typically observed if a strong Lewis

Alkylation

yield: 93%, dr: >95:5

Aldol condensation

yield: 91%, dr: 96:3

Diels–Alder reaction

yield: > 99%, dr: 94:6

[2+2] Cycloaddition

yield: > 95%, dr: >95:5
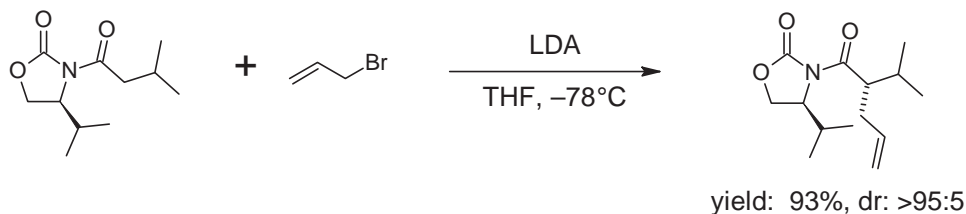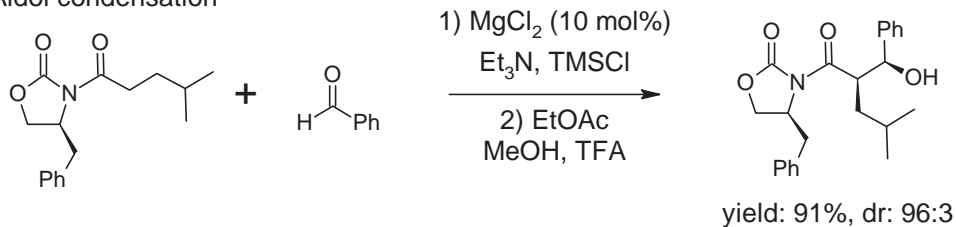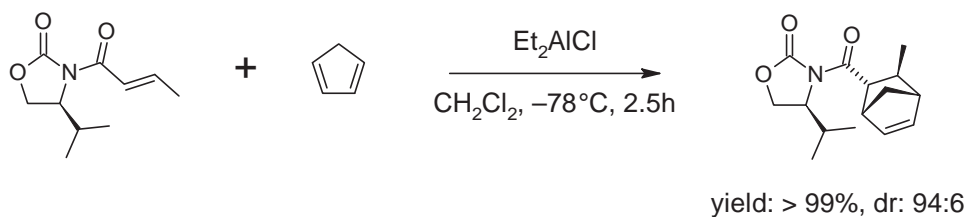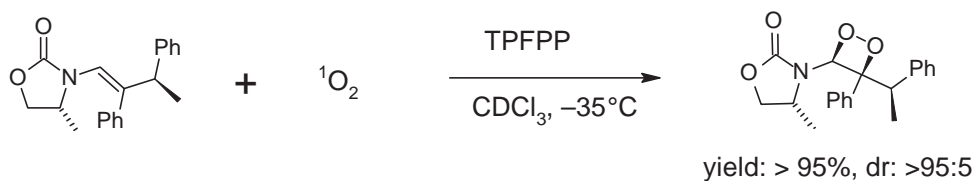
heterogeneous Hydrogenation

yield: 95%, dr: 97:3
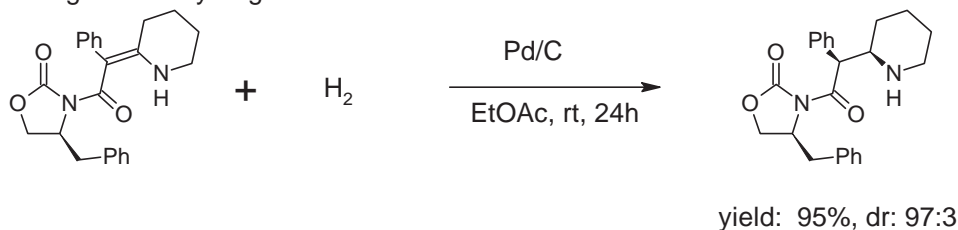
Figure 4.19: *A selection of stereoselective reactions using the Evans auxiliary.*[171,173,189–192]
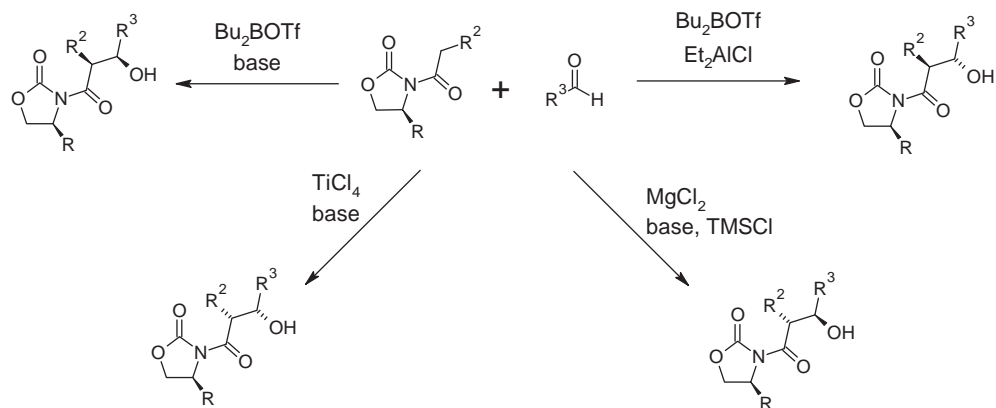
Figure 4.20: *Stereocomplementary aldol products accessible using the Evans auxiliary and different conditions.* [171] *Note: For clarity the products are not drawn in their most stable conformation.*

acid with more than one coordination site (*e.g.*, MgX_2, ZnX_2, $TiCl_4$, $SnCl_4$, $AlCl_3$, and Me_2CuLi) is used in a non-coordinating solvent (*e.g.*, toluene and CH_2Cl_2). If the Lewis acid has only one coordination site available (due to its electronic structure, non-dissociating anions or complexation by the solvent), the rotamer with minimized dipole interactions is usually energetically favored. [171] However, depending on the conditions, the energies of the rotamers of the Lewis acid–substrate complexes can be close to each other and difficult to predict. Thus methods for the experimental discrimination and determination of those structures are highly desired.

4.3.1   Lewis Acid Catalyzed Diels–Alder Reactions

Out of the many reactions using the Evans auxiliary, we chose the Lewis acid cat-alyzed Diels–Alder reaction as proof of principle system to demonstrate the power of P2D-IR spectroscopy for structure determination and the investigation of reac-tion mechanism. [195–199] The Diels–Alder reaction is a [2+4] cycloaddition forming a cyclohexene ring by the fusion of a conjugated diene and a (substituted) alkene, referred to as dienophile. [198–200] Cycloadditions are belonging to the most important reactions in organic synthesis, mainly due to their high yield and the high regio- and stereoselectivity. [200] The Diels–Alder reaction allows in principle the formation of four stereogenic centers. The reaction mechanism is illustrated in Fig. 4.21.

Electron withdrawing groups such as conjugated carbonyl groups on the dienophile speed up the reaction significantly. The use of Lewis acids as catalysts to decrease the electron density of the dienophile (and therefore lower the energy of the LUMO) enhances this effect and thus facilitates the reaction at lower temperatures. [196,198,199] Lowering the temperature usually increases the selectivity of a reaction because there is less thermal energy available and thus only the most stable conformers of the re-actants are significantly populated. Moreover, there is only less energy available to overcome the activation energy and thus only the reaction(s) with low activation energies will proceed. Using prochiral reactants in a Diels–Alder reaction, only the relative stereoselectivities are defined, but not the the absolute stereoselectivities since the attacks from both sides (so called *Si*-face and *Re*-face) are energetically equal. The absolute stereochemistry of the Diels–Alder reaction can be induced by using
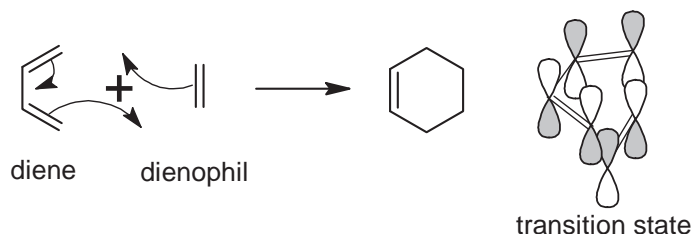
Figure 4.21: *Reaction mechanism of the Diels–Alder reaction. The transition state is illustrated with the important orbital interactions (between the HOMO of the diene and LUMO of the dienophile) on the right.*

chiral catalysts or chiral substrates. Prochiral substrates can be transformed into chiral ones by attaching chiral auxiliaries such as chiral oxazolidinones. Enantiose-lective, Lewis acid catalyzed Diels–Alder reactions of *N*-crotonyloxayolidinone (**1**) as dienophile were introduced by Evans *et al.*[173,176] They observed exceptional high diastereoselectivities when using Et_2AlCl as Lewis acid (also for other, related reactions) and explained the observed major product by the formation of a chelate.[201,202] The reaction of **1** with cyclopentadiene (see Fig. 4.22) became a showcase example for both, the use of the Evans auxiliary and also the dictation of the intermediate conformation by chelation.[187,199] It is noteworthy that other Lewis acids that are known to form chelates readily, were not as stereoselective as Et_2AlCl (see Fig. 4.22).[202]

Even tough this reaction is widely known and the mechanism is well accepted by organic chemists, there are only a few studies on the structure of the substrate **1** and the intermediate under reaction conditions.[203–207] Only recently, Bakalova *et al.* suggested based on DFT calculations and 2D-NMR experiments an alternative mechanism involving a di-aluminum species instead of a chelate as reactive inter-mediate (see Fig. 4.22).[203] For the proof-of-principle studies presented here, $SnCl_4$ and $Mg(ClO_4)_2$ were chosen as Lewis acids. Both Lewis acids are commonly used in synthesis and well known to form chelates.[171,181,182,184,185,193,200,207–211] Thus they provide a reliable system to investigate whether P2D-IR spectroscopy is in practice really able to detect conformational changes. Additionally, these two Lewis acids lead to significant shifts in the FTIR spectra of **1** and are much easier to handle than Et_2AlCl; in particular they do not start to burn when exposed shortly to air or moisture.

Lewis acid	equiv	A (%)	B (%)	C+D (%)
$SnCl_4$	1.1	71	23	6
$TiCl_4$	1.1	66	25	9
$ZrCl_4$	1.4	87	12	1
$AlCl_3$	1.0	49	32	19
$EtAlCl_2$	1.1	58	34	8
Et_2AlCl	1.4	93	5	2
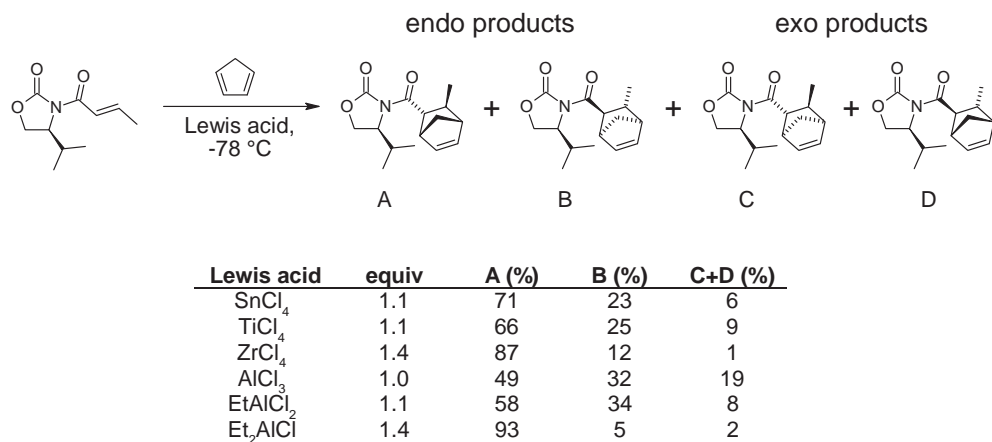
Figure 4.22: *Lewis acid catalyzed Diels–Alder reaction of **1** with cyclopentadiene with various Lewis acids. The table summarizes the observed product ratios for various Lewis acids.* [173] *The proposed transition states are illustrated on the bottom.* [173,203] *The arrows mark the steric interactions that are proposed to determine the stereoselectivity.*

Chapter 5

Structure of *N*-Crotonyloxazolidinone
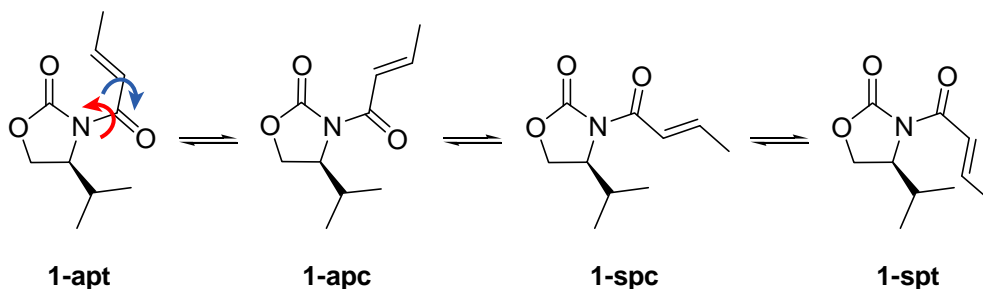
Figure 5.1: *Possible conformers of **1**. They can be transformed into each other by rotation around the N–C bond (red arrow) or the C–C bond (blue arrow).*

In order to understand the mechanisms of the reactions, where **1** is the substrate, it is essential to know the structure of **1** under reaction conditions. The conformers shown in Fig. 5.1 were discussed as potential solution structures of **1**.[203,206] They can be transformed into each other by rotations around the σ-bonds of the crotonyl moiety. Therefore, the two carbonyl groups can be arranged in a synperiplanar (sp) or antiperiplanar (ap) manner. The alkenyl group can stand *s-cis* (c) or *s-trans* (t) to the crotonyl carbonyl group. Most organic chemists draw the structure of **1** in the conformation **1-spc**, probably since they assume that the conformer **1-spc** is the one that reacts.[171,173,177,178,180,184,212,213] However, this does not imply that this would be the conformation present in solution.

From a basic point of view, one would expect that the conformation is lowest in energy that minimizes steric interactions and dipolar repulsion. The dipole interaction is most favorable, if the oxygens of the two carbonyl groups are as far apart from each other as possible. This is the case in the conformations, in which the two carbonyls are antiperiplanar to each other. However, this induces an unfavorable steric interaction to the isopropyl group attached to the oxazolidinone ring, which is estimated to be less important though. Minimal steric interactions between oxazolidinone ring and crotonyl chain are present when the carbonyl and alkenyl group are arranged *s*-cis. Combining these two contributions, **1-apc** is expected to be the favored structure.

These very basic considerations are in agreement with NMR and DFT studies on **1** and similar systems. [183,203,213,214]

Crystal structures of similar substances show an antiperiplanar arrangement of the carbonyl groups. [180] Additional NMR studies, *e.g.*, NOE studies, of **1** support that the two carbonyl groups are antiperiplanar, however cannot determine the structure unequivocally. [203,213] The NMR spectra of **1** are discussed in detail in chapter 5.2. Since the four conformers differ considerably in the relative orientation of the carbonyl groups and the alkenyl group, P2D-IR spectroscopy in the spectral range of the vibrations of these groups should allow to measure the conformation and identify the predominant species in solution.

5.1   P2D-IR Spectroscopy

The stretching vibrations involving the alkenyl and the two carbonyl groups of **1** in CH_2Cl_2 appear as three bands at $1638\,cm^{-1}$ (ν_1), $1686\,cm^{-1}$ (ν_2), and $1776\,cm^{-1}$ (ν_3) in the FTIR spectrum. The corresponding P2D-IR spectra are shown in Fig. 5.2 for parallel (left) and perpendicular polarization conditions(right). They are dominated by the three intense diagonal peaks of ν_1, ν_2, and ν_3. A fourth, much weaker, diagonal peak is located at $\approx 1725\,cm^{-1}$, downshifted by $\approx 50\,cm^{-1}$ from the diagonal peak at position A. This peak can be assigned as ^{13}C satellite of the peak at position A (see chapter 5.1.4 for a detailed discussion). In addition to the diagonal peaks, cross
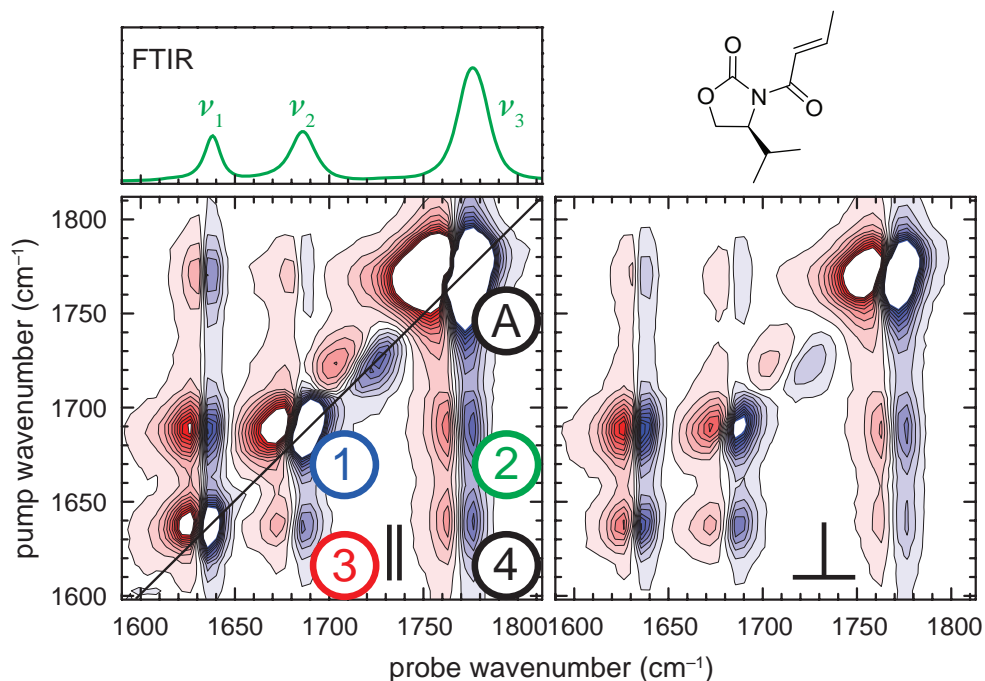
Figure 5.2: *P2D-IR spectra of **1** in CH_2Cl_2 (1.5 ps). Left: parallel polarization; right: perpendicular polarization. The contour lines are spaced by 0.05 mOD. Signals larger than $\pm 0.5\,mOD$ are truncated. Numbers see text. The FTIR spectrum is shown in the top panel for reference.*

peaks between all three stretching vibrations occur, indicating that the vibrations are coupled to each other and thus not localized on a specific bond. [15,94]

As already discussed in chapter 2.2.3, the anisotropy of the signals in a P2D-IR spectrum gives access to the angles between the involved transition dipole moments. A visualization of the anisotropy in the P2D-IR spectra of **1** is shown in Fig. 5.3. The anisotropy is only shown for regions where $\Delta\alpha_{\parallel} > 0.05\,\text{mOD}$ and where the anisotropy is in the range between –0.2 and 0.4. Especially where several peaks overlap, the anisotropy can be beyond the meaningful range. The diagonal peaks show an anisotropy of $\approx$0.4 (red), while all cross peaks have smaller anisotropies.

5.1.1 Time Dependence of the Anisotropy

The measured anisotropy is time-dependent since the molecules rotate on the time scale of a P2D-IR measurement, *i.e.*, within the delay time (see chapter 2.2.3). Therefore, it is essential to measure the time dependence of the anisotropy and extrapolate it to a delay time of t = 0 in order to obtain exact values for angles between the transition dipole moments θ (see chapter 2.2.3). Fig. 5.4 shows the time dependence of the anisotropy the diagonal peak of ν_3 (Fig. 5.2 pos. A) in blue. The time dependent signals for parallel (red) and perpendicular (black) polarization used to determine the anisotropy are shown on top. The signal size increases in both polarizations up to a maximum at $\sim$0.5 ps because of finite pulse durations and decays due to vibrational relaxation. The anisotropy data points in the region when pump and probe pulses overlap (gray) were not used for the analysis. With increasing delay time the
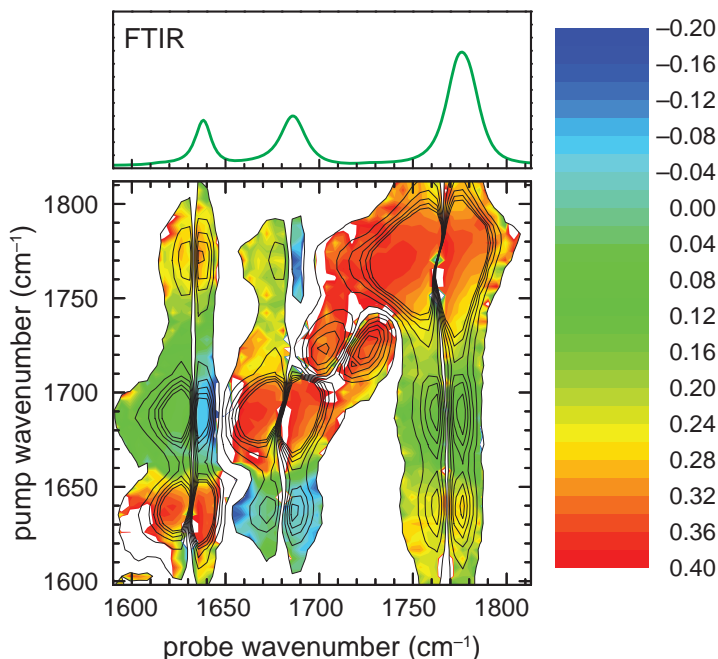
Figure 5.3: *2D-IR anisotropy spectrum of **1** in CH_2Cl_2 (cf. Fig. 5.2). The colors indicate the anisotropy, while the contour lines show the signal intensities for parallel polarization (see Fig. 5.2, left). The anisotropy is only shown for regions where $\Delta\alpha_{\parallel} > 0.05\,\text{mOD}$ and where $-0.2 < r < 0.4$.*
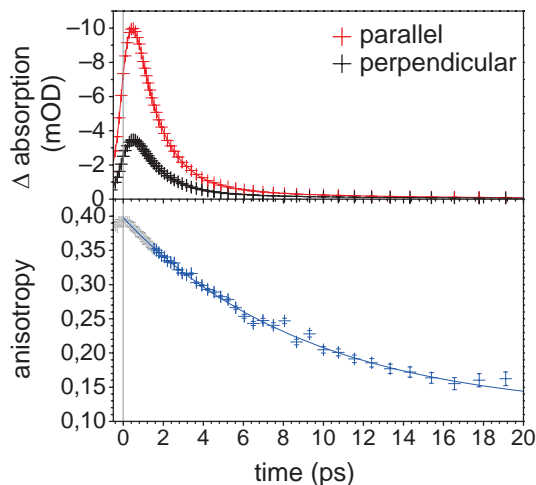
Figure 5.4: *Top: Time dependence of the diagonal peak intensity (bleach) ν_3 (cf. Fig. 5.2 pos. A) for parallel (red) and perpendicular polarization (black) in CH_2Cl_2. Bottom: Time dependence of the anisotropy calculated from the data points shown above (blue line: exponential fit to the data points with a time delay of more than 1.5 ps (blue), gray data points indicate the region when pump and probe pulses overlap in time).*

anisotropy decreases due to rotational diffusion of the molecules. When pump and probe pulse interact with exactly the same transition dipole moment, the angle θ must by definition be $0°$. Thus, the true value for the anisotropy is 0.4 (see Eq. 14). The blue line shows a single exponential fit to the data from 1.5 ps to 20 ps with a life time (*i.e.*, rotational correlation time) of 9.2(2) ps and an offset of 0.112(4) indicating an additional rotational process that is slower than ~50 ps. The fit reaches a value of $r = 0.398(9)$ at $t = 0$ ps. This is in excellent agreement with the exact value of 0.4 and proves the correctness of the measurement. Measuring and evaluating the diagonal peak anisotropy serves as internal validation of the measurement.

A linear fit to the data from 1.5 ps to 5 ps leads to an anisotropy of 0.382(2) at $t = 0$ ps (fit not shown). The systematic error of 0.02 in anisotropy by using a linear fit instead of an exponential fit is maximal for angles of $0°$ and corresponds to a systematic error of ~$10°$ in the angle. The error drops rapidly with increasing angle between the two transition dipole moments. For angles larger than $20°$ the systematic error in anisotropy is expected to be smaller than 0.01, corresponding to a systematic error in angle of $\approx 1°$ (compare Fig. 5.5 right). This is smaller than our estimated experimental error. A linear fit of the data therefore is sufficient and used for analyzing the anisotropies having the advantage that only the data points for short time delays need to be measured (here only until 5 ps instead of until 20 ps). This reduces the measurement time by a factor of more than 3, if all data points shall have a similar signal-to-noise ratio.

The anisotropy of the diagonal peak of the vibration ν_2 shown in Fig. 5.5 in blue, (*cf.* Fig. 5.2 pos. 1) linearly extrapolates to 0.379(4), which again is in good agreement with the exact value of 0.4. For the cross peak between ν_2 and ν_3 shown in green (*cf.* Fig. 5.2 pos. 2), the anisotropy is 0.104(3) for zero delay time. Using eq. 14, this corresponds to an angle θ between the transition dipoles of $44° \pm 3°$. The stated errors include the fit error as well as estimated experimental errors. The same analysis

of the cross peaks between the vibrations ν_1 and ν_2 (red, *cf.* Fig. 5.2 pos. 3) and between ν_1 and ν_3 (black, *cf.* Fig. 5.2 pos. 4) result in angles of $57° \pm 2°$ and $28° \pm 3°$, respectively. The single exponential fits of the data are shown in light gray to illustrate that the linear fits hardly deviate at $t = 0$ ps. All exponential fits lead to a decay time between 5.5 ps and 11.5 ps and an offset indicating the presence of an additional, slower rotational correlation time, which is estimated to be larger than 50 ps. It is noteworthy that also heating effects could cause such an offset in the anisotropy for long delay times. [215] This artifact cannot be ruled out completely, however, it is expected not to affect the angles determined *via* the anisotropy at short times.
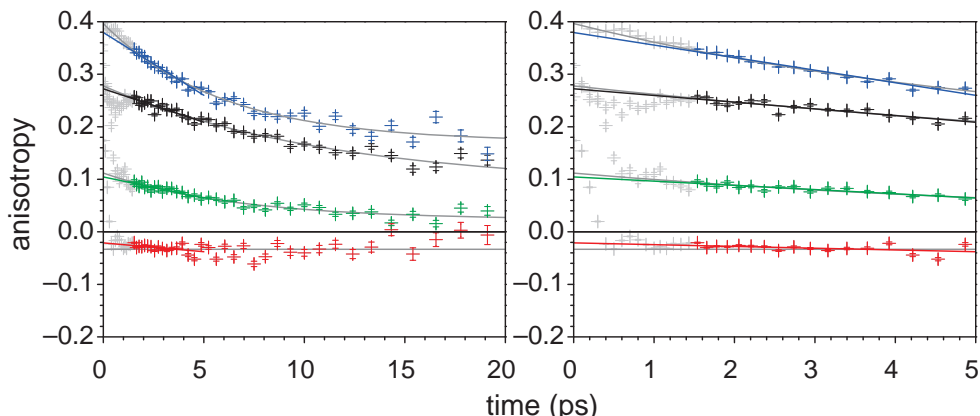
Figure 5.5: *Time dependence of the anisotropy for the signals (bleach) of **1** in CH_2Cl_2 labeled in Fig. 5.2. Left: full dataset; right: data from 0 ps to 5 ps. Diagonal peak ν_2: blue (cf. Fig. 5.2 pos. 1); cross peak ν_2/ν_3: green (cf. Fig. 5.2 pos. 2); cross peak ν_1/ν_2: red (cf. Fig. 5.2 pos. 3); cross peak ν_1/ν_3: black (cf. Fig. 5.2 pos. 4). The straight, colored lines are linear fits to the data from 1.5 ps to 5 ps; the gray curves single exponential fits to the data from 1.5 ps to 20 ps.*

5.1.2 Solvent Dependence

Similar measurements and analyses were performed for **1** in MeCN and toluene (see Fig. 5.6). Table 5.1 summarizes the results. The different solvents had little affect on the measured angles, showing that the same conformer exists in all investigated solvents, both polar and unpolar. This finding is in agreement with the similarity of the IR absorption spectra in the solvents. The anisotropy decays differ in the various solvents, though, and roughly correlate with the viscosities of the solvents. This is best seen when comparing the anisotropy decays of diagonal peak ν_2 (blue) in the various solvents. If the molecules are surrounded by a solvent with low viscosity, they tumble faster than if they were surrounded by a more viscous solvent.
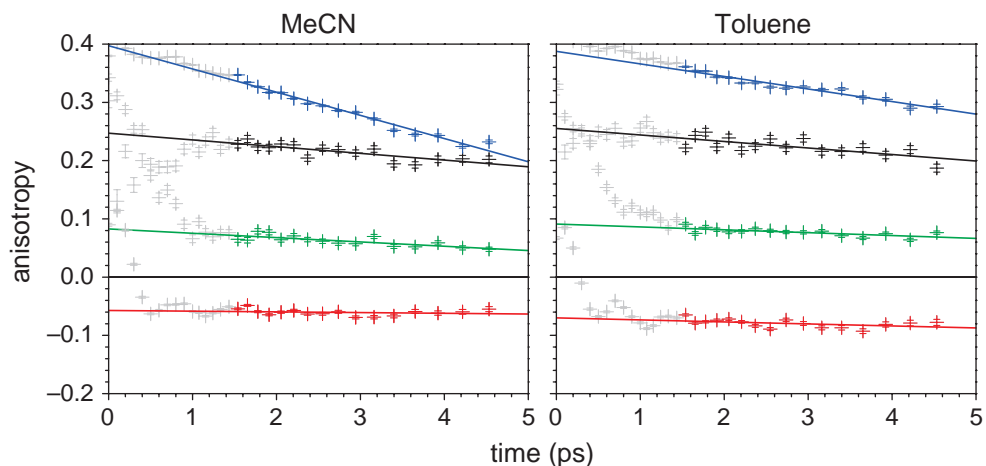
Figure 5.6: *Time dependence of the anisotropy for the signals (bleach, cf. labeled positions in Fig. 5.2) of 1 in MeCN and toluene. Diagonal peak ν_2: blue (cf. Fig. 5.2 pos. 1); cross peak ν_2/ν_3: green (cf. Fig. 5.2 pos. 2); cross peak ν_1/ν_2: red (cf. Fig. 5.2 pos. 3); cross peak ν_1/ν_3: black (cf. Fig. 5.2 pos. 4). The straight, colored lines are linear fits to the data from 1.5 ps to 5 ps.*

Table 5.1: *Solvent dependence of the angles between the transition dipole moments of 1.*

	MeCN	CH_2Cl_2	Toluene
ν_1/ν_2 (°)	60 ± 2	57 ± 2	62 ± 2
ν_1/ν_3 (°)	30 ± 3	28 ± 3	29 ± 3
ν_2/ν_3 (°)	47 ± 3	44 ± 2	46 ± 2
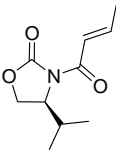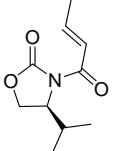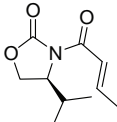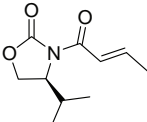
5.1.3 Comparison with DFT Calculations[i]

In the ideal case were the vibrations are localized on individual bonds, the angles between transition dipole moments directly correspond to bond angles in the molecule. However, in most cases the vibrations are delocalized over more than one bond, [169] as it is also the case here and the direction of the transition dipole moment with respect to the molecule is required to determine the structure. The vibrations and their transition dipole moments of a molecule can be determined using quantum chemical calculations. The transition dipole moments for the four conformers of **1** shown in Fig. 5.1 were calculated using DFT. The details of the calculations such as used basis sets and solvent models are discussed in chapter 15 in the appendix of this thesis.

Table 5.2 summarizes the DFT results for **1** in CH_2Cl_2 and compares them with the experimental values. The calculations for the conformer **1-apc** agree very well with the experimentally determined angles. Only small deviations were observed. The angles involving the transition dipole ν_1 deviate by 7° while the other angle deviates by only 1°. All other conformers show large differences to the measured values for at least one angle (up to 37° for the angle between ν_1/ν_3 in the case of **1-spt**). A good measure for the overall deviation of the calculations from the experiment is the sum of the single deviations ($\Delta_{tot} = \sum |\Delta_i|$). This is 15° for **1-apc** and more than 50°

---

[i]All presented DFT calculations of **1** and its complexes were done by Jens Bredenbeck.

Table 5.2: *Comparison of the experimentally determined angles and frequencies of **1** in CH$_2$Cl$_2$ with the results of the DFT calculations (M06/6-31+G(d,p)/PCM/Bondi). The total structural deviation is expressed as $\Delta_{tot} = \sum |\Delta_i|$.*

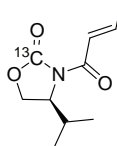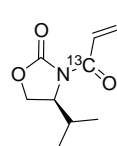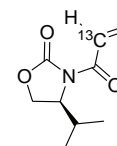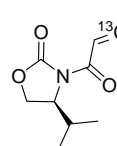|	exp.	**1-apc**	**1-apt**	**1-spt**	**1-spc**
angles					
ν_1/ν_2 (°)	57 ± 2	64 (Δ=7)	33 (Δ=24)	74 (Δ=17)	67 (Δ=10)
ν_1/ν_3 (°)	28 ± 3	21 (Δ=7)	54 (Δ=26)	65 (Δ=37)	42 (Δ=14)
ν_2/ν_3 (°)	44 ± 2	43 (Δ=1)	40 (Δ=4)	52 (Δ=9)	71 (Δ=27)
Δ_{tot} (°)		15	54	62	51
vibrational energies					
ν_1 (cm^{-1})	1638	1694 (Δ=56)	1714 (Δ=76)	1717 (Δ=79)	1703 (Δ=65)
ν_2 (cm^{-1})	1686	1741 (Δ=55)	1735 (Δ=49)	1742 (Δ=56)	1744 (Δ=58)
ν_3 (cm^{-1})	1777	1831 (Δ=54)	1836 (Δ=59)	1847 (Δ=70)	1857 (Δ=80)
calculated Gibbs energies					
ΔG_{298} (kcal/mol)		0.0	3.6	6.0	3.3

for all other conformers. Also the calculated frequencies for **1-apc** match the experimental values best. The calculated vibrational energies are not corrected and include errors mainly caused by neglecting the anharmonicity of the vibrations, having an incomplete basis set and therefore incomplete electron correlations, and solving the Schrödinger equation only approximate.[216–218] Usually this correction is done by multiplying the calculated frequencies with a uniform scaling factor, which is determined by comparison of calculations with a data base of experimental data.[217,218] However, for the used basis set no reliable scaling factor is known. Hence, the frequencies are compared directly. If there is a more or less constant offset between the experimental values for ν_{1-3} and the calculations, the calculations are considered to match well. A constant offset ($\approx$55 cm^{-1}) is only obtained for **1-apc**, which would correspond to a uniform scaling factor of 0.97. Comparing the entire spectrum (see Fig. 5.8), the calculation for **1-apc** (shown in red) reproduces the experimental FTIR spectrum (shown in black) best, both looking at the frequencies and the relative peak intensities. In conclusion, the comparison of the DFT calculations to the experimental vibrational energies and angles of **1** in CH$_2$Cl$_2$ leads to the well-founded conclusion that **1-apc** is the conformation present in solution. This conformation is also calculated to be lowest in energy (see Table 5.2)

The vibrations ν_1, ν_2, and ν_3 in **1-apc** are visualized by the displacement vectors shown in Fig. 5.7. The directions of the corresponding transition dipole moments are depicted by the green arrows. The angles between those are measured in a P2D-IR experiment. In the calculation of **1-apc**, the alkenyl and carbonyl groups lie in a plane. As a consequence, the sum of the angles ν_1/ν_3 (21°) and ν_3/ν_2 (43°) equates exactly the angle ν_1/ν_2 (64°). In the experiment, this is not the case. The sum of

ν_1 (1694 cm^{-1}) ν_2 (1741cm^{-1}) ν_3 (1831 cm^{-1})
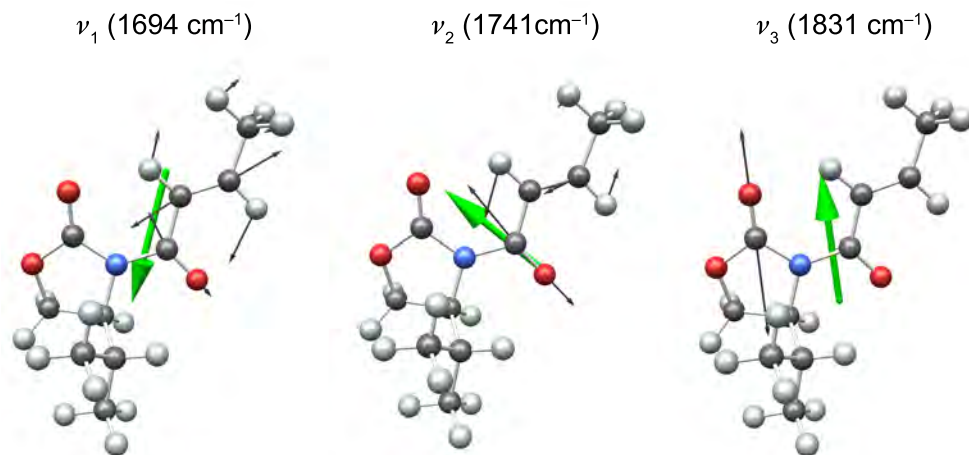
Figure 5.7: *Displacement vectors describing the vibrations ν_1, ν_2, and ν_3 of **1-apc** in CH_2Cl_2 (M06/6-31+G(d,p)/PCM/Bondi). The direction of the corresponding transition dipole moment is shown in green.*

ν_1/ν_3 (28°) and ν_3/ν_2 (44°) exceeds the angle ν_1/ν_2 (57°) by 15°. This implies that in solution the alkenyl and carbonyl groups do not lie in a single plane, but are somehow twisted. Most likely, the crotonyl chain rotates slightly around the C–N bond. A similar effect was observed in the crystallographic studies (see chapter 5.3). It is noteworthy that the observed deviation from planarity does not necessarily need to be static, meaning that the structure always is twisted by the same angle. It can also be a dynamic effect, meaning that there is an ensemble of structures around planar geometry in which some molecules are twisted to the left and some to the right. However, on average the structure is planar. The two cases can be distinguished by doing similar measurements at low temperatures. If there is a distribution of structures, the distribution around the minimal energy structure becomes narrower at lower temperatures. The measurements then probe different ensembles of structures at high and low temperature, causing a temperature dependence of the measured angles.

Comparing the experimental results with the DFT calculations for **1** in MeCN and in toluene (see Table 5.3) leads to the very same conclusions, namely **1-apc** being the predominant conformer present in solution and the structure being not completely planar. The twist seems to be of similar magnitude in all three solvents.
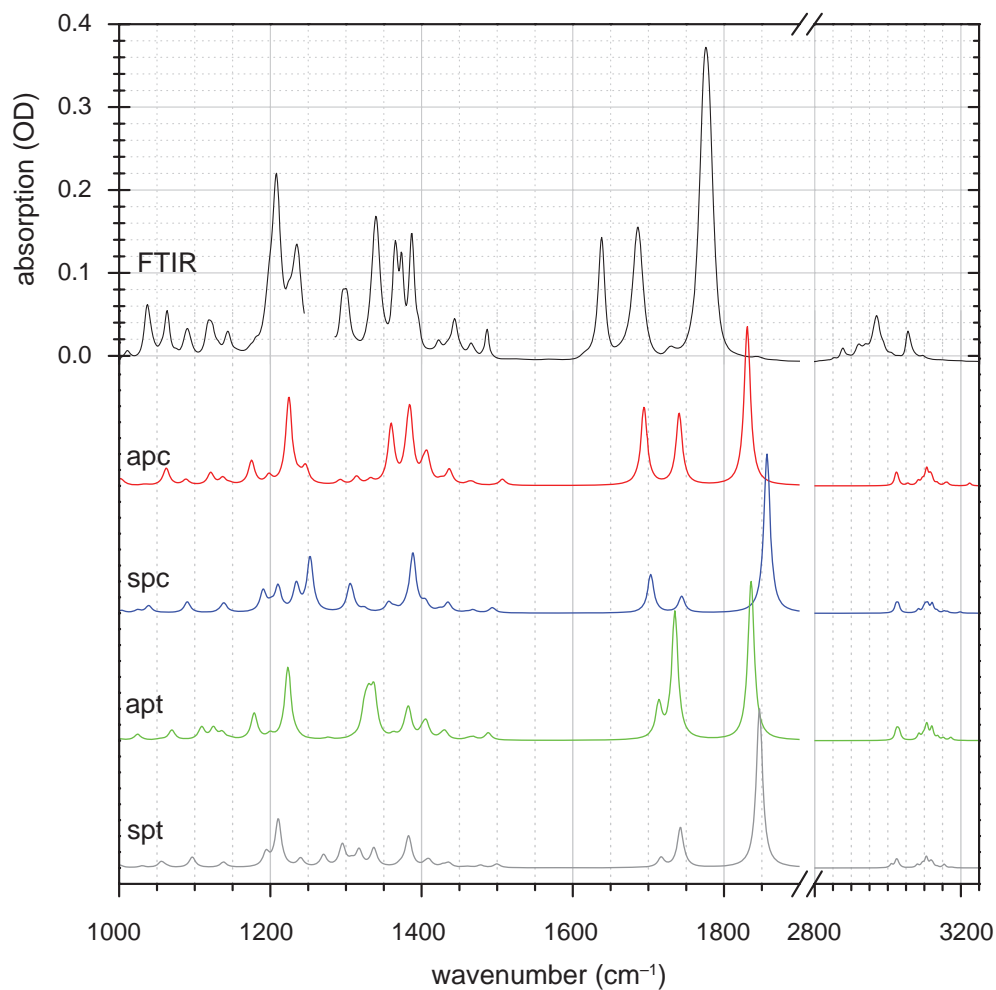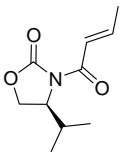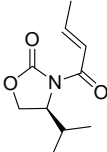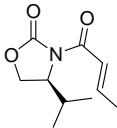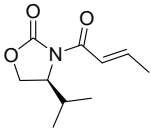
Figure 5.8: *Comparison of the experimental FTIR spectrum of **1** in CH_2Cl_2 (39 mM, black) with the calculated spectra for the four conformers of **1** in CH_2Cl_2 (M06/6-31+G(d,p)/PCM/Bondi, colored). The region between $1245\,\mathrm{cm}^{-1}$ and $1285\,\mathrm{cm}^{-1}$ is omitted in the experimental data since CH_2Cl_2 absorbs strongly there.*
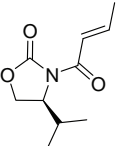
Table 5.3:   *Comparison of the experimentally determined angles and frequencies of **1** in MeCN and toluene with the results of the DFT calculations (M06/6-31+G(d,p)/PCM/Bondi). The total structural deviation is expressed as $\Delta_{tot} = \sum |\Delta_i|$.*

	exp.	**1-apc**	**1-apt**	**1-spt**	**1-spc**

<center>ACETONITRILE</center>

angles

ν_1/ν_2 (°)	61 ± 2	61 (Δ=0)	27 (Δ=34)	89 (Δ=28)	61 (Δ=0)
ν_1/ν_3 (°)	30 ± 3	17 (Δ=13)	47 (Δ=17)	77 (Δ=47)	38 (Δ=8)
ν_2/ν_3 (°)	47 ± 3	45 (Δ=2)	41 (Δ=6)	49 (Δ=2)	81 (Δ=34)
Δ_{tot} (°)		15	57	77	42

vibrational energies

ν_1 (cm^{-1})	1639	1690 (Δ=51)	1708 (Δ=69)	1712 (Δ=73)	1697 (Δ=58)
ν_2 (cm^{-1})	1687	1734 (Δ=47)	1728 (Δ=41)	1730 (Δ=43)	1734 (Δ=47)
ν_3 (cm^{-1})	1776	1820 (Δ=44)	1825 (Δ=49)	1830 (Δ=54)	1841 (Δ=65)

calculated Gibbs energies

ΔG_{298} (kcal/mol)		0.0	3.3	4.8	2.0

<center>TOLUENE</center>

angles

ν_1/ν_2 (°)	62 ± 2	70 (Δ=8)	67 (Δ=5)	71 (Δ=9)	72 (Δ=10)
ν_1/ν_3 (°)	29 ± 3	28 (Δ=1)	85 (Δ=56)	64 (Δ=35)	50 (Δ=21)
ν_2/ν_3 (°)	46 ± 2	41 (Δ=5)	41 (Δ=5)	58 (Δ=12)	58 (Δ=12)
Δ_{tot} (°)		14	66	56	43

vibrational energies

ν_1 (cm^{-1})	1639	1706 (Δ=67)	1725 (Δ=86)	1726 (Δ=87)	1719 (Δ=80)
ν_2 (cm^{-1})	1688	1760 (Δ=72)	1757 (Δ=69)	1775 (Δ=87)	1774 (Δ=86)
ν_3 (cm^{-1})	1783	1861 (Δ=78)	1867 (Δ=84)	1890 (Δ=107)	1896 (Δ=113)

calculated Gibbs energies

ΔG_{298} (kcal/mol)		0.0	4.0	8.7	5.3

5.1.4 Isotopologue Signals

Using DFT calculations, also the vibrational shifts for the ^{13}C isotopologues can be determined. Table 5.4 summarizes the calculated vibrational shifts for the relevant ^{13}C isotopologues of **1-apc** compared to the all-^{12}C compound in CH_2Cl_2. The positions of the diagonal peaks shifted by more than $10\,cm^{-1}$ are marked with green crosses in the P2D-IR spectrum in Fig. 5.9. The following analysis focuses on these signals.

Table 5.4: *Calculated shifts of the vibrational wavenumbers for the isotopologues of **1-apc** in CH_2Cl_2 (M06/6-31+G(d,p)/PCM/Bondi).*

	(cm^{-1})	$\Delta\ (cm^{-1})$	$\Delta\ (cm^{-1})$	$\Delta\ (cm^{-1})$	$\Delta\ (cm^{-1})$
ν_1	1694	0	−21	−22	−25
ν_2	1741	−1	−22	−5	−6
ν_3	1831	−46	−1	0	0

Figure 5.9: *Calculated positions (green crosses) for the diagonal peaks of the ^{13}C isotopologues in the P2D-IR spectrum of **1-apc** in CH_2Cl_2 (M06/6-31+G(d,p)/PCM/Bondi). The black crosses mark the vibrations of the all ^{12}C isotopologue. The calculated vibrational energies are corrected by $-55\,cm^{-1}$ (cf. Table 5.4).*

Based on the calculations, distinct diagonal peak at $\approx 1725\,\text{cm}^{-1}$ is assigned as the ^{13}C satellite of vibration ν_3. The ^{13}C isotopologue signal of vibration ν_2 strongly overlaps with the positive part of the main diagonal signal, why it is hardly seen. The three ^{13}C isotopologue signals of vibration ν_1 also overlap with the positive part of the main diagonal peak. These peaks, which happen to be approximately at the same position, are expected to be one to two contour lines in size in Fig. 5.9 and are seen weakly in the lower left corner in light blue.

The size of the satellite peak of ν_3 is approximately $6\% \pm 2\%$ of the main peak. Based on the natural abundance of ^{13}C one would expect 1.1%. However, the signal size in a 2D-IR spectrum depends linearly on the pump intensity (see chaper 2). There is about 1.7 times more pump light at the position of the ^{13}C vibration than at the ^{12}C vibration, as the spectrum of the OPA has approximately a Gaussian line shape (center $\approx 1690\,\text{cm}^{-1}$, FWHM $\approx 180\,\text{cm}^{-1}$). Accounting in addition for the 100 times higher absorption at the main peak compared to the isotopologue peak, the excitation probability is ~ 3.5 times higher for the isotopologue molecules than for the ^{12}C compounds. Combining the higher excitation probability with the natural abundance of 1.1%, one expects an isotopologue signal of $\sim 3.9\%$ of the main peak. Including effects of the pixelation of the detector, the isotope signal of the vibration is expected to be approximately $3.9\% \pm 0.8\%$ of the main peak, which corresponds to what is measured. The different contributions to the signal size are recapitulated in Table 5.5. These contributions also apply for signals originating from other species, *e.g.*, minor conformers. Of course, also differences in the transition dipole moments of the vibrations influence the signal size. The transition dipole moments are assumed to be equal, because various isotopologues of the very same conformer are compared. This assumption is in agreement with the DFT calculations.

Table 5.5: *Factors contributing to the signal size (maximal intensity) of the isotopologue signal compared to the main peak.*

contribution to the signal size	factor
relative concentration (*i.e.*, natural abundance)	1.1%
saturation effects (absorption)	~ 2.0
difference in anharmonicity	0.98
difference in the transition dipole moment	1.0
OPA intensity	~ 1.7
pixelation of the detector	$\pm 20\%$

5.1.5   Minor Conformers

The signal sizes of the isotopologues in the P2D-IR spectra provide an inherent measure for the sensitivity of the measurement. Thus the concentration of other species, *i.e.*, other conformers, possibly present in solution can be estimated, if their band positions are known. For the various conformers of **1** the vibrational energies were determined using DFT (see Table 5.2). The positions of the expected diagonal peaks for the various conformers are shown in Fig. 5.10, corrected by a constant offset of $-55\,\text{cm}^{-1}$.

The band positions for **1-apc** fit very well to the experimental spectrum. For the **1-spc** conformer, the calculated high energy vibration (see Fig. 5.10 pos. 1) is nicely
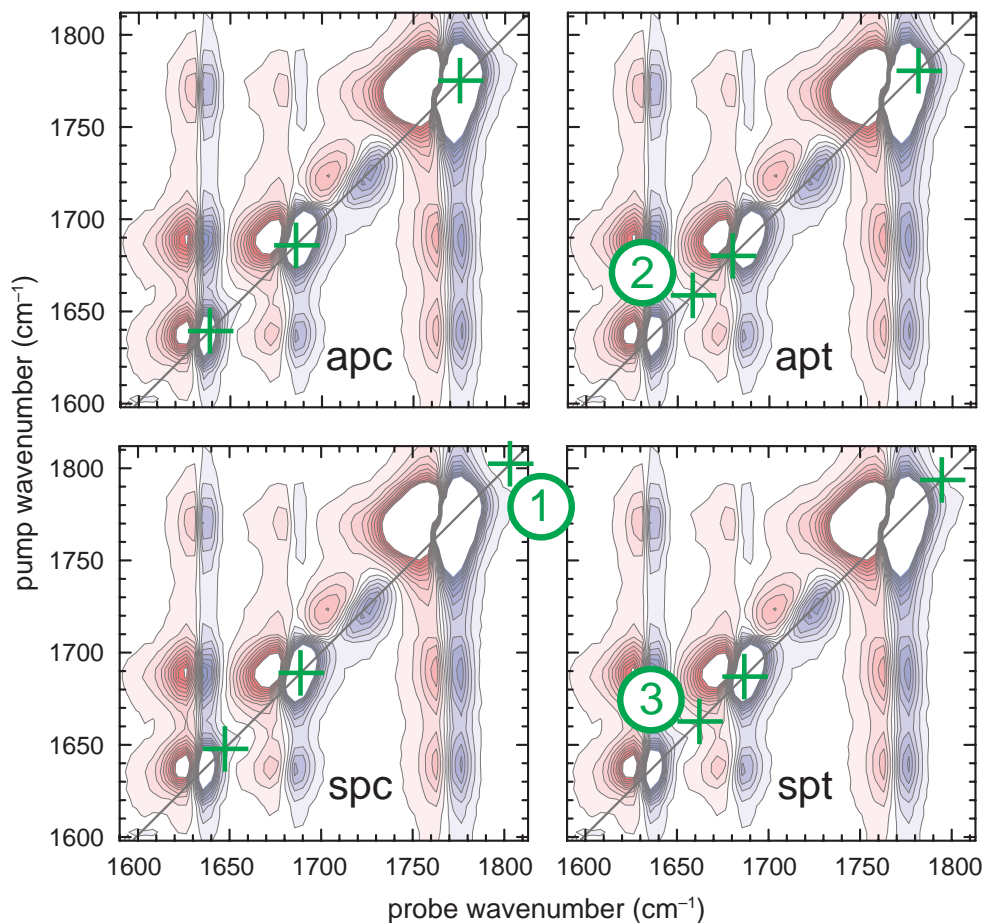
Figure 5.10: *Calculated positions (green crosses) for the diagonal peaks of the various conformers in the P2D-IR spectrum of* **1**. *All calculated vibrational energies are corrected by* $-55\,\mathrm{cm}^{-1}$ *(cf. Table 5.2). Numbers see text.*

separated from all other bands. No signal at that position could be observed. Assuming a similar transition dipole moment as for the main conformer, an assumption that is consistent with the DFT calculation, the population of **1-spc** is therefore less than 0.2%. This value is in good agreement with a ΔG_{298} of 3.3 kcal/mol calculated using DFT (see Table 5.2). As already mentioned in the introduction of this chapter, **1-spc** is the conformation usually drawn in reaction equations by organic chemists and assumed to be the precursor of the product in the Diels–Alder reaction.

For the conformers **1-apt** and **1-spt** the bands are closer to the bands of the main conformer. The best positions to estimate the upper limit for the population of these conformers are pos. 2 and 3. Due to potential overlap with the bands of the conformer **1-apc**, the signal would need to be approximately three contour lines large to be observed. Based on this rough estimate, one can conclude that the overall population of **1-apt** and **1-spt** is less than 5%.

5.2   NMR Spectroscopy[ii]

Figure 5.11 presents the ^{1}H (top) and ^{13}C NMR spectrum (bottom) of **1** in CD_2Cl_2 at ambient conditions. The assigment of the peaks based on the shifts and couplings is shown by the color code.[203–206,213] The F is used to denote that **1** is *free* (*i.e.*, uncomplexed), in contrast to the complexed structures (assigned with C) discussed in the following chapters. The additional signals are due to dichloromethane ([1]H: 5.3 ppm; [13]C: 54 ppm, not labeled), water ([1]H: 1.5 ppm, "∼") and grease ([1]H: around 0.1 ppm, "#").
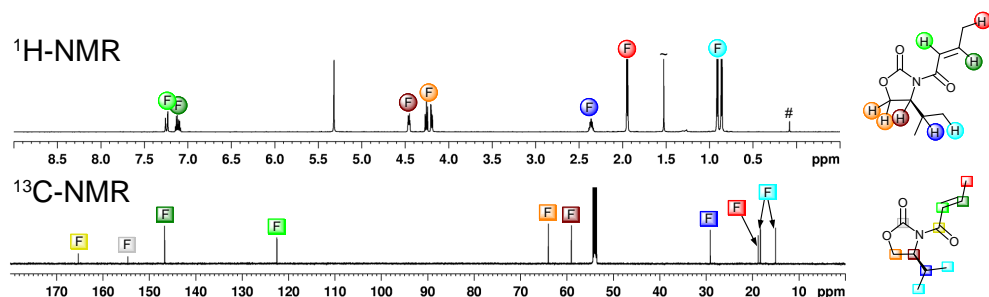
Figure 5.11: *NMR spectra of **1** (13 mM) in CH_2Cl_2. Top: ^{1}H NMR (600 MHz, 298 K); bottom: ^{13}C NMR (151 MHz, 298 K). The assignment is shown by the colored circles (^{1}H NMR) and squares (^{13}C NMR).*

In order to analyze the conformation of **1** using NMR techniques, a NOESY spectrum of **1** in CD_2Cl_2 was recorded, analogous to the experiments of **1** in MeCN done by Bakalova *et al.*[203] The symmetrized ^{1}H NOESY spectrum shown in Fig. 5.12 only shows NOE cross peaks between the protons within the crotonyl group and between the protons within the auxiliary (containing the oxazolidinone ring and the isopropyl group). No NOE cross peaks between the protons of the two subsets were observed.[203] These signals would appear at positions 1 and 2 labeled in the spectrum.

The NOE cross peaks show opposite sign compared to the diagonal peaks. In contrast to all other cross peaks, the cross peaks between the two olefinic protons (see pos. 3) show the same sign as a diagonal peak. This is caused by a spin-spin correlated cross peak (COSY artifact), which dominates the NOE signal at the same position.

The NOE is very distance dependent and therefore a good measure to test whether the protons are close to each other.[154] The presence of a NOE signal proves two protons being close to each other. The distances between the protons of the oxazolidinone or isopropyl group and the protons of the crotonyl group less than 3.5 Å are highlighted by the colored lines in the structural formulas shown in Fig. 5.13. NOE signals between protons closer than 3.5 Å can normally be observed in small molecules (see chapter 4.1.2). The absence of the peaks at pos. 1 and 2 was used in the literature to deduce that **1-apc** is the predominant conformer in solution.[203,213] The argumentation is based on one (in the case of **1-apt**) or two missing signals (in the case of **1-spt**). As discussed in chapter 4.1.2 the absence of a NOE signal does not necessarily prove that the protons are far tough. It just does not prove them being close to

---

Figure 5.12: ^1H *NOESY (600 MHz, 298 K) spectrum of* **1** *(13 mM) in* CH_2Cl_2. *Negative signals are shown in red, positive in black. The 1D* ^1H *NMR signals are shown for reference. Numbers see text.*
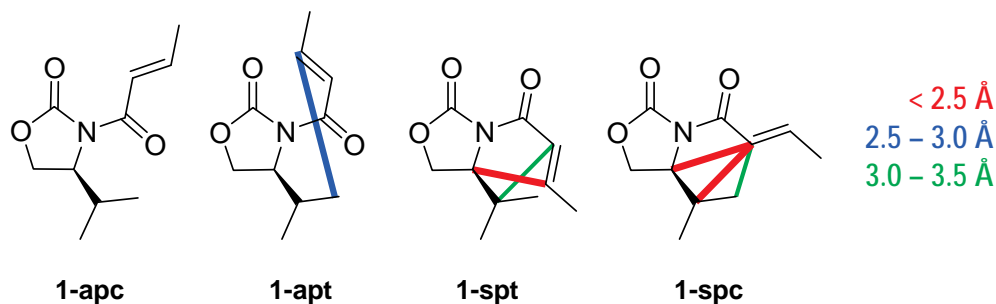
Figure 5.13: *Illustration of the distances between the protons of the crotonyl chain and the isopropyl group. Distances larger than 3.5 Å are not highlighted. For the highlighted proton pairs, NOEs might occur.*

each other. Hence, the argumentation based on missing signals is not incontrovertible. Nevertheless, it is in agreement with the conclusions drawn from the P2D-IR experiments. Structural details such as the observed twist in the molecule cannot be resolved using NOESY, since the NOESY experiment does not probe the structure directly but only reveals if protons are close.

5.3   Crystallography[iii]
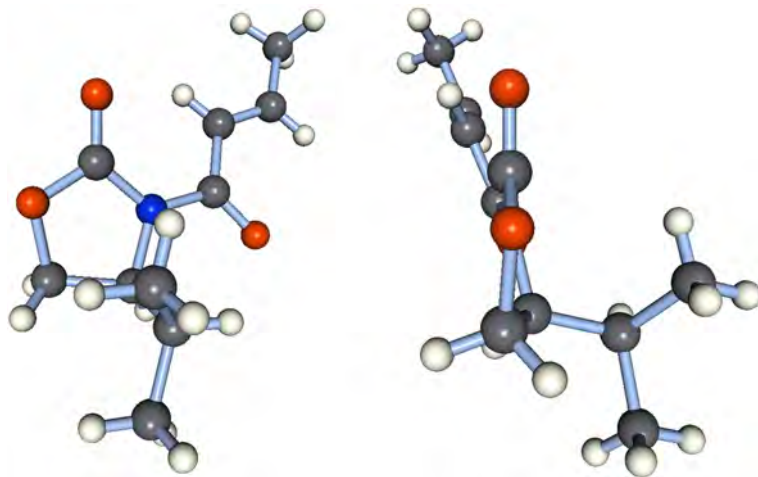
Figure 5.14: *Crystal structure[iv] of* **1**. *Left: front view; right: side view.*

1 also adopts the conformation **1-apc** in a crystal. The crystal structure of enantiomerically pure **1** is shown in Fig. 5.14. It was observed that the molecule is slightly nonplanar, meaning that the alkenyl and carbonyl groups do not lie in one plane. This finding coincides with the P2D-IR experiment, which also indicates a nonplanar structure. Thus the crystal structure suggests that the twist is a static property of the molecule and not dynamic.

[iii]The crystal structure was measured and analyzed by Frank Hampel (Friedrich-Alexander-University Erlangen-Nürnberg) and reproduced by courtesy of the group of Peter R. Schreiner, Liebig University Giessen.

Chapter 6

Structure of the Major Tin Complex
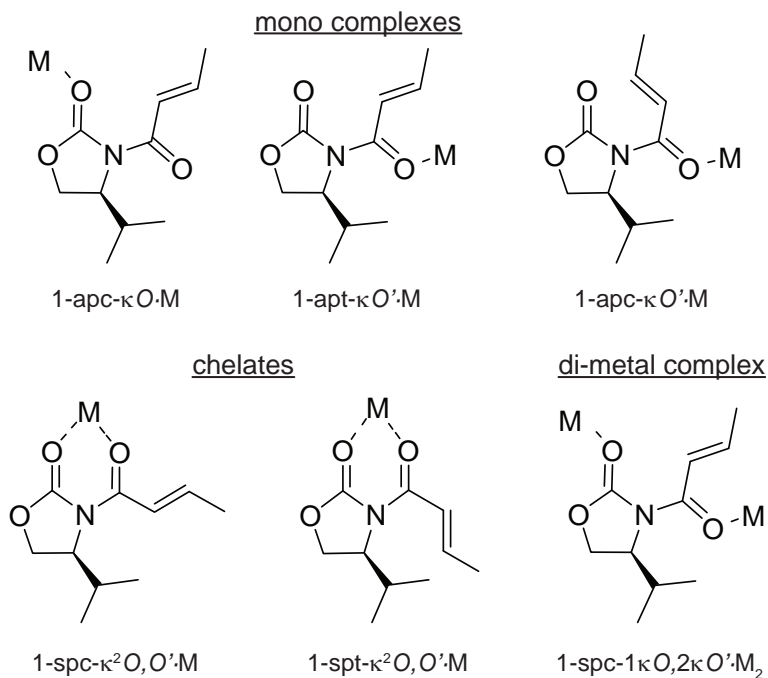
Figure 6.1: *Discussed structures of the Lewis acid–**1** complexes. Not all possible conformations and configurations are shown. The complexes are labeled with their names based on the kappa nomenclature (IUPAC).* [219,220]

As already introduced in chapter 4.3.1, several complexes of a Lewis acid with **1** were discussed in the literature. [173,195,202–205,213] They can basically be classified by the number of Lewis acids needed to form the complex. Under the reaction conditions the Lewis acid is usually used in catalytic amount or slight excess. For that reason the discussion will be mainly limited to the mono-complexes and the bi-complexes, which have been examined (amongst others) by the groups Evans and Santos, be-

cause. [173,203,205] The complexes are illustrated in Fig. 6.1. The shown complexes differ in the complexation site of the Lewis acid [M] and also in the conformation of **1**, both influencing decisively the reaction pathway and the stereochemistry of the product. These differences also alter the vibrations and therefore the direction of their transition dipole moments. Hence the complexes should all be distinguishable and identifiable by P2D-IR spectroscopy, which makes it a valuable tool for understanding the reaction.

It is noteworthy that for some Lewis acids, *e.g.*, Et_2AlCl, the chelates only can be formed in the presence of two Lewis acids. [202,204] In a concentration dependent study these complexes behave as they would be bi-complexes. However, this is not expected for the two Lewis acids ($SnCl_4$ and $Mg(ClO_4)_2$) used in the studies presented here.

6.1 FTIR Studies[i]

Adding the Lewis acid $SnCl_4$ to a solution of **1** leads to a complex formation, which can nicely be followed by FTIR spectroscopy (see Fig. 6.2, left). The vibrational energies of the complex **1**·$SnCl_4$ are red shifted compared to free **1**. The alkenyl and carbonyl vibrations of **1**·$SnCl_4$ in CH_2Cl_2 absorb at $1567\,cm^{-1}$ (ν_1'), $1633\,cm^{-1}$ (ν_2'), and $1726\,cm^{-1}$ (ν_3'). With increasing amount of the Lewis acid, the concentration of **1**·$SnCl_4$ increases, too. The shape of the FTIR spectrum of **1**·$SnCl_4$ does, in the range studied here, not change significantly with higher $SnCl_4$ concentration. If more than one complex is formed, this is an indication that all under these conditions observed complexes show the same concentration dependence. This implies that they all have the same stoichiometry. At threefold excess of $SnCl_4$ (red curve), almost all oxazolidinone molecules are complexed. It is noteworthy that the extinction coefficient of ν_3' is approximately twice of the one of ν_3, while the other two bands do not change their intensity much upon complexation but only shift in wavenumber.
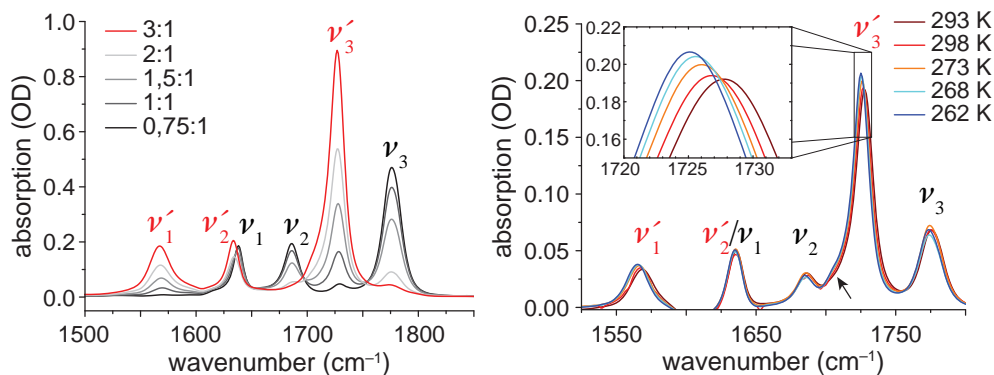
Figure 6.2: *Left: FTIR spectra of various **1**-SnCl₄ mixtures. The concentration of **1** was kept constant (32 mM) while the SnCl₄ concentration was varied from 18 mM to 96 mM. The SnCl₄:**1** ratio is given in the legend. Right: Temperature dependence of the FTIR spectrum of a mixture of **1** (20 mM) and SnCl₄ (36 mM). The negative signal around $1600\,cm^{-1}$ is caused by a subtraction artifact.*

Lowering the temperature of a solution in which both, **1** and **1**·$SnCl_4$, are present by 30 K does not lead to major modulations in the FTIR spectrum (see Fig. 6.2, right).

---

[i]The shown spectra were measured by Sabrina Steinwand.

Especially no significant difference in the equilibrium constant was observed in this temperature range. Only small changes become visible. To begin with, basically all bands become slightly narrower and therefore the maximum peak intensity increases. Secondly, the complex vibrations ν'_1 and ν'_3 shift slightly to lower energies. Such a shift could for example be caused by a smaller distance between the Lewis acid and the binding site(s) of **1** leading to a stronger interaction or by an altered solvation shell. Both effects, the shift and the increase of the maximum peak intensity are readily seen in the enlarged inset for ν'_3. A small shoulder is arising at lower temperatures around 1710 cm^{-1} (marked with an arrow) and shows that there is at least one additional complex formed in low concentrations differing in conformation or configuration.

6.2 P2D-IR Spectroscopy

As in the FTIR, the signals in the P2D-IR spectra shift to lower frequencies upon complex formation (see Fig. 6.3). The P2D-IR spectrum of **1**·SnCl$_4$ also shows three intense diagonal peaks and six cross peaks between them. The cross peaks II and IV gain intensity due to the increased extinction coefficient of ν'_3 and become as intense as the diagonal peaks. In contrast to the spectrum obtained for **1**, the diagonal peaks have in particular a distorted shape, *i.e.*, are smeared out along the diagonal. This is mainly caused by minor complexes and is discussed in detail in chapter 8. In this chapter the signals of the main conformer are focused on.
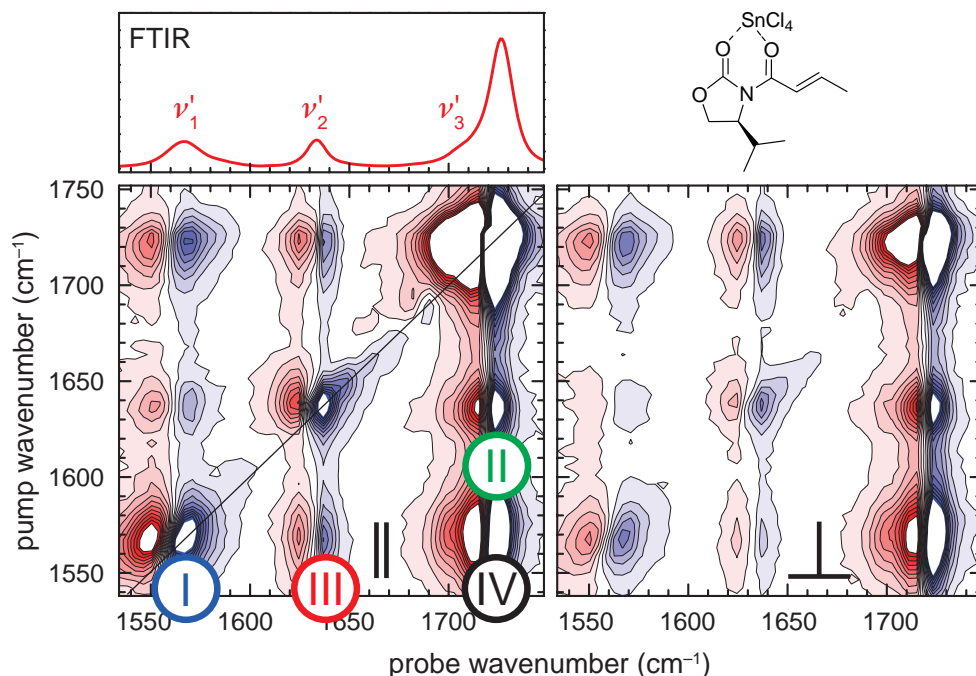
Figure 6.3: *P2D-IR spectra of **1**·SnCl$_4$ in CH$_2$Cl$_2$ ($c_\mathbf{1}$ = 6 mM, $c_{\mathrm{SnCl_4}}$ = 47 mM, 1.5 ps). Left: parallel polarization; right: perpendicular polarization. The contour lines are spaced by 0.03 mOD. Signals larger than ±0.3 mOD are truncated. Numbers see text. The FTIR spectrum is shown in the top panel for reference.*
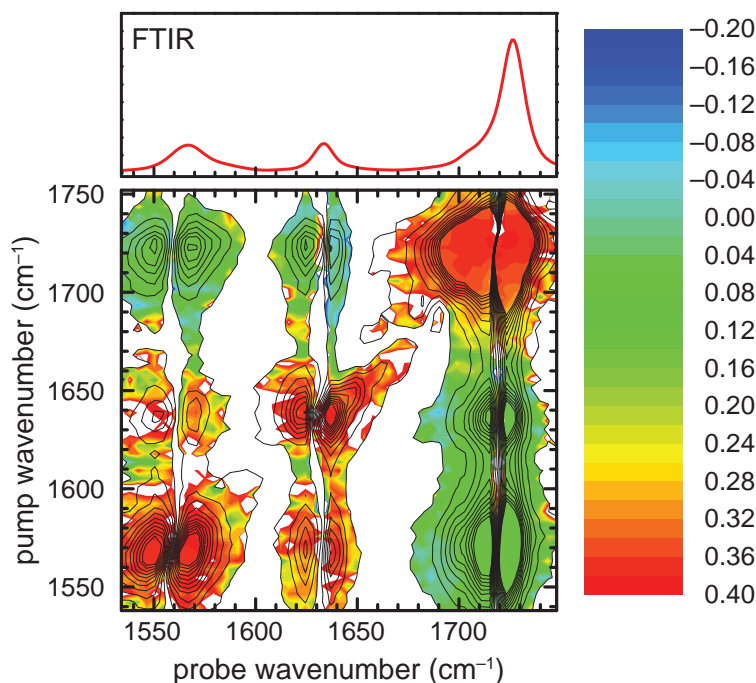
Figure 6.4: *2D-IR anisotropy spectrum of $\mathbf{1} \cdot SnCl_4$ in $CH_2 Cl_2$ ($c_{\mathbf{1}} = 6\,mM$, $c_{SnCl_4} = 47\,mM$; cf. Fig. 6.3). The colors indicate the anisotropy, while the contour lines show the signal intensities for parallel polarization (see Fig. 6.3, left). The anisotropy is only shown for regions where $\Delta\alpha_{\parallel} > 0.03\,mOD$ and where $-0.2 < r < 0.4$.*

6.2.1   Time Dependence of the Anisotropy

The anisotropy of the signals in the P2D-IR spectrum of $\mathbf{1} \cdot SnCl_4$ is visualized in Fig. 6.4 for a delay of 1.5 ps. Figure 6.5 shows the time dependence of the anisotropy of the negative part of the peaks labeled in Fig. 6.3. The differences compared to free $\mathbf{1}$ are quite apparent (*cf.* Fig. 5.5). First, the measured anisotropies differ strongly, reflecting a considerable reorientation of the transition dipoles. For instance, the extrapolated anisotropy of the cross peak between the two low wavenumber modes (ν'_1/ν'_2) of $\mathbf{1} \cdot SnCl_4$ is 0.379(8) (red data points) while the corresponding cross peak for $\mathbf{1}$ (ν_1/ν_2) shows an anisotropy of –0.021(5) (*cf.* Fig. 5.5, red data points). This illustrates the structural change induced by the complexation of $SnCl_4$. The obtained angles for $\mathbf{1} \cdot SnCl_4$ are summarized in Table 6.1.

Secondly, the anisotropy decay is much slower for $\mathbf{1} \cdot SnCl_4$ than the anisotropy decay for free $\mathbf{1}$, reflecting the larger size of the complex. This difference is more clearly illustrated in Fig. 6.6 by comparing the anisotropy decay of diagonal peaks of $\mathbf{1} \cdot SnCl_4$ and $\mathbf{1}$ directly. On the left side, the bands ν_3 and ν'_3 are compared to each other. Monoexponential fits to the data with a fixed starting value of 0.4 and no offset result in rotational correlation times of 13.2(2) ps and 27.7(3) ps corresponding to rotational diffusion constants of 79.2(10) ps and 166(2) ps for free and complexed $\mathbf{1}$, respectively. It is important to compare vibrations with a similar direction of the transition dipole moment, since the tumbling rate of the molecule depends on the direction relative to the molecule. Both, ν_3 and ν'_3 are aligned parallel to the carbonyl
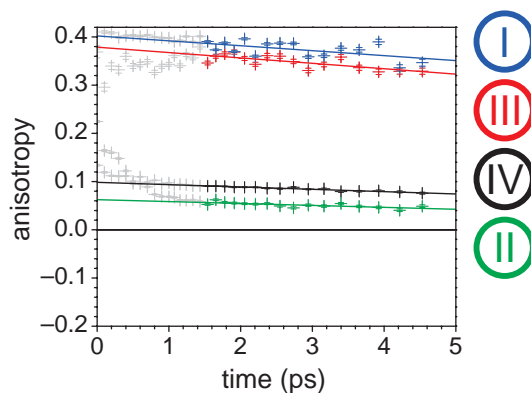
Figure 6.5: *Time dependence of the anisotropy for the signals (bleach) of $\mathbf{1}\cdot SnCl_4$ in CH_2Cl_2 labeled in Fig. 6.3. Diagonal peak ν'_2: blue (cf. Fig. 6.3 pos. I); cross peak ν'_2/ν'_3: green (cf. Fig. 6.3 pos. II); cross peak ν'_1/ν'_2: red (cf. Fig. 6.3 pos. III); cross peak ν'_1/ν'_3: black (cf. Fig. 6.3 pos. IV). The straight, colored lines are linear fits to the data from 1.5 ps to 5 ps.*

group of the oxazolidinone ring (see Fig. 5.7 and 6.7). Comparing the anisotropy decay of the bands ν_2 and ν'_1, which happen to be both aligned the same with respect to the oxazolidinone ring, the slow down is even more pronounced. Monoexponential fits lead to rotational correlation times of 11.16(15) ps for $\mathbf{1}$ and 40(5) ps for $\mathbf{1}\cdot SnCl_4$. The deceleration along the direction of those transition dipole moments is almost twice as pronounced as along the carbonyl group of the oxazolidinone ring.
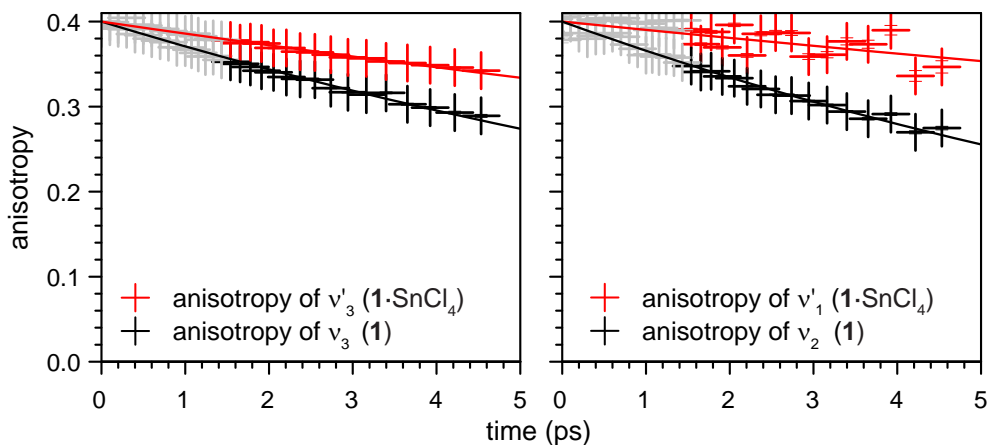
Figure 6.6: *Comparison of the anisotropy decay of diagonal peaks of $\mathbf{1}$ (black) and $\mathbf{1}\cdot SnCl_4$ (red). Left: Comparison of ν_3 and ν'_3; right: Comparison of ν_2 and ν'_1.*

6.2.2   Comparison with DFT Calculations

The DFT calculations allow us to relate the measured transition dipole moments to the structure of the complex. The comparison shown in Table 6.1 identifies the chelate **1-spc-$\kappa^2 O, O'$·**SnCl$_4$ as the main structure, which is calculated to be lowest in energy. The calculated angles for this structure agree best to the experimentally determined angles. All other calculated structures show much larger deviations reflected by the larger overall deviation Δ_{tot}. The calculated frequencies and intensities also support this conclusion as can readily be seen in the comparison of the experimental and simulated FTIR spectra in Fig. 6.8. The calculated alkenyl and carbonyl vibrations of **1-spc-$\kappa^2 O, O'$·**SnCl$_4$ are shifted by a constant value of approximately 52 cm^{-1} compared to the measured spectrum in CH$_2$Cl$_2$, corresponding to an uniform scaling factor of 0.97. For the other species, the shifts strongly vary. The vibrations of **1-spc-$\kappa^2 O, O'$·**SnCl$_4$ in CH$_2$Cl$_2$ are illustrated in Fig. 6.7.
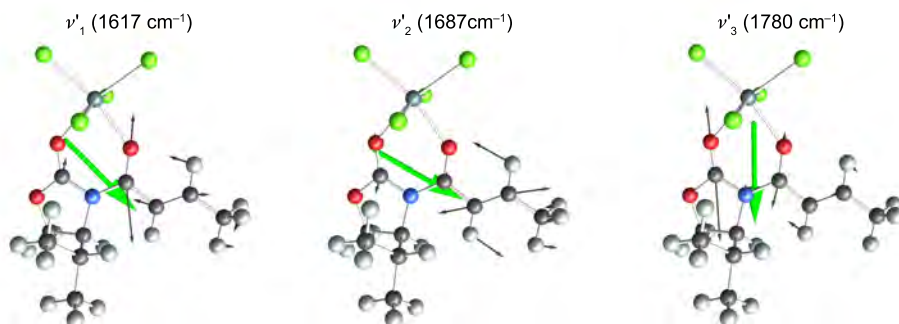
Figure 6.7: *Displacement vectors describing the vibrations ν'_1, ν'_2, and ν'_3 of* **1-spc-$\kappa^2 O, O'$·**SnCl$_4$ *in CH$_2$Cl$_2$ (M06/6-31+G(d,p)/PCM/SDD/Bondi). The direction of the corresponding transition dipole moment is shown in green.*
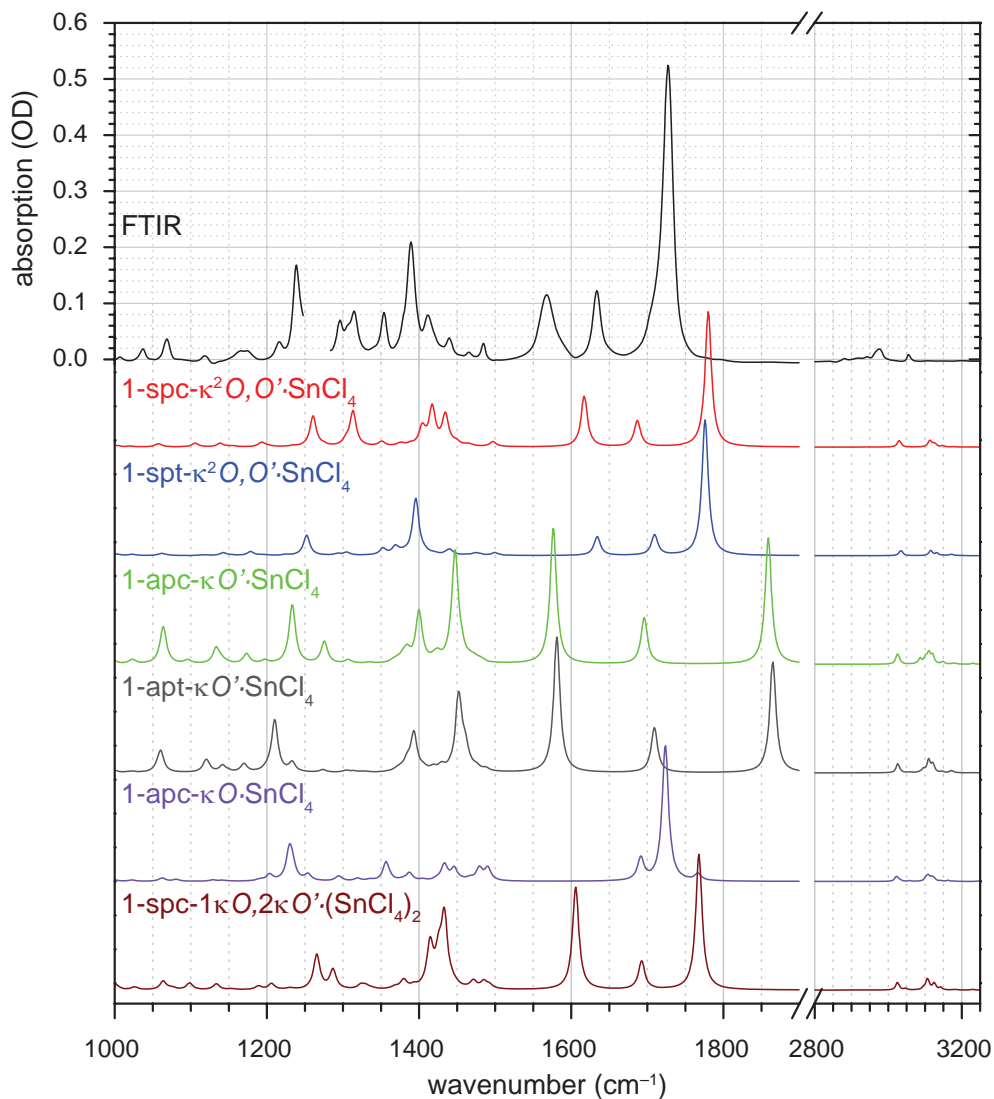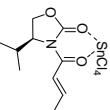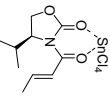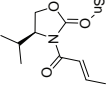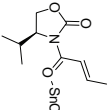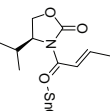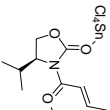
Figure 6.8: *Comparison of the experimental FTIR spectrum of $\mathbf{1}\cdot SnCl_4$ in CH_2Cl_2 ($c_\mathbf{1}$ = 6 mM, c_{SnCl_4} = 47 mM, black) with the calculated spectra for the various conformers of $\mathbf{1}\cdot SnCl_4$ in CH_2Cl_2 (M06/6-31+G(d,p)/PCM/SDD/Bondi, colored). The region between $1245\,cm^{-1}$ and $1285\,cm^{-1}$ is omitted in the experimental data since CH_2Cl_2 absorbs strongly there.*

Table 6.1: *Comparison of the experimentally determined angles and frequencies of **1**-SnCl$_4$ in CH$_2$Cl$_2$ with the results of the DFT calculations (M06/6-31+G(d,p)/PCM/SDD/Bondi). The total structural deviation is expressed as $\Delta_{tot} = \sum |\Delta_i|$.*
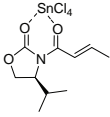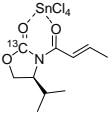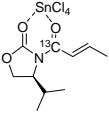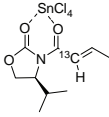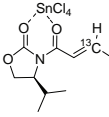
	exp.	1-spc-κ²O,O'	1-spt-κ²O,O'	1-apc-κO	1-apc-κO'	1-apt-κO'	1-apc-1κO,2κO'
angles							
ν'_1/ν'_2 (°)	11 ± 6	16 (Δ=5)	24 (Δ=13)	56 (Δ=45)	81 (Δ=70)	38 (Δ=27)	84 (Δ=73)
ν'_1/ν'_3 (°)	45 ± 2	46 (Δ=1)	20 (Δ=25)	80 (Δ=35)	20 (Δ=25)	44 (Δ=1)	5 (Δ=40)
ν'_2/ν'_3 (°)	49 ± 2	61 (Δ=12)	42 (Δ=7)	44 (Δ=5)	61 (Δ=12)	38 (Δ=11)	89 (Δ=40)
Δ_{tot} (°)		18	45	85	107	39	153
vibrational energies							
ν'_1 (cm^{-1})	1567	1617 (Δ=50)	1634 (Δ=67)	1691 (Δ=124)	1576 (Δ=9)	1581 (Δ=14)	1606 (Δ=39)
ν'_2 (cm^{-1})	1633	1687 (Δ=54)	1710 (Δ=77)	1724 (Δ=91)	1696 (Δ=63)	1709 (Δ=76)	1693 (Δ=60)
ν'_3 (cm^{-1})	1727	1780 (Δ=53)	1776 (Δ=49)	1766 (Δ=39)	1859 (Δ=132)	1865 (Δ=138)	1768 (Δ=41)
calculated Gibbs energies							
ΔG_{298} (kcal/mol)		0.0	6.5	8.4	6.7	10.2	—[i]

[i] The free energy of the di-tin-complex cannot be set into relation to the monocomplexes.

6.2.3 Isotopologue Signals

The DFT calculations also give access to the vibrational shifts of the ^{13}C isotopologues of the chelate **1-spc-$\kappa^2 O, O'$**·SnCl$_4$ compared to the all-^{12}C complex in CH$_2$Cl$_2$ (see Table 6.2). The positions of the bands shifted by more than 10 cm^{-1} are shown in Fig. 6.9. As it is also the case for **1**, only the isotopologue vibration of ν_3' at around 1690 cm^{-1} is observed in the spectrum since this vibration has the largest extinction coefficient. Regarding the size of the signals, essentially the same considerations as for the isotopologue signals in **1** apply (see chapter 5.1.4).

Table 6.2: *Calculated shifts of the vibrational wavenumbers for the isotopologues of* **1-spc-$\kappa^2 O, O'$**·*SnCl$_4$ in CH$_2$Cl$_2$ (M06/6-31+G(d,p)/PCM/SDD/Bondi).*

	(cm^{-1})	Δ (cm^{-1})	Δ (cm^{-1})	Δ (cm^{-1})	Δ (cm^{-1})
ν_1'	1617	−5	−35	−6	−4
ν_2'	1687	−8	−2	−19	−23
ν_3'	1780	−35	−6	−1	−1

Figure 6.9: *Calculated positions (green crosses) for the diagonal peaks of the* [13]*C isotopologues in the P2D-IR spectrum of* **1-spc-$\kappa^2 O, O'$**·*SnCl$_4$ in CH$_2$Cl$_2$ (M06/6-31+G(d,p)/PCM/SDD/Bondi). The black crosses mark the vibrations of the all-*[12]*C isotopologue. The calculated vibrational energies are corrected by −52 cm^{-1} (cf. Table 6.2).*

6.3   NMR Spectroscopy[ii]

NMR spectroscopy was used previously to investigate the structure of Lewis acid complexes of **1**.[203–205,213] Castellino used NMR to study also complexes between **1** and $SnCl_4$.[205] The results are compared below to the measurements presented here. The 1D ^1H and ^{13}C NMR spectra of **1**·$SnCl_4$ in CH_2Cl_2 are depicted in Fig. 6.10. The olefinic protons (green balls) and also the olefinic carbons (green squares) of **1** shift strongly upon complexation. Moreover, both carbon atoms of the carbonyl groups undergo a strong down shift indicating that both carbonyl groups are involved in the complex formation of **1** with $SnCl_4$.
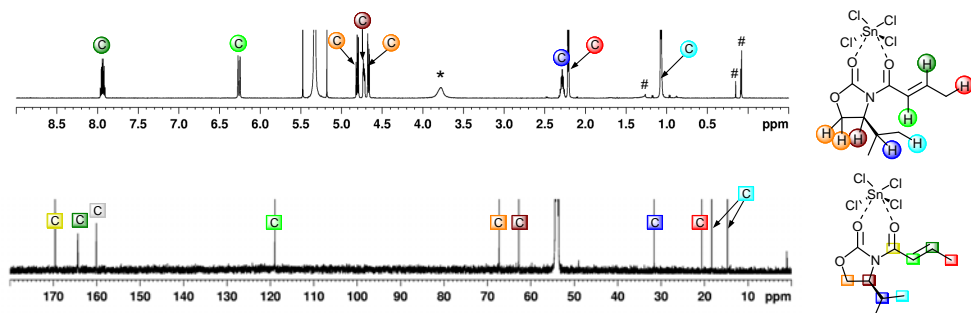
Figure 6.10: NMR spectra of **1**·$SnCl_4$ in CH_2Cl_2 ($c_\mathbf{1} = 13\,mM$, $c_{SnCl_4} = 38\,mM$). Top: ^1H NMR (600 MHz, 298 K); bottom: ^{13}C NMR (151 MHz, 298 K). The assignment is shown by the colored circles (^1H NMR) and squares (^{13}C NMR). "#" labels signals originating from silicon grease, while the broad signal labeled with "∗" are due to hydrolyzed $SnCl_4$ species.

Cooling the sample by 50 K to 252 K does not lead to significant changes in the ^1H NMR spectrum (see Fig. 6.11). Only very small drifts in the chemical shifts were observed. This leads to the conclusion that the structure of the complex is the same at room temperature and at temperatures usually used for the reaction.
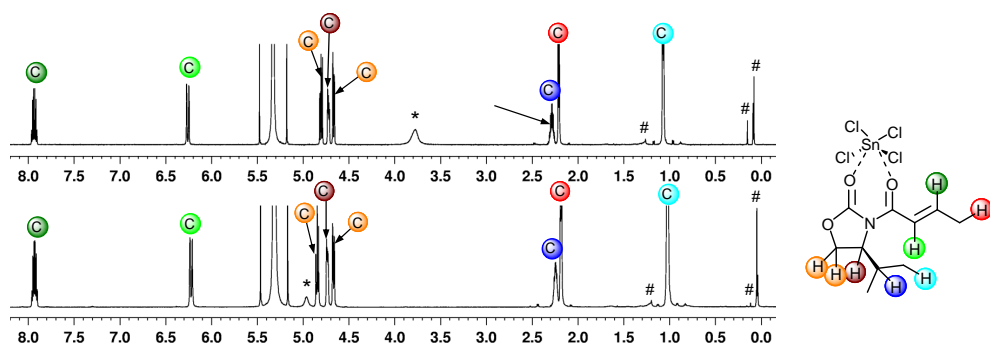
Figure 6.11: Temperature dependence of the ^1H NMR (600 MHz) spectrum of **1**·$SnCl_4$ in CH_2Cl_2 ($c_\mathbf{1} = 13\,mM$, $c_{SnCl_4} = 38\,mM$). Top: 300 K; bottom: 252 K. The assignment is shown by the colored circles.

In contrast to the ^{1}H NMR spectrum, the ^{119}Sn NMR spectrum (Fig. 6.12) changes considerably upon changing the temperatures. At room temperature (top) two broad signals at –192 ppm and –613 ppm were observed. The signals at –192 ppm were assigned to SnCl$_4$ that is not complexed to **1**. The signal at –613 ppm is due to **1**·SnCl$_4$.[205] After cooling the sample to 251 K the signal at –613 ppm sharpens strongly and shifts slightly to –617 ppm. This indicates that the broadening of this peak at room temperature is due to an exchange between free and complexed SnCl$_4$, which is basically frozen out at 251 K. This exchange is not seen in the ^{1}H NMR spectrum since **1** is complexed most of the time and only a negligible amount of **1** is free in solution. The signal at –192 ppm shifts downfield to –168 ppm and remains broad while it becomes asymmetric. The remaining inhomogeneity could be caused by a self aggregation of SnCl$_4$ as it is known to occur for SnF$_4$.[221]
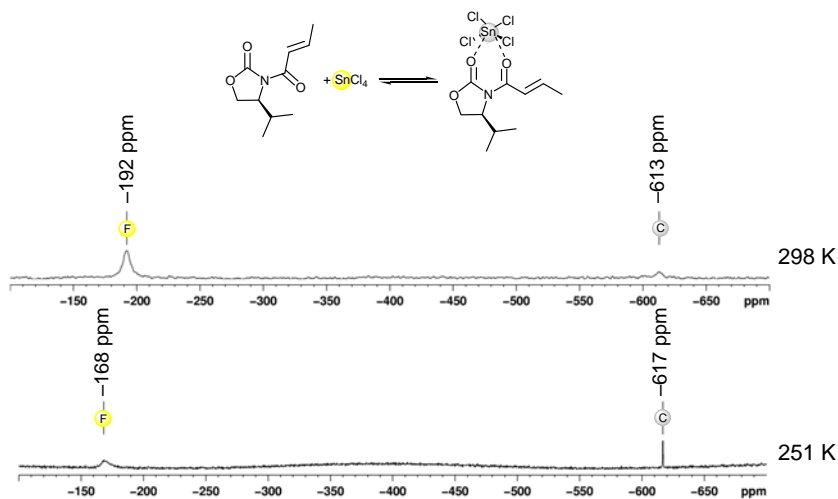
Figure 6.12: *Temperature dependence of the ^{119}Sn NMR (224 MHz) spectrum of **1**·SnCl$_4$ in CH$_2$Cl$_2$ ($c_{\mathbf{1}} = 13$ mM, $c_{\mathrm{SnCl_4}} = 38$ mM). Top: 298 K; bottom: 251 K. The assignment is shown by the colored circles.*

The ^{1}H NOESY spectrum of the complex **1**·SnCl$_4$ measured with a 3:1 ratio is shown in Fig. 6.13. In addition to the cross peaks observed for free **1** (see Fig. 5.12), the spectrum of **1**·SnCl$_4$ also contained cross peaks between one proton of the crotonyl group (marked in light green) and the Evans auxiliary. These signals are marked by the arrows in the spectrum. The proton pairs causing these cross peaks are connected in the chemical structure next to the spectrum. No cross peaks to the olefinic proton marked in dark green were detected. The observed correlation signals imply that olefinic proton marked in light green is close to the Evans auxiliary while the other olefinic proton (dark green) is further apart. This is realized in the conformation **1-spc** (see Fig. 5.13. Thus the complexation of SnCl$_4$ leads to a rotation around the amide bond of **1**. In combination with the observation that both carbonyl groups seem to be involved in the complex formation and sterical considerations, the ^{1}H NOESY suggests that the complex formed is the chelate **1-spc-$\kappa^2 O,O'$·SnCl$_4$**. This is in agreement with the structure suggested by Castellino based on conclusions drawn from one dimensional ^{1}H, ^{13}C and ^{119}Sn NMR experiments and also with the main structure identified by the P2D-IR experiments.[205]
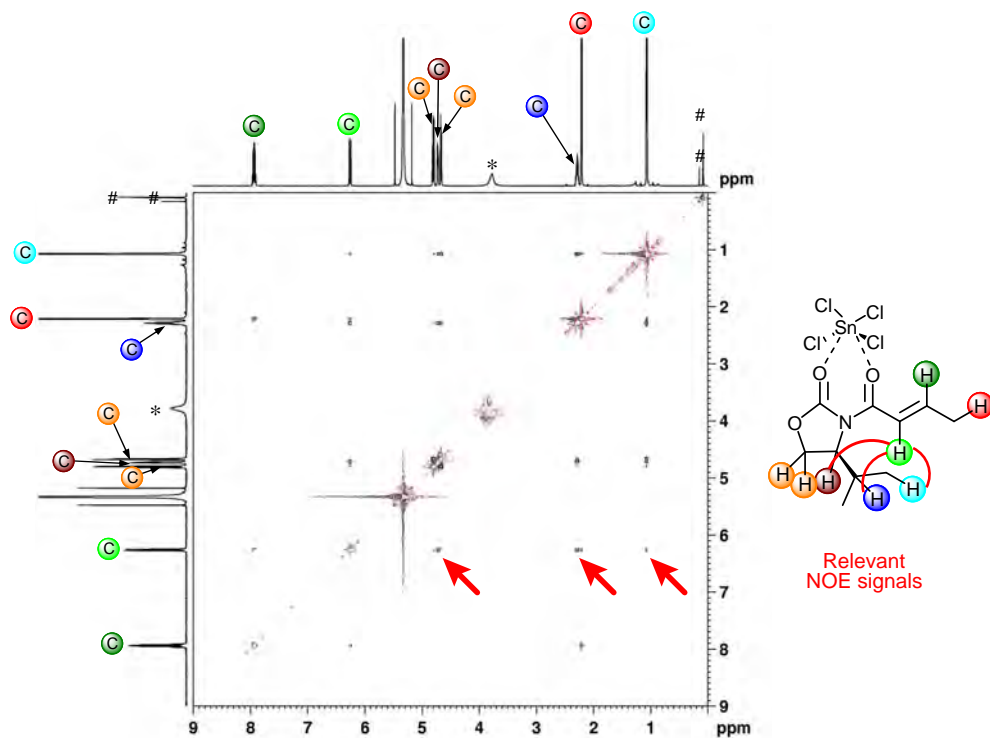
Figure 6.13: ^1H NOESY (600 MHz, 298 K) spectrum of **1**·$SnCl_4$ in CH_2Cl_2 ($c_1 = 13$ mM, $c_{SnCl_4} = 38$ mM). Negative signals are shown in red, positive in black. The 1D ^1H NMR signals are shown for reference. The red arrows highlight the NOESY cross peaks that additionally show up upon $SnCl_4$ complexation.

Chapter 7

Structure Determination in Mixtures

The capability of analyzing the structure of molecules in mixtures is highly desirable in order to be able to elucidate reaction mechanisms. Under reaction conditions, the important molecules and intermediates usually exchange fast or are short-lived. The ultrafast time resolution makes P2D-IR spectroscopy particularly well suited for structure determination under these conditions when standard techniques such as NMR are beyond their limits (see chapter 4.1). In the previous two chapters, P2D-IR spectroscopy was used to determine the structure of **1** and **1**·$SnCl_4$ separately. Here two procedures are introduced that allow to determine the structure of molecules that are in a fast equilibrium with each other, the *anisotropy method* and the *annihilation method*. The anisotropy method is the method that already was used in the previous chapters for the structure determination of the pure species.

Figure 7.1 shows the P2D-IR spectrum of an equimolar mixture of **1** and $SnCl_4$ in CH_2Cl_2. Under these conditions, both free **1** and **1**·$SnCl_4$ are present in a fast equilibrium. Thus both species were observed in the FTIR spectrum of the mixture (see black curve in the top panel). For comparison, the scaled FTIR spectra of the neat solutions of **1** (green) and **1**·$SnCl_4$ (red), which sum up to the spectrum of the mixture, are shown too. In the very same manner, also the P2D-IR spectra (Fig. 7.1) are a sum of the signals of **1** and **1**·$SnCl_4$ in CH_2Cl_2. The coupling pattern of free **1** is highlighted by the green grid and is (within the noise) identical to the one observed for the measurement of only **1** in CH_2Cl_2 (*cf.* Fig. 5.2). The signals used for the analysis later on are labeled with the Arabic numbers 1–4. The red grid connects the main signals in the spectrum for the complex **1**·$SnCl_4$. This spectrum is also the same as measured for a solution containing only **1**·$SnCl_4$ (*cf.* Fig. 5.2). The Roman numbers I–IV refer to the peaks of **1**·$SnCl_4$. The equilibrium being dynamic does not interfere with the measurement. The rotation around the single bonds and the complexation are much slower than the time resolution of the P2D-IR experiment. Thus the equilibrium appears as if it would be static. If the dynamic processes interconnecting the two species would occur on roughly the same timescale as the delay times in the experiment, the two signal sets could not be detected separately, but additional cross peaks between the two species would occur as it is used in EXSY-2D-IR spectroscopy (*e.g.*, see chapter 2.2.2). But even under these conditions, the angles are in principle accessible.
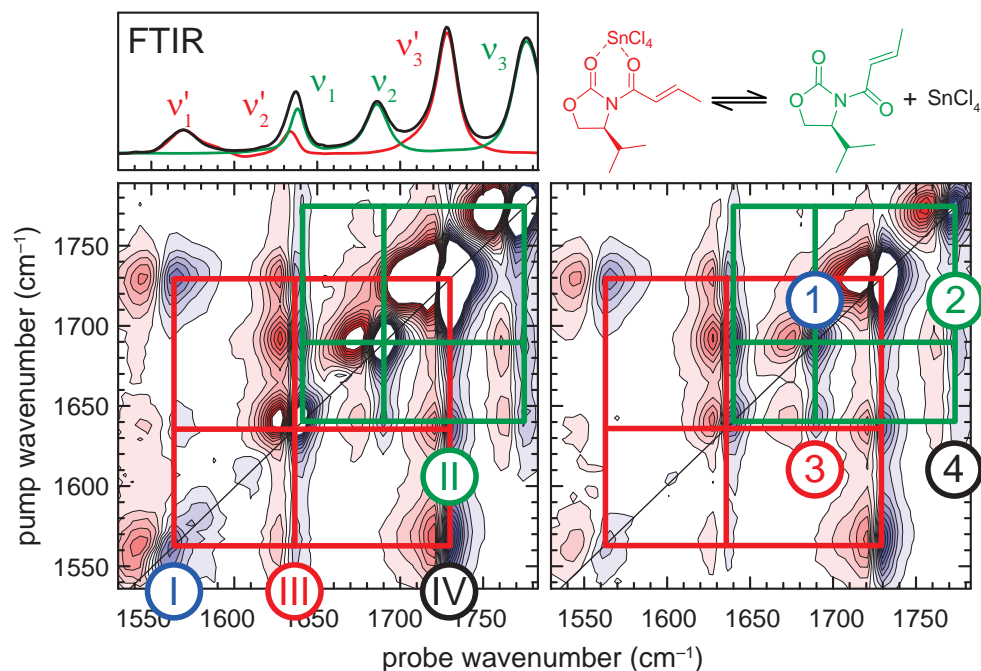
Figure 7.1: *P2D-IR spectra of a mixture of* **1** *and* **1·SnCl₄** *in* CH_2Cl_2 *(*$c_1 = 24\,mM$, $c_{SnCl_4} = 24\,mM$, *1.5 ps). Left: parallel polarization; right: perpendicular polarization. The contour lines are spaced by 0.05 mOD. Signals larger than* $\pm 0.5\,mOD$ *are truncated. The signals that belong to the same molecule are connected by the grids (green:* **1***; red:* **1·SnCl₄***). The FTIR spectra of the mixture (black),* **1** *(green), and* **1·SnCl₄** *(red) are shown in the top panel for reference. Numbers see text.*
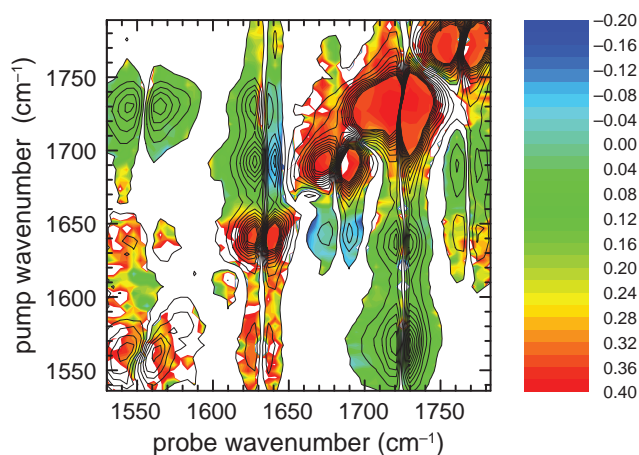
Figure 7.2: *2D-IR anisotropy spectrum of a mixture of* **1** *and* **1·SnCl₄** *in* CH_2Cl_2 *(*$c_1 = 24\,mM$, $c_{SnCl_4} = 24\,mM$; *cf. Fig. 7.1). The colors indicate the anisotropy, while the contour lines show the signal intensities for parallel polarization (see Fig. 7.1, left). The anisotropy is only shown for regions where* $\Delta\alpha_{\parallel} > 0.05\,mOD$ *and where* $-0.2 < r < 0.4$.

The 2D-IR spectrum of the mixture is the sum of the spectra of the individual species in the mixture and thus the anisotropy plot shown in Fig. 7.2 also contains the signal anisotropies of the individual species. However, the detected anisotropy spectrum is not simply the sum of the 2D anisotropy spectra, but a weighted sum, for which the weighting factors are determined by the amplitude of the corresponding peak. This gets important, if peaks overlap significantly. In these cases the measured anisotropies do not give direct access to the individual angles in the molecule(s). Thus the anisotropy method reaches its limits. The annihilation method introduced in chapter 7.2 proves to be particularly powerful in cases when individual signals (partially) overlap.

7.1   The Anisotropy Method

The anisotropy method is the method that was already applied before to determine the angles of **1** and **1**·SnCl$_4$ in solution. Using this approach, one looks at the time dependent anisotropy of the peak maximum and extrapolates the anisotropy to zero time delay. The extrapolation assures that the determined angles are not distorted by rotational diffusion. This approach is suitable when the (cross) peaks do not overlap significantly as it is also the case for the dominant peaks in the mixture of **1** and **1**·SnCl$_4$ investigated here. The time dependent anisotropies of the labeled signals of **1** (Arabic numbers) and **1**·SnCl$_4$ (Roman numbers) are extrapolated to zero in Fig. 7.3. The extrapolated anisotropies and deduced angles, which are summarized in Table 7.1, are - within the experimental errors - the same as measured for the pure species. Therefore the same conclusions apply as presented before, *i.e.*, that **1** adopts the conformation **1-apc** and the main Sn complex formed is **1-spc-$\kappa^2 O, O'$**·SnCl$_4$. This proves that mixtures can be analyzed in the very same manner as pure species and that it is possible to determine the structure of fast interconverting molecules. However, the anisotropy method, in which the anisotropy of the cross peaks is directly evaluated, assumes the anisotropy being constant over the cross peak and therefore is only applicable, if the peaks do not overlap significantly.
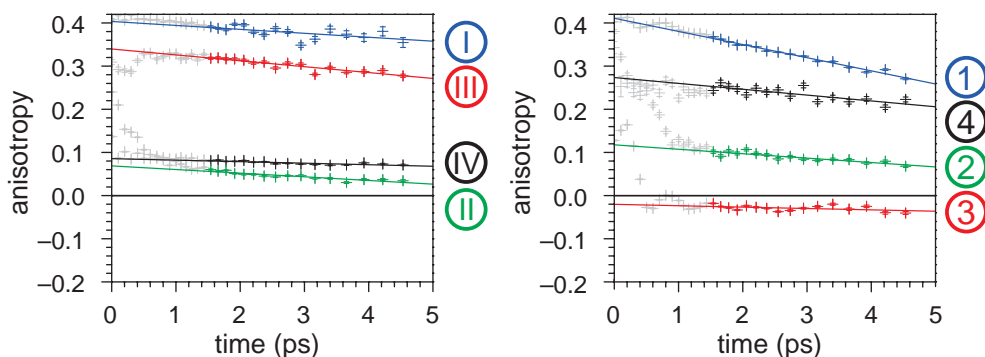
Figure 7.3: *Time dependence of the anisotropy for the signals (bleach) in the P2D-IR spectrum of a mixture of **1** and **1**·SnCl$_4$ in CH$_2$Cl$_2$ labeled in Fig. 7.1. Left: signals of **1**·SnCl$_4$; right: signals of **1**. The straight, colored lines are linear fits to the data from 1.5 ps to 5 ps.*

Table 7.1: *Angles between the transition dipole moments of **1** and **1**·SnCl$_4$ determined in a mixture in CH$_2$Cl$_2$ (cf. Fig. 7.1 and 7.3). The obtained angles are compared in the last column with the measurement of the pure substances.*

cross peak	modes	anisotropy $r(0)$ mixture	angle θ (°) mixture	angle θ (°) pure
II	ν_2'/ν_3'	0.069(3)	48 ± 2	49 ± 2
III	ν_1'/ν_2'	0.340(5)	18 ± 4	11 ± 6
IV	ν_1'/ν_3'	0.086(2)	46 ± 2	45 ± 2
2	ν_2/ν_3	0.102(2)	43 ± 2	44 ± 2
3	ν_1/ν_2	$-0.020(5)$	57 ± 2	57 ± 2
4	ν_1/ν_3	0.273(8)	27 ± 3	28 ± 3

7.2 The Annihilation Method

For overlapping peaks the measured anisotropy cannot be used to derive the individual angles in a straight forward and unique manner by just looking at the anisotropy at one point of the peak as it is done in the anisotropy method. An alternative approach, the annihilation method, can be used in these cases. Single cross peaks are selectively annihilated by taking weighted differences of the spectra recorded with parallel and perpendicular polarization ($\Delta\alpha_\parallel - x\Delta\alpha_\perp$). According to eq. 15 the ratio x of the signals between the spectra measured with parallel and perpendicular polarization also gives direct access to the transition dipole moment angle. In doing so, the band shape of the peaks is also accounted for and thus the single contributions to the signal (*i.e.*, the overlapping peaks) can be identified and analyzed independently. This approach is exemplified in Fig. 7.4 for the mixture of **1** and **1**·SnCl$_4$ already analyzed above. The top left spectrum shows the measured P2D-IR spectrum for parallel polarization conditions (*cf.* Fig. 7.1 left). All other spectra are weighted differences between parallel and perpendicular polarization, in which the weighting factor x were chosen such that the signals at the marked positions (colored circles) were annihilated. The required weighting factors x are shown in the insets and from these the angles between the transition dipole moments are calculated. The cross peak between ν_2 and ν_3 disappears for example for a weighting factor of $x = 1.3 \pm 0.05$, which corresponds to an angle of $46°\pm 2°$. The measured ratios x and the determined angles are summarized in Table 7.2 for the signals of **1** (green grids) and in Table 7.3 for the **1**·SnCl$_4$ signals (red grids).

7.3 Discussion

Due to the experimental effort of measuring the entire 2D-IR spectrum instead of selected cuts used for the anisotropy method, only one set of spectra with a delay time of 1.5 ps is evaluated. Thus it is not possible to extrapolate the ratio x to zero delay time, which gives rise to a systematic error on the derived angles originating from rotational diffusion of the molecules within the first 1.5 ps. This error can be estimated using the anisotropy plots shown in Fig. 7.3. Table 7.2 and 7.3 compare the fitted anisotropy at zero delay and at a delay of 1.5 ps. The deviation between the angles determined at these two delays equates to the systematic error of the angles
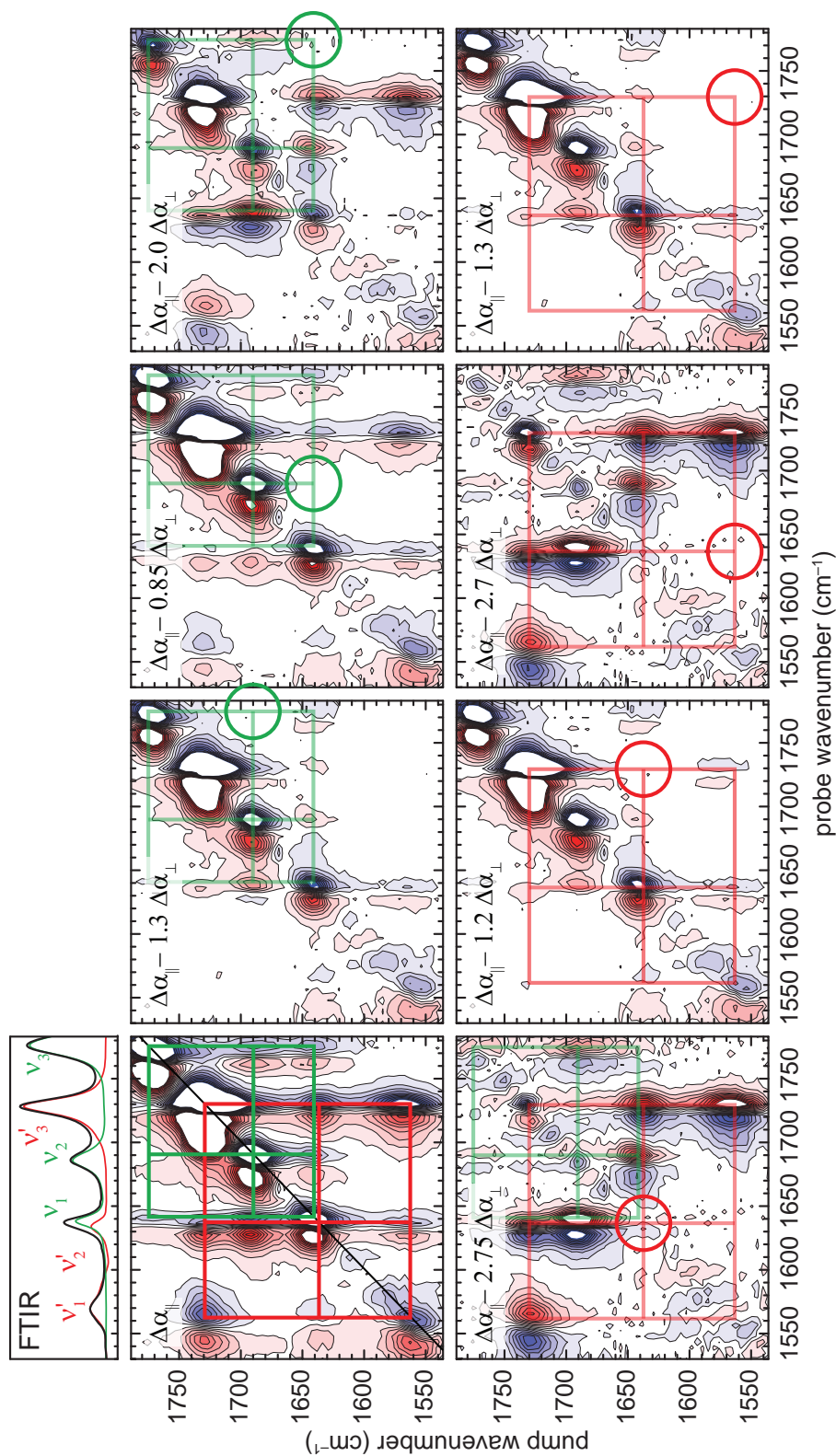
Figure 7.4: *Differences between the P2D-IR spectra of a mixture of **1** and **1**·$SnCl_4$ in CH_2Cl_2 ($c_1 = 24\,mM$, $c_{SnCl_4} = 24\,mM$, $1.5\,ps$) with parallel and perpendicular polarization (cf. Fig. 7.1). The wighting factors given in the insets are chosen such that the peaks highlighted by the circles annihilate. The contour lines are spaced by $0.04\,mOD$. Signals larger than $\pm 0.4\,mOD$ are truncated. The signals that belong to the same molecule are connected by the grids (green: **1**; red: **1**·$SnCl_4$).*

determined by only looking at a delay of 1.5 ps. It is apparent that the systematic error is largest for the diagonal peak, *i.e.*, small angles between the involved transition dipole moments, and drops as expected significantly with increasing angles. For angles larger than 20° the observed systematic error is at maximum 3°. From a theoretical point of view, the systematic error disappears for magic angles and for slow rotational diffusion. Within the experimental errors, the angles deduced from the fitted anisotropy at t = 1.5 ps and deduced by annihilating the cross peaks using the spectra measured with parallel and perpendicular polarization at a delay time of t = 1.5 ps agree. Thus it is shown that the annihilation method works and the two methods are equivalent when the bands do not overlap.

If one contrasts the two methods, the anisotropy method has the advantage that only cuts of the 2D-IR spectra need to be measured. This reduces the measurement time dramatically and therefore allows to measure many different time points and to eliminate the influence of the rotational diffusion by extrapolating the anisotropy to zero time delay. The noise is much smaller than for the annihilation method because the data points are measured more often. On the other hand the annihilation method allows to investigate also systems in which bands are overlapping significantly and are not accessible by the anisotropy method as will be shown in chapter 8. In particular, also the two dimensional structure of a peak can be investigated, which gives information about the inhomogeneity of the spectra and therefore of the structures of the species. This allows also to detect minor species present in solution, which is the subject of the following chapter and makes the annihilation method in principle much more powerful than the anisotropy method.

The systematic error in the annihilation method can be reduced significantly by shortening the delay time, often referred to as population time. This can be accomplished by replacing the Fabry–Perot pulse with a pulse pair or a pulse generated by a pulse shaper, *e.g.*, a Gaussian pump pulse.[53,87,88] A photon echo setup also allows to reduce the population time significantly, in a similar way as using a pulse pair. Moreover it is highly desirable to reduce the measurement time of a complete P2D-IR spectrum so that the measurement of many delay times becomes reasonable without reducing the signal-to-noise ratio. This can be achieved, *e.g.*, by using a laser system with a higher repetition rate and by getting rid of the need to chop the excitation pulse(s).[222]

7.3.1   Polarization Angle Scanning 2D-IR Spectroscopy

The annihilation method is similar to the polarization angle scanning (PAS) 2D-IR spectroscopy introduced by Cho and co-workers.[105–107] In PAS 2D-IR, several 2D-IR spectra with different polarization conditions are measured. The polarization conditions between the laser pulses are stepwise changed between the measurements in order to alter the cross peak intensities. In a simplified picture, this procedure experimentally weights the parallel and perpendicular spectra differently for each measurement. After the measurements, the peak intensities are fitted as function of the polarization conditions. The conditions, when the signals are annihilated give access to the angle between the transition dipole moments. In order to carry out the annihilation using only two separate measurements for parallel and perpendicular polarization like in the present work, it is essential that the measurements are carried out under the same conditions, *i.e.*, that the laser power does not change between the measurements. This is accomplished here by a quasi simultaneous measurement of the spectra with the two different polarization conditions.

Table 7.2: *Detailed comparison of the determined anisotropies and angles for **1** in CH_2Cl_2 determined by the anisotropy method and the annihilation method.*

Peak	ν_2/ν_2 (Fig. 7.1 pos. 1)	ν_1/ν_2 (Fig. 7.1 pos. 3)	ν_1/ν_3 (Fig. 7.1 pos. 4)	ν_2/ν_3 (Fig. 7.1 pos. 2)
fitted time dependence of the anisotropy				
Anisotropy extrapolated to 0ps	0.411(3)	−0.020(5)	0.273(8)	0.117(4)
Determined angle (°)	–[i]	57 ± 2	27 ± 3	43 ± 2
Anisotropy at 1.5ps	0.365(2)	−0.025(3)	0.253(4)	0.102(2)
Determined angle (°)	14 ± 4	57 ± 2	30 ± 2	45 ± 2
Systematic error (°)	14	0	3	2
annihilation method				
$\Delta\alpha_\parallel/\Delta\alpha_\perp$ measured at 1.5 ps	2.75 ± 0.15	0.85 ± 0.15	2.0 ± 0.25	1.3 ± 0.05
Calculated anisotropy	0.37 ± 0.02	−0.05 ± 0.06	0.25 ± 0.05	0.09 ± 0.02
Determined angle (°)	13 ± 5	60 ± 7	30 ± 5	46 ± 2

[i] Not determinable. Because the two pulses interact with the very same transition dipole moment, the real angles is 0°.

Table 7.3: *Detailed comparison of the determined anisotropies and angles for **1**-SnCl4 in CH_2Cl_2 determined by the anisotropy method and the annihilation method.*

Peak	ν'_2/ν'_2 (Fig. 7.1 pos. 1)	ν'_1/ν'_2 (Fig. 7.1 pos. 3)	ν'_1/ν'_3 (Fig. 7.1 pos. 4)	ν'_2/ν'_3 (Fig. 7.1 pos. 2)
fitted time dependence of the anisotropy				
Anisotropy extrapolated to 0ps	0.403(9)	0.340(5)	0.086(2)	0.069(3)
Determined angle (°)	0 ± 7	18 ± 4	46 ± 2	48 ± 2
Anisotropy at 1.5ps	0.390(5)	0.319(3)	0.0804(10)	0.056(2)
Determined angle (°)	7 ± 5	22 ± 2	47 ± 2	49 ± 2
Systematic error (°)	7	4	1	1
annihilation method				
$\Delta\alpha_\parallel/\Delta\alpha_\perp$ measured at 1.5 ps	2.75 ± 0.15	2.75 ± 0.25[ii]	1.3 ± 0.05	1.2 ± 0.05
Calculated anisotropy	0.37 ± 0.02	−0.36 ± 0.04	0.09 ± 0.02	0.06 ± 0.02
Determined angle (°)	13 ± 5	15 ± 8	46 ± 2	49 ± 2

[ii] Between 2.35 and 2.85.

7.4   NMR Spectroscopy[i]

In contrast to FTIR and 2D-IR spectroscopy, the NMR spectrum of a fast exchanging mixture is not the sum of the individual spectra, but an average spectrum. [99,151] This is readily seen in the ^{1}H NMR titration experiment at room temperature shown in Fig. 7.5. The spectrum on the top shows the ^{1}H NMR spectrum of pure **1** in CH_2Cl_2 while the spectrum of **1**·$SnCl_4$ recorded in a solution of **1** with an excess of **1**·$SnCl_4$ is displayed on the bottom. The spectrum in the middle is the ^{1}H NMR spectrum of an equimolar solution of **1** and **1**·$SnCl_4$, similar to the conditions used to measure the P2D-IR spectrum shown in Fig. 7.1. At these conditions only broad, averaged peaks can be observed that do not belong to any of the single species. Because the exchange rate is fast compared to the time resolution of the NMR experiment, the signals are motionally averaged. Here, the system is in the fast exchange regime, which means that two spectra collapse to a single spectrum. This implies that the exchange rate between free **1** and the complex **1**·$SnCl_4$ is faster than $1.3\,\text{ms}^{-1}$ (coalescence) at ambient conditions.
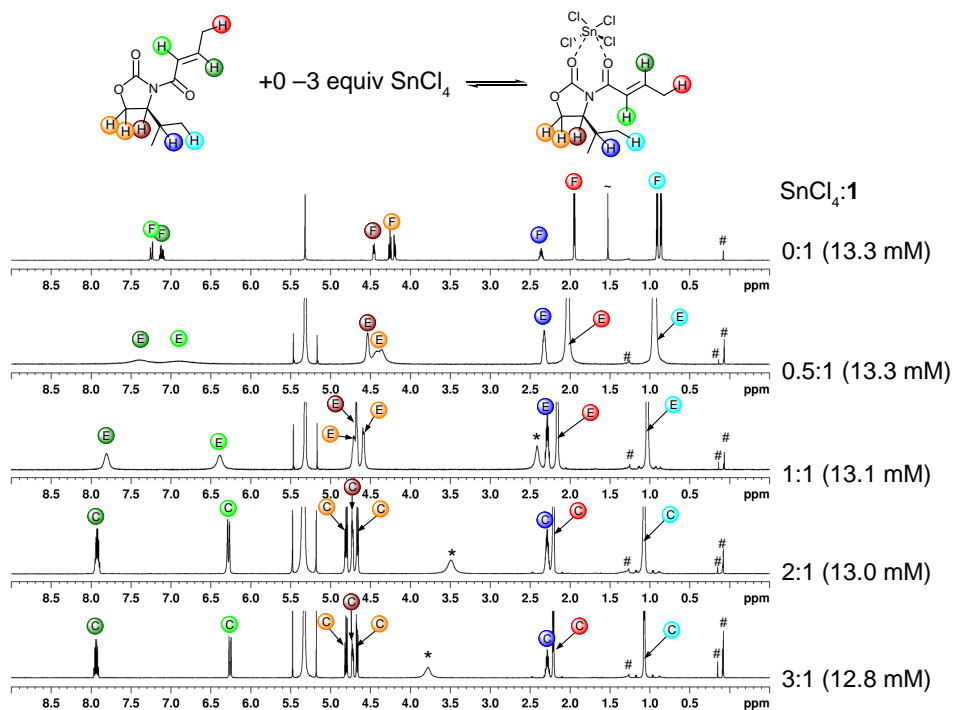
Figure 7.5: ^{1}H NMR (600 MHz, 298 K) titration experiment of **1** with increasing amounts of $SnCl_4$ in CH_2Cl_2. The assignment is shown by the colored circles. F assigns signals of free **1**, C of the complex **1**·$SnCl_4$. Signals labeled with E are motionally averaged signals of both species.

Cooling of the sample to 251 K and 245 K leads to a separation of the signal (see Fig. 7.6). At low temperatures, the exchange is decelerated significantly and the regime is altered from fast exchange to slow exchange. Thus the spectra at low temperatures basically contain the spectra of the individual species.
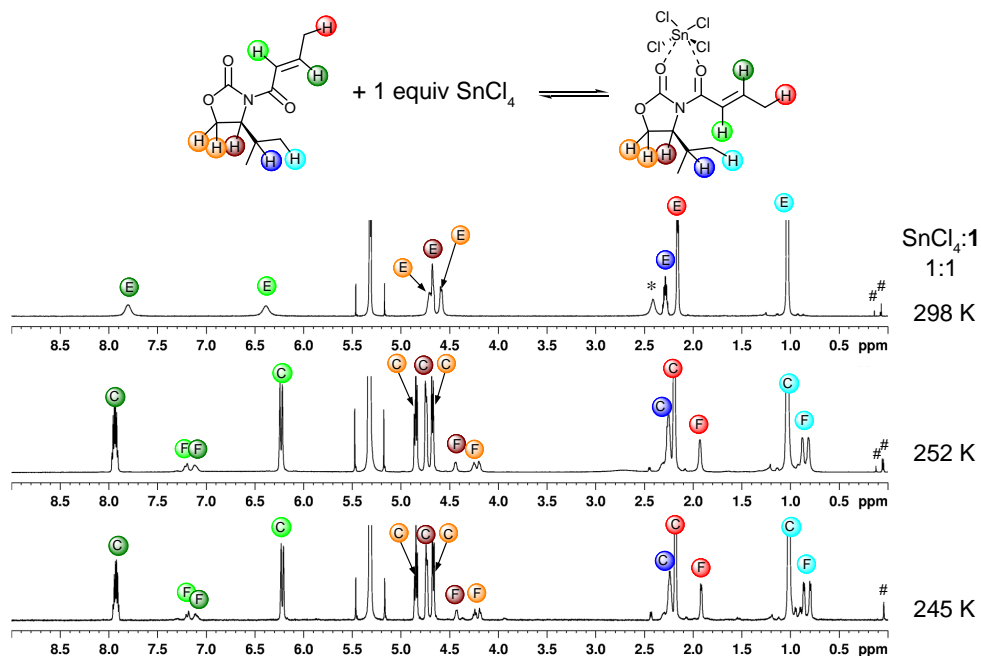
Figure 7.6: *Temperature dependence of the ^1H NMR spectrum (600 MHz) of a mixture of **1** and **1**·SnCl$_4$ in CH$_2$Cl$_2$ ($c_1 = 13$ mM, $c_{SnCl_4} = 13$ mM). The assignment is shown by the colored circles. F assigns signals of free **1**, C of the complex **1**·SnCl$_4$. Signals labeled with E are motionally averaged signals of both species.*

As it is the case for the 1D ^{1}H NMR spectrum, the ^{1}H NOESY of an equimolar mixture at r.t. (Fig. 7.7) shows an average of the ^{1}H NOESY spectrum of **1** (see Fig. 5.12) and of **1**·SnCl$_4$ (see Fig. 6.13). In the fast exchange regime, the properties cannot be assigned to a single species anymore. NOE cross peaks between two protons in this spectrum only imply that the two protons are close to each other in one of the species present in solution. They do not tell, which of the species causes the signals.

To sum up, the low inherent time resolution inhibits the structure determination of both species under these conditions using NMR techniques. P2D-IR spectroscopy therefore complements the standard technique NMR very well when dynamics limit its interpretability.
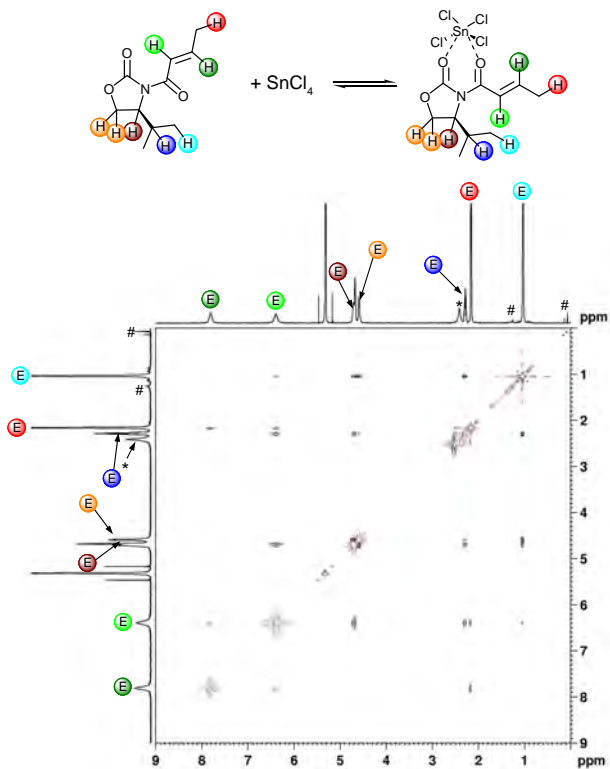
Figure 7.7: ^1H NOESY (600 MHz, 298 K) spectrum of a mixture of **1** and **1**·SnCl$_4$ in CH$_2$Cl$_2$ ($c_1 = 13$ mM, $c_{\text{SnCl}_4} = 13$ mM). Negative signals are shown in red, positive in black. The 1D ^1H NMR signals are shown for reference.

Chapter 8

Identification of Additional Tin Complexes
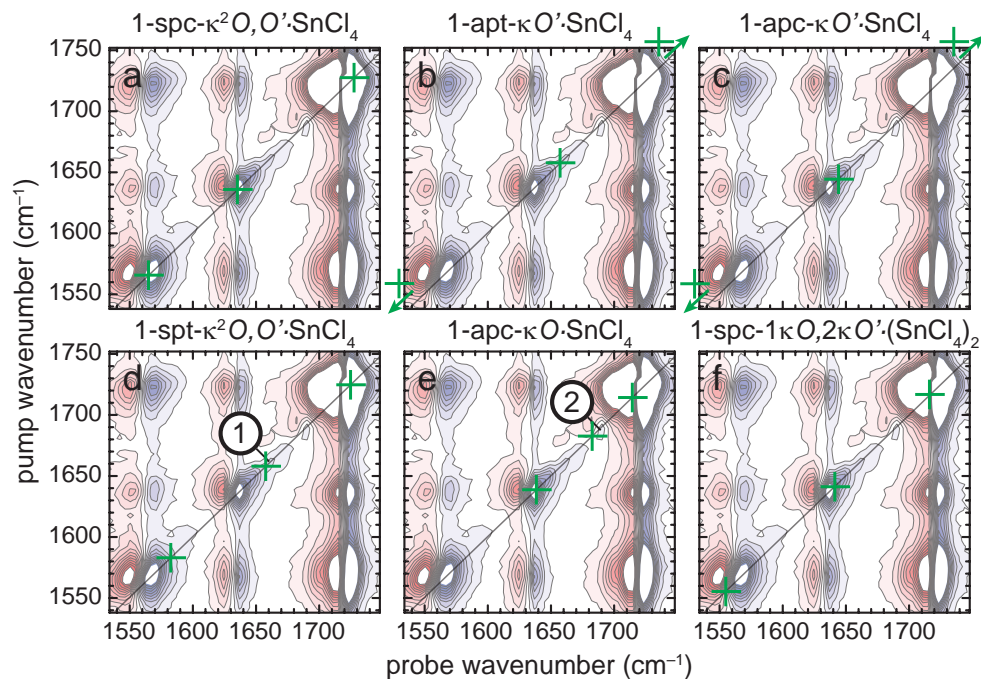
Figure 8.1: *Calculated positions (green crosses) for the diagonal peaks of various conformers in the P2D-IR spectrum of **1**·SnCl$_4$. All calculated vibrational energies are corrected by $-52\,cm^{-1}$ (cf. Table 6.1). Numbers see Text.*

So far, only the dominant signals in the P2D-IR spectra containing the tin complexes have been discussed and **1-spc-$\kappa^2 O, O'$·**SnCl$_4$ was identified as the major complex. The calculated properties of the other complexes do not resemble the main signals. In Fig. 8.1 the calculated vibrational energies (corrected) for the various discussed complexes (for the structures see Fig. 6.1) are overlaid with the experimental P2D-IR spectrum. As already determined in chapter 6 the calculated en-

ergies for **1-spc-$\kappa^2 O, O'$·**SnCl$_4$ coincide nicely with the spectrum (Fig. 8.1 a). For both, **1-apt-$\kappa O'$·**SnCl$_4$ (Fig. 8.1 b) and **1-apc-$\kappa O'$·**SnCl$_4$ (Fig. 8.1 c) two of the calculated frequencies are outside of the measurement window. Another measurement focusing on the region around $1800\,\text{cm}^{-1}$ (not shown) showed no additional signal where the carbonyl vibrations of these two complexes are expected absorb. Thus, these two complexes can be ruled out. In contrast, at all calculated band positions for **1-spt-$\kappa^2 O, O'$·**SnCl$_4$ small signals emerging as shoulder of the main peaks (see Fig. 8.1 d, *e.g.*, pos. 1) were observed and is discussed in more detail in chapter 8.1 (minor species A). Using the signal size at pos. 1, the upper limit for the concentration of this species can be estimated to be 15%. For **1-apc-κO·**SnCl$_4$, the calculated vibrations also lie on top of observed signals. However, the signal at pos. 2 was already identified as isotopologue signal (see chapter 6.2.3). The signal size is in the range expected for an ^{13}C isotopologue and hence this complex can basically be ruled out (less than 0.25%) too. The vibrational frequencies of the di-tin-complex **1-apc-1κO,2$\kappa O'$·**(SnCl$_4$)$_2$ (Fig. 8.1 f) are quite similar to the ones of the major species. However there is no evidence for the presence of this species, which was discussed in the literature as alternative intermediate.[203–205] See also chapter 8.3 for a discussion concerning the complex formed with a large excess of SnCl$_4$ present in solution (minor species C).

In addition to the major complex, at least three additional complexes of **1** with SnCl$_4$ were observed in the P2D-IR spectra using the annihilation method and are discussed in the following. The minor species A and B show the same concentration dependence as the major species while species C only was observed at with a very large excess of SnCl$_4$.

8.1   Minor Species A

One minor species becomes apparent in the cross peak between ν'_3 and ν'_1 (see Fig. 8.2). The high energy shoulder of the band ν'_1, referred to as ν^A_1, couples to a different part of the band ν'_3 (black lines) than the main band (red lines) and shows a slightly different anisotropy indicating different geometries in the molecule. This is readily seen since the two signals disappear at distinct weighted differences illustrated in Fig. 8.2 d and e. The weighting factors for which the two parts of the cross peak disappear in Fig. 8.2 correspond to angles of 46° for the main species and 41° for the minor species. Therefore, the angle between ν^A_1 and ν^A_3 needs to be at least 5° smaller than for the main species (ν'_1/ν'_3). It is difficult to extract the unperturbed line shapes for both the minor species A and the major species because the bands strongly overlap and the fraction of molecules leading to this cross peak is very small ($<15\%$). Thus it is also difficult to judge at which weighting factor the unperturbed signal of the major species is left over in the difference. As a consequence the difference in angle could in principle be larger than 5°, but hidden by overlapping effects – even though these are strongly reduced by the annihilation method.

The measurement definitely shows that the angle between the transition dipole moment belonging to ν^A_1, the high energy shoulder of ν'_1, and the transition dipole moment of ν^A_3 is smaller than for the main band. The corresponding cross peak between ν^A_3 and ν^A_1 shows the same effect (see Fig. 8.2 b and c). This inhomogeneity shows the same concentration dependence as the main complex **1**·SnCl$_4$ and were observed by NMR techniques to date. The finding of an angle less than 41°, combined with the calculated vibrational frequencies, could be interpreted as the presence of small amounts
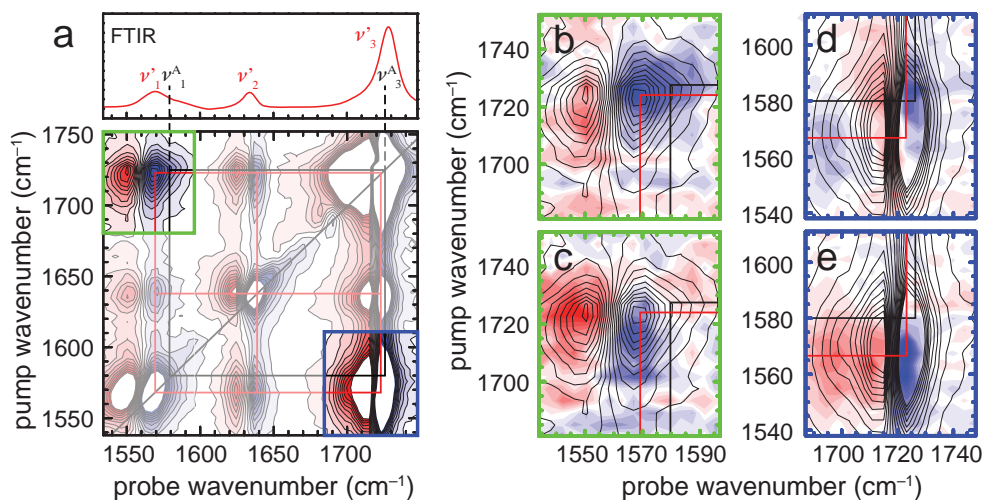
Figure 8.2: a: P2D-IR spectrum (parallel, 1.5 ps) of a solution of **1** (6 mM) and SnCl$_4$ (47 mM) in CH$_2$Cl$_2$. The grids indicate the observed coupling pattern (red: main species; black: species A). The contour lines are spaced by 0.04 mOD. Signals larger than ±0.4 mOD are truncated. The FTIR is shown in the top panel. b to e: Differences between the P2D-IR spectra measured with parallel and perpendicular polarization. Only the regions highlighted in Fig. a are shown. The colored contours are spaced by 6 µOD The contour lines of the signal in Fig. a are overlaid for reference. b: $\Delta\alpha_{\parallel} - 1.25\Delta\alpha_{\perp}$. c: $-(\Delta\alpha_{\parallel} - 1.35\Delta\alpha_{\perp})$. d: $\Delta\alpha_{\parallel} - 1.1\Delta\alpha_{\perp}$. e: $-(\Delta\alpha_{\parallel} - 1.35\Delta\alpha_{\perp})$.

of the chelate **1-spt-$\kappa^2 O, O'$**·SnCl$_4$ in solution. Figure 8.3 compares the calculated vibrational energies for the main conformer in solution (**1-spc-$\kappa^2 O, O'$**·SnCl$_4$, red crosses) and the calculated vibrational energies of **1-spt-$\kappa^2 O, O'$**·SnCl$_4$ (black crosses) with the experimental P2D-IR spectrum. As already mentioned before, at all positions where one would expect the signals of conformer **1-spt-$\kappa^2 O, O'$**·SnCl$_4$, there are signals on the diagonal. Assuming that (only) **1-spt-$\kappa^2 O, O'$**·SnCl$_4$ causes these signals, the population of this conformer can be estimated by the signal size to be less than 15%. The position of the bands (black crosses) also fit well to the coupling pattern observed for the minor species (highlighted by the black grid, *cf.* Fig. 8.2). In the experiment, the angle between the transition dipole moments of the low and high energy vibration (ν_1^A and ν_3^A) is at least 5° smaller for the minor species A than for the main conformer. The calculation predicts an angle of 20° for **1-spt-$\kappa^2 O, O'$**·SnCl$_4$, which is 26° smaller than for the main conformer. So also the smaller angle is reproduced by the calculation. Unfortunately, the cross peaks to the vibration around 1658 cm^{-1} are not reliably seen. This can be caused by the weak intensity of the signals in combination with strong overlapping effects and similar angles to the main species. The angles between the band in the middle and the two others calculated for **1-spt-$\kappa^2 O, O'$**·SnCl$_4$ only vary by less than 10° from the ones measured for the major species. Taking all observations together, the observed signals can be explained by the presence of the chelate **1-spt-$\kappa^2 O, O'$**·SnCl$_4$ in low concentrations. The presence of conformer **1-spt-$\kappa^2 O, O'$**·SnCl$_4$ was hypothesized by Castellino in his NMR study as a potential cause of the low observed stereoselectivity, however this claim was without direct spectroscopic support. [205] It is noteworthy that our experiment does not prove the presence of it, but only gives a spectroscopic

indication. Experiments with higher spectral resolution and more infrared excitation power may possibly identify the minor species unequivocally by detecting all cross peaks and allowing more precise measurements of the angles.
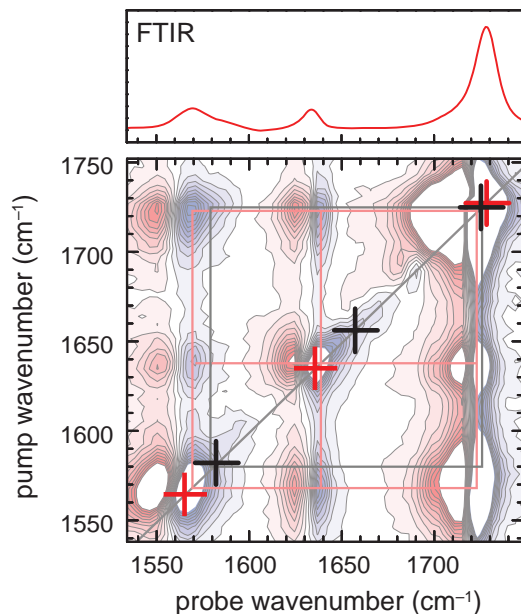

Figure 8.3: *Comparison of the calculated vibrational energies for **1-spc-$\kappa^2 O, O'$·SnCl$_4$** (red) and **1-spt-$\kappa^2 O, O'$·SnCl$_4$** (black) with the P2D-IR spectrum (parallel polarization). The grids indicate the observed coupling pattern for the main species (red) and species A (black). All calculated vibrational energies are corrected by $-52\,\mathrm{cm}^{-1}$ (cf. Table 6.1).*

8.2   Minor Species B

A second minor species (species B, see Fig. 8.4) shows vibrations at $\approx 1570\,\mathrm{cm}^{-1}$ (ν_1^B), $\approx 1635\,\mathrm{cm}^{-1}$ (ν_2^B) and $\approx 1700\,\mathrm{cm}^{-1}$ (ν_3^B). The band ν_3^B appears as a shoulder on the low energy side of band ν_3' and the corresponding diagonal peak overlaps with the diagonal peak of the main species. The presence of the additional diagonal peak is clearly seen in the slice of the P2D-IR spectrum at $1699\,\mathrm{cm}^{-1}$, which is shown Fig. 8.4 b (blue). The population of the minor species B can be estimated by comparison with the signal originating from the ^{13}C isotopologue (see Fig. 8.4 b, red curve) to be around 2–4% under these conditions. The cross peak between ν_1^B and ν_3^B can be seen in the difference between parallel and perpendicular polarization shown in Fig. 8.4 c (black arrow). The angle between the transition dipole moments involved is larger than the angle between ν_1' and ν_3', *i.e.*, larger than 46°. A more precise determination of the angle is inhibited by the strong overlap of the entire peak with the excited state absorption region of the cross peak between ν_1' and ν_3'. Additionally the angle between the transition dipole moments ν_2^B and ν_3^B is larger than the angle between ν_2' and ν_3', *i.e.*, larger than 49°. The corresponding cross peak is nicely seen in the difference spectrum shown in Fig. 8.4 d (highlighted by the black arrows). The cross peaks of the main species and species B overlap here too, which makes a more
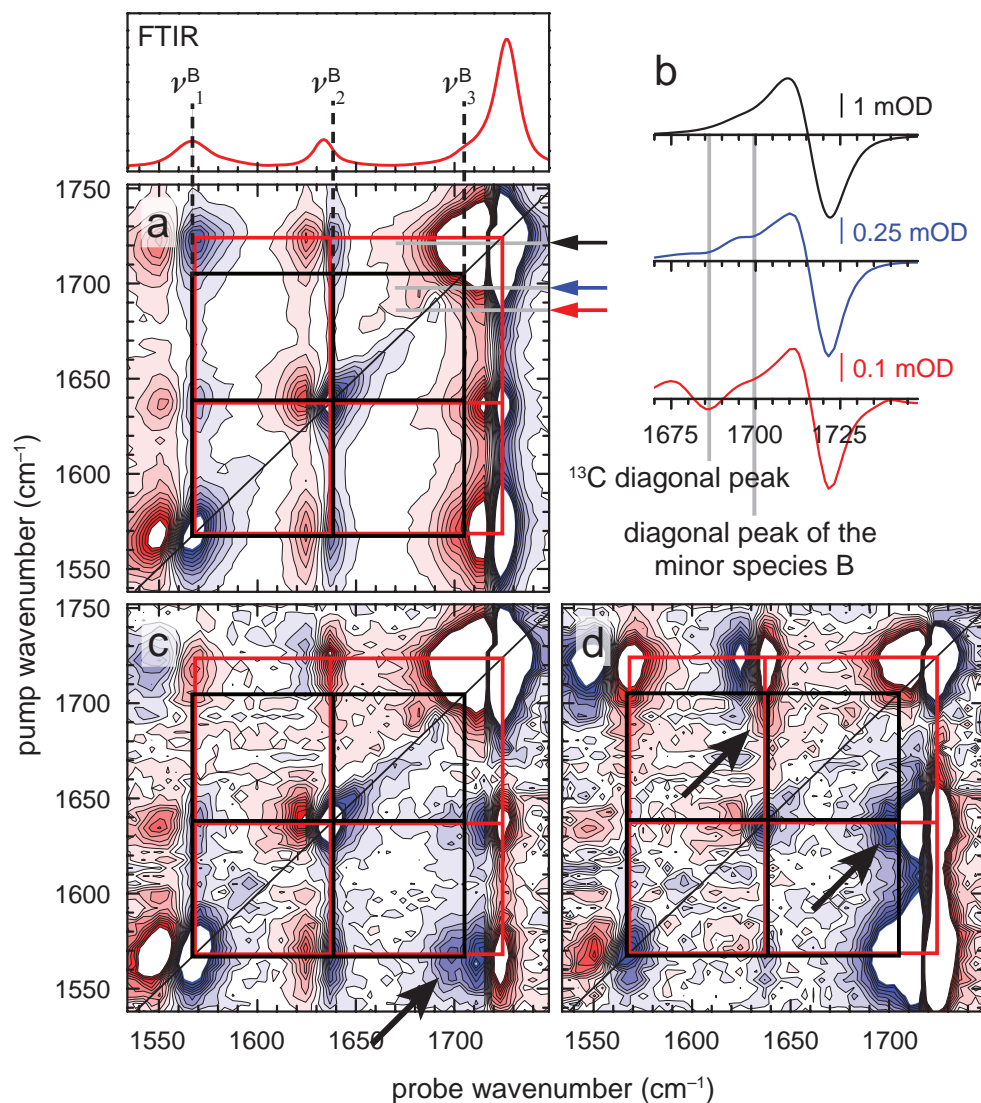
Figure 8.4: a: P2D-IR spectrum (parallel polarization, 1.5 ps) of $1 \cdot SnCl_4$ in CH_2Cl_2 ($c_1 = 24\,mM$, $c_{SnCl_4} = 24\,mM$). The grids highlight the coupling pattern of the main species (red) and of species B (black). The contour lines are spaced by 0.04 mOD. Signals larger than $\pm 0.4\,mOD$ are truncated. b: Slices through the spectrum shown in Fig. a at the marked positions. c and d: Differences between the P2D-IR spectra measured with parallel and perpendicular polarization. The contour lines are spaced by $8\,\mu OD$. Signals larger than $\pm 0.09\,mOD$ are truncated. c: $\Delta\alpha_\parallel - 1.5\Delta\alpha_\perp$. d: $\Delta\alpha_\parallel - 2.25\Delta\alpha_\perp$.

precise measurement of the angle also unfeasible. None of the structures investigated with DFT calculations reflects the experimentally determined frequencies and angles. Therefore, the signal cannot be assigned to a chemical structure. It is noteworthy that at low temperatures a shoulder on the low energy side of the band ν_3' emerged in the FTIR measurements (see Fig. 6.2, black arrow), approximately at the same wavenumber as ν_3^B. It could be possible that both, the shoulder observed in the FTIR spectrum and the coupling pattern observed in the P2D-IR spectra are caused by the same species. Thus species B may be considerably populated at temperatures usually used in $SnCl_4$ catalyzed Diels–Alder reactions (195 K) and important for understanding the observed selectivities. P2D-IR experiments under typical reaction conditions, *i.e.*, at 195 K will lead to a deeper insight on the relevance of species B.

8.3   Minor Species C

In solutions with a large excess of $SnCl_4$, additional vibrations are observed in the FTIR spectra (see Fig. 8.5 top panel). The coupling between them is highlighted in the 2D-IR spectra with the black grid, while the coupling pattern of the main species is indicated in red. Due to strong overlapping effects, only the cross peaks between ν_1^C and ν_3^C and between ν_2^C and ν_3^C are seen. The angles between the corresponding transition dipole moments can be determined by annihilating the cross peaks to $56°\pm 8°$ between ν_1^C and ν_3^C (see Fig. 8.5 topright) and to $50°\pm 6°$ between ν_2^C and ν_3^C (see Fig. 8.5 bottomleft)). The angle between ν_1' and ν_2' (main species) is determined to be $15°\pm 4°$, which is in perfect agreement with the angle determined earlier (see Table 6.1). The concentration dependence of this species implies that several $SnCl_4$ molecules are needed to form this species. The only complex with two Lewis acid molecules discussed in the literature for $SnCl_4$ is the di-tin-complex **1-apc-1κO,2κO′·**$(SnCl_4)_2$. A comparison of the calculation for **1-apc-1κO,2κO′·**$(SnCl_4)_2$ (see Table 6.1) with the experiment excludes this complex as the source of the signal of species C since neither the angles nor the vibrational energies are reproduced. In fact, there is no evidence for the formation of **1-apc-1κO,2κO′·**$(SnCl_4)_2$ under these conditions, although this structure was proposed as alternative key intermediate for the Lewis acid Et_2AlCl.[203] Species C may be formed between **1** and a $(SnCl_4)_x$ cluster. The presence of $(SnCl_4)_x$ clusters under these conditions was hypothesized based on $SnCl_4$ NMR experiments (see chapter 6.3). The concentration of minor species C can be roughly estimated to ~25% by integrating the (scaled) FTIR spectra at high and medium excess of $SnCl_4$.

In order to obtain a P2D-IR spectrum that only contains signals caused by species C, the spectrum measured with medium excess of $SnCl_4$ (major species, see Fig. 6.3) can be subtracted from the measurement with a high $SnCl_4$ excess as it is illustrated in Fig. 8.6. The P2D-IR spectrum with medium excess of **1**·$SnCl_4$ is scaled such that the signals of the major species disappear. Therefore only the signals growing in at higher excess of the Lewis acid remain. Unfortunately, this did not work perfectly in the shown example. Especially in the gray shaded region there are still remaining signals of the major species visible. This is an artifact caused by the differences of the two measurements. As described in chapter 2 the signal size observed in the 2D-IR spectrum depends on the intensity of the pump pulses and therefore on the spectrum of the OPA. The two spectra compared in Fig. 8.6 were collected at different dates with different OPA spectra. Therefore, the subtraction is not expected to be perfect. Nevertheless, the subtraction is fine in the region of interest where the signals of
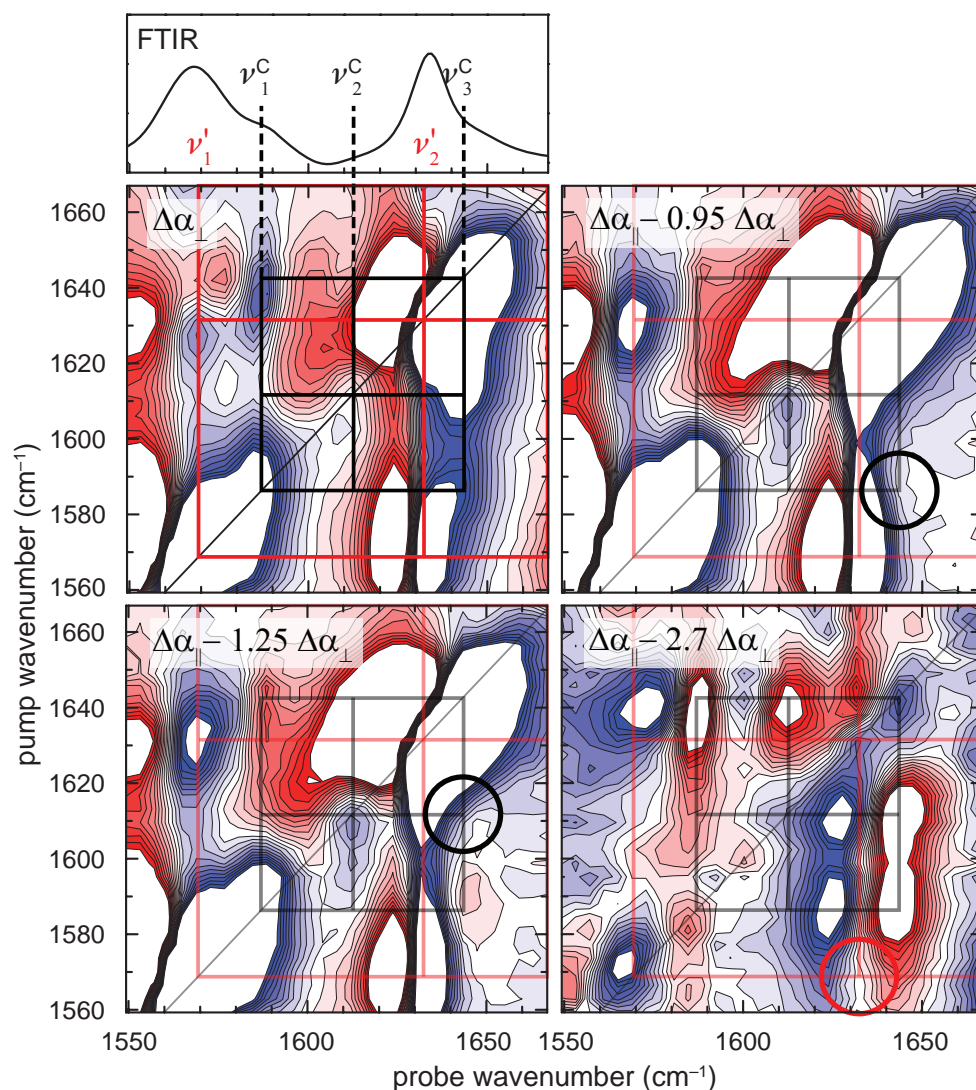
Figure 8.5: *Differences between the P2D-IR spectra (1.5 ps) of a solution of **1** and excess $SnCl_4$ in CH_2Cl_2 ($c_1 = 28\,mM$, $c_{SnCl_4} = 531\,mM$). The weighting factors of the spectra with parallel and perpendicular polarization are given in the insets. The contour lines are spaced by $9\,\mu OD$. Signals larger than $\pm 0.1\,mOD$ are truncated. Signals belonging to the same species are connected by the grids (red: main complex; black: minor complex C). The colored circles highlight the position of the annihilated peaks. The FTIR spectrum of the sample is shown in the top panel for reference.*
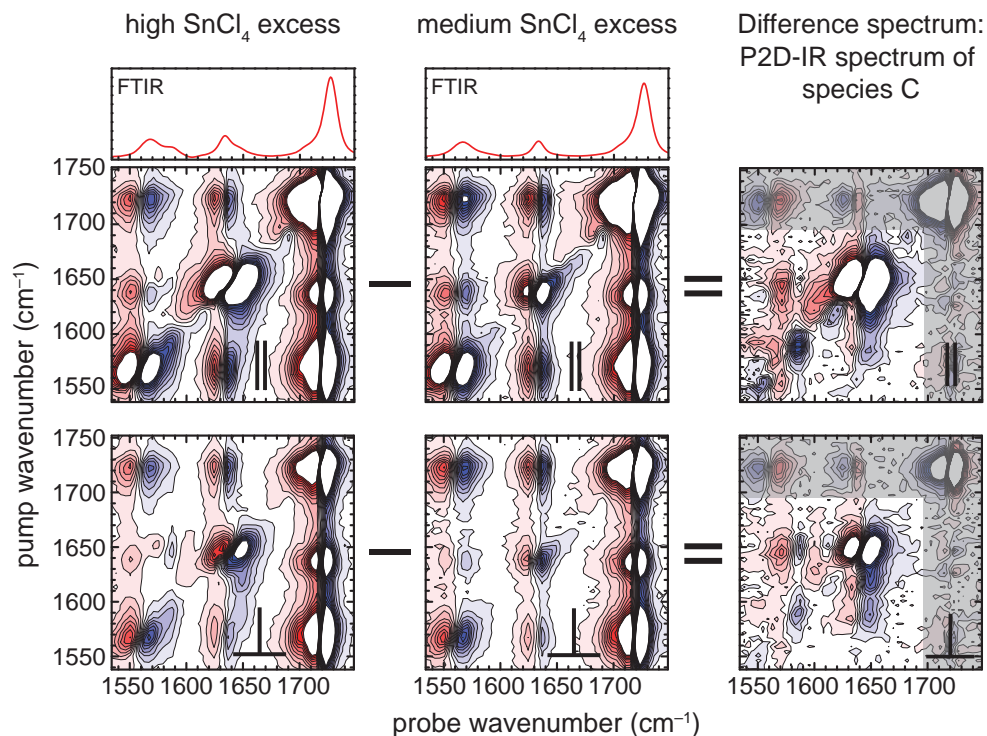
Figure 8.6: *The differences between the P2D-IR spectra with a large excess of SnCl$_4$ (left) and the P2D-IR spectra of with medium excess of SnCl$_4$ (middle) reveal the P2D-IR spectra of species C (right; the contour lines are spaced by 10 μOD). The gray area is dominated by subtraction artifacts, which are discussed in the text.*

species C are. These double difference spectra can now be analyzed in the very same manner as the directly measured spectra and lead to the same conclusions as drawn before (ν_1^C/ν_3^C: 58$°$± 10$°$, ν_2^C/ν_3^C: 52$°$± 10$°$). The larger noise in these spectra compared to the spectra showed in Fig. 8.5 is mainly caused by the lower sample concentration, the broader OPA spectrum, and the fewer number of scans. It is not primarily a consequence of the subtraction.

8.3.1 NMR Spectroscopy[i]
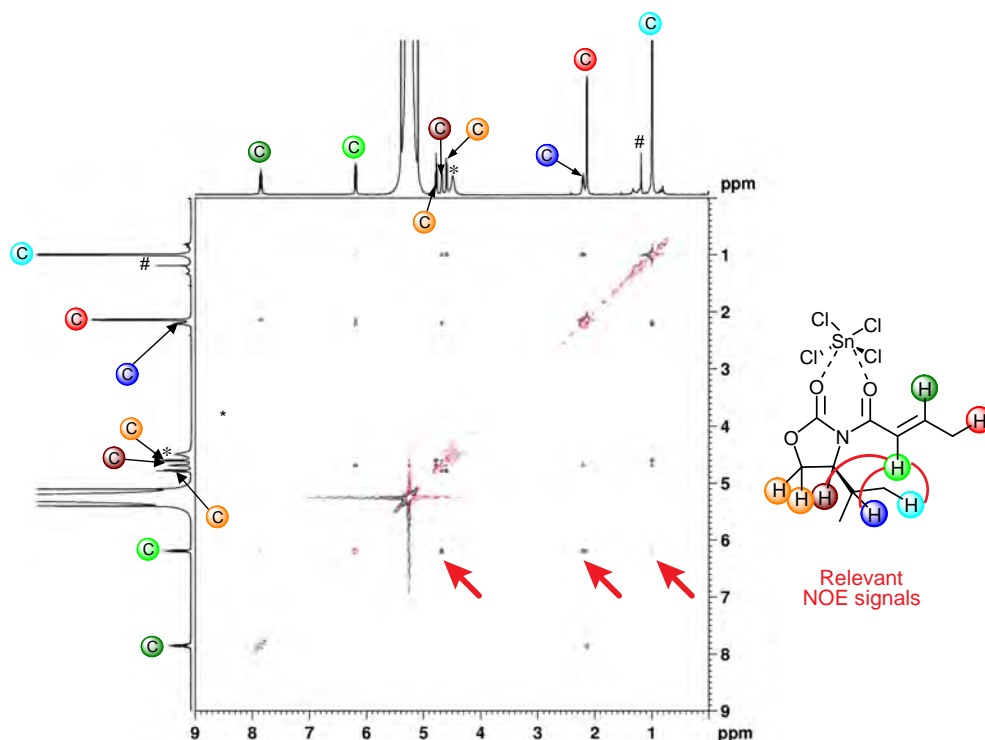
Figure 8.7: ^1H NOESY (600 MHz, 298 K) spectrum of a solution of **1** and $SnCl_4$ in CH_2Cl_2 ($c_1 = 28$ mM, $c_{SnCl_4} = 530$ mM). Negative signals are shown in red, positive in black. The 1D ^1H NMR signals are shown for reference.

In contrast to the FTIR and P2D-IR spectra, the ^1H NOESY spectrum (Fig. 8.7 measured under the same conditions as the P2D-IR spectra shown in Fig. 8.5) looks basically the same as the one measured for the main species (see Fig. 6.13). There is no evidence for an additional species formed, neither in the chemical shifts nor in the observed NOE cross peaks. This is remarkable, since the concentration of minor species C under these conditions is approximately 25%. This example again shows nicely the complementarity and the difference in sensitivity of NMR and P2D-IR spectroscopy. On the other hand it also indicates that the structure of the substrate (**1**) is not significantly different in species C and the major species.

8.4   Summary of the Detected Species

The use of the annihilation method enabled the detection and tentative assignment of three minor species. Their properties are summarized in Table 8.1. The identification of these may have a large impact on understanding the observed selectivities in the reaction. Minor species A for example will lead to the opposite diastereomer in the Diels–Alder reaction than the major species.

Table 8.1: *Overview of the detected and tentatively assigned **1**·SnCl$_4$ complexes.*

	Main species		species A		species B		species C	
vibrational energies (cm^{-1})								
	ν'_1	1567	ν_1^A	$\approx$1575	ν_1^B	$\approx$1570	ν_1^C	$\approx$1590
	ν'_2	1633			ν_2^B	$\approx$1635	ν_2^C	$\approx$1610
	ν'_3	1727	ν_3^A	$\approx$1730	ν_3^B	$\approx$1700	ν_3^C	$\approx$1645
measured angles[i] (°)								
	ν'_1/ν'_2	15 $\pm$ 8						
	ν'_1/ν'_3	46 $\pm$ 2	ν'_1/ν'_3	<41	ν_1^B/ν_3^B	>46	ν_1^C/ν_3^C	56 $\pm$ 8
	ν'_2/ν'_3	46 $\pm$ 2			ν_2^B/ν_3^B	>49	ν_2^C/ν_3^C	50 $\pm$ 6
populations[ii] (%)								
		>80		<15		2–4		_[iii]
Determined structures								
	1-spc-κ^2O,O'		possibly 1-spt-κ^2O,O'		–		possibly complex with $(SnCl_4)_x$	

[i] Measured at a delay time of 1.5 ps.
[ii] At low and moderate SnCl$_4$ concentrations.
[iii] Only populated wit a large excess of SnCl$_4$.

Chapter 9

Structure of the Magnesium Complex

For Mg^{2+} as Lewis acid in principle the same complexes are probable as for $SnCl_4$ (see Fig. 6.1). Only the mono-complexes between $Mg(ClO_4)_2$ and **1** are discussed in this thesis (structures see Table 9.1), because the **1**·$Mg(MeCN)_x$ complexes are only formed at higher excess of $Mg(ClO_4)_2$. From previous FTIR studies it is known that $Mg(ClO_4)_2$ dissociates completely in MeCN and, without any additional ligand, the Mg^{2+} ions are hexacoordinated by the solvent.[223] At the concentrations used in the following experiments, no close ion pairs were observed. Thus it is assumed that for the complexes that are formed in a solution of $Mg(ClO_4)_2$ and **1** in MeCN also no close ion pairs exist and the residual complexation sites are occupied by MeCN molecules.

Bakalova *et al.* used $Mg(ClO_4)_2$ as a reference system that forms a chelate with **1** for their NMR studies on the complexes between Et_2AlCl and **1**. From the observed NOE cross peaks, they and also Kanai *et al.* and Desimoni *et al.* concluded that $Mg(ClO_4)_2$ forms a chelate with **1** in the spc conformation, analog to what was observed here for $SnCl_4$ as Lewis acid.[203,207,213] There was no indication in the NMR spectra for additional species present in solution. Thus, also for the P2D-IR experiments similar results are expected.

9.1 FTIR Studies[i]

The complex formation between $Mg(ClO_4)_2$ and **1** in MeCN can be observed by FTIR spectroscopy (Fig. 9.1 left). Upon complexation, the vibrational frequencies of **1** shift to lower energies ($\nu_1^* = 1616\,\text{cm}^{-1}$, $\nu_2^* = 1650\,\text{cm}^{-1}$, and $\nu_3^* = 1762\,\text{cm}^{-1}$), similar as it is the case for the Lewis acid $SnCl_4$. However, the shifts are smaller and also the changes in the transition dipole moments upon complexation are less pronounced. The FTIR signal of the complex increases approximately proportionally to the $Mg(ClO_4)_2$ concentration, which indicates that also here a mono complex is formed. Decreasing the temperature from room temperature to 253 K led to a small shift of the equilibrium constant towards the complex and to a slight narrowing of all bands (spectra not shown). Especially at high $Mg(ClO_4)_2$ concentrations, a

---

[i]The shown spectra were measured by Sabrina Steinwand.
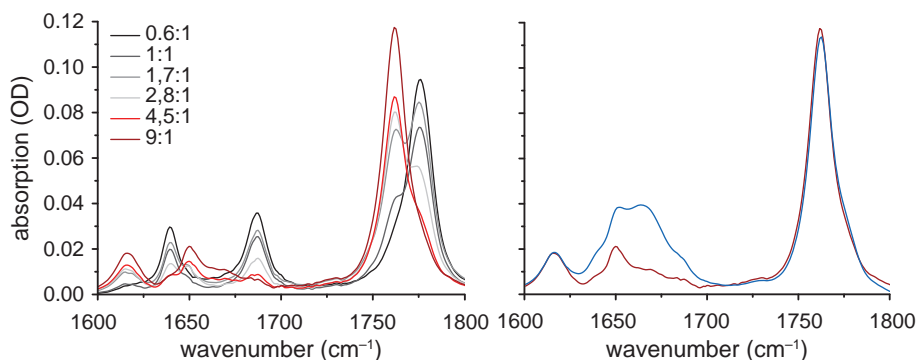
Figure 9.1: Left: FTIR spectra of various **1**-Mg(ClO₄)₂ mixtures in MeCN. The concentration of **1** was kept constant (12 mM) while the Mg(ClO₄)₂ concentration was varied from 7 mM to 0.11 M. The Mg(ClO₄)₂:**1** ratio is given in the legend. Right: FTIR spectrum of a solution of **1** (12 mM) and Mg(ClO₄)₂ (0.11 M) in MeCN directly after preparation (blue) and after storage over molecular sieve for more than 12 hours (dark red).

small broad band around $1670\,\mathrm{cm^{-1}}$ was observed. This is probably due to residual water in the solution, which complexes to Mg^{2+} ions. $Mg(ClO_4)_2$ is known to be very hygroscopic and this band was even more pronounced when the solutions were prepared without molecular sieve (see Fig. 9.1 right).

9.2 P2D-IR Spectroscopy
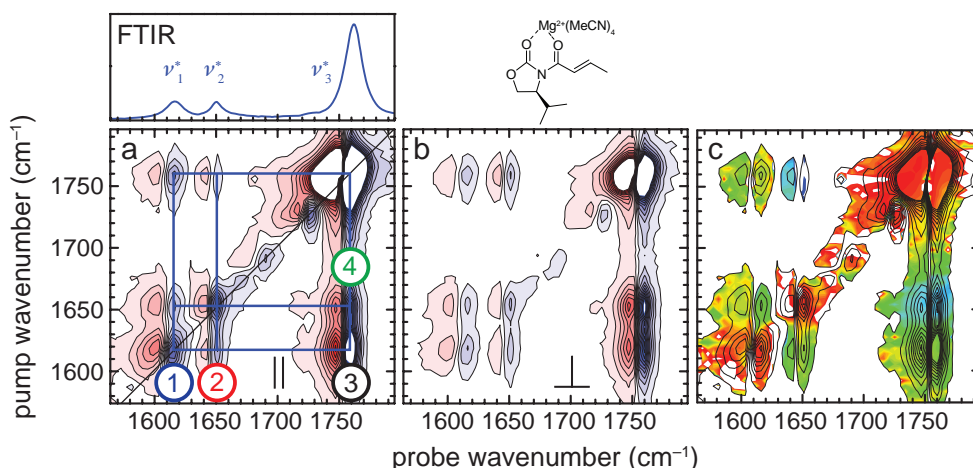
Figure 9.2: a and b: P2D-IR spectra (1.5 ps) of a solution of **1** (34 mM) and Mg(ClO₄)₂ (0.38 M) in MeCN for parallel (a) and perpendicular polarization (b). The contour lines are spaced by 0.05 mOD. Signals larger than ± 0.5 mOD are truncated. Numbers see text. The FTIR spectrum is shown in the top panel for reference. c: 2D-IR anisotropy spectrum. The colors indicate the anisotropy (color code see, e.g., Fig. 6.4), while the contour lines show the signal intensities for parallel polarization (see Fig. a). The anisotropy is only shown for regions where $\Delta\alpha_\parallel > 0.05\,mOD$ and where $-0.2 < r < 0.4$.

The P2D-IR spectra of $\mathbf{1}\cdot\mathrm{Mg(MeCN)}_x$ in MeCN (Fig. 9.2 show nine dominating peaks, three diagonal peaks and six cross peaks between them. These peaks are connected by the blue grid, which highlights the coupling pattern for the major species. Additionally, there are three smaller signals along the diagonal, which are discussed in detail in chapter 9.2.3 and 9.2.4). First, the signals of the major species are focused on.

9.2.1 Time Dependence of the Anisotropy
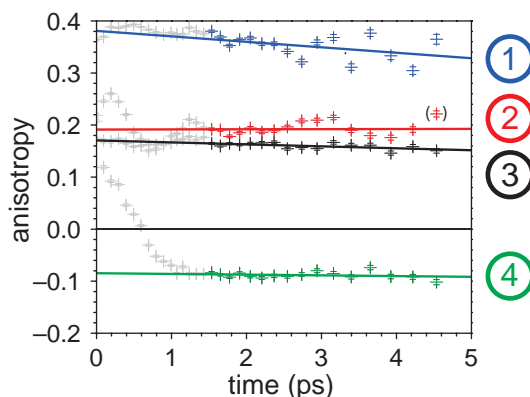
Figure 9.3: *Time dependence of the anisotropy for the signals (bleach) of $\mathbf{1}\cdot\mathrm{Mg(MeCN)}_x$ in MeCN labeled in Fig. 9.2. Diagonal peak ν_1^*: blue (cf. Fig. 9.2 pos. 1); cross peak ν_1^*/ν_2^*: red (cf. Fig. 9.2 pos. 2); cross peak ν_1^*/ν_3^*: black (cf. Fig. 9.2 pos. 3); cross peak ν_2^*/ν_3^*: green (cf. Fig. 9.2 pos. 4). The straight, colored lines are linear fits to the data from 1.5 ps to 5 ps. The data point in brackets is omitted for the analysis.*

The time dependent anisotropies of the peaks numbered in Fig. 9.2 are shown in Fig. 9.3. The data with a delay time between 1.5 ps and 5 ps were linearly extrapolated (straight lines) to determine the initial anisotropies. For the diagonal peak of ν_1^* (blue, pos. 1), the anisotropy extrapolated to 0.38(2), which is in good agreement with the value of 0.4 expected for a diagonal peak. The cross peak between ν_1^* and ν_2^* (red, pos. 2) showed an initial anisotropy of 0.191(10). Using eq. 14, this leads to an angle θ of $36°\pm3°$. Like before, the error of $3°$ includes the estimated experimental errors and the standard deviation of the linear fit. The extrapolation of the time dependent anisotropy for the cross peaks between ν_1^* and ν_3^* (black, pos. 3) and between ν_2^* and ν_3^* (green, pos. 4) results in angles of $38°\pm2°$ and $64°\pm2°$, respectively. The experimentally determined angles between the transition dipole moments are summarized in Table 9.1.

For the fit of the time dependent anisotropy at pos. 2 (ν_1^*/ν_2^*), the last data point with a delay time of 4.5 ps was omitted. Figure 9.4 compares the fit of the measured anisotropy with and without the last data point shown in brackets. The fit without the last data point (straight line) extrapolated to an anisotropy of r(0 ps) = 0.191(10), corresponding to an angle of $36°$. The fit with all shown red data points led to an anisotropy of r(0 ps) = 0.183(2). This corresponds to an angle between the transition dipole moments of $37°$. The two determined angles differ only by $1°$, which is less than our experimental error. However, the dashed fit shows an increase of the anisotropy with longer delay time. Such a long term rise in anisotropy is physically not reason-
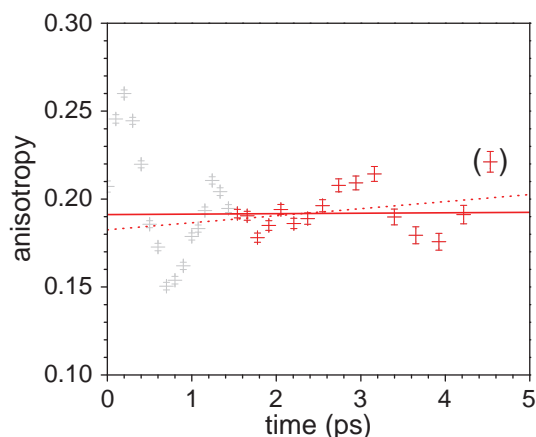
Figure 9.4: *Anisotropy fit of the cross peak ν_1^*/ν_2^* with (dashed line) and without the last data point (straight line) shown in brackets.*

able. The positive slope of the fit is caused by an oscillation on the anisotropy, which could be due to a coherent effect between the two involved vibrations, which are close in energy. The period of the oscillation roughly agrees with the energy gap between ν_1^* and ν_2^*. Similar effects were observed for rhodium dicarbonylacetylacteonate by the groups of Fayer and Tokmakoff. [224,225]

In a similar way as observed for $\mathbf{1}\cdot\mathrm{SnCl}_4$, the rotational diffusion is slower for $\mathbf{1}\cdot\mathrm{Mg(MeCN)}_x$ than for $\mathbf{1}$ in MeCN. The anisotropy decay of ν_2 is compared to the one of ν_1^* in Fig. 9.5. The rotational correlation time increases from 8.4(2) ps (ν_2) to 20(2) ps (ν_1^*) upon complexation. The increase in the rotational correlation time is a little bit smaller than observed for $\mathbf{1}\cdot\mathrm{SnCl}_4$, but in the same order of magnitude. Thus, the two complexes $\mathbf{1}\cdot\mathrm{Mg(MeCN)}_x$ and $\mathbf{1}\cdot\mathrm{SnCl}_4$ are similar in shape and size.
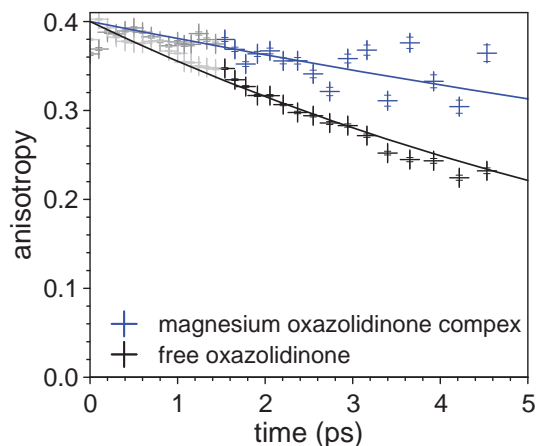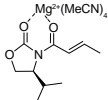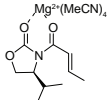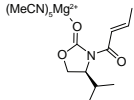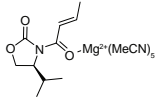
Figure 9.5: *Comparison of the anisotropy decay of diagonal peaks of $\mathbf{1}$ (black, ν_2) and $\mathbf{1}\cdot\mathrm{Mg(MeCN)}_x$ (blue, ν_1^*) in MeCN.*

9.2.2 Comparison with DFT Calculations

To deduce the actual structure of the complex between **1** and $Mg(ClO_4)_2$ in MeCN from the transition dipole angles, the vibrational frequencies and also the transition dipole moments were calculated for the mono-complexes shown in Table 9.1. Previous studies showed that $Mg(ClO_4)_2$ dissociates completely in MeCN and is, at low concentrations, sixfold coordinated by the solvent.[223] Hence only complexes between Mg^{2+} and **1** were calculated, in which the rest of the six coordination sites were occupied by MeCN. The results are summarized in Table 9.1. The calculated angles of **1-spc-κ^2O, O'**·$Mg(MeCN)_4$ fitted very well to the experiment and showed only an overall deviation of 13°. In addition, the calculated vibrational energies for **1-spc-κ^2O, O'**·$Mg(MeCN)_4$ matched best to the experimental data. The calculated vibrational frequencies coincide with the experimental ones after scaling by 0.97. For all other calculated species, both the calculated angles and vibrational frequencies deviate strongly from the measurements. The comparison of the angles resulted in overall deviations of at least 48°. The deviation for a single angle was at maximum 32° for the angle between ν_2^* and ν_3^* for the complex **1-apc-κO**·$Mg(MeCN)_5$; the scaled vibrational frequencies deviated by $42\,cm^{-1}$ for ν_2^* in this conformer. The comparison therefore led to the conclusion that the primarily formed complex is chelate **1-spc-κ^2O, O'**·$Mg(MeCN)_4$, the same conformer as identified as major species for **1**·$SnCl_4$.
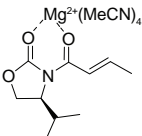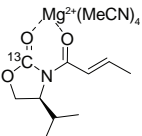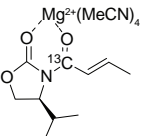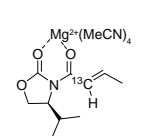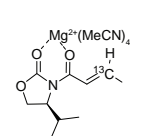
Table 9.1: *Comparison of the experimentally determined angles and frequencies of* **1**·$Mg(MeCN)_x$ *in MeCN with the results of the DFT calculations (M06/6-31+G(d,p)/PCM/Bondi). The total structural deviation is expressed as* $\Delta_{tot} = \sum |\Delta_i|$.

	exp.	1-spc-κ^2O, O'	1-spt-κ^2O, O'	1-apc-κO	1-apc-$\kappa O'$
angles					
ν_1^*/ν_2^* (°)	36 ± 3	35 (Δ=1)	43 (Δ=7)	58 (Δ=22)	67 (Δ=31)
ν_1^*/ν_3^* (°)	38 ± 2	40 (Δ=2)	26 (Δ=12)	26 (Δ=12)	8 (Δ=30)
ν_2^*/ν_3^* (°)	64 ± 2	74 (Δ=10)	35 (Δ=29)	32 (Δ=32)	64 (Δ=0)
Δ_{tot} (°)		13	48	66	61
vibrational energies					
ν_1^* (cm^{-1})	1616	1666 (Δ=50)	1679 (Δ=63)	1690 (Δ=74)	1673 (Δ=57)
ν_2^* (cm^{-1})	1650	1707 (Δ=57)	1715 (Δ=65)	1744 (Δ=94)	1719 (Δ=69)
ν_3^* (cm^{-1})	1762	1810 (Δ=48)	1806 (Δ=44)	1807 (Δ=45)	1836 (Δ=74)

9.2.3   Isotopologue Signals

The calculations of the isotopologue vibrations allow the identification of the signals caused by isotopologues and are summarized in Table 9.2. The bands experiencing a shift of more than $10\,\mathrm{cm^{-1}}$ are marked by the green crosses in Fig. 9.2.3. Like it also was the case for the P2D-IR spectra of **1** and **1**·SnCl$_4$, only the isotopologue band of ν_3^* is clearly seen at $\approx 1725\,\mathrm{cm^{-1}}$. The other isotopologue signals are too weak to be clearly observed.

Table 9.2: *Calculated shifts of the vibrational wavenumbers for the isotopologues of* **1-spc-κ^2O,O′·Mg(MeCN)$_4$** *in MeCN (M06/6-31+G(d,p)/PCM/SDD/Bondi).*

	(cm^{-1})	Δ (cm^{-1})	Δ (cm^{-1})	Δ (cm^{-1})	Δ (cm^{-1})
ν_1^*	1666	−3	−31	−14	−15
ν_2^*	1607	−9	−6	−12	−15
ν_3^*	1810	−36	−6	−1	−1

Figure 9.6: *Calculated positions (green crosses) for the diagonal peaks of the* ^{13}*C isotopologues in the P2D-IR spectrum of* **1-spc-κ^2O,O′·Mg(MeCN)$_4$** *in MeCN (M06/6-31+G(d,p)/PCM/Bondi). The black crosses mark the vibrations of the all-^{12}C isotopologue. The calculated vibrational energies are corrected by –51 cm^{-1} (cf. Table 9.2).*

9.2.4 Minor Species

In addition to the signals analyzed so far (originating from the major species and its isotopologue) two additional, weak signals exist (see Fig. 9.7, pos. A and B). These could belong to additional complexes formed between **1** and Mg^{2+} in MeCN. Knowledge about these species is a prerequisite to understand the observed stereoselectivity of the Lewis acid catalyzed Diels–Alder reactions, as they can result in side products, *i.e.*, other stereomers. For illustration, the calculated vibrational energies of the various complexes are marked by the green crosses in Fig. 9.7. All frequencies are corrected by $-51\,cm^{-1}$. As already discussed before, the calculations for **1-spc-$\kappa^2 O, O'$**·$Mg(MeCN)_4$ agree with the measurements for the major species.

The other chelate conformation, **1-spt-$\kappa^2 O, O'$**·$Mg(MeCN)_4$, is calculated to absorb at similar positions as the major species. At all those positions, signals were observed. Especially the middle band coincides with a small band at $1670\,cm^{-1}$ (see
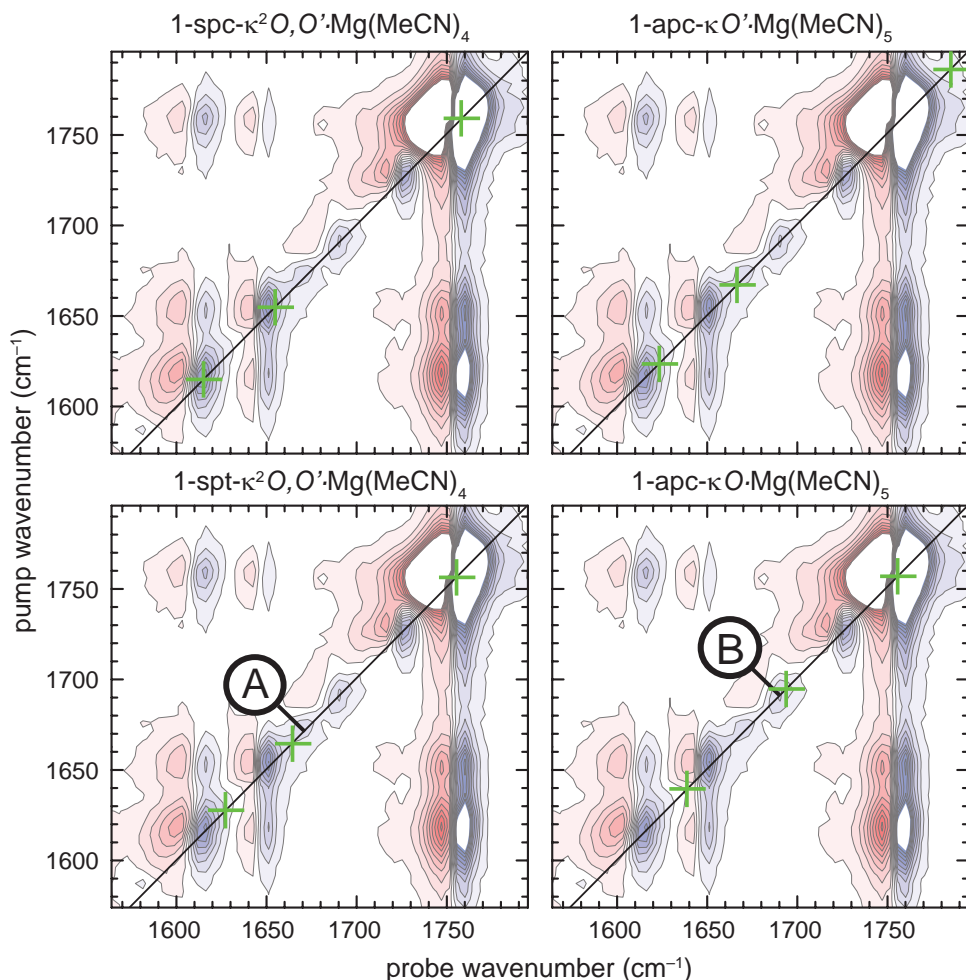
Figure 9.7: *Calculated positions (green crosses) for the diagonal peaks of various conformers in the P2D-IR spectrum of $\mathbf{1}\cdot Mg(MeCN)_x$. All calculated vibrational energies are corrected by $-51\,cm^{-1}$ (cf. Table 9.1).*

Fig. 9.7 pos. A). Hence, this band could possibly be caused by the presence of this species, which was also proposed as a minor species formed between $SnCl_4$ and **1**. However **1-spt-κ^2O, O'**·Mg(MeCN)$_4$ is calculated to be 5.2 kcal/mol higher in energy than the major species, **1-spc-κ^2O, O'**·Mg(MeCN)$_4$. **1-apc-$\kappa O'$**·Mg(MeCN)$_5$ is calculated to absorb at pos. A, too. However, the signal for the vibration with largest wavenumber of this species is very weak, much weaker than one would expect.

No cross peaks for the band at pos. A were observed and thus there is no proof for the existence of any of the two species. From the FTIR spectra shown in Fig. 9.1 it is known that also water in the solution causes a signal at $1670\,cm^{-1}$. Even though molecular sieve was used to adsorb the water it is likely that still small amounts of water remained in solution leading to the diagonal peak at pos. A. In order to definitely assign this peak, additional experiments are required. The samples should be completely water free and the experiment should allow to detect the cross peaks to this band if they exist, *i.e.*, experiments with better signal-to-noise ratio and higher spectral resolution.

The positions of the vibrations of the complex **1-apc-κO**·Mg(MeCN)$_5$ also overlap with peaks observed in the spectrum, particularly with the diagonal peak at pos. B (Fig. 9.7) located at $\approx 1690\,cm^{-1}$. If one zooms into the P2D-IR spectrum, a weak cross peak to a band at $\sim 1645\,cm^{-1}$ is observed (see Fig. 9.8, pos. I). The position of the bands fit to the calculated vibrational energies of **1-apc-κO**·Mg(MeCN)$_5$ ($\nu_1^* = 1639\,cm^{-1}$ and $\nu_2^* = 1693\,cm^{-1}$) and also to the bands of uncomplexed **1** in MeCN ($\nu_1 = 1643\,cm^{-1}$ and $\nu_2 = 1687\,cm^{-1}$, see Table 5.3). Using the cross peak position and also the polarization dependence, the two cannot be discriminated since the angles between the transition dipole moments of the involved vibrations are very similar (61° for **1** and 58° for **1-apc-κO**·Mg(MeCN)$_5$). Cross peaks to the band at the largest wavenumber would allow the identification of the origin of these peaks since the cross peaks differ considerably in wavenumber and in the expected anisotropy. The observed coupling pattern for **1** and the calculated one for **1-apc-κO**·Mg(MeCN)$_5$ are shown in Fig. 9.8 (**1**: green grid, **1-apc-κO**·Mg(MeCN)$_5$: black grid). The weak cross peaks that might occur here unfortunately overlap with the intense signals from the major species.

If the observed signals would be caused by free **1**, the cross peaks should appear on the high energy side of the bands of the major species (see Fig. 9.8, pos. II and III). They are expected to be approximately three contour lines large in the spectrum shown in Fig. 9.8, but they are not seen. The diagonal peak of ν_3 is also not observed. This leads to the conclusion that the signals are not caused by free **1**. However, it should be noted that due to band overlap and the signal-to-noise ratio of the spectra the presence of the cross peaks for free **1** cannot be excluded incontrovertibly. A comparison of spectra (or cuts) measured on pure **1** and **1**·Mg(MeCN)$_x$ in MeCN under exactly the same conditions could prove the absence of free **1** in solution under the conditions used here.

If the complex **1-apc-κO**·Mg(MeCN)$_5$ is responsible for the observed signals, the cross peaks with the high energy vibration would be slightly redshifted compared to the major species. The bleach part of these cross peaks would - in probe direction - lie directly between the negative and positive part of the cross peak of the major species (see Fig. 9.8, pos. IV and V). Due to the steep line shape of the cross peaks from the major species, weak cross peaks unfortunately cannot be detected in this region. The cross peaks at pos. II and IV are sitting on top of the shoulder of both, the diagonal peak ν_3^* and the cross peak ν_2^*/ν_3^* of the major species. In order to assign the peaks
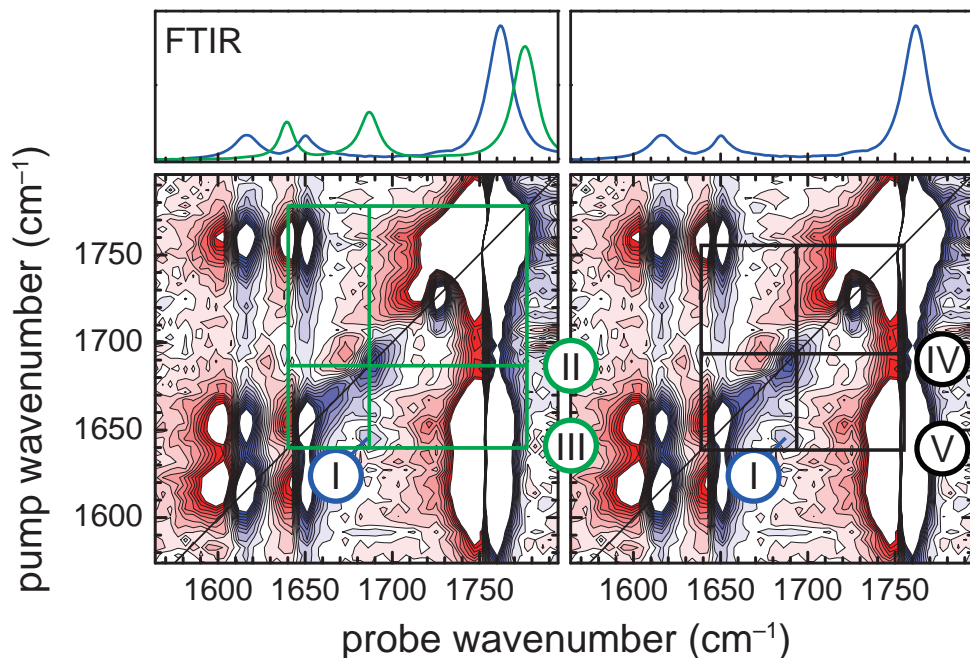
Figure 9.8: *P2D-IR spectrum of $1 \cdot Mg(MeCN)_x$ in MeCN (cf. Fig. 9.2, right). The contour lines are spaced by 6 μOD. Signals larger than ±0.06 mOD are truncated. The FTIR spectrum is shown in the top panel for reference (blue: mixture of 1 and $Mg(ClO_4)_2$, green: free 1). The grid for the coupling pattern for free 1 (green) is based on experimental data while the grid for the conformer $1\text{-apc-}\kappa O \cdot Mg(MeCN)_5$ is based on the DFT calculation (see Table 9.1, corrected by $-51\,cm^{-1}$). Numbers see text.*

II and IV unambiguously, experiments with a higher resolution in pump direction are required. Sufficient resolution might be realized by using a pulse pair instead of a narrowband Fabry–Perot pump pulse.[53,87,88]

If one assumes that the observed weak signals are only caused by additional conformations, one can very roughly rate their population. Including the shape of the OPA spectrum and also the calculated transition dipole moment, the populations are estimated to be larger than 75% for the major species ($1\text{-spc-}\kappa^2 O, O' \cdot \mathrm{Mg(MeCN)}_4$) and less than 15% for each, the species contributing to the signal at position A ($1\text{-spt-}\kappa^2 O, O' \cdot \mathrm{Mg(MeCN)}_4$ or $1\text{-apc-}\kappa O' \cdot \mathrm{Mg(MeCN)}_5$) and to the signal at position B ($1\text{-apc-}\kappa O \cdot \mathrm{Mg(MeCN)}_5$).

Chapter 10

Discussion and Conclusions

10.1 Review of the Structures and the Implications for the Reaction Mechanism of the Stereo- selective Diels–Alder Reaction

The present work revealed that **1** adopts the conformation **1-apc** in solution. Other conformers were not observed by any of the used techniques, *i.e.*, NMR, FTIR, and P2D-IR spectroscopy. P2D-IR experiments show that at least 95% of **1** exist as **1-apc**. The detailed analysis of the P2D-IR spectra indicated that at ambient temperatures (283 K) the molecule is not planar, but twisted around the bond connecting the substrate with the Evans auxiliary. The amplitude of the twist in solution could not be quantified and also the source of the twist needs further investigations. A twist was also observed in the crystal structure of **1**, however could not be reproduced by the DFT calculations. Even small rotations around this specific bond can lead to a significant change on the steric shielding of the reacting moiety and thus influence notably the observed stereoselectivities. The rotation around the amide bond as observed in the crystal structure (see Fig. 5.14) will lead to a reduced shielding and hence to a reduced steroselectivity. Especially for non-chelating catalysts, this twist is probably an important factor to rationalize the observed stereoselectivities. Because the DFT calculations are not able to reproduce this twist, one needs to be very careful when extracting steroselectivities based on the calculated structures as it was done previously. [183,203]

The conformational change of **1** induced by the Lewis acids $Mg(ClO_4)_2$ and $SnCl_4$ was resolved by P2D-IR spectroscopy. The analysis of the spectra unequivocally showed that in both cases the chelate with the substrate in the conformation **1-spc** was the dominant species, in agreement with the conclusions drawn by NMR studies. In addition to the major species, several minor species were detected and tentatively assigned using P2D-IR spectroscopy. These species were not observed using NMR techniques. In the case of $SnCl_4$ for example both, **1-spc-$\kappa^2 O, O'$·$SnCl_4$** (major complex, >80%) and **1-spt-$\kappa^2 O, O'$·$SnCl_4$** (minor complex, <15%) are present in solution. These two complexes show most likely similar reactivities, however, lead predominantly to opposite diastereomers. Knowing all the complexes present in solution is very important to understand and predict the product distribution for steroselective reactions such as the Lewis acid catalyzed Diels–Alder reaction used as an example here.

10.1.1   Outlook

The present study introduced P2D-IR spectroscopy as a powerful tool to investigate the structure of small molecules important in organic synthesis such as **1**. It paved the way for a more detailed understanding of the reaction mechanism of Lewis acid catalyzed reactions by looking at the structures of possible intermediates experimentally. However, all P2D-IR measurements were done at temperatures higher than 273 K while the reactions are usually carried out around 195 K. The next step is now to perform the P2D-IR measurements at these temperatures. In oder to facilitate these measurements, a cryostat that is compatible with the experimental setup was built. An interesting question to answer will be how the reaction mixtures alter by lowering the temperature. For the complexes between **1** and $SnCl_4$, the FTIR measurements already indicated that species B, for which the structure could not be resolved yet, becomes more populated and therefore probably important. It it also of great interest weather the substrate **1** is still twisted under these conditions.

In the introduction (see Fig. 4.22) the two proposed intermediates for the Et_2AlCl catalyzed Diels–Alder reaction were presented. The question weather Et_2AlCl forms a chelate with **1** as proposed by Evans and co-workers or a di-aluminum species as favored by Santos and co-workers will be capable by P2D-IR measurements at low temperatures. Measurements on this systems will probably have an high impact on understanding the very high observed stereoselectivities in Et_2AlCl catalyzed reactions involving the Evans auxiliary. Also the reaction mechanism involving the Lewis acid BF_3 is of great interest.[226] The comparison of various Lewis acids may facilitate a further improvement of the reactions.

When the P2D-IR experiments at low temperatures are established, the intermediate structures of many reactions become accessible and allow the spectroscopic investigation of the reaction mechanism. An interesting class of catalysts are for example catalysts interacting with the substrate *via* hydrogen bonds such as urea or squaramide based catalysts.[227–235] For most reactions, the proposed intermediates are derived by analogy to metal catalyzed reactions. A selection of reactions and their proposed intermediates are shown in Fig. 10.1. The groups most valuable for identifying the structure are colored. For the systems investigated in this thesis the spectra were only evaluated with respect to the angles between the transition dipole moments. In the case of the proposed substrate–catalyst complexes of the thiourea catalyzed Diels–Alder reaction (see Fig. 10.1),[206] this approach would allow the determination of the conformation of the substrate **1** and also a distinction between the complexes D and E. 2D-IR spectra also contain information about the proximity of vibrations, which can be accessed *via* the coupling between vibrations or the energy transfer.[22] Using this information, P2D-IR spectroscopy can for example also distinguish between the complexes A, B, and C. (see Fig. 10.1). All three complexes are expected to have different coupling constants between the carbonyl vibrations and the N–H vibrations depending on the number of hydrogen bonds. The efficiency of the energy transfer between substrate and catalyst also depends on the hydrogen bonds. Comparing the complexes A and B, the vibrations involving the crotonyl carbonyl will be much stronger coupled to the N–H vibrations of the catalyst in complex A than in complex B. For the vibrations involving the carbonyl group of the oxazolidinone ring it is the opposite. Additionally, in complex A vibrations involving the carbonyl group of the ring are likely to show a fast energy transfer to the vibrations involving the ortho hydrogens (orange) while the other carbonyl group will show a much slower and weaker energy transfer to those vibrations. In contrast to the complexes A and
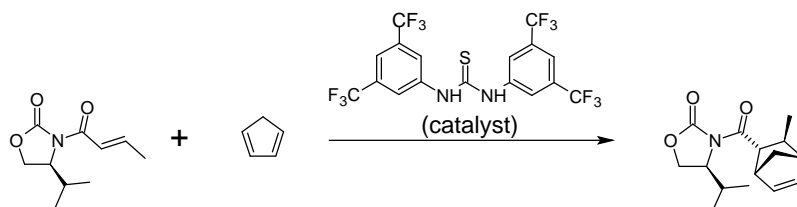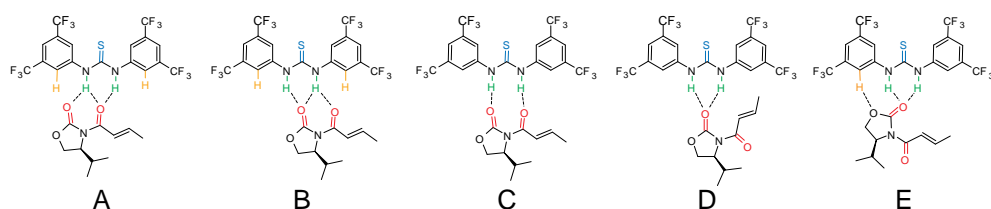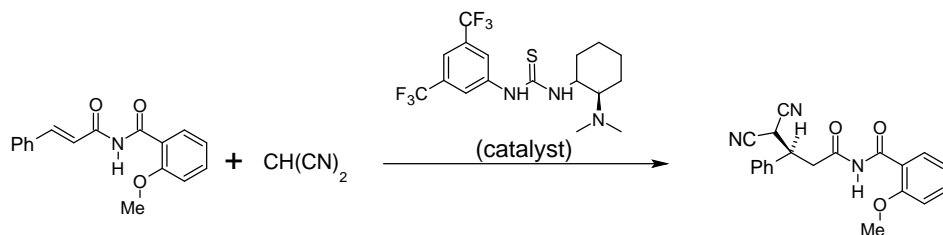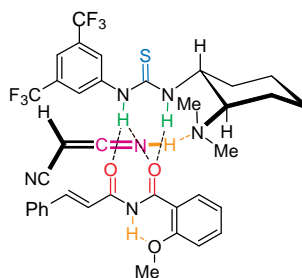
Figure 10.1: *Thiourea catalyzed Diels–Alder reaction and Thiourea catalyzed Michael addition.*[206,227] *The proposed substrate–catalyst complexes might be accessible with P2D-IR spectroscopy. Especially the vibrations involving the colored groups might be valuable for structure determination.*

B, the energy transfer in complex C should be similar, independent of which carbonyl is involved in the vibration.

Low temperatures and an improved setup may also facilitate the detection and structural characterization of ternary complexes consisting of the catalyst and the two reactants (such as the complex proposed for the thiourea catalyzed Michael addition shown in Fig. 10.1).[227] The accumulation of these species to a concentration that gives interpretable spectra is probably most feasible for photo reactions such as photo induced pericyclic reactions (in contrast to Diels–Alder reactions, which are thermally activated). Light triggered reactions are particularly well suited for the investigation with ultrafast spectroscopies, since the reaction can be started with and ultrashort laser pulse and the reaction subsequently probed by any ultrafast technique, such as, e.g., P2D-IR spectroscopy. In addition, an ultrafast T-jump can be used to initiate a reaction and precede the P2D-IR pulse sequence. These "hyphenated" techniques will be discussed in the outlook related to the technique, chapter 10.2.2. Two interesting reactions are shown in Fig. 10.2.[236–238] The analysis of the ground state structure of the substrate in the [2+2] pericyclic reaction and the population of the various conformers will lead to a deeper understanding of the observed selectivities.[237] For the phototriggered Diels–Alder reaction, the structure of the photoproduct, which is the reactant of the subsequent Diels–Alder reaction, is of great interest.[238]

[2+2] Cycloaddition
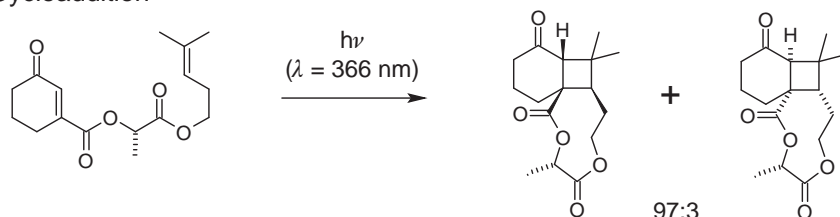
Phototriggered Diels–Alder reaction
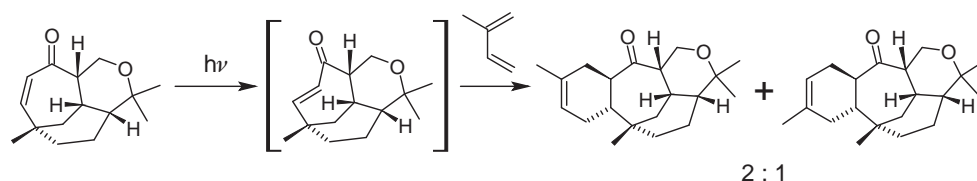
Figure 10.2: *Photoinduced reactions for which the reaction mechanism might be accessible by P2D-IR spectroscopies.*[236–238]

10.2 Structure Determination using P2D-IR Spectroscopy

The present work shows impressively that the determination of the three dimensional structure of small molecules is possible using P2D-IR spectroscopy. Moreover, P2D-IR spectroscopy allows the univocal distinction between the possible conformers of small molecules such as **1**. With the technique and analysis introduced here, the

angles between the transition dipole moments of IR active vibrations can be directly measured. Every molecule has several IR active bands. Thus the angles between the transition dipole moments of all separated bands in a molecule can in principle be measured and used for the structure determination. P2D-IR spectroscopy reaches it limit when the bands of the same molecule start to strongly overlap.

In order to determine the structure of a molecule using the measured transition dipole angles, the orientation of the transition dipole moments with respect to the molecular frame needs to be known. This relationship is not necessarily intuitive because the vibrations normally are not localized on one specific bond, but delocalized. To date, quantum chemical calculations are still needed to link the the transition dipole moments to a three dimensional structure. A comparison of calculated and measured angles then allows the identification of the structure causing the signals in the P2D-IR spectrum. The need to calculate the vibrations of a structure first in order to identify it, limits the accessible structures to the ones one thinks of to be reasonable. To date, a direct structure elucidation only using the P2D-IR spectra without quantum chemistry is not possible. However, in principle the information about the delocalization of vibrations, their couplings and thus the orientation of the transition dipole moments with respect to the molecular structure is included in the diagonal and off-diagonal anharmonicities of the peaks in the 2D-IR spectra.[46] A precise enough measurement of those is highly desired.

The unique feature of the structure determination based on the combined use of P2D-IR spectroscopy and the quantum chemical calculations is the ultrafast time resolution of the measurement. The time resolution in the range from hundreds of femtoseconds to picoseconds enables the resolution species in fast equilibria and their individual analysis. Chemical equilibrium processes are usually slower than this and thus do not interfere with the measurement. Especially due to its high time resolution, P2D-IR spectroscopy is a complementary alternative to NMR spectroscopy for structure elucidation of small molecules in solution. It has been shown that the structure of coexisting species can be retrieved even when some bands of those strongly overlap.

10.2.1   Comparison to NMR

P2D-IR and multidimensional NMR spectroscopy can complement each other very well. Both techniques have their own strengths and limitations, which are compared in the following. Here, only the capabilities with respect to determining the conformation of molecules will be discussed. The determination of the configuration and constitution is not the scope of P2D-IR spectroscopy as it was used in this thesis.

The conformational analysis with NMR is mainly based on the NOE effect, *i.e.*, classifying which nuclei are close to each other and which ones are far apart. With a lot of those constraints it is possible to deduce the structure of a molecule, as it is frequently done to determine the solution structure of proteins. Therefore, NMR is an excellent tool to determine the structure in macromolecules and proteins – targets for which P2D-IR spectroscopy is not able to solve the structure because most of the IR bands overlap. However, if the molecules become small and contain many functional groups reducing the spin density, often only few NOE signals remain. Consequently, structure determination using NMR gets difficult, as it is the case for **1**. Structural details in small molecules, such as twists, cannot always be resolved, because the distances are not measured exactly but only classified in close and far. For **1** for example, both the X-ray structure and the P2D-IR measurements indicate that the

Table 10.1: *Comparison of the features of P2D-IR and NMR spectroscopy for structure determination.*

P2D-IR spectroscopy	NMR spectroscopy
limitations	
- broad overlapping bands	- ms time resolution
- not usable for complete structure analysis of large molecules & proteins	- difficult for small, highly functionalized molecules
- experimentally advanced, under development	- limited sensitivity
- quantum chemical calculations necessary	- indirect distance information
advantages	
- high selectivity and sensitivity	- well established
- direct angle measurement	- usable as black box
- usable for highly functionalized molecules	- detailed information content
- usable for molecules with short lifetimes	- usable for large molecules & proteins

molecules are twisted. The measured NMR spectra provide no information about that, while P2D-IR spectroscopy is in particular sensitive to twists since primarily the angles are measured and evaluated.

As already mentioned before, the ultrafast time resolution is an unique feature of P2D-IR spectroscopy making it to an ideal tool to investigate the structure of intermediates and short-lived species. The inherent time resolution of NMR spectroscopy is in the range of ms. This means that all species that interconvert or react faster cannot be resolved by NMR. This is the main reason, why the minor species of the Lewis acid complexes could not be observed in the NMR spectrum. Actually most of the equilibrium processes are faster than milliseconds such as diffusion, rotation, isomerization around single bonds, complexation, and dissociation. Thus structure determination of mixtures in equilibrium is difficult and sometimes even impossible with NMR. Short lived intermediates are also not accessible.

Despite the limitations, there are many reasons, why NMR is widely used for structure determination. First of all, NMR spectra contain a lot of information on an atomic level. To mention only a few, the shifts of the individual nuclei are sensitive on the surrounding, the couplings reveal information about the connectivity of the individual atoms as well as the angles between bonds, and the NOE reports about the inter-space distances. Moreover, NMR spectroscopy is well established, NMR spectrometers are commercially available, and can (in most cases) be used as a computer controlled black box. Using existing models, the structure of the molecules can in many cases be directly retrieved without the need for more elaborate theory such as quantum chemical calculations. The P2D-IR setup is in the sense of user friendliness the direct opposite. It is, besides the 800 nm Laser and the diffractive spectrometer, home-built, experimentally advanced, still under development, and difficult to handle.

The limitations and capabilities of the the two techniques are summarized in Table 10.1. The specific properties of them define their application, *e.g.*, P2D-IR is predominately useful for very small molecules while NMR is very powerful for large substances. They complement each other more than they compete against each other.

10.2.2 Outlook

P2D-IR spectroscopy is proven to be a powerful technique for conformational analysis. It has the potential to become an integral part of organic chemists' toolbox for structure determination and the elucidation of reaction mechanisms.

However, many things can still be improved from the experimental side. Even conceptionally straight forward upgrades of the experiment will have a significant impact. The data collection for one set of spectra (*i.e.*, one complete P2D-IR measurement or a measurement of the time dependent anisotropy of four peaks) typically took around 20 hours. The use of a laser with a higher repetition rate will reduce the measurement time significantly. The implementation of a commercial laser system running at 10 kHz instead of 1 kHz will speed up the measurement by a factor of 10 – maintaining the same signal-to-noise ratio. Increasing the amount of pixels of the MCT array detector and adopting the grating of the spectrometer accordingly would allow the measurement of the entire P2D-IR spectra in one block rather than measuring them subsequently in four blocks, which need to be merged afterwards. This would save measurement time (more than a factor of 2) and avoid artifacts that can arise from merging several spectra. With only these two straight forward improvements, the measurement time for a complete P2D-IR spectrum can be reduced by a factor of 20! Or alternatively, investing the same measurement time, this two implementations would reduce the noise by a factor of larger than 4.

The signal size scales linearly with the power of the pump pulse and therefore also an increase in the mid-IR power will increase the signal-to-noise or alternatively reduce the measurement time. The high-power OPA, used, *e.g.*, in the measurements described in part III of this thesis, generates approximately three times more mid-IR power. Maintaining the same signal-to-noise, this high-power OPA would reduce the measurement time by another factor of 9. Implementing all improvements leading to a faster measurement time, the data collection of the spectra with the same quality would only need less than 10 minutes instead of 20 hours!

The much faster data collection will facilitate the measurement of two samples directly after each other, without any changes to the setup. This enables to subtract one spectrum from each other without inducing significant artifacts. Hence, mixtures can be much easier analyzed when one or more species can be measured on its own. In Diels–Alder reaction mixtures like investigated here, the spectrum of **1** could for example be completely extinguished and only the substrate catalyst complexes are left in those double difference spectra. Or the spectrum of the complex at very high $SnCl_4$ concentrations could nicely be isolated. The double difference spectra will have a great impact on identifying intermediate structures in real reaction mixtures, in particular if one measures the spectra of the reactants and products individually and deletes them from the P2D-IR spectra measured during the course of the reaction. Changes in the solution could be followed online by P2D-IR spectroscopy, similarly to what is done with FTIR nowadays.

In addition to reducing the measurement time, increasing both, the time resolution and the spectral resolution of the experiment is a key step to improve the method. In the experiment as it was used in this thesis, the shape of the pump pulse set the limit of how close pump and probe pulse can be in time without overlapping. This time was around 1.2 ps to 1.5 ps, depending on the order of the Fabry–Perot. During this time rotational diffusion already occurs making it necessary to measure the time dependence of the anisotropy and extrapolating it to zero delay time. Reducing this time significantly such that rotational diffusion has only negligible effects, P2D-IR

spectra with only one single delay time would be enough to determine the angles between the transition dipole moment (using the annihilation method) to a very high accuracy – comparable to the accuracy achieved by the anisotropy method. A beneficial side effect of reducing the delay time (also referred to a s population time) is that also vibrational relaxation has less effect and thus the signals will be roughly 30% larger. In principle, the delay time can be reduced to around 200 fs to 300 fs, twice pulse length of the mid-IR pulses generated by the OPA, by replacing the Fabry–Perot.

There are two possibilities to do so that are conceptionally different. One is to replace the (in frequency-domain) Lorentzian shaped narrowband pump pulse by, *e.g.*, a Gaussian shaped pump pulse generated in a pulse shaper.[53] In the time-domain this pulse is also Gaussian shaped and thus much shorter than the pulse generated by the Fabry–Perot Etalon. Changing the shape of the narrowband pump pulse allows to reduce the delay time while keeping the possibility of measuring cuts through the spectrum, *e.g.*, fixing the pump wavenumber and measuring many different time delays. In addition to the time resolution, also the spectral resolution is (moderately) enhanced by using Gaussian shaped pump pulses instead of Lorentzian shaped pump pulses since the tails of the pulses are more confined.[53]

The alternative approach to improve the time resolution and at the same time the spectral resolution significantly is to replace the narrowband pump pulse with a pulse pair.[53,87,88] The minimal time delay for this kind of measuring the 2D-IR spectra is limited by the pulse length of the mid-IR pulses of the OPA. The spectral resolution along the pump axis is defined by how many different time delays between the pulse pair (commonly referred to as coherence time) are measured.[46] The difference in spectral resolution compared to the pump-probe approach using the Fabry–Perot is immense and would, *e.g.*, definitely help to characterize the minor complex species of **1** in more detail. However, this method has two main drawbacks. First, it is not possible to measure cuts through the 2D-IR spectrum. This would actually not harm if the P2D-IR spectra are collected at a short population time, since the time dependence of the peak anisotropies is not required anymore and all important information can be retrieved from a single P2D-IR scan. Secondly, measuring a complete P2D-IR spectrum takes longer than using a narrowband pump pulse. How much it takes longer depends on the desired spectral resolution. Using a photon echo setup instead of the collinear pulse pair would basically be equivalent.[87,88]

The decrease of measurement time and the higher spectral resolution achievable will pave the way for many applications of P2D-IR spectroscopy. Basically, structure determination of intermediates with P2D-IR spectroscopy could be used as probing technique wherever FTIR is used nowadays to detect intermediates. P2D-IR spectroscopy might even be more sensitive than FTIR because as a consequence of having two axes the peaks are usually better resolved.[46] The combination with other techniques will make P2D-IR spectroscopy even more versatile. Some possible "hyphenated" techniques and their potential impact are exemplified in the following:

The combination of a *UV/VIS pulse* with 2D-IR spectroscopy has already been established.[38,55,60,239,240] As already mentioned before, the UV/VIS pulse can be used to start a reaction. By changing its time delay to the P2D-IR sequence, the kinetics and structure of the intermediate can be investigated simultaneously. The combination of an *ultrafast temperature jump* with P2D-IR spectroscopy is possible, too.[241–243] This combination may allow probing the reaction mechanism of thermally activated reactions, such as Diels–Alder reactions. The temperature jump would in

analogy to the UV/VIS pulse facilitate a reaction. The combination of P2D-IR spectroscopy with an *IR-UV/VIS double-resonance* pulse sequence, also designed during my PhD studies, could be very valuable. The idea behind the IR-UV/VIS double resonance experiment is that the UV/VIS pulse is only absorbed by the molecule if it absorbed an IR photon before.[244,245] Thus the IR absorption spectrum can be used for selecting which molecule in a mixture will absorb the UV/VIS photon and react afterwards. Using this technique it may be possible to control which species (*e.g.*, conformer) reacts and a combination with P2D-IR spectroscopy will give insights to the relationship between the conformers and the products and may identify the important intermediates.[246]

Part III

Conformational Dynamics of Proteins
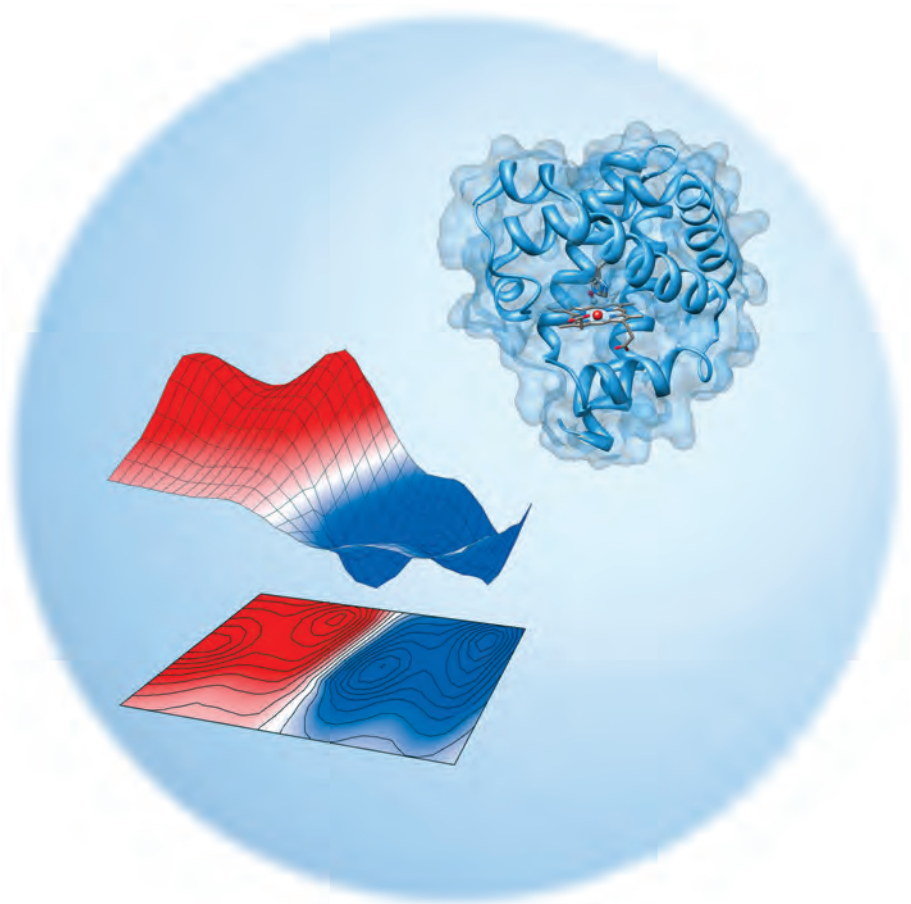
Chapter 11

Motivation

The function of a protein is related to both its structure and its dynamics. [247] It is well accepted nowadays that proteins would not be functional if they were completely rigid. It is also well known that proteins generally can adopt more than one conformation. Some proteins can, *e.g.*, form fibrils or prions, both of which are misfolded proteins (*i.e.*, proteins in a non-native conformation), which sometimes lead to diseases such as Alzheimer's disease or Creutzfeldt-Jakob disease. In solution, proteins do not exist in a single conformation; instead an ensemble of various, interconverting states exist. [248,249] Often a protein adopts various conformations during its reaction cycle. An illustrative example is myoglobin (Mb). In its crystal structure, there is no open passage from the heme, where Mb binds and stores oxygen, to the outside of the protein. [250] Thus Mb needs to change its conformation to facilitate the transport of oxygen from the solution to the heme or *vice versa*. [247,249,251]

It is also important to know the the surrounding of a protein. The solvent or membrane surrounding a protein strongly influences its the structure and also its dynamics. Therefore, protein dynamics cannot be understood completely without taking into account the influence of the solvent (*i.e.*, water): in addition to stabilizing some conformation, the solvent provides thermal energy through collisions with the protein and dissipates excess energy produced during a reaction.

The structure determines the degrees of freedom and the conformational space that can be sampled by the protein. There are flexible parts that can adopt many possible conformations and rigid parts that do not move a lot. Each protein conformation has a distinct energy. These energies can be summarized in an energy landscape. [247,252,253] The energy landscape of a protein is structured by barriers separating more or less defined minima. High barriers separate taxonomic states. [247] These states can be fully characterized. Lower barriers subdivide the areas of the taxonomic states further and further into different substates. Because these many substates interconvert rapidly and their populations are low, they cannot all be fully characterized. According to Frauenfelder and co-workers, the energy landscape is not an inherent property of the protein, but is influenced significantly by the solvent. [252–255] In their model, the energy landscape is structured into tiers of different order. The top tier, CS0, corresponds to the taxonomic states. In Mb these states are called A_0, A_1, and A_3. The subsequent tiers are structured based on the rates that have been observed for the interconversion between the different states of this tier. [256] The faster the exchange rate is, the higher the order of the tier. Since the rates are temperature dependent, the definition of the tiers may be temperature de-

pendent as well. Frauenfelder proposed that the first three tiers CS0, CS1, and CS2 are important for function.[253,256] In Mb, the interconversion between the states of CS1 are determined by the fluctuations in the hydration shell of a protein and the exchange dynamics within CS2 by the fluctuations in the bulk solvent.[254] The rates of these processes are dominated by the solvent or, in other words, slaved to the solvent dynamics.

The motivation for studying the conformational dynamics of Mb in this thesis is to gain a deeper insight into the relationship between protein dynamics, structure and solvent properties. The investigations are driven by questions such as:

- Which structural changes are needed for the protein to move from one state to another?

- What factors determine, influence, or limit protein dynamics?

- Is there a dominating factor? Are the dynamics caused by the protein or imposed by the solvent?

- How fast can conformational changes in a protein be? Where is the speed limit and what defines it?

- Is it possible to reach the maximal rate for a particular protein reaction by increasing the temperature before the protein denatures?

- If slaving occurs, how fast can protein slaving be? So far, slaving has to our best knowledge only been shown for dynamics slower than nanoseconds.[254] Is there also slaving on a picosecond time scale?

11.1 Kinetic Models

In the following sections, some of the models describing the the temperature dependence of reaction rates will be briefly introduced. They will be used for the discussion the measured data in chapter 12.

11.1.1 Arrhenius Relation[257,258]

The temperature dependence of reaction rates is most commonly described by the Arrhenius equation. Arrhenius observed in gases that the reaction rates k become faster by increasing the temperature T and formulated the relationship:

$$k = Ae^{-\frac{E_a}{k_b T}}. \tag{37}$$

The equation is from its origin purely empiric. For gases, the pre-exponential factor A can be understood as number of collisions per time. This factor is also often called frequency factor. Its value is typically smaller than 10^{18}. The exponential term describes the probability, how many collisions lead to a reaction. E_a can be interpreted as activation energy. In the case of gases it describes how much kinetic energy the particles need to have in order to react. Usually it is assumed that the frequency factor and the activation energy are temperature independent, which is often true for a limited temperature range. Arrhenius-like behavior is often observed in condense phase, too.

11.1.2 Transition State Theory[257–260]

Transition state theory is one example how the reaction rates and their temperature dependence can be derived theoretically. Here, only the basic assumptions shall be summarized. Transition state theory assumes that there exists an activated complex, a small energy minimum at the top of the energy barrier between reactants and products. The activated complex is in equilibrium with the reactant(s). For forming the product(s), the activated complex needs to cross the very small barrier in order to decay. The rate for crossing this barrier is given by the vibrational frequency of the activated complex along the reaction coordinate. When putting everything together for a bimolecular reaction, the Eyring equation is obtained:

$$k = c\frac{k_b T}{h}e^{-\frac{E_a}{k_b T}}.$$ (38)

The constant c contains all additional constants such as the transition probability from the activated complex to the product(s) and the partition functions of the reactants and the activated complex. E_a is the free Energy difference between the reactants and the activated complex, k_b and h are the Boltzmann constant and Planck's constant, respectively. In contrast to the Arrhenius relation, the prefactor here is temperature dependent.

11.1.3 Super-Arrhenius Relation

For dynamics in glasses, supercooled liquids and proteins it was observed that the dynamics do not behave Arrhenius-like, but follow the relationship:[261–264]

$$k = Ae^{-\frac{E_a}{k_b T^2}}.$$ (39)

It is also used, if an evaluation according to Arrhenius leads to much too high frequencies in the pre-exponential factor.[263] This experimental relationship was also theoretically investigated.[265,266] However, in the present thesis it will be treated as an empirical relationship.

11.1.4 Kramers Theory[260,267,268]

Kramers theory is based on the on a classic particle moving on a double well potential. One well describes the reactants, the other one the product state. The movements of the particle are driven by fluctuations (Brownian motion) and influenced by friction. In the case of strong friction, one obtains Kramers equation for the overdamped regime:

$$k = \frac{A}{\gamma}e^{-\frac{E_a}{k_b T}}.$$ (40)

The prefactor A contains information of the curvature of the potential and γ denotes the friction in the system. The energy barrier between the two potential wells is given by E_a. The friction γ is often interpreted as arising from the dynamic viscosity $\eta(T)$ of the solvent, which itself is temperature dependent. Hence, Kramers equation is regularly formulated as:

$$k = \frac{A'}{\eta(T)}e^{-\frac{E_a}{k_b T}}.$$ (41)

The (modified) Kramers equation clearly shows the influence of the solvent on the reaction rates. If the energy barrier between the two states is small, the temperature dependence of the exponential term vanishes. The temperature dependence of the prefactor, *i.e.*, the solvent viscosity, consequently dominates temperature dependence of the reaction rates. This is also the case, if the energy barrier E_a is dominated by the entropy and thus the contribution of the enthalpy is negligible. E_a then scales approximately linearly with the temperature (Gibbs equation).

The term slaving, which used to describe the dependence of protein dynamics on the solvent viscosity, describes exactly the case when the temperature dependence of the exponential term becomes negligible.

11.2   Myoglobin

Myoglobin (Mb) is a globular protein consisting of eight alpha helices and has with its 153 amino acids a molecular mass of $\approx 17\,\text{kDa}$. The structure is illustrated in Fig. 11.1.[269] It is mainly found in muscle tissue and is responsible for oxygen transport and storage. The oxygen is bound to a heme, the prosthetic group of Mb. Other small ligands such as carbon monoxide (CO), nitric oxide (NO), and cyanide (CN) also bind to the heme of Mb. The binding of these ligands is also biologically relevant because those ligands are endogenous poison. CO binds ~ 40 times stronger to Mb and thus blocks the binding site for the storage and transport of oxygen.

Due to its high natural abundance and its properties it is the best studied protein. This is the reason why it is also named "The hydrogen atom of biology".[248] The first crystal structure of Mb was measured in 1958.[250,270] It was the first crystal structure of a protein. There is no open channel in the static structure of Mb through which the ligands could diffuse from solution to the binding site. Thus, structural fluctuations are necessary for ligand uptake and release.[248,249] The mechanism of release of CO is fairly well understood nowadays.[247,249,251,271] Carbonmonoxy myoglobin (MbCO) is preferred for these studies due to its stronger binding to the heme, the possibility to photolyze the CO from the heme with UV/VIS light, and the fact that CO (in contrast to O_2) can be detected by FTIR spectroscopy. Three taxonomic states of Mb can be distinguished based on the IR spectrum: A_0, A_1, and A_3.[272] A_1 is the dominating species at pH = 7. The corresponding structures of A_0 and A_1 are known. The assignment of these structures was proven by quantum chemical calculations, crystallography, and additional studies investigating, *e.g.*, the pH dependence of the Mb spectra.[269,273–276]

The main difference between the two structures is that in A_0 the distal Histidine (His64) is protonated and points into the solvent. In A_1 the distal histidine is in its neutral form and points towards the binding site. The hydrogen that is bound to N^ϵ interacts with the ligand *via* a hydrogen bond. The origin of A_3 is less clear though.[274] FTIR studies indicate a stronger interaction between the distal histidine and CO ligand because of its band position. Thus it is proposed that the histidine points more towards the binding site (see Fig. 11.1).[269,274] Crystallographic studies found an additional Xe docking site compared to state A_1.[40,277] Since this docking site is located on the opposite side of the heme, it is proposed that A_1 and A_3 differ not only by the His64 orientation but on a larger scale, *e.g.*, the alignment of the α-helices. This interpretation is also supported by recent quantum chemical calculations, pressure release experiments and crystallographic studies of the Mb mutant L29W.[261,263,274,278]
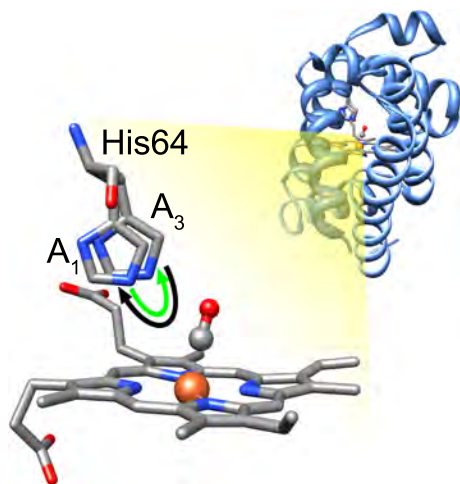
Figure 11.1: *Crystal structure of carbonmonoxy myoglobin (pdb: 1a6g).*[269] *The active site containing the the heme, the distal histidine and the complexed carbonmonoxide are enlarged. The states A$_1$ and A$_3$ are assumed to differ by the orientation of the distal histidine.*

The dynamics of the interconversion of the taxonomic states of Mb were subject of many investigations.[247,274] Flash photolysis studies and temperature derivative spectroscopy at cryogenic temperatures used the different rebinding rates of the two states to investigate the dynamics between them.[263] Pressure release experiments monitored the exchange process below 200 K.[261,263] At room temperature a 2D-IR vibrational echo experiment has investigated the exchange for the Mb mutant L29I.[40,42] Additionally MD simulations have been applied.[279] In the following, the results and conclusions of some of the studies shall be introduced in more detail.

The data obtained by Johnson *et al.* using flash photolysis and by Iben *et al.* using pressure release are illustrated in Fig. 11.2.[261,263] For their measurements, sperm whale Mb was dissolved in a glycerol-potassium carbonate buffer (pH = 11) mixture (75%/0.25% volume/volume (v/v); weight proportion $w \approx 0.8$). Since an Arrheinius fit to the data led to unphysically large preexponential factors ($\approx 10^{31}\,\text{s}^{-1}$), they used the Super-Arrhenius relation (which they called Ferry relation) to fit the data.[263] For the overall exchange between A$_1$ and A$_3$ they found a preexponential factor of $A_F = 10^{16.4\pm1.4}\,\text{s}^{-1}$ and an energy barrier of $E_F = 9.9 \pm 0.4\,\text{kJ/mol}$. Using the Ferry relation worked fine for the exchange between A$_1$ and A$_3$ and also for the exchange between A$_0$ and A$_1$ + A$_3$ at temperatures below 270K. The two data points above (see Fig. 11.2 filled squares) deviate from the fit and show some kind of saturation effect. Johnson *et al.* supposed that this deviation could be caused by protonation-deprotonation becomming rate limiting or by couplings to the solvent dynamics. For the exchange between A$_1$ and A$_3$ no flattening of the temperature dependence was observed. Extrapolation of the fit to higher temperatures predicts overall exchange rates of $k_{obs}(0\,^\circ\text{C}) \approx 10^{8.3}\,\text{s}^{-1}$, $k_{obs}(20\,^\circ\text{C}) \approx 10^{9.3}\,\text{s}^{-1}$, and $k_{obs}(40\,^\circ\text{C}) \approx 10^{10.2}\,\text{s}^{-1}$.

Fenimore *et al.* set the conformational dynamics in relation to the temperature dependence of the solvent viscosity, more precisely to the temperature dependent dielectric relaxation rate coefficient $k_{diel}(T)$.[254] They found that the conformational dynamics as well as other processes such as ligand binding show the same temperature
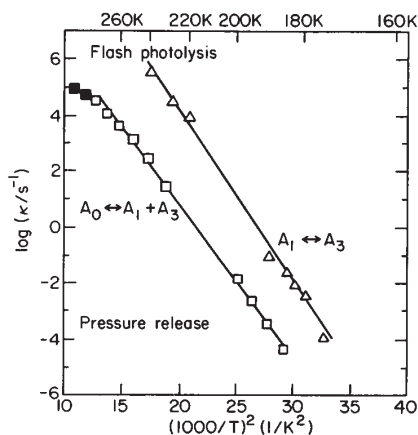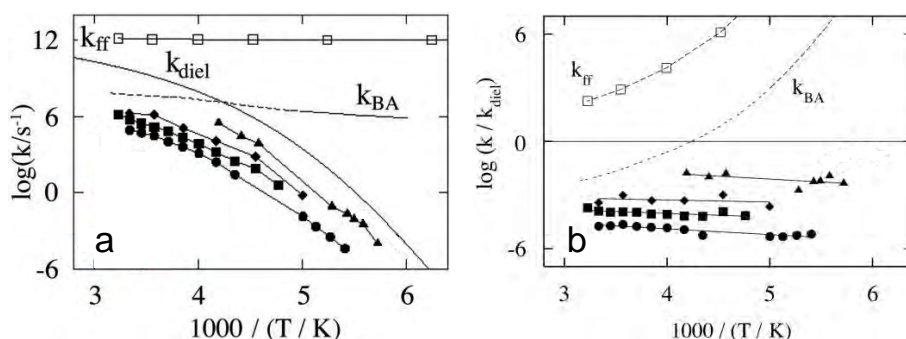
Figure 11.2: *Temperature dependence of the exchange rate between the taxonomic states A_1 and A_3 (triangles) and between the taxonomic states A_0 and $A_3 + A_1$ (squares) of MbCO at low temperatures. Reproduced with permission from [263], copyright 1996, Elsevier.*

dependence (see Fig. 11.3).[254] Their conclusion from this comparison is that the protein dynamics are slaved to the solvent dynamics. For the exchange between A_1 and A_3, which is the fastest process addressed by Johnson *et al.*, the difference between an Arrhenius (or Super-Arrhenius) type behavior and being slaved to the solvent is not obvious because the experimental data points (triangles) follow approximately a straight line in the Arrhenius plot shown in Fig. 11.3 a. Extrapolation based on the relation to $k_{diel}(T)$ to higher temperatures predicts overall exchange rates of $k_{obs}(0\,^\circ\text{C})$ $\approx 10^{6.8}\,\text{s}^{-1}$, $k_{obs}(20\,^\circ\text{C}) \approx 10^{7.6}\,\text{s}^{-1}$, and $k_{obs}(40\,^\circ\text{C}) \approx 10^{8.0}\,\text{s}^{-1}$ for the same solvent, *i.e.*, glycerol-buffer mixture (75%/0.25% v/v). For other solvents, *e.g.*, neat buffer, the rates are expected to deviate.

Figure 11.3: *a: The temperature dependence of the exchange rate between the taxonomic states A_1 and A_3 (triangles) and between the taxonomic states A_0 and $A_3 + A_1$ (circles) of MbCO is compared to the temperature dependence of the dielectric rate constant k_{diel}. The other data points reflect CO release (filled squares), equilibrium fluctuations after hole burning (diamonds) and dephasing of of the CO stretching mode (open squares, labeled with k_{ff}). These data points as well as the rebinding rate k_{BA} will not discussed here. b: Temperature dependence of the ratio k/k_{diel} of the data shown in Fig. a. Both figures were adapted with permission from [254], copyright 2002, National Academy of Sciences, USA.*

11.2.1 2D-IR Spectroscopy of Myoglobin

2D-IR spectroscopy on the amide I and II bands of Mb was used to understand spectral features of proteins mainly containing α-helices.[280–282] The spectral properties of the B states of Mb, the initially formed states after CO photolysis were investigated using transient 2D-IR exchange spectroscopy of the carbon monoxide bands. [283]

Fayer and co-workers used 2D-IR vibrational echo spectroscopy to investigate the switching between A_1 and A_3 in carbonmonoxy L29I myoglobin (L29I MbCO).[40,42] The 2D-IR spectra for various delay times are reproduced in Fig. 11.4. [42] Note that the axes are interchanged compared to the convention used in this thesis. In Fig. 11.4 the x-axis is the pump axis (ω_τ) and the y-axis the probe axis (ω_m). The color code is also inverted compared to the convention used in this thesis. Red corresponds here to signals originating from the 0–1 transitions and blue to signals caused by the 1–2 transitions. When comparing the spectra two major changes become visible. With increasing delay time, the intense diagonal signals change become rounder with increasing delay time. This change reflects spectral diffusion, *i.e.*, conformational fluctuations within one state. Additionally, cross peaks occur with increasing waiting time. The occurrence of cross peaks is due to the conformational switching between A_1 and A_3.
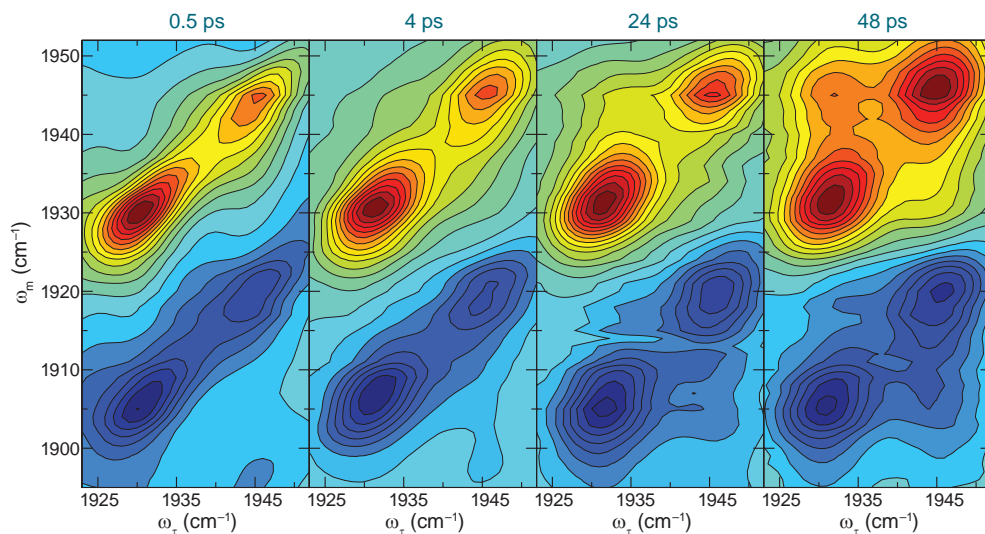
Figure 11.4: *EXSY-2D-IR spectra of L29I MbCO at room temperature. Reproduced with permission from [42], copyright 2009, Annual Reviews. Note that pump and probe axis are interchanged compared to the convention used in this thesis. The color code is inverted, too.*

In order to obtain rate constants, Fayer and co-workers fitted the spectra and extracted the volumes of the individual peaks. These volumes correspond to populations and are shown in Fig. 11.5. [40,42] The lines show fits to the data. The fit of the time dependence is based on following assumptions: The relaxation time of the signals in the broadband IR pump-probe spectra is equal to the vibrational relaxation time constant of the corresponding states. Thus, the vibrational relaxation time constants can be measured independently and are not part of the fit. This assumption is only true if the states do not exchange and the effects of this assumption are discussed in detail in chapter 12.3. Additionally, rotational diffusion was neglected. Based on

these assumptions they fitted only one exchange rate. The fitted model consists of the relaxation time constants $T_1(A_1) = 25$ ps and $T_1(A_3) = 19$ ps and the exchange rate $t_{ex} = 47 \pm 8$ ps. In contradiction to the stated model, the diagonal signals in Fig. 11.5 decay with an overall time constant smaller than 9 ps, much faster than their model reveals (17.4 ps and 14.3 ps).
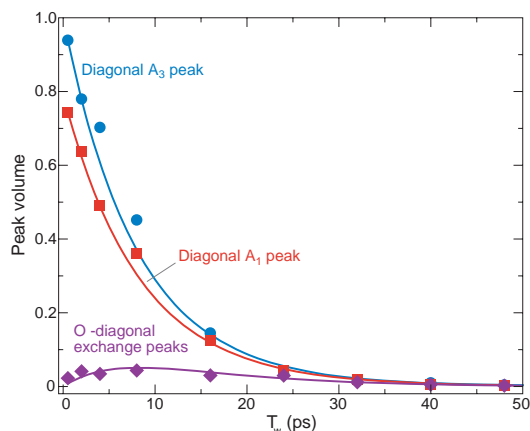
Figure 11.5: *Time dependence of the peak volumes in the EXSY-2D-IR spectra shown in Fig. 11.4. The lines are fits to the experimental data. Reproduced with permission from [42], copyright 2009, Annual Reviews.*

In their publication Fayer and co-workers state that the measured exchange time of 47 ± 8 ps is different but consistent with the extrapolation based on the Super-Arrhenius relation proposed by Johnson *et al.* In an additional study, Fayer and co-workers investigated the exchange of A_1 and A_3 in the double mutant T67R/S92D Mb and obtained an exchange time constant of 76 ± 10 ps using the same fit procedure. [284]

11.2.2 Scope of this Work

The scope of this work is to investigate the temperature dependence of the conformational dynamics between A_1 and A_3 in the temperature range between $0\,°C$ and $40\,°C$. This should give additional insights into the mechanism and allow a discrimination between the models proposed by Johnson *et al.* and Fenimore *et al.* The focus will be on L29I MbCO, the mutant which was also subject of the study by Fayer and co-workers. L29I MbCO has the advantage compared to wild type MbCO that A_1 and A_3 are similarly populated. In addition to L29I MbCO, also the spectra for sperm whale MbCO (wild type) and its mutants V68W, L29W, and the triple mutant L29Y H64L V68T (YLT) were collected. The band positions for wt MbCO, L29I MbCO, and V68W MbCO are very similar; only the band intensities differ. [40,276,285] The band positions of L29W MbCO are shifted to higher wavenumbers. [276,278,286] In contrast to the other mutants, the crystal structures of the taxonomic states are known for L29W MbCO. [278]

Chapter 12

L29I Myoglobin

12.1 EXSY-2D-IR Spectroscopy
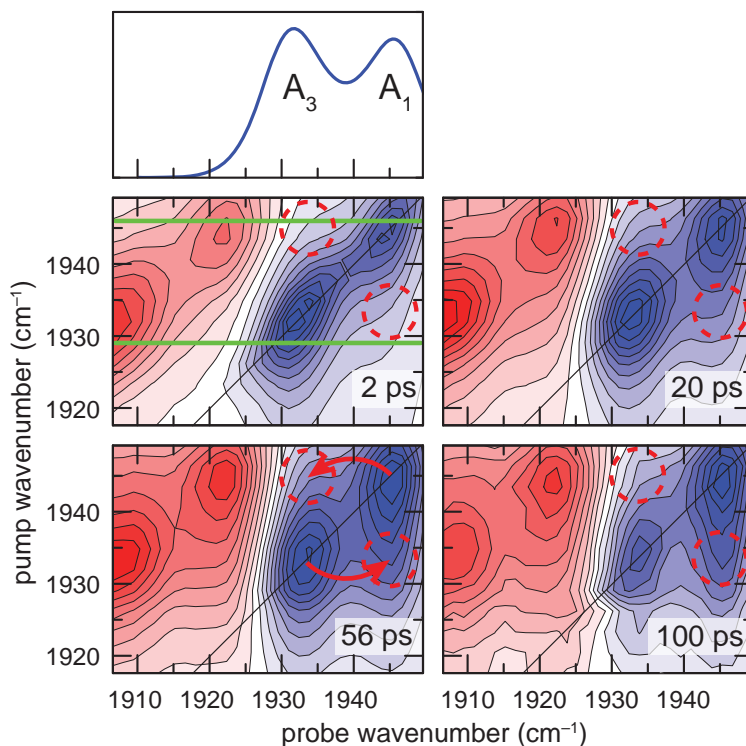
Figure 12.1: *EXSY-2D-IR spectra of L29I MbCO at 20°C for various delay times. The individual spectra are scaled to the maximal intensity. Red dashed circles indicate the position of the cross peaks and the two green lines highlight where cuts were measured (see Fig. 12.2). The FTIR spectrum is shown in the top panel for reference.*

The EXSY-2D-IR spectra of L29I MbCO are shown in Fig. 12.1 for the delay times of 2 ps, 20 ps, 56 ps, and 100 ps. The corresponding FTIR spectrum is displayed in the top panel for reference. L29I MbCO shows two CO absorption bands, one

at $\approx 1932\,\mathrm{cm}^{-1}$ (A_3) and one at $\approx 1945\,\mathrm{cm}^{-1}$ (A_1). At a delay time of 2 ps, only diagonal peaks were observed. They are elongated along the diagonal, indicating spectral inhomogeneity of the bands. This inhomogeneity disappears for longer delay time and is already absent at 20 ps. The peaks are not tilted anymore but upright. In addition, cross peaks appear with increasing delay time. The positions of those are indicated by the red dashed circles. The relative intensity at these positions raises from 2 ps, where almost no intensity is observed to 100 ps where the cross peak marked by the low right circle is of similar intensity as the corresponding diagonal peak with the same pump wavenumber (A_3). Because the spectra were measured using a frequency-domain setup, the peaks are elongated along the pump axis. This causes that the cross peaks are not resolved from the diagonal peaks at the same probe wavenumber and only appear as shoulder of the peak. This is different to the spectra measured by Fayer and co-workers (*cf.* Fig. 11.4) using a time-domain experiment in the BOXCARS geometry. [40] Besides this, the two sets of spectra are qualitatively the same for the same time delays. Our measurements exceed the time range measured by Fayer and co-workers by a factor of two.

12.1.1 Cuts

For the evaluation of the population dynamics, cuts through the EXSY-2D-IR spectra were measured for many delay times. The positions of the cuts are indicated by the green lines in Fig. 12.1. The lower cut is referred to as pump 1, the higher cut as pump 2. Figure 12.2 (left) shows the cuts for delay times between 2 ps (red) and 100 ps (blue) in the top and middle row. The positions of the narrowband pump pulses are indicated by the black arrows (top: pump 2; middle: pump 1). At the bottom,
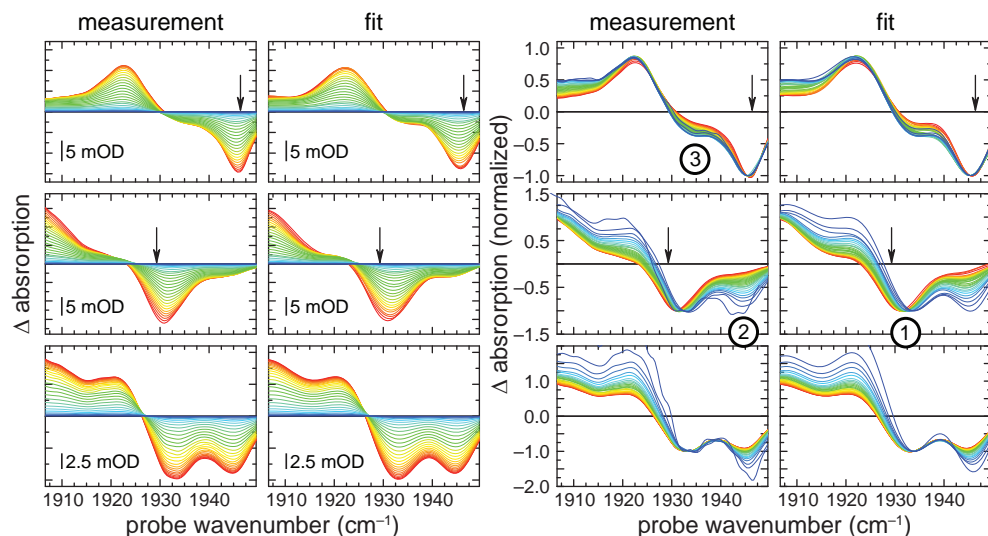
Figure 12.2: *Cuts through the EXSY-2D-IR spectra (top and middle) and broadband pump-probe spectra (bottom) of L29I MbCO. The positions of the narrowband pump pulses are indicated by the black arrows. Left: Absolute intensity spectra. Right: Spectra normalized to the intensity of one band. The time delays were varied from 2 ps (red) to 100 ps (blue). The fits of the spectra (see chapter 19.1) are shown next to the measurement. Numbers see text.*

the broadband pump-probe spectra for the same delay times are shown. Delay times smaller than 2 ps were not evaluated as pump and probe pulses overlap in the EXSY-2D-IR measurements. The measured spectra were fitted by four Gaussians according to the routine described in chapter 19.1 (appendix). The fits are displayed next to the measured spectra. In the unscaled spectra, the decrease of the signal size due to vibrational relaxation (T_1 relaxation) dominates the time evolution. In order to (mostly) eliminate the intensity changes caused by relaxation, the scaled spectra are shown on the right side of Fig. 12.2. The EXSY-2D-IR cuts were scaled to the initially excited band, the broadband pump-probe spectra to the band belonging to A_3. In the EXSY-2D-IR cuts two processes become nicely visible: spectral diffusion within one state and exchange between the two states A_1 and A_3. Spectral diffusion leads to a shift of the band position, most evident at position 1 in Fig. 12.2 for the band of A_3. The exchange becomes apparent in the increase of both cross peaks in the scaled EXSY-2D-IR cuts (see Fig. 12.2, pos. 2 and 3). It is important that both cross peaks increase. If only one would increase and the other decrease, it would be likely that this effect is caused by different relaxation rates of the bands. This is not the case here.

The unscaled band areas in the pump-probe spectra (both, narrowband and broadband) resemble the populations of the excited vibrations. Thus, the time evolution of the band areas resembles the population dynamics of the states and can be used to investigate the exchange dynamics in the protein.

12.2 Population Dynamics

In order to analyze the population dynamics measured by the pump-probe spectra, a simple model is assumed to describe the exchange between the two states A_1 and A_3 in Mb. The model is depicted in Fig. 12.3. It involves the populations of vibrationally excited carbon monoxide in the two conformational states of the protein (A_1 and A_3), their vibrational relaxation time constants (T_1), and their exchange time constants (t_{ex}). The populations $[A_1]$ and $[A_3]$ are given by the differential equations:

$$\frac{d}{dt}[A_1] = -\frac{1}{T_1(A_1)}[A_1] - \frac{1}{t_{ex}(A_1)}[A_1] + \frac{1}{t_{ex}(A_3)}[A_3] \tag{42}$$

$$\frac{d}{dt}[A_3] = -\frac{1}{T_1(A_3)}[A_3] - \frac{1}{t_{ex}(A_3)}[A_3] + \frac{1}{t_{ex}(A_1)}[A_1], \tag{43}$$

and the start populations $[A_1]_0$ and $[A_3]_0$.
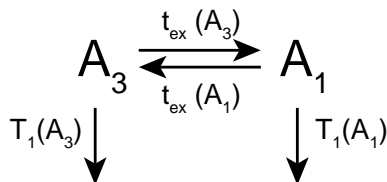
Figure 12.3: *Model for the exchange process in Mb, i.e., the conformational dynamics. Only the vibrational excited molecules are considered.*

The signal sizes of the bands are proportional to the product of the population and the transition dipole moment of the vibrations. Here we assumed that the transition

dipole moments of the CO vibration in both conformational states of MbCO are equal ($\epsilon_{rel} = 1$). Thus, the signal size of the bands are directly proportional to the populations with one scaling factor for each set of spectra (pump 1, pump 2, and broadband). Using this model, the band areas (fitted) of all spectra were fitted simultaneously. The equilibrium constant $K = t_{ex}(A_1)/t_{ex}(A_3)$ was deduced from the fit of the FTIR spectrum (see Fig. 12.6) and and used as input for the fit. It was 0.904 for the measurements at $20\,°C$. The details of the population fit are described in chapter 19.2 (appendix). Figure 12.4 shows the fitted curves in comparison to the band areas. The obtained time constants for exchange and relaxation are summarized in the model next to the curves.

The CO vibrations in the conformational states A_3 and A_1 relaxed with time constants of $19\,ps \pm 3\,ps$ and $17\,ps \pm 3\,ps$, respectively. The time constants for the exchange between the process were $87\,ps$ ($t_{ex}(A_3)$) and $79\,ps$ ($t_{ex}(A_3)$). The errors on the exchange time constants are estimated to be smaller than a factor of 2. This large errors are caused by the fact that the bands cannot be selectively excited due to band overlap and the spectral width of the pump pulse used for the EXSY-2D-IR experiments. Additionally, vibrational relaxation being faster than exchange between the states leads to very small exchange signals. For a detailed discussion of the errors and its origins, see chapter 19.2 (appendix), where also all fitted parameters (start populations, scaling factors, and time constants) are listed in Table 19.1. For the main conclusions drawn in chapter 14 the errors are sufficient.

The modeled and measured time dependence agree pretty well. Residual deviations could be caused by artifacts caused by errors in the fitted band areas due to non-Gaussian line shapes (for a detailed discussion see chapter 19.1 (appendix)) or multiexponential decay and nonlinear exchange dynamics going beyond the used model. Nonlinear exchange dynamics are expected if the conformational change is slaved to the solvent.[253,254]
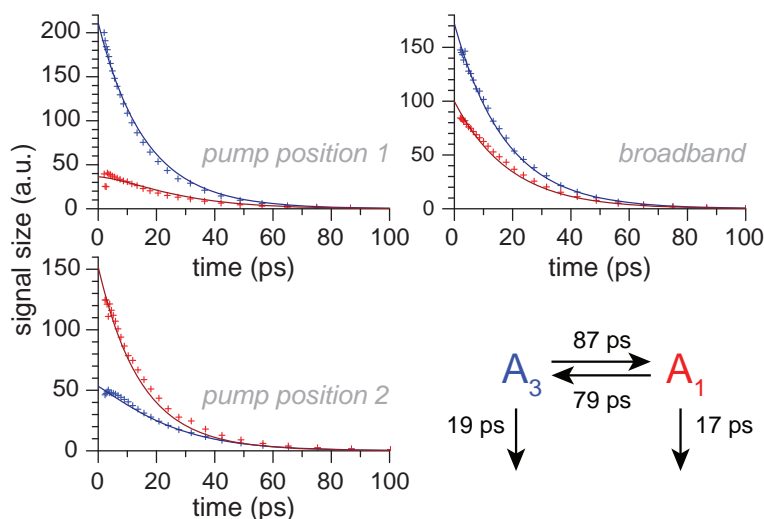
Figure 12.4: *Time dependence of the signal intensities (band areas) in the EXSY-2D-IR cuts and the broadband pump-probe spectra of L29I MbCO. The band areas (crosses) were obtained by the fits illustrated in Fig. 12.2. The lines show the simultaneous fit of the time dependence based on the exchange model. The fitted time constants are specified.*

12.3 Comparison to the Time Constants Proposed by Fayer *et al.*

The rates obtained in our measurements for relaxation and exchange have roughly the same magnitude as published by Fayer and co-workers. [40] Nevertheless, the deviations are apparent. In the present study the exchange time constants were determined to be 87 ps and 79 ps, while Fayer and co-workers found a time constant of 47 ps for both directions. This discrepancy is mainly caused by the procedure how Fayer and co-workers deduced the relaxation rate constants. In their study, they fitted the intensity decay in the broadband spectra with single exponentials and attributed the obtained time constants of 19 ps and 25 ps to the vibrational relaxation time of the vibrations. In doing so they omitted the exchange between the bands, which influences the population dynamics in the broadband spectra considerably. If we fit the absorption change in the broadband spectra with single exponentials, we obtain the same overall relaxation time constants of 19 ps and 25 ps, indicating that the measured spectra agree. However, it is a fundamental error to equate the overall population decay with the vibrational relaxation time T_1. The second inconsistency in the fit done by Fayer and co-workers is that they report an equilibrium constant of $K = 0.9$ on the one hand, but on the other hand they state that the time constants for both directions are the same, *i.e.*, $K = 1$.

In order to illustrate that the time constants published by Fayer and co-workers do not fit our experiment, the model with the proposed time constants was fitted to our data by fitting the start populations and scaling factors. The fit is overlaid with the experimental data in Fig. 12.5. The fitted time dependence of the signal of A_1 (red data points) in the broadband spectrum (Fig. 12.5 top right) shows a much slower decay than what is found experimentally. This is exactly the error that is introduced by neglecting the exchange process in the broadband population dynamics.
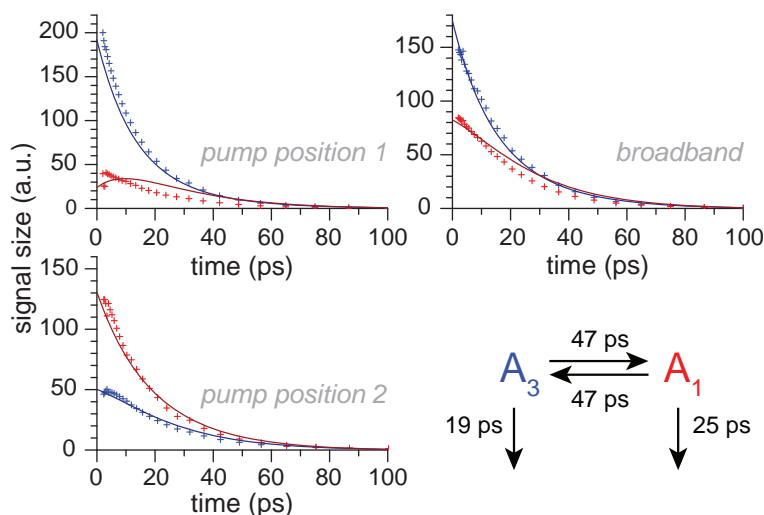
Figure 12.5: *Comparison of the measured time dependent signal intensities (crosses) with the fit based on the proposed model by Fayer and co-workers (lines). The model is sketched on the low right corner.*

Additionally, the cross peak dynamics for the spectra measured at pump position 1 Fig. 12.5 top left) are not reproduced nicely by the fit. The fit shows a rise in the signal size that was not observed experimentally and also the intensity decays much slower in the fit than in reality.

12.4   Temperature Dependence
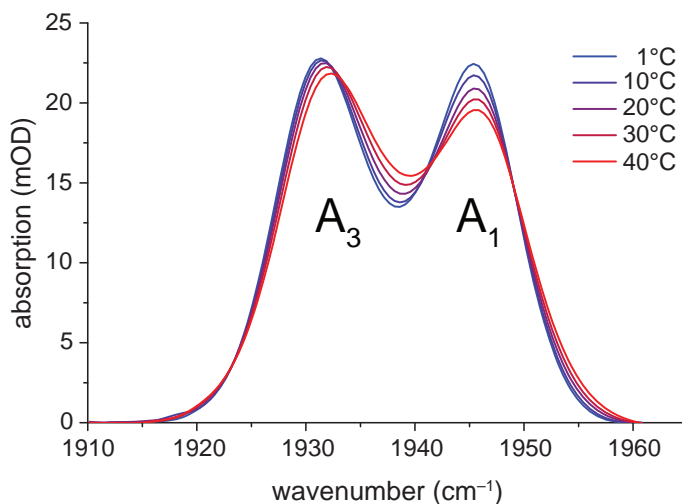
Figure 12.6: *Temperature dependent FTIR spectra of L29I MbCO. The spectra were measured and kindly provided by Karin Nienhaus (Karlsruhe Institute of Technology).*

The main focus of this work is to investigate the temperature dependence of the exchange rate. The temperature dependence of the FTIR spectrum of L29I MbCO between $1\,°C$ and $40\,°C$ is shown in Fig. 12.6. Intensity changes reflect in first approximation the change of the equilibrium constant. Transition dipole moments can be assumed to be independent of the temperature in this range and ϵ_{rel} is assumed to be 1 (see chapter 12.2). The intensity changes and the determined equilibrium constants K are summarized in Table 12.1. In addition to the changes in the band intensity, the bands become broader and the band position of the conformation A_3 shifts to higher wavenumber. The changes in the line shapes indicate that the conformations of the protein are more flexible and less defined at $40\,°C$ than at $1\,°C$.

Table 12.1: *Temperature dependence of the relative band areas in the FTIR spectrum and the deduced equilibrium constants.*

Temperature	$[A_3]$	$[A_3]$	K
$1\,°C$	0.516	0.488	0.946
$10\,°C$	0.518	0.482	0.930
$20\,°C$	0.525	0.475	0.904
$30\,°C$	0.530	0.470	0.888
$40\,°C$	0.532	0.467	0.878
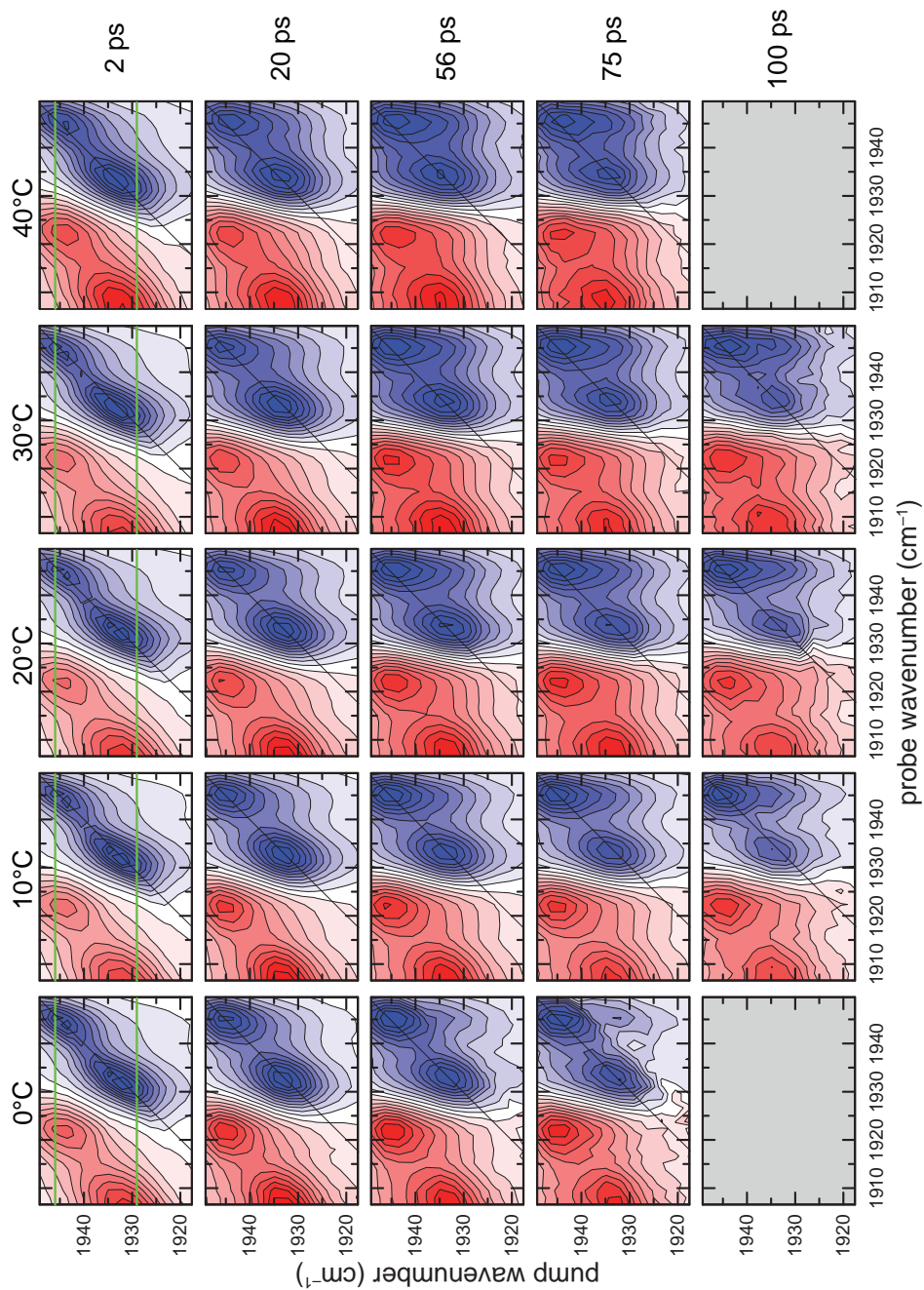
Figure 12.7: *Temperature dependent EXSY-2D-IR spectra of L29I MbCO. The individual spectra are scaled to the maximal intensity.*
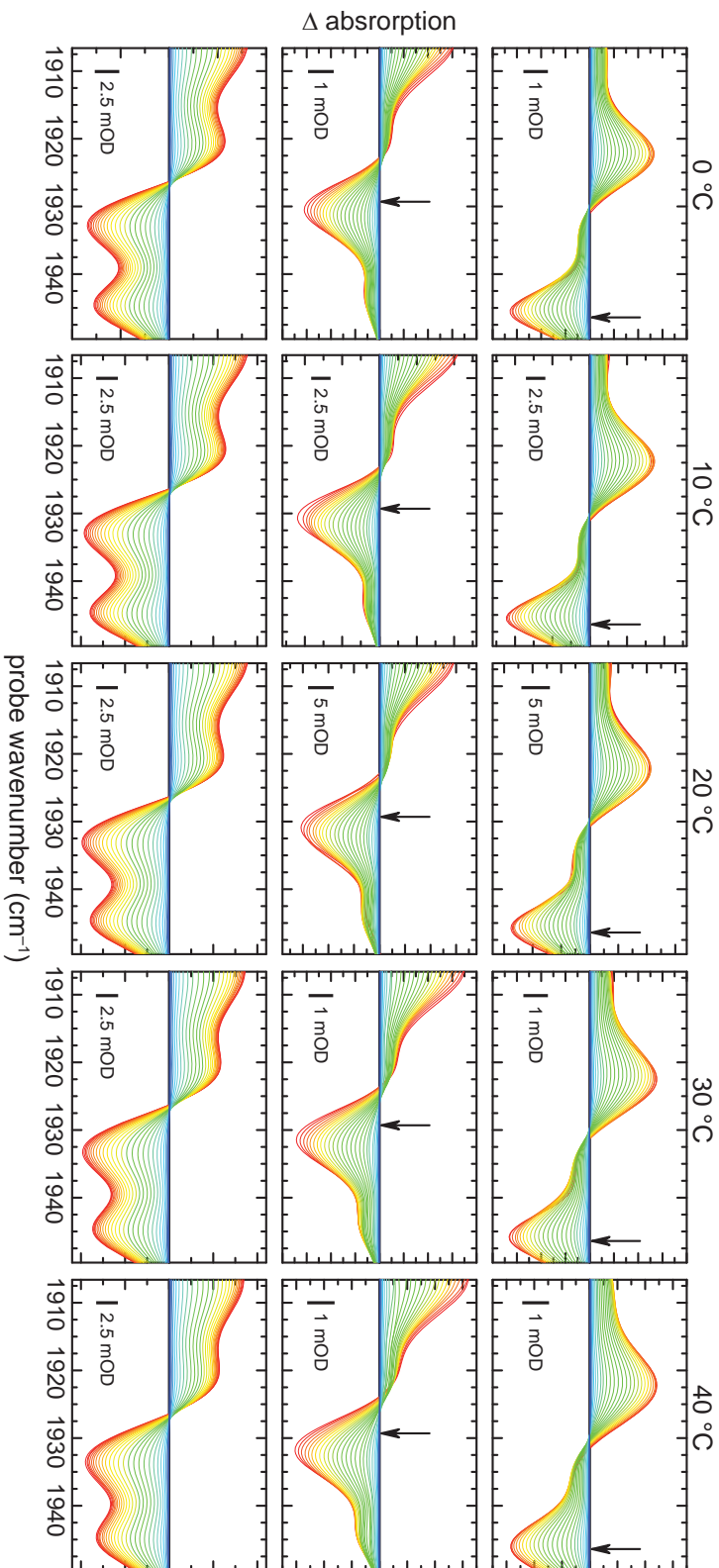
Figure 12.8: *Temperature dependent EXSY-2D-IR cuts (top and middle) and broadband pump-probe spectra (bottom) of L29I MbCO. The arrows indicate the positions of the narrowband pump pulses. The delay between pump and probe pulses was varied from 2 ps (red) to 100 ps (blue). Here the fitted spectra are shown. The directly measured spectra are shown in Fig. 20.3.*
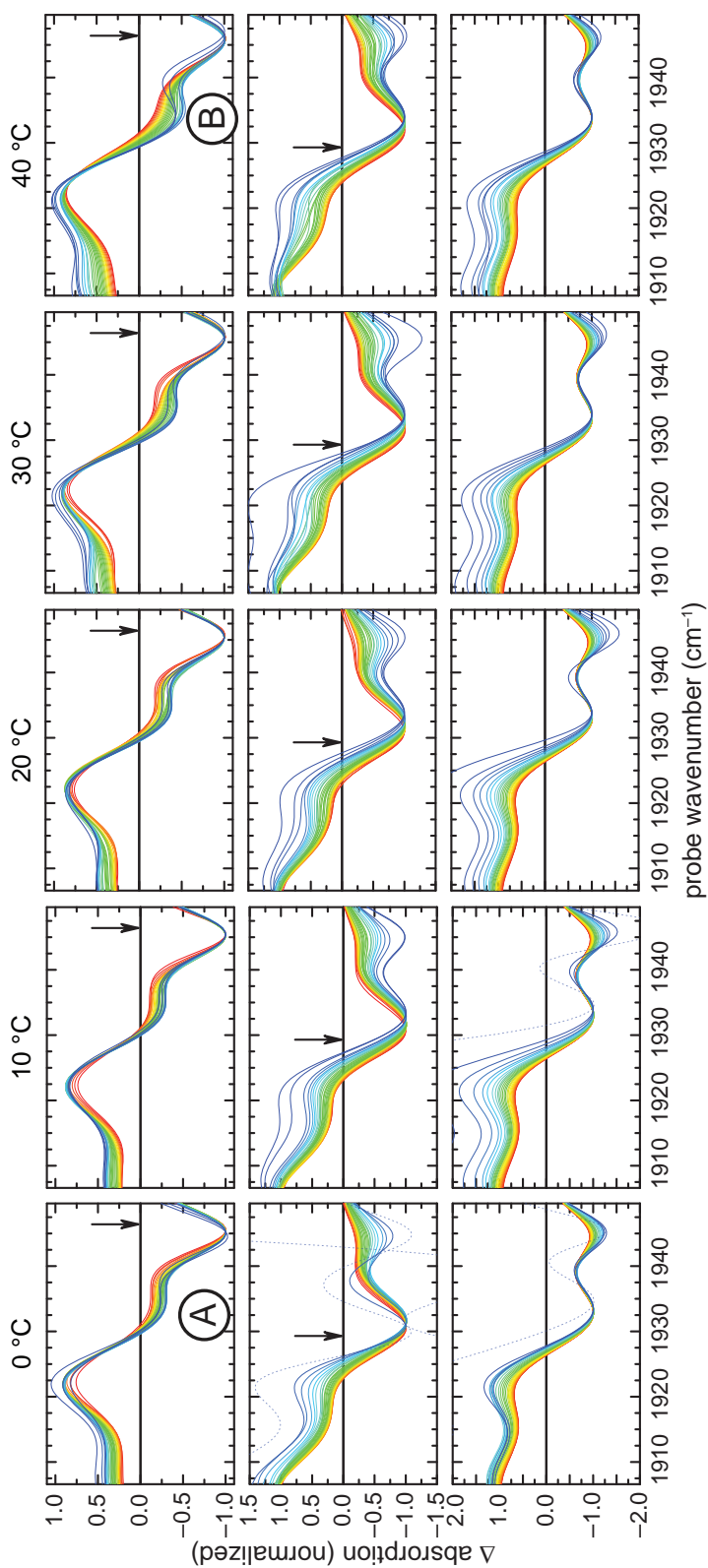
Figure 12.9: *Temperature dependent EXSY-2D-IR cuts (top and middle) and broadband pump-probe spectra (bottom) of L29I MbCO. The arrows indicate the positions of the narrowband pump pulse. The delay between pump and probe pulses was varied from 2 ps (red) to 100 ps (blue). The spectra are scaled to the intensity of one band. Here the fitted spectra are shown. The directly measured spectra are shown in Fig. 20.4.*

Figure 12.7 shows the temperature dependence of the 2D-IR spectra with various delay times (2 ps, 20 ps, 56 ps, 75 ps, and 100 ps) for the same temperature range (between 0 °C and 40 °C). At first glance there are only minor differences between the spectra seen, mainly reflecting the changes also observed in the FTIR spectrum. The general time dependence of the spectra is the same at all measured temperatures. There are also only minor differences in the time dependence of the EXSY-2D-IR cuts at the positions indicated by the green lines in Fig 12.7. The EXSY-2D-IR cuts and also the broadband pump-probe spectra of L29I MbCO are compared for the same temperatures in Fig. 12.8 (fitted spectra, raw data see appendix Fig. 20.3). A small temperature dependence can be observed in the scaled spectra shown in Fig. 12.9 (fitted spectra, raw data see appendix Fig. 20.4). The cross peak between A_1 and A_3 (pump position 2, top row) increases less at 0 °C (Fig. 20.4, pos. A) than at 40 °C (pos. B). Despite this, the spectra look (within signal to noise) identical.

Figure 12.10 summarizes the time dependence of the fitted band intensities of the EXSY-2D-IR cuts for the various temperatures (0 °C: blue, 40 °C: red). The relative cross peak intensities (cross peak intensity / diagonal peak intensity) are compared, too. The time dependence of the peak intensities shows basically the same as what was seen in the cuts and scaled cuts directly. They are hardly temperature dependent. Only for the relative cross peak intensity at pump position 2 a significant temperature dependence can be observed.

Fitting the time dependence of the signal intensities in the EXSY-2D-IR cuts and the broadband pump-probe spectra simultaneously as described in chapter 12.2 and 19.2 leads to the time constants summarized in Table 12.2 (see Table 19.1 for all fitted parameters and Fig 19.4 for the graphic comparison of fits and experimental data). The overall exchange rates were calculated as:

$$k_{obs} = \frac{1}{t_{ex}(A_1)} + \frac{1}{t_{ex}(A_3)}. \tag{44}$$

The confidence intervals are specified in brackets.

Table 12.2: *Summary of the fitted time constants of the population dynamics of L29I MbCO.*

Temperature	0 °C	10 °C	20 °C	30 °C	40 °C
$T_1(A_1)$ (ps)	17.0 ± 3	16.6 ± 3	16.7 ± 3	16.1 ± 3	14.4 ± 3
$T_1(A_3)$ (ps)	19.0 ± 3	18.6 ± 3	18.8 ± 3	19.3 ± 3	19.7 ± 3
$t_{ex}(A_3)$ (ps)	136 (68, 272)	116 (58, 232)	87 (43, 174)	95 (47, 190)	70 (35, 140)
$t_{ex}(A_1)$ (ps)	129 (65, 258)	108 (54, 216)	79 (39, 158)	84 (42, 168)	61 (31, 122)
k_{obs} (10^9s^{-1})	15 (8, 30)	18 (6, 36)	24 (12, 48)	22 (11, 44)	31 (15, 61)
$\log(k_{obs})$	10.2 ± 0.3	10.3 ± 0.3	10.4 ± 0.3	10.4 ± 0.3	10.5 ± 0.3

The relaxation time constants are the same within the error for all temperatures. There is also no clear trend observable. The exchange times and the observed overall exchange rates are also the same within the experimental error. However, there is a clear trend visible. The exchange rate gets faster (the exchange time constants
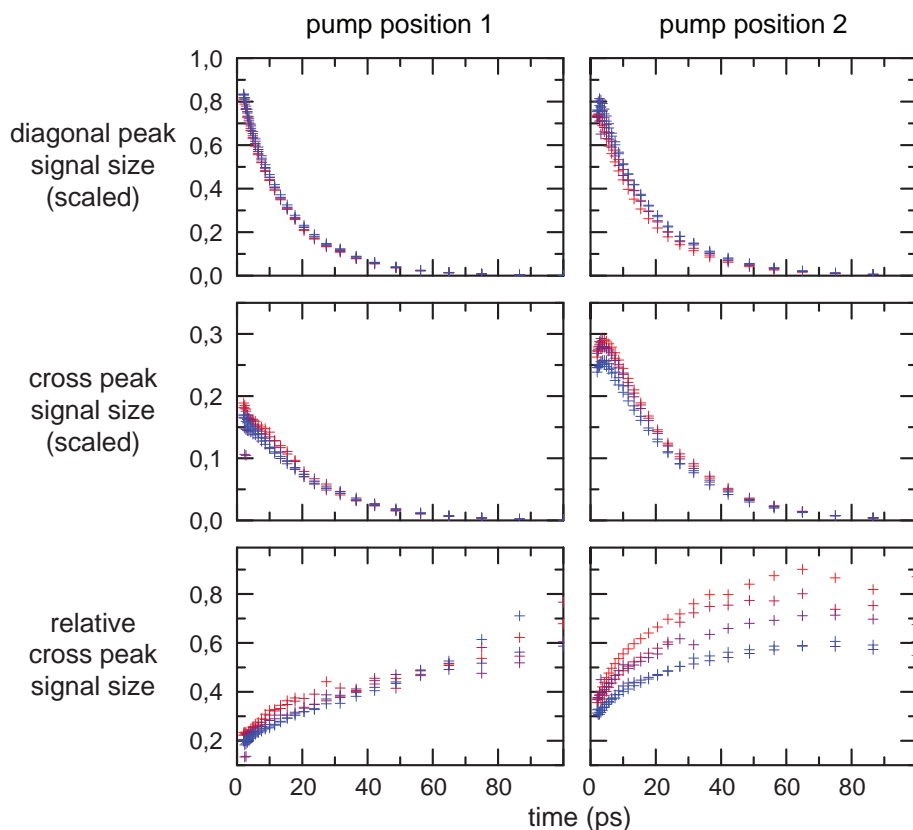
Figure 12.10: *Time dependence of the signal sizes (band areas) in the EXSY-2D-IR cuts and the broadband pump-probe spectra of L29I MbCO as a function of temperature. The temperatures vary from 0° C (blue) to 40° C (red) in steps of 10° C. The band areas were obtained by the fits illustrated in Fig. 12.8. For comparison, the signal intensities are scaled to the total signal intensity of the according spectra with a delay of 2 ps. The fits of the population dynamics for all temperatures are shown in Fig. 19.6.*

smaller) with increasing temperature. Over the complete temperature range investigated (40 °C) the rates double.

The presented time constants were obtained by a fit assuming that the transition dipole moments are equal in both conformational states of the protein. Executing the fits without keeping the transition dipole moments fixed yields in very similar time constants and the very same temperature dependence of those (see appendix chapter 19.2).

12.5 Comparison to the Super-Arrhenius Dependence Proposed by Johnson *et al.*
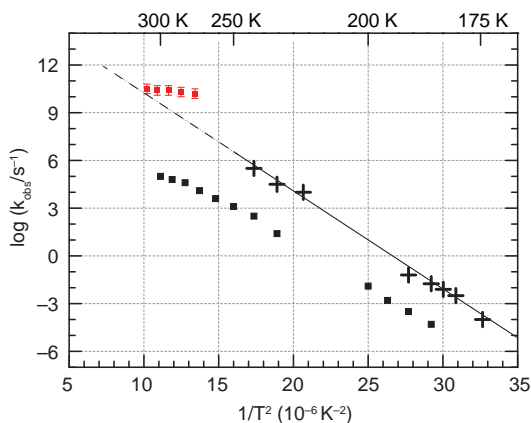
Figure 12.11: *Temperature dependence of of the exchange rates k_obs in L29I MbCO (red data points). The measurements are compared to the measurements on wild type Mb by Johnson et al. (black data points; the data were kindly provided by G. Ulrich Nienhaus (Karlsruhe Institute of Technology)), which are reproduced in Fig. 11.2.*[263]

Figure 12.11 compares our data (red) to the data (black crosses) and fit (black line) of Johnson *et al.* for the exchange between A_1 and A_3.[263] The proposed Super-Arrhenius dependence (straight line) is extrapolated to the temperature range of the measurements presented here (dashed line). The extrapolation predicts for high temperatures roughly the same rates as measured. However, our data show a faster exchange rate than expected from extrapolating the fit by Johnson *et al.* (the data points are above the extrapolated line), particularly for lower temperatures. Additionally, the temperature dependence of the exchange process is weaker than expected by the Super-Arrhenius relation, showing up in a smaller slope between the data.

Figure 12.12 opposes the measured population dynamics with the population dynamics expected based on Super-Arrhenius relation proposed by Johnson *et al.* for the temperature dependence and the experimentally found exchange rate at $20\,°C$. Details of the simulations and the underlying time constants are summarized in chapter 19.2.2 (appendix). The differences between simulated and measured population dynamics are quite obvious, in particular when comparing the cross peak populations (middle row) and the ratios between cross peak population and diagonal peak population (third row). At $40\,°C$ (red) the simulated cross peak population increases significantly for short times, goes through a maximum, and decays afterwards (Fig. 12.12 pos. 1). At $0\,°C$ (blue), the simulated population decays only and no initial increase is visible (Fig. 12.12 pos. 2). In contrast to the simulation, the experimental curves lie on top of each other and show the same time dependence for all measured temperatures (Fig. 12.12 pos. 3). In the graphs comparing the ratio of cross peak population and diagonal peak population the simulations show features that were not observed in the experiment. At $40\,°C$, the simulated ratio reaches a constant value within $20\,ps$ (Fig. 12.12 pos. 4). The time dependence of the ratio simulated for $0\,°C$ (Fig. 12.12 pos. 5) does not reach a constant value and additionally the curve has opposite cur-
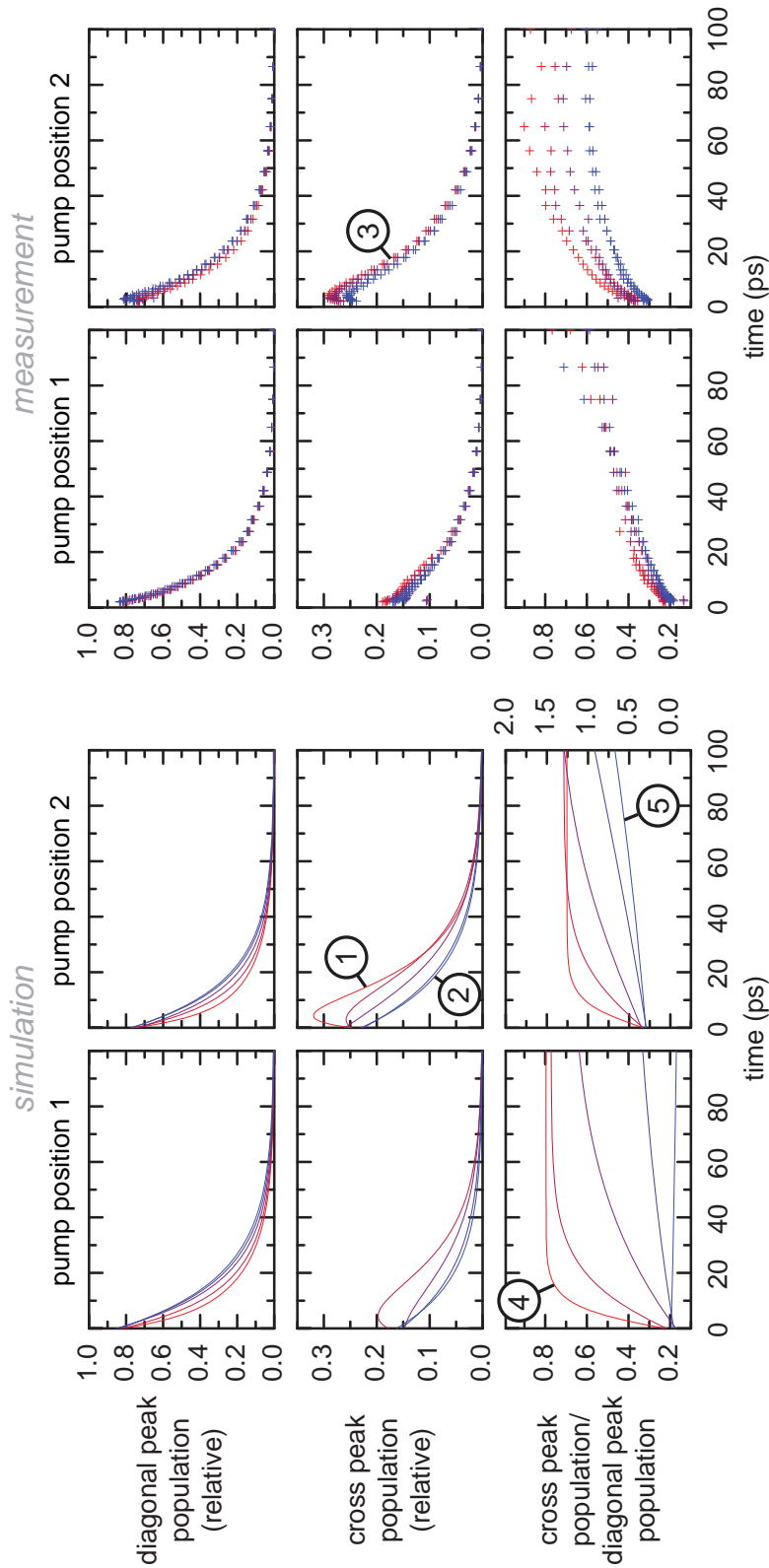
Figure 12.12: *Expected temperature dependence of the population dynamics in L29I MbCO. The simulations are based on the fit of Johnson et al. (slope of the black line in Fig. 12.11) and the measured exchange rate at 20°C. The measured population dynamics are repeated for comparison on the right (see also Fig. 12.10). Numbers see text.*
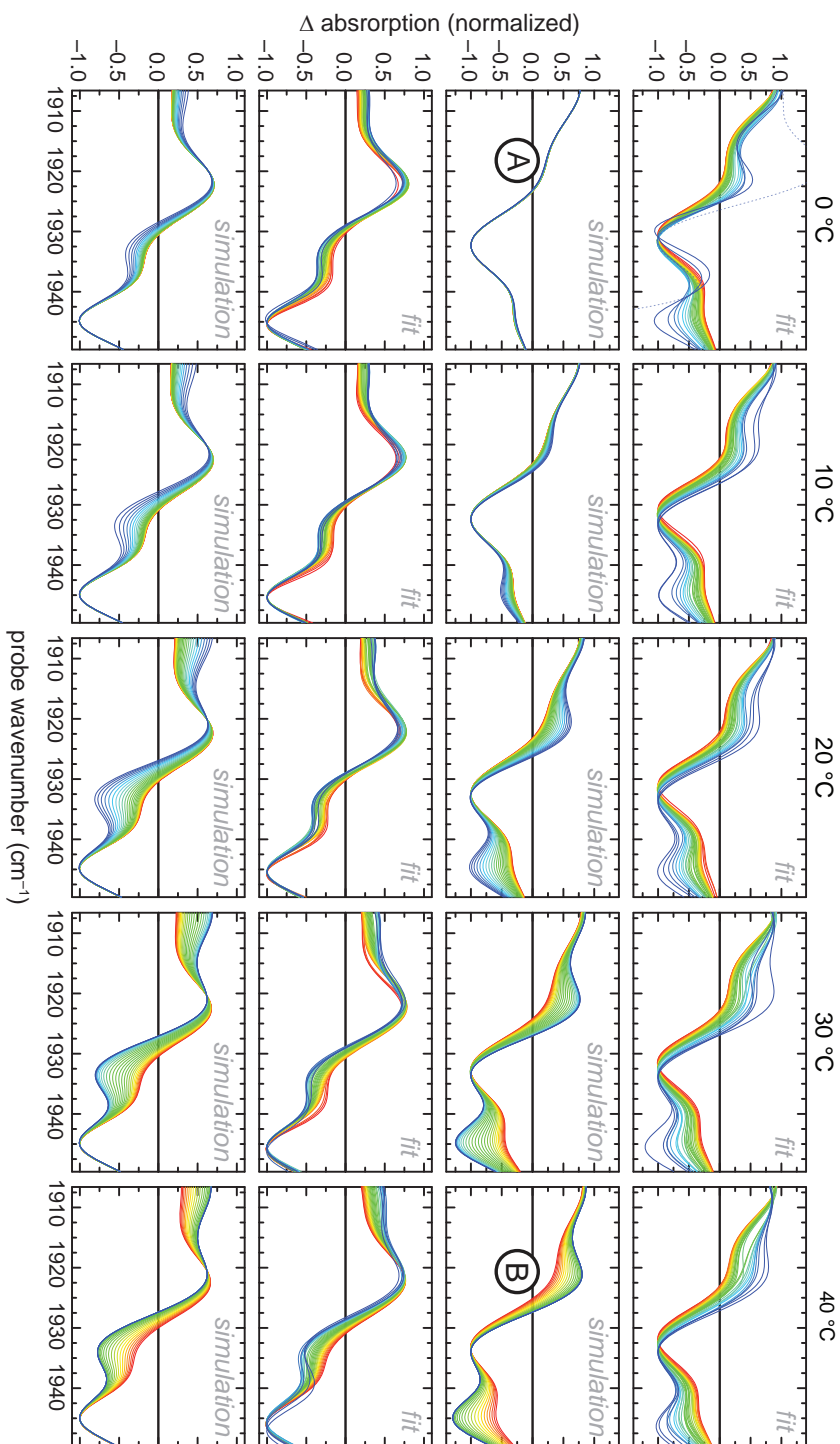
Figure 12.13: *Comparison between fitted and simulated EXSY-2D-IR cuts for the various temperatures. The simulations are based on the simulated population dynamics shown in Fig. 12.12 assuming the same temperature dependence as observed for low temperatures in wild type Mb and the exchange rate measured at 20°C. All spectra were scaled to the intensity of the initially excited band. The unscaled spectra are shown in Fig. 19.7. Labels see text.*

vature compared to the curve at 40 °C. These large differences between the ratios are not seen in the experiment. Particularly the curvature of the curves do not change.

The differences between the simulated population dynamics and the measured data becomes even more apparent by comparing the simulated and measured EXSY-2D-IR cuts (scaled, Fig. 12.13). For pump position 1 (top rows), the simulation at 0 °C shows no change of the spectral shape with increasing delay time (Fig. 12.13 pos. A). All scaled spectra lie on top of each other. For 40 °C, the evolution of the cross peak and thus the dependence of the spectral shape on the delay time is clearly seen (Fig. 12.13 pos. B). In the experimental data, the time dependence of the spectral shape is similar for all temperatures. Qualitatively the same trend is also seen for pump position 2 (bottom rows).

To sum up, Fig. 12.12 and Fig. 12.13 show clearly that the measured temperature dependence of the population dynamics of L29I MbCO deviate significantly from the Super-Arrhenius relation proposed by Johnson *et al.* based on their data of wild type MbCO at cryogenic temperatures. The mutation will have an influence on the rate, however, it is unlikely that it changes the temperature dependence so strongly.

12.6   Comparison to the Solvent Viscosity

To understand what is causing the temperature dependence of the exchange rates, it is important to point out the differences between the samples investigated. Our data were measured for the sperm whale Mb mutant L29I in a potassium phosphate buffer (D_2O, pD = 7) whereas the data obtained by Johnson *et al.* and Iben *et al.* were measured for sperm whale Mb (wild type) in a glycerol-potassium carbonate buffer (pH = 11) mixture (75%/0.25% *v/v*; $w \approx 0.8$).[261,263] The viscosities of the two solvents differ significantly. Moreover, the viscosities of them show different temperature dependences. Fenimore *et al.* already pointed out that the temperature dependence of the solvent viscosity determines the temperature dependence of the dynamics of certain processes in proteins.[254]

Figure 12.14 compares the temperature dependence of the viscosities to the temperature dependence of the exchange between the conformations A_1 and A_3 as well as between the conformation A_0 and the conformations A_1 and A_3. The straight lines show the temperature dependence of the viscosities (blue: glycerol-buffer mixture ($w = 0.8$), red: water).[287–289] The dashed lines are shifted compared to the straight lines (italic numbers specify the amount of the shift). They overlay almost perfectly with the temperature dependence of the protein dynamics (data points), indicating that the temperature dependence of the conformational dynamics between the Mb substates is determined by the solvent and not by the protein itself, *i.e.*, the conformational dynamics being slaved to the solvent. When plotting the exchange rates as function of the viscosity (Fig. 12.15), a linear relationship was observed. The slope of ≈ -1 in the logarithmic plot implies that the exponential factor in Kramers equation (see eq. 41) does, for this process, not significantly depend on the Temperature. Consequently, there is no significant enthalpic barrier between the two states A_1 and A_3 and the barrier is mainly entropic.
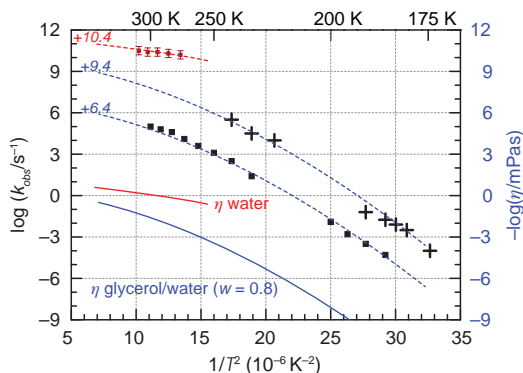
Figure 12.14: *Temperature dependence of of the exchange rates k_{obs} in Mb (dark red data points: L29I MbCO, black data points: wt MbCO;[263] kindly provided by G. Ulrich Nienhaus (Karlsruhe Institute of Technology)) and the viscosities of the used solvents (straight lines, scale on the right side of the graph).[287,288] The temperature dependence of the solvent viscosities are shifted for comparison (dashed lines). The shifts are specified by the italic numbers next to the curves.*
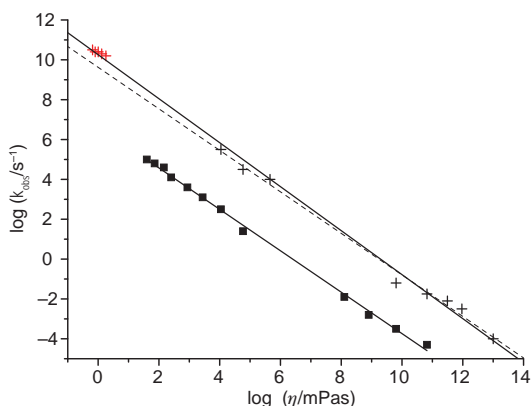
Figure 12.15: *Dependence of of the exchange rates k_{obs} in Mb (red data points: L29I MbCO, black data points: wt MbCO;[263] kindly provided by G. Ulrich Nienhaus (Karlsruhe Institute of Technology)) on the viscosities of the used solvents. The crosses are the rates of the exchange between A_1 and A_3 while the squares denote the exchange rate between A_0 and $A_1 + A_3$. Fits to the data are shown by the straight lines. The dashed line shows the fit of only the black crosses.*

The absolute value of the rate may depend on the protein itself leading to a shift of the fit in Fig. 12.15. Based on the data in Fig. 12.15 there might be a small shift between the rates of L29I MbCO and wt MbCO (compare red data points and dashed line). However, based on the actual data basis the shift cannot be definitely proven. If there is a shift, it could also be caused by solvent properties other than viscosity such as the size of the solvent molecules, the dielectric constant, or specific interactions between the protein and the solvent (*e.g.*, hydrogen bonding).

Chapter 13

Wild Type and Additional Mutants

In addition to the study on L29I MbCO, temperature dependent EXSY-2D-IR spectra were also measured for sperm whale MbCO (wild type) and its mutants L29W MbCO, V68W MbCO and YLT MbCO. These spectra show also only a weak temperature dependence, similar to the spectra of L29I MbCO. In this chapter, the two dimensional spectra are shown. The time and temperature dependence of the cuts through the spectra and of the broadband pump-probe spectra are shown in chapter 20 in the appendix. Because the bands overlap stronger than for L29I, a quantitative analysis of the data for the wild type and mutants presented here was not feasible. Thus, the spectra are discussed only on a phenomenological level. No time constants were determined.

13.1 V68W Myoglobin

V68W MbCO shows two bands in the IR spectrum originating from bound CO ($\approx$1932 cm^{-1}: A$_3$; $\approx$1949 cm^{-1}: A$_1$). At 0 °C they are of similar intensity while at 44 °C the band at lower wavenumber is more intense than the band at higher wavenumber. The diagonal peaks in the EXSY-2D-IR spectra behave accordingly (see Fig. 13.1). This is most obvious in the spectra with a delay time of 1.5 ps. Despite this, there are no significant temperature dependent differences in the spectra. From the scaled EXSY-2D-IR cuts (appendix Fig. 20.8) one can estimate that the exchange rates between the conformational states are similar to the ones in L29I MbCO.
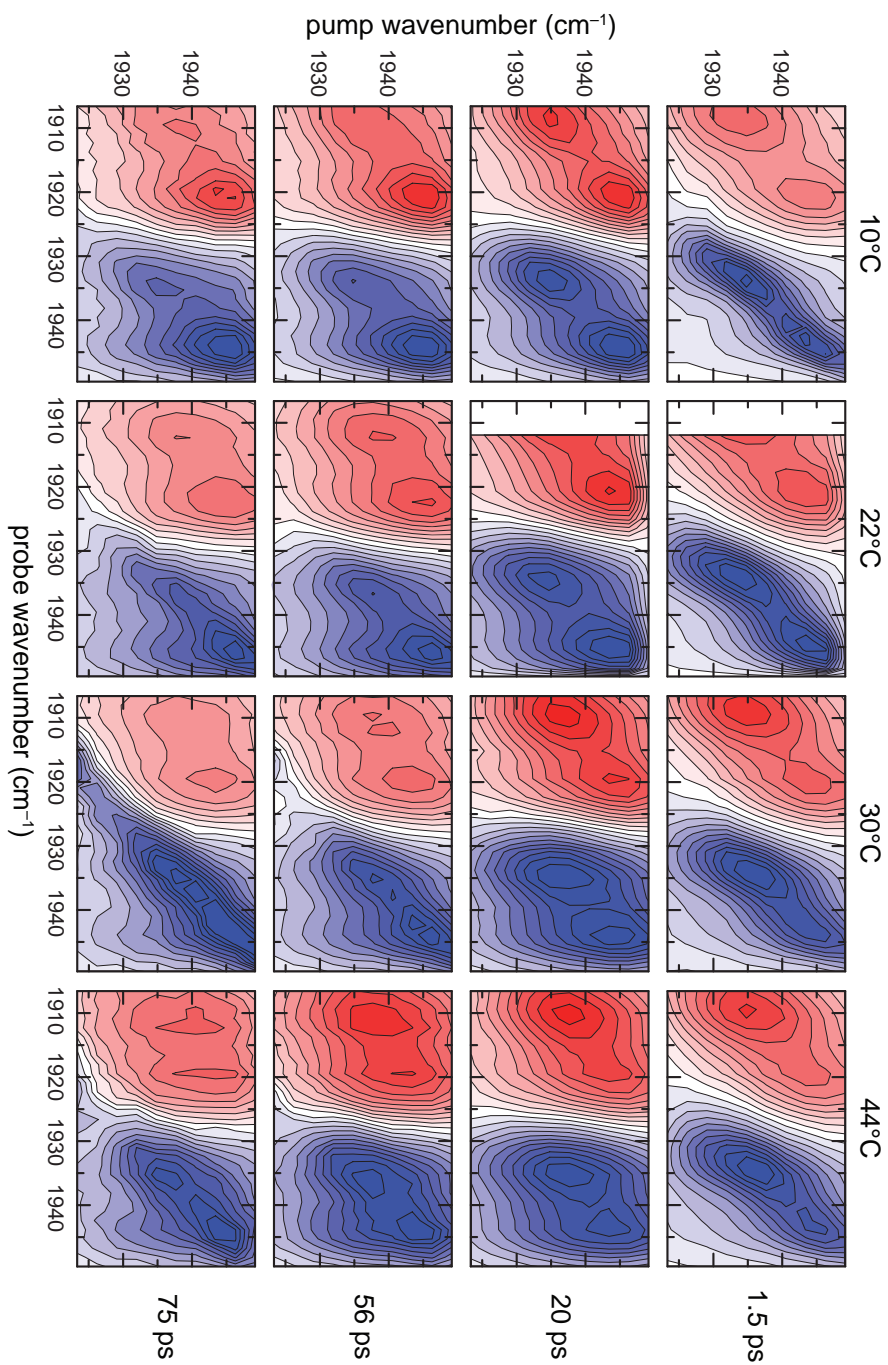
Figure 13.1: *Temperature dependent EXSY-2D-IR spectra of V68W MbCO. The spectrum at 30°C with at delay of 75 ps shows strong scattering artifacts. The individual spectra are scaled to the maximal intensity.*

13.2   Wild Type Myoglobin

The IR spectrum of MbCO (wild type) shows at pH 7 two bands, a weak band belonging to the conformational state A_3 ($\approx 1932\,cm^{-1}$) and a much stronger band belonging to the state A_1 ($\approx 1944\,cm^{-1}$). The 2D-IR spectra shown in Fig. 13.2 also show one strong diagonal peak (A_1) and one weak diagonal peak (A_3). Due to the close proximity of the two bands and the large intensity differences, the cross peaks appearing at longer time lead to a stronger elongation of the peaks along the pump axis. They are not visible as distinct peaks. The spectra at all measured temperatures look essentially the same. A weak temperature dependence is seen in the cuts through the EXSY-2D-IR spectra (appendix Fig. 20.2).
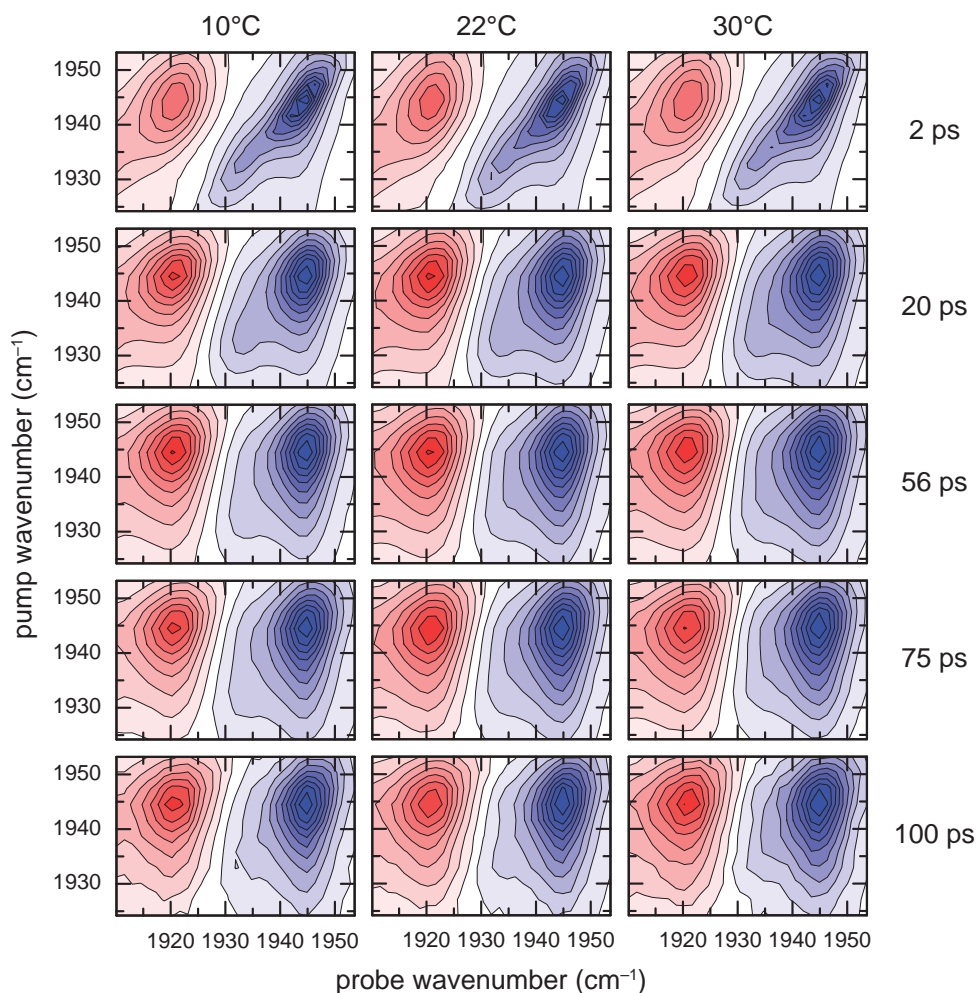
Figure 13.2: *Temperature dependent EXSY-2D-IR spectra of MbCO (wild type). The individual spectra are scaled to the maximal intensity.*

13.3   L29W Myoglobin

L29W MbCO shows two CO bands at $\approx 1945\,\mathrm{cm}^{-1}$ and $\approx 1957\,\mathrm{cm}^{-1}$. Due to the strong band overlap only an elongated diagonal peak is observed in the EXSY-2D-IR spectra with a delay time of 1.5 ps (Fig 13.3). Due to the loss of band inhomogeneity, the two peaks become visible as distinct peaks for longer delay times. The spectra at 22 °C and 37 °C differ in the signal intensities of the bands, mainly caused by the temperature dependence of the relaxation rates. There is no evidence for an exchange between the states in the picosecond time range since no cross peaks are observed (see also scaled EXSY-2D-IR cuts Fig. 20.6).
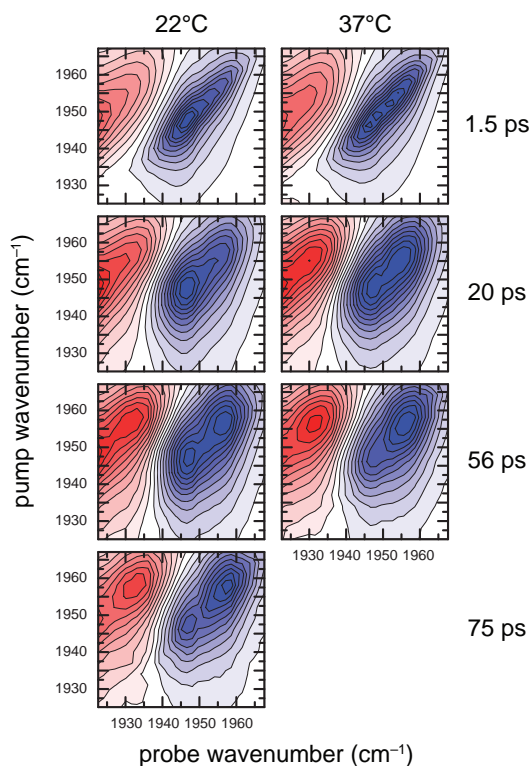
Figure 13.3: *Temperature dependent EXSY-2D-IR spectra of L29W MbCO. The individual spectra are scaled to the maximal intensity.*

13.4   YLT Myoglobin

The triple mutant YLT MbCO shows three bands after CO binding leading to three diagonal peaks in the EXSY-2D-IR spectra (Fig. 13.5). From the EXSY-2D-IR spectra and the cuts (see Fig. 20.10) one can infer that the conformational states causing the bands at low and high wavenumber exchange on a picosecond time scale. This is best seen in the spectra with a delay time of 56 ps (or 75 ps) at 30 °C shown in Fig. 13.5. The well resolved cross peak in the upper right corner uncovers the conformational exchange. The temperature dependence of this exchange seems to be

more pronounced than for the conformational dynamics in L29I MbCO (see Fig. 13.5 and 20.10). The middle band shows no clear, well resolved cross peak, which however might be caused by the low intensity of the band.
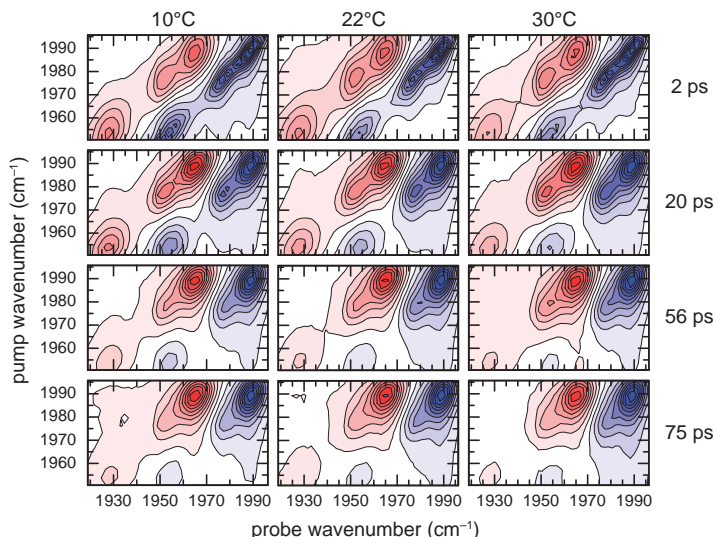
Figure 13.4: *Temperature dependent EXSY-2D-IR spectra of YLT MbCO. The spectra are merged from two measurements and scaled to the maximal intensity.*
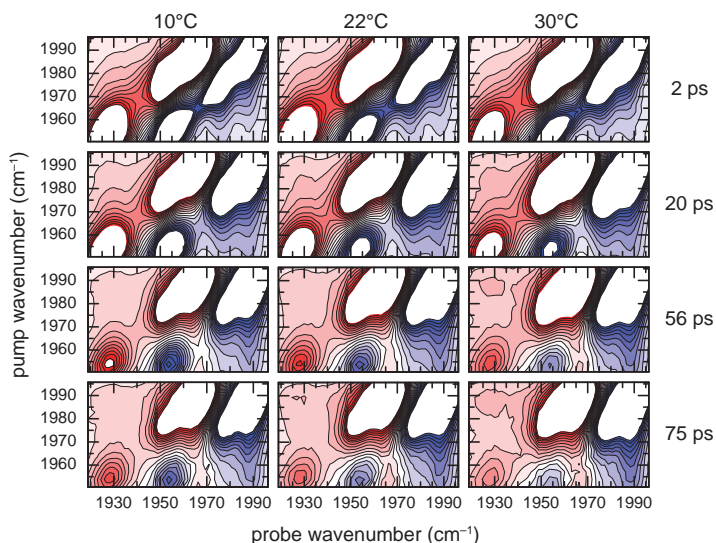
Figure 13.5: *Temperature dependent EXSY-2D-IR spectra of YLT MbCO. The spectra are merged from two measurements and scaled to 20% of the maximal intensity.*

Chapter 14

Discussion and Conclusion

14.1   Protein Dynamics

To summarize, our measurements on L29I MbCO show only a weak temperature dependence of the conformational switching between A_1 and A_3. The change of the rate constants is proportional to the change of the solvent viscosity. Thus the measurements support the concept of Frauenfelder and co-workers implying that the dynamics of the exchange between the taxonomic substates in Mb are slaved to the solvent. This is to our best knowledge the first study that showed that slaving to the solvent also is important for dynamics in the picosecond time range. Comparing the dependence of the rate constants with the viscosity over 14 orders of magnitude (in a temperature range of almost $150\,°C$) shows a clear linear correlation between the rate constant and the inverse viscosity. Since an influence of the viscosity of the bulk solvent is expected mainly for large range conformational changes, or data indicate that the transition between A_1 and A_3 includes large range reorientations and not only the rotation of a single residue. This is in line with the appearance of an additional Xe pocket in A_3 found by X-ray crystallography, MD simulations, and the dependence of the equilibrium between the states on pressure. In order to understand the structural origin of the two states, additional investigations are needed. Most promising are probably MD simulations. Because the exchange rates show no additional temperature dependence besides the dependence on the viscosity, it can be concluded that the barrier between the conformational states is dominated by entropic effects. An enthaplic contribution can, if it exists, be neglected. The temperature dependence of the conformational dynamics over the complete range of measured temperatures cannot be described by the Super-Arrhenius relation as proposed by Johnson *et al.* The deviations of our measurements from this relation are apparent.

A word of caution seems to be appropriate here. Our study was performed with another Mb mutant and in another solvent than the study by Johnson *et al.* Thus, not only the temperature has been modified, but also the solvent, the mutant and indirectly the viscosity of the solvent changed. In order to have a reliable data set, it would be desirable to have a consistent data set over many orders of magnitude in the exchange time constant. This would involve the same solvent, the same protein/mutant, and the same concentration. Only the temperature should be changed. One difficulty is that changing the temperature influences, as discussed above, the viscosity. And the viscosity also affects the exchange rate. It is hard to disentangle the

two contributions. Ideally one would have a solvent that does not change the viscosity over the temperature range studied but at the same time does not alter the native structure of the protein. Alternatively one could test the influence of the viscosity separately by changing the solvent or solvent composition. However, solvent protein interactions may alter the conformation of the protein. The vibrational frequencies are sensitive to the conformation of a protein and FTIR spectroscopy should therefore allow to crosscheck the protein folding. Since we have good reasons to assume that the bulk viscosity of a solution influences the exchange rates between conformational states, also the protein concentration is likely to affect the structural dynamics.

In the studies presented here, we did not make sure that the concentration of the sample was the same for all measurements. Since the broadband spectra and the EXSY-2D-IR cuts were not measured on the same sample, this may also influence the obtained rate constants slightly.

14.2   2D-IR Spectroscopy

This study proved 2D-IR spectroscopy being a powerful tool to investigate fast equilibrium dynamics of proteins. The temperature dependence of the spectra allowed to discriminate protein slaving and other proposed models for the temperature dependence of the conformational exchange. The spectra of L29I MbCO could be analyzed in detail and the exchange rates were obtained. However, the error bars on the exchange rates are quite large. This is based on three main factors. First, vibrational relaxation is limiting the observation window. Because in the system studied here, the vibrational relaxation rates are much faster than the exchange rate, the signals where the exchange shows up are very small. Hence it is desirable to circumvent vibrational relaxation. This could be realized by a IR-UV double resonance experiment. [246] From Raman experiments it is known that the Fe–CO vibration is coupled to the Soret band of Mb. [290,291] Thus it is likely that a double resonance experiment would work. This would increase the time window for measuring the conformational exchange by several orders of magnitude and therefore allow a much better data quality. The second factor leading to the large error bar in the exchange time constant is the difficulty to extract the band areas out of the spectra as the bands overlap strongly and the band shapes change as function of delay time. Moreover, the region of the measured spectra is limited in the current setup causing cut spectra. Two changes to the setup would facilitate significantly better fits of the spectra. First, a detector with a larger amount of pixels in combination with a matching grating would enhance both the spectral resolution and the spectral window observable. Consequently, all peaks could be measured completely within one measurement. Additionally, Gaussian shaped pump pulses would result in Gaussian shaped signals, which would stay Gaussian shaped for all delay times. Due to spectral diffusion, only the line widths would change slightly for small delay times. Moreover, Gaussian shaped pump pulses would enhance the selectivity of the excitation, the third limiting factor in the present study. These experimental changes would also allow a quantitative analysis of the measurements on wt MbCO, V68W MbCO, and L29W MbCO. Possibly, also YLT MbCO could be analyzed quantitatively.

More precise determination of the exchange rates would make temperature dependent 2D-IR spectroscopy even more powerful and would allow a detailed comparison of various mutants and also the investigation of enthalpic barriers between the conformational states at physiological temperatures would become feasible.

Part IV

Appendix

Chapter 15

Calculations[i]

All calculations were performed using the Gaussian09 suite of programs, using density functional theory (DFT) with Truhlar's hybrid meta-exchange-correlation functional M06 in conjunction with the 6–31+G(d,p) basis set. [292,293] Calculations on Sn containing species were performed using a 6–31+G(d,p) basis set with Stuttgart/Dresden effective core potentials (SDD) on the Sn atom. [294] The M06 functional was recommended for calculations of organometallic species and for studies of non-covalent interactions, thermochemistry, and kinetics. [293] The 6–31+G(d,p) basis set was chosen because a further increase of basis set size and thus computational costs led only to minor changes in the calculated transition dipole angles (Fig. 15.1. The influence of the solvent was taken into account by the self-consistent reaction field (SCRF) method, using the polarizable continuum model (PCM) with van der Waals radii of Bondi with the Gaussian09 default scaling of 1.1 and explicit hydrogen atoms. [295,296] The frequently used united atom topological models UAHF and UAKS do not take into account hydrogen atoms explicitly to create the solute cavity. Calculations using these models in some cases resulted in unphysically long C–H bond lengths and low C–H stretching frequencies and were therefore not used. The results of the calculations are summarized in the following sections.

---

[i]All presented DFT calculations of **1** and its complexes were done by Jens Bredenbeck.
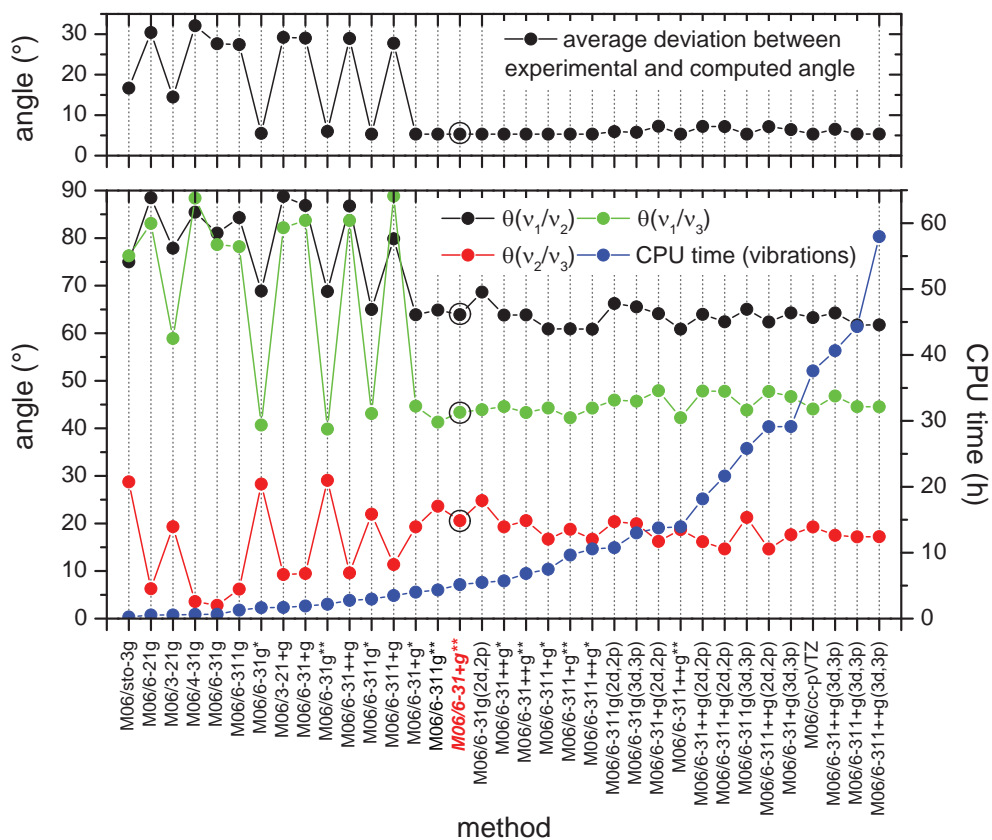
Figure 15.1: *Transition dipole angles of **1-apc** in CH_2Cl_2, computed with various basis sets with the M06/PCM/Bondi approach, ordered by computational effort. Top: Average deviation between experimental and calculated angles. Bottom: Calculated angles and CPU time for the normal mode calculation.*

15.1 *N*-Crotonyloxazolidinone

Table 15.1: *Summary of the DFT calculations (M06/6-31+G(d,p)/PCM/Bondi) of the relevant isotopologues of **1-apc** in CH$_2$Cl$_2$.*
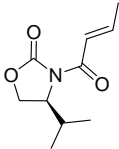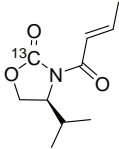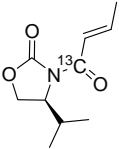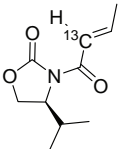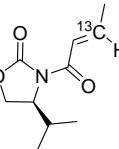
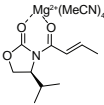|					
angles					
ν_1/ν_2 (°)	64	59	79	63	66
ν_1/ν_3 (°)	21	17	3	29	33
ν_2/ν_3 (°)	43	43	77	34	33
vibrational energies					
ν_1 (cm^{-1})	1694	1694	1673	1672	1669
ν_2 (cm^{-1})	1741	1740	1719	1736	1735
ν_3 (cm^{-1})	1831	1785	1830	1831	1831

Table 15.2: *Summary of the DFT calculations (M06/6-31+G(d,p)/PCM/Bondi) of various conformers of **1** in different media.*

	1-apc	1-apt	1-spt	1-spc
ACETONITRILE				
angles				
ν_1/ν_2 (°)	61	27	89	61
ν_1/ν_3 (°)	17	47	77	38
ν_2/ν_3 (°)	45	41	49	81
vibrational energies				
ν_1 (cm^{-1})	1690	1708	1712	1697
ν_2 (cm^{-1})	1734	1728	1730	1734
ν_3 (cm^{-1})	1820	1825	1830	1841
calculated Gibbs energies				
ΔG_{298} (kcal/mol)	0.0	3.3	4.8	2.0
DICHLOROMETHANE				
angles				
ν_1/ν_2 (°)	64	33	74	67
ν_1/ν_3 (°)	21	54	65	42
ν_2/ν_3 (°)	43	40	52	71
vibrational energies				
ν_1 (cm^{-1})	1694	1714	1717	1703
ν_2 (cm^{-1})	1741	1735	1742	1744
ν_3 (cm^{-1})	1831	1836	1847	1857
calculated Gibbs energies				
ΔG_{298} (kcal/mol)	0.0	3.6	6.0	3.3
TOLUENE				
angles				
ν_1/ν_2 (°)	70	67	71	72
ν_1/ν_3 (°)	28	85	64	50
ν_2/ν_3 (°)	41	41	58	58
vibrational energies				
ν_1 (cm^{-1})	1706	1725	1726	1719
ν_2 (cm^{-1})	1760	1757	1775	1774
ν_3 (cm^{-1})	1861	1867	1890	1896
calculated Gibbs energies				
ΔG_{298} (kcal/mol)	0.0	4.0	8.7	5.3
VACUUM				
angles				
ν_1/ν_2 (°)	74	88	74	72
ν_1/ν_3 (°)	33	68	67	55
ν_2/ν_3 (°)	41	39	62	4
vibrational energies				
ν_1 (cm^{-1})	1717	1728	1733	1726
ν_2 (cm^{-1})	1780	1781	1808	1803
ν_3 (cm^{-1})	1896	1900	1933	1938
calculated Gibbs energies				
ΔG_{298} (kcal/mol)	0.0	4.1	10.4	8.4

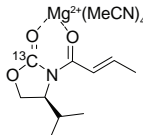## 15.2 *N*-Crotonyloxazolidinone–SnCl$_4$ Complexes

Table 15.3: *Summary of the DFT calculations (M06/6-31+G(d,p)/PCM/Bondi) of the isotopologues of **1-spc-κ^2O, O′**·SnCl$_4$ in CH$_2$Cl$_2$.*
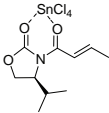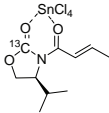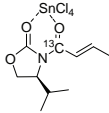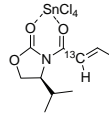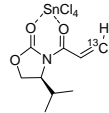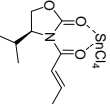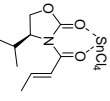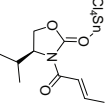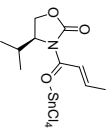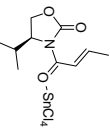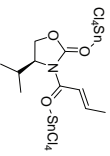
angles					
ν'_1/ν'_2 (°)	16	9	21	25	26
ν'_1/ν'_3 (°)	46	56	42	46	48
ν'_2/ν'_3 (°)	61	47	62	70	72
vibrational energies					
ν'_1 (cm^{-1})	1617	1612	1582	1611	1613
ν'_2 (cm^{-1})	1687	1679	1685	1668	1664
ν'_3 (cm^{-1})	1780	1745	1774	1779	1779
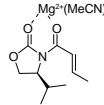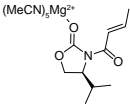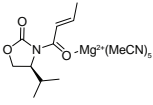
Table 15.4: *Summary of the DFT calculations (M06/6-31+G(d,p)/PCM/SDD/Bondi) of various **1**·SnCl$_4$ complexes in CH$_2$Cl$_2$.*

	1-spc-κ^2O,O'	1-spt-κ^2O,O'	1-apc-κO	1-apc-$\kappa O'$	1-apt-$\kappa O'$	1-apc-$1\kappa O,2\kappa O'$
angles						
ν_1'/ν_2' (°)	16	24	56	81	38	84
ν_1'/ν_3' (°)	46	20	80	20	44	5
ν_2'/ν_3' (°)	61	42	44	61	38	89
vibrational energies						
ν_1' (cm^{-1})	1617	1634	1691	1576	1581	1606
ν_2' (cm^{-1})	1687	1710	1724	1696	1709	1693
ν_3' (cm^{-1})	1780	1776	1766	1859	1865	1768
calculated Gibbs energies						
ΔG_{298} (kcal/mol)	0.0	6.5	8.4	6.7	10.2	_[i]

[i] The free energy of the di-tin-complex cannot be set into relation to the monocomplexes.

15.3 *N*-Crotonyloxazolidinone–Mg(MeCN)$_x$ Complexes
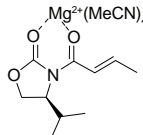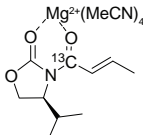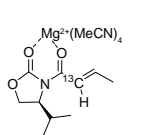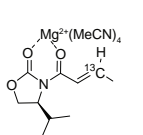
Table 15.5: *Summary of the DFT calculations (M06/6-31+G(d,p)/PCM/Bondi) of various* **1**·Mg(MeCN)$_x$ *complexes in MeCN.*

	1-spc-$\kappa^2 O, O'$	1-spt-$\kappa^2 O, O'$	1-apc-κO	1-apc-$\kappa O'$
angles				
ν_1^*/ν_2^* (°)	35	43	58	67
ν_1^*/ν_3^* (°)	40	26	26	8
ν_2^*/ν_3^* (°)	74	35	32	64
vibrational energies				
ν_1^* (cm^{-1})	1666	1679	1690	1673
ν_2^* (cm^{-1})	1707	1715	1744	1719
ν_3^* (cm^{-1})	1810	1806	1807	1836
calculated Gibbs energies				
ΔG_{298} (kcal/mol)[i]	0.0	5.2	_[i]	_[i]
ΔG_{298} (kcal/mol)[ii]	_[ii]	_[ii]	0.1	0.0

[i] The free energy of **1-spc-$\kappa^2 O, O'$**·Mg(MeCN)$_4$ was chosen as reference and set to 0.0 kcal/mol. The free energies of **1-apc-κO**·Mg(MeCN)$_5$ and **1-apc-$\kappa O'$**·Mg(MeCN)$_5$ cannot be set into relation to since they differ in the amount of complexing MeCN molecules.
[ii] The free energy of **1-apc-$\kappa O'$**·Mg(MeCN)$_5$ was chosen as reference and set to 0.0 kcal/mol. The free energies of **1-spc-$\kappa^2 O, O'$**·Mg(MeCN)$_4$ and **1-spt-$\kappa^2 O, O'$**·Mg(MeCN)$_4$ cannot be set into relation to since they differ in the amount of complexing MeCN molecules.

Table 15.6: *Summary of the DFT calculations (M06/6-31+G(d,p)/PCM/Bondi) of the isotopologues of* **1-spc-$\kappa^2 O, O'$**·Mg(MeCN)$_4$ *in MeCN.*

angles					
ν_1'/ν_2' (°)	35	6	40	59	63
ν_1'/ν_3' (°)	40	47	29	44	47
ν_2'/ν_3' (°)	74	34	68	77	70
vibrational energies					
ν_1' (cm^{-1})	1666	1663	1635	1652	1651
ν_2' (cm^{-1})	1707	1698	1701	1695	1692
ν_3' (cm^{-1})	1810	1774	1804	1809	1809

Chapter 16

NMR Spectroscopy[i]

16.1 Method

^{1}H, ^{13}C, and ^{119}Sn NMR spectra were recorded on a Bruker Avance III spectrometer ([1]H: 600.13 MHz; [13]C: 150.90 MHz; [119]Sn: 223.79 MHz) equipped with a 5 mm broadband Z-gradient probe (maximum gradient strength 53.5 G/cm). The [119]Sn chemical shifts were referenced against external SnMe$_4$ (δ([119]Sn) = 0.0 ppm). The temperatures for all measurements were calibrated with a Bruker methanol sample and were controlled by a Bruker BVT 3000 temperature unit. The data were collected and processed by TOPSPIN software (Bruker). The two-dimensional experiments were performed using Bruker standard pulse sequences and parameters. The phase-sensitive (TPPI method) ^{1}H NOESY were recorded using a mixing time of 1 s. [297] The experimental details of the NOESY experiment are summarized in Table 16.1.

16.2 Labels in the NMR Spectra

For the assignment, the NMR spectra are depicted with colored circles (^{1}H) or squares (^{13}C). Circles and squares depicted with "C" are the signals of the **1**·SnCl$_4$ complex; the ones with "F" are signals of free **1**. Signals that cannot be assigned to a single species due to fast exchange (motional averaging) are assigned with "E". Signals from water are marked with "∼", hydrolyzed SnCl$_4$ species are labeled with "∗", and signals from (silicon) grease are labeled with "#". [298] CHDCl$_2$ and CH$_2$Cl$_2$ lead to the signal at 5.3 ppm in the ^{1}H NMR spectra. The much smaller signals at 5.2 ppm and 5.5 ppm (^{1}H NMR) are due to coupling between the protons and the ^{13}C atoms in dichloromethane. In the ^{13}C NMR, dichloromethane causes the huge signal around 54 ppm.

---

[i]All NMR spectra were measured by Katharina M. Lippert and Heike Hausmann.

Table 16.1: *Experimental details of the* ^1H *NOESY experiments.*

F2 - Acquisition Parameters			Gradient Channel		
INSTRUM	spect		GPNAM1	SINE.100	
PROBHD	a5 mm PABBO BB-		GPNAM2	SINE.100	
PULPROG	noesygpph		GPZ1	40.00	%
TD	2048		GPZ2	–40.00	%
SOLVENT	CD2Cl2		P16	1000.00	μsec
NS	64				
DS	16		F1 - Acquisition Parameters		
SWH	8351.204	Hz	ND0	1	
FIDRES	4.082619	Hz	TD	256	
AQ	0.1225204	sec	SFO1	600.1924	MHz
RG (pure **1**)	1030		FIDRES	32.660954	Hz
RG (1:1 mixture)	406		SW	13.931	ppm
RG (3:1 mixture)	1030		FnMODE	States-TPPI	
DW	59.800	μsec			
DE	6.50	μsec	F2 - Processing Parameters		
TE	298.2	K	SI	1024	
d0	0.00004388	sec	SF	600.1900218	MHz
D1	1.41807902	sec	WDW	QSINE	
D16	0.00010000	sec	SSB	2	
D8	1.00000000	sec	LB	0.00	Hz
IN0	0.00011960	sec	GB	0	
ST1CNT	128		PC	1.40	
TAU	0.49890000	sec			
			F1 - Processing Parameters		
Channel f1			SI	1024	
NUC1	1H		MC2	States-TPPI	
P1	12.50	μsec	SF	600.1902218	MHz
p2	25.00	μsec	WDW	QSINE	
PL1	–2.00	dB	SBB	2	
SFO1	600.1923891	MHz	LB	0.00	Hz
			GB	0	

Chapter 17

Crystallography[i]

17.1 Method

A suitable crystal of **1** was mounted on a loop of a diffractometer (SuperNova, Dual, Cu at zero, Atlas). The crystal was kept at 173.1 K during data collection. Using Olex2, the structure was solved with the ShelXS structure solution program using direct methods and refined with the ShelXL refinement package using least squares minimization. [299,300] The crystal structure of **1** can be retrieved free of charge from the Cambridge Crystallographic Database (CCDC 867200).

17.2 Crystallographic Details of *N*-Crotonyloxazolidinone

The crystallographic data are summarized in Table 17.2 and 17.1. For more details see ref. [297] and the Cambridge Crystallographic Database (CCDC 867200).

Table 17.1: *Fractional atomic coordinates of the crystal structure of* **1**.

Atom	X $(10^{-4}a)$	Y $(10^{-4}b)$	Z $(10^{-4}c)$	U_{eq} (10^{-3}Å^2)
O12	4019(3)	2861(2)	3888.7(10)	43.6(4)
O13	820(3)	3052(2)	4306.5(9)	38.4(4)
O21	1196(3)	31(2)	2376.4(10)	44.6(5)
N11	1286(3)	1604(2)	3335(1)	33.2(4)
C12	2244(4)	2539(3)	3834.6(12)	35.1(5)
C14	−1209(4)	2574(3)	4071.4(13)	37.5(5)
C15	−808(4)	1247(3)	3569.8(12)	33.7(5)
C21	2137(4)	1003(3)	2695.1(13)	33.6(5)
C22	4078(4)	1647(3)	2426.0(13)	36.4(5)
C23	5042(4)	1062(3)	1861.1(14)	39.1(6)
C24	6996(4)	1636(3)	1547.7(15)	45.9(6)
C31	−972(4)	−280(3)	3934.2(14)	39.5(5)
C32	−3222(5)	−594(3)	4131.3(17)	50.3(7)
C33	410(5)	−447(3)	4601.4(15)	48.3(7)

---

[i]The crystal structure was measured and analyzed by Frank Hampel (Friedrich-Alexander-University Erlangen-Nürnberg).

Table 17.2: *Crystal data and structure refinement of **1**.*

Identification code	PRS01_2
Empirical formula	$C_{10}H_{1}5NO_3$
Molecular weight	197.23 g/mol
Temperature	173.1 K
Crystal system	orthorhombic
Space group	$P2_12_12_1$
a	6.5299(6) Å
b	8.9959(9) Å
c	18.2744(16) Å
α	90.00°
β	90.00°
γ	90.00°
Volume	1073.48(17) Å^3
Z	4
ρ_{calc}	1.220 mg/mm^3
m	0.743 mm^{-1}
F(000)	424
Crystal size	$0.14 \times 0.07 \times 0.02$ mm^3
2Θ range for data collection	9.68° to 146.84°
Index ranges	$-7 \leq h \leq 8, -10 \leq k \leq 11, -7 \leq l \leq 21$
Reflections collected	3169
Independent reflections	2046[R(int) = 0.0385]
Data/restraints/parameters	2046/0/131
Goodness-of-fit on F2	1.068
Final R indexes [I $\geq 2\sigma$(I)]	R$_1$ = 0.0516, wR$_2$ = 0.1213
Final R indexes [all data]	R$_1$ = 0.0610, wR$_2$ = 0.1304
Largest diff. peak/hole	0.197 eÅ^3/−0.205 eÅ^3
Flack Parameter	0.0(17)

Chapter 18

Sample Preparation

18.1 Structure Determination of Reactive Intermediates

18.1.1 Oxazolidinone Synthesis[i]

All materials were obtained from commercial suppliers and were used without further purification, unless noted otherwise. (S)-4-Isopropyl-oxazolidin-2-one was prepared as described by Benoit *et al.*[212] (4S)-3-((E)-2-Butenoyl)-4-(1-methylethyl)-2-oxazolidinone (**1**) was synthesized following the protocol of Evans *et al.*[173] and stored under reduced pressure in a desiccator over P_2O_5. The enantiomeric purity was determined by polarimetry and was identical to that reported by Evans *et al.*[173] Tetrahydrofuran was dried over KOH, then distilled from sodium and stored under argon over sodium. Purification of **1** was achieved by flash chromatography (silica gel 60; particle size 230-400 mesh). Commercial, dry $Mg(ClO_4)_2$ was dried further for 4 hours at $104\,^{\circ}C$ and 10^{-3} mbar prior to use.

18.1.2 Sample Preparation for the 2D-IR and FTIR Measurements

For the 2D-IR and FTIR measurements of **1** a 37 mM solution in the denoted solvent was used. The **1**·$SnCl_4$ complex was prepared by solving **1** (6.3 mM) and tin(IV) chloride (47 mM) in CH_2Cl_2. Partial complexation was achieved in a 1:1 solution of **1** and $SnCl_4$ (24 mM) in CH_2Cl_2. The **1**·$Mg(MeCN)_x$ complex was prepared by solving **1** (34 mM) and dry $Mg(ClO_4)_2$ (0.38 mM) in dry MeCN. The solution was shaken with molecular sieve for 12 hours to remove residual water. The solutions then were suck into the flow cell using a small syringe.

---

[i]**1** was synthesized and provided by Katharina M. Lippert and Kira Hof, Group of Peter R. Schreiner, Liebig University Giessen

18.1.3 Sample Preparation for the NMR Measurements[ii]

For the NMR investigations, CD_2Cl_2 was dried over molecular sieve (4 Å). A $SnCl_4$ solution in CH_2Cl_2 (1 M) was purchased from Sigma Aldrich. All substances were filled into oven dried NMR tubes under positive argon pressure. The samples were additionally degassed through three freeze/thaw cycles and then the NMR tubes were melted off.

18.2 Conformational Dynamics of Proteins

Sperm whale Mb (wild type) as well as the mutants L29W Mb, V68W Mb and YLT were kindly provided by Karin Nienhaus (group of G. Ulrich Nienhaus, Karlsruhe Institute of Technology). The Mb samples were already dissolved in phosphate buffer, reduced with sodium dithionite, and loaded with CO. They were stored at –21 °C. Directly before the measurements, the sample was thawed and aerated again with carbon monoxide for two hours using the setup shown in Fig. 18.1. Immediately before the measurement, the sample was centrifuged to avoid scattering and filled into a flow cell with an optical pathlength of 100 μm.
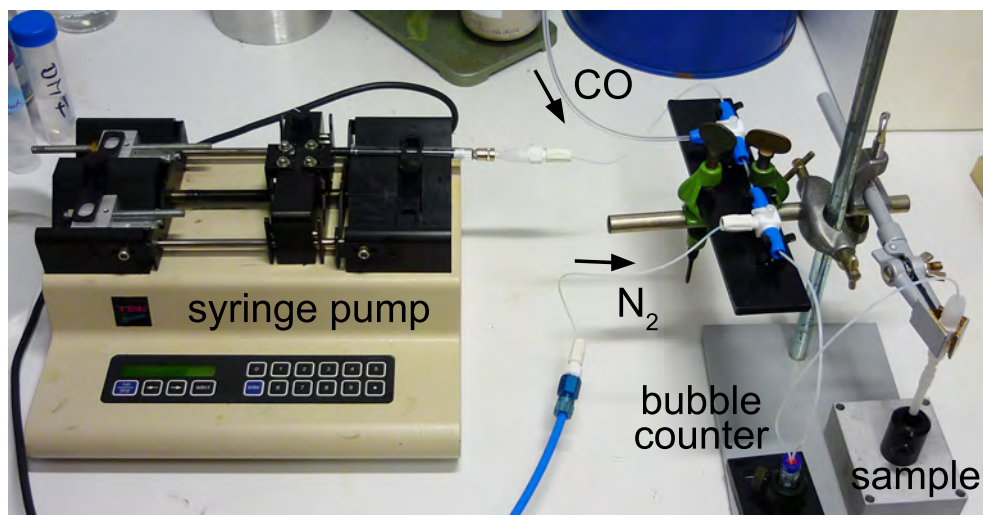
Figure 18.1: *Setup for flushing the Mb sample with nitrogen and carbon monoxide.*

The Mb mutant L29I was kindly provided as freeze-dried sample by Karin Nienhaus (group of G. Ulrich Nienhaus, Karlsruhe Institute of Technology). It was stored at room temperature until usage. All other chemicals were obtained from commercial suppliers and used without further purification. A potassium buffer was prepared by dissolving 0.13 g KH_2PO_4 and 0.25 g K_2HPO_4 in 10 ml D_2O. The pD value of the buffer solution was 7.0. For the EXSY-2D-IR measurements, 21.4 mg of the powder were added to 45 μl of potassium phosphate buffer in a small glass vial and sealed afterwards. It was crucial that the Mb powder was added subsequently (and slowly) to the buffer while stirring and not *vice versa*. It is also not recommended to vortex the sample. Dissolving Mb completely took approximately two hours. The sample was

---

[ii]All NMR spectra were measured by Katharina M. Lippert and Heike Hausmann

stirred slowly for an additional hour while the vial was flushed with nitrogen using the setup illustrated in Fig. 18.1 to get rid of oxygen in the solution. Afterwards, the sample was flushed intensely with carbon monoxide for approximately ten minutes such that no nitrogen remained in the setup and additional 20 min at a flushing rate of 4 ml/h. 5 μl of a freshly prepared sodium dithionite solution (120.4 mg $Na_2S_2O_4$ in 500 μl sodium phosphate buffer) were dripped to the Mb solution while still stirring and flushing with carbon monoxide. The solution turned red upon reduction of the Mb. It was important that the sodium dithionite solution was dripped directly into the Mb solution and did not run down along the wall of the vial. Finally, the solution was stirred and flushed with carbon monoxide (1 ml/h) for additional four hours to complete CO binding.

The flow cell with an optical path length of 100 μm was first completely filled with D_2O and after also the spacer became wet completely the cell was dried with nitrogen. Subsequently, a syringe was added to the tube and sealed gas tight. Then the whole cell including the syringe was twice filled with nitrogen and thereafter filled twice with carbon monoxide. Directly before the measurement, the solution was centrifuged for 2 min at 7000 rpm and sucked into the prepared flow cell using a syringe.

Some of the L29I samples were prepared slightly differently leading to different sample concentrations. The general procedure however was the same.

Chapter 19

Analysis of the Myoglobin Data

All measured spectra were background corrected using a background recorded at negative delay times, *i.e.*, when the probe pulse hits the sample before the pump pulse or recorded at very long delay times, where the signals decayed already. Typically, negative delay times were used as background for 2D-IR spectra with a short delay time (less than 25 ps) and very long delay times were used as background for the 2D-IR spectra with delay times longer than 25 ps. For the time scans, usually very long delay times were used to reduce the offset due to sample heating at long delay times where the signal was small.

Because pixel number 5 regularly led to artifact signals, the measured signal at pixel 5 was replaced after the measurement by the average of the signals measured at pixel 4 and 6 for the measurements of L29I MbCO, wild type MbCO, L29W MbCO, and YLT MbCO. In addition, the signal measured at pixel 10 was replaced by the average of the signals measured using pixel 9 and 11 for the measurements of L29I MbCO.

The 2D-IR spectra of YLT MbCO shown in Fig. 13.4 and 13.5 were measured in two blocks and merged (at 1948 cm^{-1}) without any changes to the signal size.

19.1 Fit of the Spectra (L29I Myoglobin)

The cuts through the 2D-IR spectra and the broadband pump-probe spectra of L29I MbCO were fitted by a script written in *Mathematica 7.0* using the implemented function *NonlinearModelFit*. Each single spectrum was fitted with four Gaussians and an offset. Gaussian line shape was assumed because the FTIR spectra also could be fitted very well with two Gaussians. Thus it is expected to reproduce the line shape in the broadband pump-probe spectra very well. For the cuts through the pump-probe 2D-IR spectrum the measured line shape will deviate from Gaussian for small delay times though because the initial band shape is a convolution of the Lorentzian shaped pump pulse and the Gaussian shaped absorption band of the molecule. Due to spectral diffusion, the band shape will change towards the band shape observed in the broadband pump-probe spectra with increasing delay time. Even though it is known for the 2D-IR cuts that the line shape will change, Gaussian line shape is assumed for all spectra to make the fit more robust.

For all four Gaussians the central frequencies and the line widths were fitted individually. The area of the positive and the negative part of one peak were linked together to assure that they have the same intensity. Including the offset, eleven parameters were fitted to each spectrum consisting of 31 data points (from which only 29 were independent to each other because of the corrections described before).

The broadband fits converge fastest and most reliable if the spectrum of the first delay time is fitted roughly by eye to find appropriate starting values keeping the offset to zero. Based on these starting values, only the areas of the bands were fitted initially. In a subsequent step, all parameters were fitted using the manual line shapes and the initially fitted band areas as starting values.

The fit of the broadband pump-probe spectrum recorded with a delay time of 2 ps is shown in Fig. 19.1 for illustration. The fitted function (gray line) is overlaid with the measured data points (black crosses). The individual fitted bands are shown by the colored lines (cyan, blue, orange, and red), the offset by the green line. The main error source for the fit of the spectrum and thus the obtained band areas, the information required for the analysis of the conformational dynamics, is that the bands are not completely covered by the measurement. Especially the band at lowest wavenumber (cyan fit) is cut more than half.
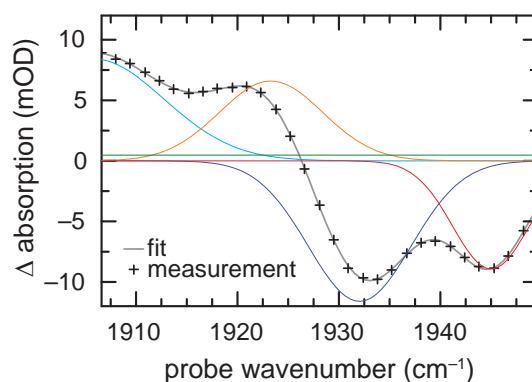
Figure 19.1: *Fit of the measured broadband pump-probe spectrum of L29I MbCO (2 ps). The measured data are shown as crosses, the fits of the single bands, the offset and the entire spectrum are shown by the lines.*

The fitted parameters for all delay times are shown in Fig. 19.2 for the fit of the broadband spectra measured at 20° C. The evolution of the single parameters is a good basis to judge consistency of the fit. If the parameters would strongly vary and not relate to the parameters of the fits for similar delay times, the validity of the obtained areas would be questionable. However, if the single parameters vary only little between the different spectra, as it is the case here, the fit is consistent and the retrieved areas are trustworthy. The parameters for the line widths and band positions are almost constant. Slight systematic changes in the band positions are probably due to heating of the sample. Also the time dependence of the offset is mainly caused by heating of water. The initial offset was also directly observed by comparing the signal at negative delay times and very long delay times. An additional contribution to the offset may be caused by fit artifacts, which could have their origin in band shapes deviating from being Gaussian and and the fact that the bands are not measured completely but cut.
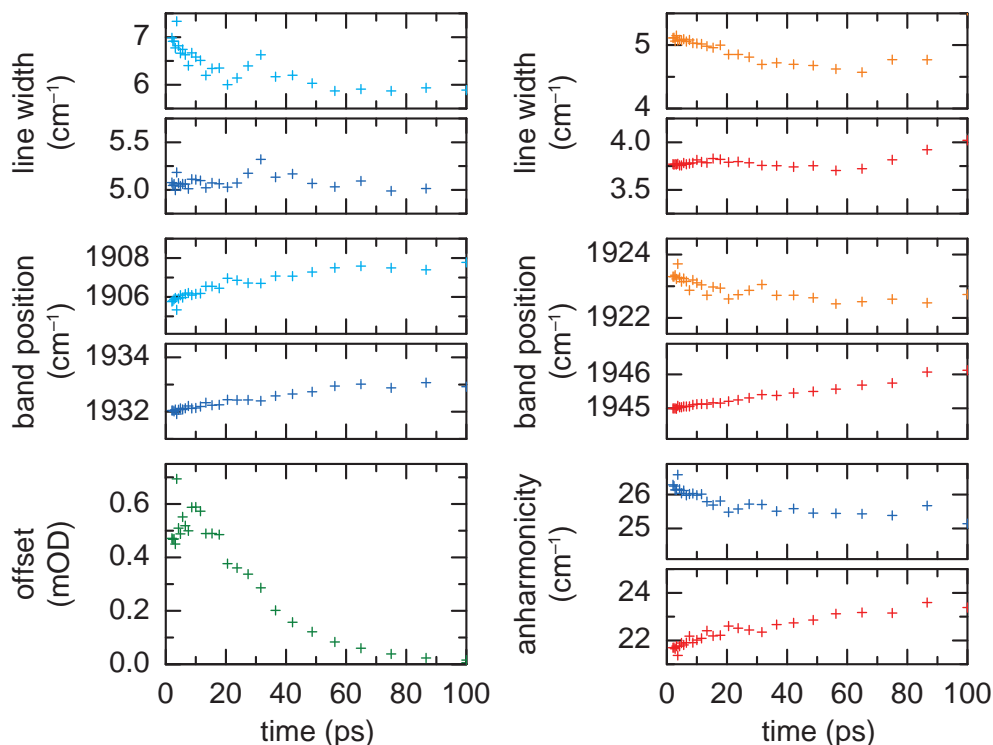
Figure 19.2: *Time dependence of the fitted line widths, central wavenumbers, and offset for the broadband pump-probe spectra (20°C). The colors correspond to the colors of the bands in Fig. 19.1.*

The fit of the 2D-IR cuts, the narrowband pump-probe spectra, is based on the broadband fit described above. For each spectrum, the fitted broadband spectrum was used to start with. The areas were then fitted keeping the bands constant and forcing the offset to be zero. In a subsequent step, the band positions were additionally fitted – using the last fit as starting point and restricting the bands to move $2\,\mathrm{cm}^{-1}$ at most. Finally, all parameters were fitted to each spectrum. In this fit, the central wavenumber of the bands was still restricted to deviate $2\,\mathrm{cm}^{-1}$ at most. Additionally the maximal allowed line width was the maximal bandwidth of the broadband fit plus $0.1\,\mathrm{cm}^{-1}$. These restrictions were required to assure that the bands do not get artificially broad to compensate the non–Gaussian shape of the initially excited peak, which is at short delay times $\sim$4 times as intense as the other peak. Despite these restrictions, it is still likely that up to a certain extend the fit results in slightly too big line widths and consequently too large band areas for the weaker signals (the cross peak).

For this fit, the evolution of the parameters also provides a reliable basis to judge the consistency of the fit. Figure 19.3 shows the evolution of the parameters for the fit of the 2D-IR cut at pump position 2 ($1946\,\mathrm{cm}^{-1}$) measured at $20\,°\mathrm{C}$. The initially pumped band (red data points) shift within the first $10\,\mathrm{ps}$ from the initially pumped wavenumber to the central wavenumber of the band and broadens at the same time. This is expected because of spectral diffusion. The final band position and line shape agree to the broadband spectrum. The fit of the cross peaks (blue and
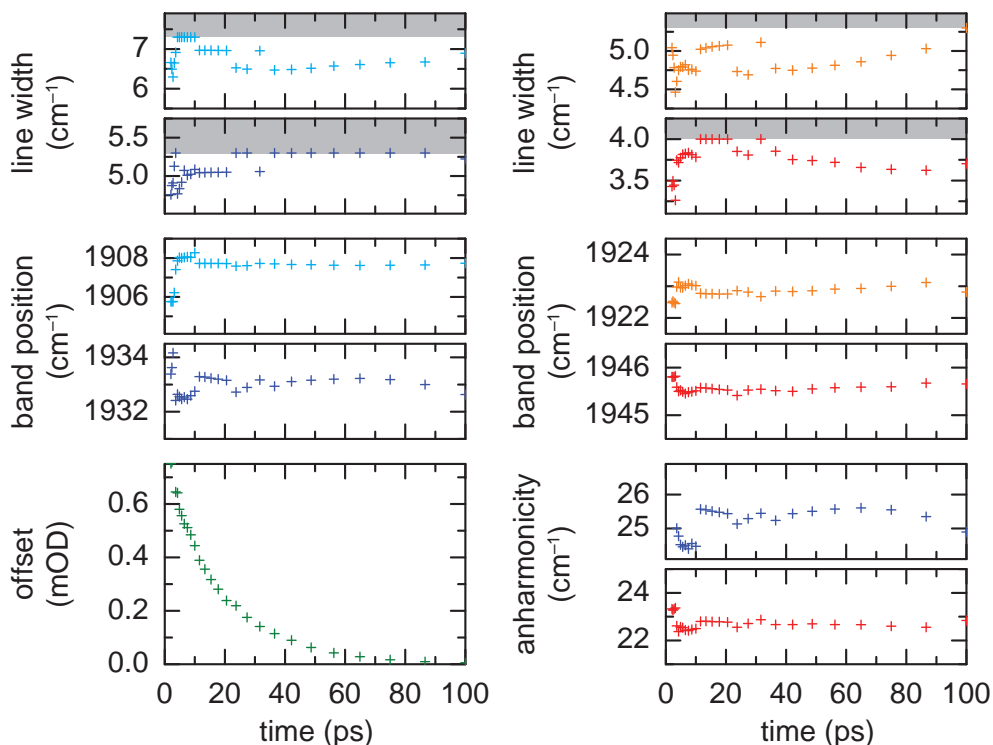
Figure 19.3: *Time dependence of the fitted line widths, central wavenumbers, and offset for the EXSY-2D-IR cut at pump position 2 (A_1, $20\,°C$). The colors correspond to the colors of the bands in Fig. 19.1. The gray shaded regions were not allowed in the fit.*

cyan data) also show an initial (within the first 5 ps) wavenumber drift, accompanied by fluctuations of the line width. These fluctuations indicate that a considerable part of the band is used to compensate for differences between the real line shape and the fitted Gaussians. The offset additionally compensates for the these deviations. Heating of the sample as it was observed using broadband pump pulses had only a negligible impact when using narrowband pump pulses.

The error on the band areas caused by the line shape is estimated to be less than 15% for delay times below 5 ps and decreasing rapidly with increasing delay time. In order to reduce this error significantly two main experimental changes would be needed: First of all, a higher spectral resolution in combination with the ability to measure the spectral region of interest completely. This would allow to judge the line shape more precisely and would increase the number of data points per parameter. Secondly, an excitation with Gaussian shaped pump pulses (instead of Lorentzian shaped ones) would be preferential because the convolution of two Gaussians again is a Gaussian.

19.2   Fit of the Population Dynamics

The population dynamics of L29I MbCO were fitted according to the model introduced in chapter 12.2. The model neglects rotational diffusion of the protein. The

rotational diffusion of Mb can be neglected since it is orders of magnitude slower than the longest delay time measured (100 ps *vs.* 10 ns).[301] Additionally, the model indirectly assumes that the carbonyl group does not change its orientation when the protein changes its conformation because it does not account for the polarization dependence of the spectra. The spectra were measured with parallel relative polarization of pump and probe pulses to maximize the signal instead of measuring at magic angle, for which the signal size is independent of the orientations. This is in accordance to literature where the carbonmonoxide orientation was found to differ not significantly between the states A_1 and A_3.[113,302]

The areas of the bands received by the fit of the spectra described in chapter 19.1 were fitted using a self written *Mathematica 7.0* fit routine mainly based on a slightly modified version of the function MRFit, a multiple-response fitting tool (http://library.wolfram.com/infocenter/TechNotes/280/). This routine facilitated the simultaneous fit of all areas (diagonal and cross peak intensity for both pump positions and the intensity of both bands in the broadband pump-probe spectra). In order to account for the information content cross peaks were weighted 5 times stronger than diagonal peaks. The signals in the broadband spectra were weighted twice. To compensate for intensity differences between the different sets of spectra, the signals of each spectrum were additionally weighted. The weighting factor was determined by the inverse of the fitted intensity of both bands at 0 ps. These weighting factors were adjusted iteratively (manually) until intensity and scaling factor matched.

The starting values for the fit were determined as follows: The scaling factors, *i.e.*, the initial intensities of the band was the the sum of the areas of both bands for the shortest delay time evaluated (2 ps). The start populations were calculated by the fraction of the corresponding band of the total intensity for the shortest delay time. The relaxation constants were obtained by a monoexponential fit of the decay of the signals in the broadband spectra from 2 ps to 10 ps. The start value for the exchange rate from A_3 to A_1 was set to 50 ps.

The equilibrium constant and the relative transition dipole moments of the CO vibrations were not fitted. The transition dipole moments were assumed to be equal for both states, *i.e.*, the relative transition dipole moment was fixed to 1. Using this assumption, the equilibrium constant was derived from the FTIR measurements (see Fig. 12.6) by fitting the band areas and deriving the equilibrium populations (see chapter 12.4).

The results of all fits are summarized in Table 19.1.

In order to estimate the error bars on the exchange rates, fits of the data measured at 20 °C with various fixed exchange rates were performed. The fits for exchange rates $t_{ex}(A_3)$ of 43.5 ps (dotted lines), 86.9 ps (colored lines), and 174 ps (dashed lines) are compared in Fig. 19.4. The fits based on half the exchange time (dotted lines) and based on twice the exchange time (dashed line) deviated considerably from the experimental data. The deviations are best seen in the lower graphs where the relative cross peak intensity (cross peak intensity / diagonal peak intensity) is plotted. From this comparison it can be concluded that the exchange rate is definitely within half the obtained rate and twice the obtained rate. A more precise refinement is not possible, basically because the measured areas at short delay times have an error in the range of 10% to 15% as discussed above. Even though this error is quite large, on the logaritmic scale in Fig. 12.11 it appears neglible. The accuracy of the relaxation times is estimated to be ±3 ps based on various fits with different weighting factors for the spectra.

Table 19.1: *Summary of the input parameters, all fitted parameters, and the derived parameters for the fit of the population dynamics of L29I MbCO.*

Temperature	0 °C	10 °C	20 °C	30 °C	40 °C
input parameters					
ϵ_{rel}	1	1	1	1	1
K	0.946	0.930	0.904	0.888	0.878
fitted parameters					
$T_1(A_1)$ (ps)	17.0	16.6	16.7	16.1	14.4
$T_1(A_3)$ (ps)	19.0	18.6	18.8	19.3	19.7
$t_{ex}(A_3)$ (ps)	136	116	86.9	94.8	69.6
$[A_3]_0$ (pump 1)	0.837	0.846	0.853	0.822	0.819
$[A_1]_0$ (pump 2)	0.230	0.226	0.260	0.248	0.247
$[A_3]_0$ (broadband)	0.614	0.624	0.633	0.633	0.638
scaling factor pump 1	48.9	169.4	247.5	58.2	54.3
scaling factor pump 2	43.7	153.5	205.4	52.1	49.9
scaling factor broadband	225.9	272.0	271.8	264.1	265.3
derived parameters					
$t_{ex}(A_1)$ (ps)	129	108	78.6	84.1	61.1
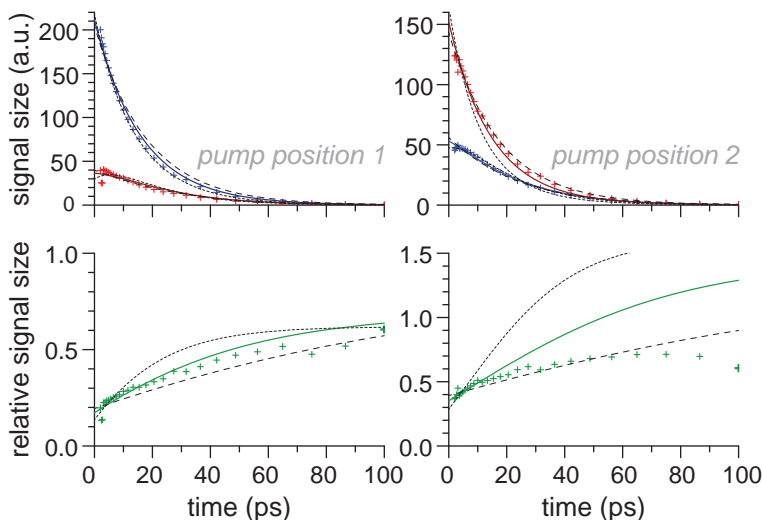
Figure 19.4: *Fitted signal intensities in the EXSY-2D-IR cuts of L29I MbCO at 20 °C assuming various exchange rates. Colored lines: Free fit of the experimental data. Dashed lines: Fit assuming a two fold slower exchange rate. Dotted lines: Fit assuming a two fold faster exchange rate. The experimental data are shown as crosses. At the bottom the relative cross peak intensities (cross peak intensity / diagonal peak intensity) are illustrated.*

For the fit used and described above it has been assumed that the transition dipoles moments of the CO vibration in both states are the same. Even though this assumption is quite common, there is to our best knowledge no experimental proof for it. A study comparing the transition dipole moments of various Mb mutants found that the transition dipole moments of the bound CO vary up to 20%. [303] Thus it may be reasonable that the transition dipole moments of the CO vibration vary between the different states. In an alternative fit, the transition dipole moment was left free. The ratio of the band intensities in the FTIR spectrum was used to retain the product $K \cdot \epsilon_{rel}$. The start population of the state A_3 in the broadband pump-probe spectrum was calculated by:

$$[A_3]_0 = \frac{1}{1 + K\epsilon_{rel}}. \tag{45}$$

The fit parameters are summarized in Table 19.2. Using this fit, the exchange times vary only slightly compared to the fit assuming $\epsilon_{rel} = 1$ and are the same within the estimated error. The fitted total exchange rates,

$$k_{obs} = 1/t_{ex}(A_3) + t_{ex}(A_1), \tag{46}$$

are compared with each other for the two different fits in Table 19.3. The two fit curves are compared in Fig. 19.5 for the measurement at 20 °C. There is hardly any difference observable by eye.

The precision of the fits of the population dynamics could be improved significantly by the experimental improvements discussed in chapter 19.1. Additionally, the use of shorter pump pulses, *e.g.*, Gaussian shaped pulses, would allow to measure shorter time delays. At short time delays the dynamics of the cross peak is dominated by the exchange process (leading to an increase of the signal size) and only later on

Table 19.2: *Summary of the input parameters, all fitted parameters, and the derived parameters for the alternative fit of the population dynamics of L29I MbCO.*

Temperature	0 °C	10 °C	20 °C	30 °C	40 °C
input parameters					
$K \cdot \epsilon_{rel}$	0.946	0.930	0.904	0.888	0.878
fitted parameters					
ϵ_{rel}	0.649	0.631	0.629	0.638	0.632
$T_1(A_1)$ (ps)	17.4	17.2	17.5	16.9	15.5
$T_1(A_3)$ (ps)	18.4	18.0	18.3	18.7	19.2
$t_{ex}(A_3)$ (ps)	106	90.8	68.0	76.7	58.4
$[A_3]_0$ (pump 1)	0.771	0.777	0.785	0.748	0.742
$[A_1]_0$ (pump 2)	0.162	0.156	0.182	0.176	0.176
scaling factor pump 1	54.4	189.4	277.3	65.6	61.8
scaling factor pump 2	60.9	217.9	286.0	72.2	68.8
scaling factor broadband	274.2	332.9	332.3	320.1	321.8
derived parameters					
K	1.46	1.47	1.44	1.39	1.39
$t_{ex}(A_1)$ (ps)	154	134	97.7	107	81.2
$[A_3]_0$ (broadband)	0.514	0.518	0.525	0.530	0.532
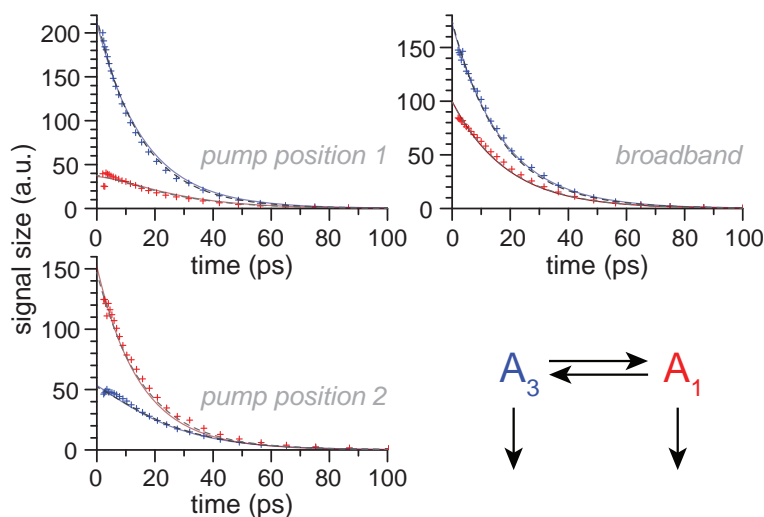
Figure 19.5: *Fitted signal intensities in the EXSY-2D-IR cuts and broadband pump-probe spectra at 20° C. Colored lines: Fit of the experimental data assuming the same transition dipole moments for both A_1 and A_3. Dashed lines: Fit of the experimental date keeping the transition dipole moments free. The experimental data are shown as crosses.*

Table 19.3: *Comparison of the fitted exchange rates k_{obs} for the two different fits.*

| | $\epsilon_{rel} = 1$ | | ϵ_{rel} fitted | |
Temperature	k_{obs} $(10^9 \mathrm{s}^{--1})$	$\log(k_{obs})$	k_{obs} $(10^9 \mathrm{s}^{--1})$	$\log(k_{obs})$
0 °C	15.1	10.2 ± 0.3	15.9	10.2 ± 0.3
10 °C	17.9	10.3 ± 0.3	18.5	10.3 ± 0.3
20 °C	24.1	10.4 ± 0.3	24.9	10.4 ± 0.3
30 °C	22.4	10.4 ± 0.3	22.4	10.4 ± 0.3
40 °C	30.7	10.5 ± 0.3	29.4	10.5 ± 0.3

vibrational relaxation gets dominating (leading to the decrease of the signal). This is the case even if the exchange process is slower than the relaxation process, which is common in EXSY-2D-IR spectroscopy. Especially for slow exchange processes like observed in Mb it is desirable to get rid of the signal decay caused by vibrational relaxation (T_1 relaxation). This could become possible using a double resonance experiment, where the initial vibrational excitation is transfered selectively to a longer lived state.[246]

The most significant impact on the precision of the obtained exchange rates would have the selective excitation the individual bands . When measuring cuts, this would need narrower pump pulses, which however would be longer in time. Here again, Gaussian shaped pulses would be beneficial. If a completely selective excitation is not possible, *e.g.*, because of too strong band overlap, a precise measurement of the pump pulse spectra and the broadband OPA spectrum would allow to calculate the start populations of the bands and thus reduce the amount of parameters to be fitted.

Global fit analysis for the spectra is not usable for the set of spectra because the line shape of the bands in the EXSY-2D-IR cuts change. This would induce severe fit artifacts in global fit analysis.

19.2.1 Temperature Dependence

The fits of the the spectra measured from $0\,°C$ to $40\,°C$ are illustrated in Fig. 19.6. The band areas are scaled by the scaling factor. Thus the curves represent the population in the states (as $\epsilon_{rel} = 1$). The experimental data scaled with the same factors are shown for comparison on the right.

19.2.2 Simulation of the Spectra

For the simulation of the spectra, the line shapes and band positions of the broad-band pump-probe spectra at a delay of $2\,ps$ were used as basis (spectral diffusion was not accounted for in the simulation). For simulating the population dynamics and thus the band areas, the same model as for the fit of the population dynamics described in chapter 12.2 and 19.2 was used. The relaxation rates and the start populations were adopted from the fits. The equilibrium constants were retrieved from the FTIR measurements. The exchange rates were computed based on the exchange rate measured for $20\,°C$ and the gradient of the fit found by Johnson *et al.* for the temperature dependence of the exchange rates of wild type MbCO at low temperatures (see Fig. 11.2).[263] Table 19.4 summarizes all used time constants for calculating the population dynamics at the various temperatures.

Table 19.4: *Summary of the time constants for the simulation of the 2D-IR cuts at various temperatures.*

Temperature	$0\,°C$	$10\,°C$	$20\,°C$	$30\,°C$	$40\,°C$
$T_1(A_1)$ (ps)	17.0	16.6	16.7	16.1	14.4
$T_1(A_3)$ (ps)	19.0	18.6	18.8	19.3	19.7
$t_{ex}(A_3)$ (ps)	1068	285	86.9	29.7	11.2
$t_{ex}(A_1)$ (ps)	1010	265	78.6	26.4	9.89

The simulations are opposed to the measurement in Fig. 19.7. The differences between the simulation and the measurement are more evident in Fig. 12.13, where the spectra are scaled to the initially pumped band.
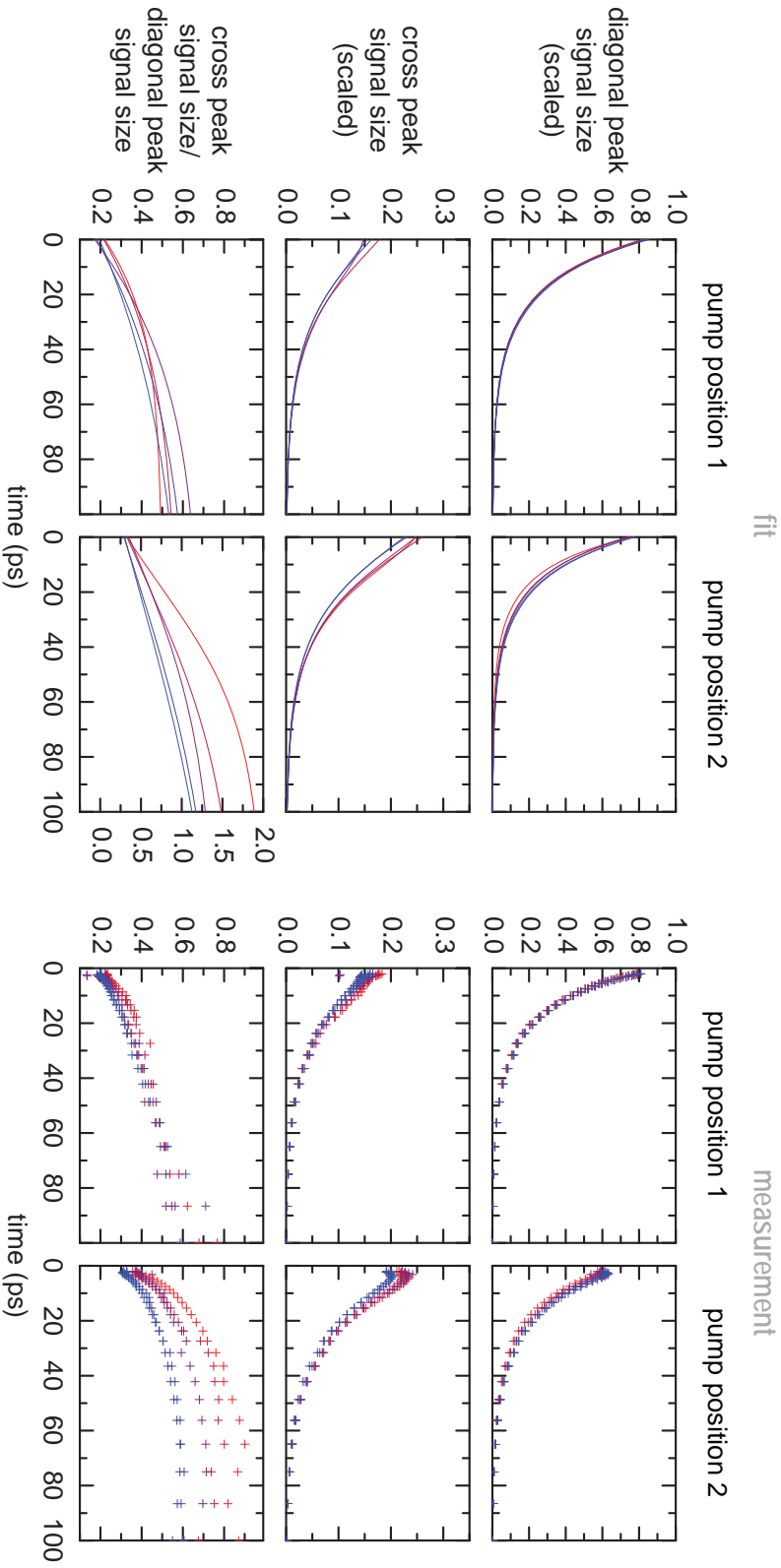
Figure 19.6: *Left: Fitted population dynamics in the EXSY-2D-IR cuts and the broadband pump-probe spectra as a function of temperature. Right: Time dependence of the signal intensities (band areas) in the EXSY-2D-IR cuts and the broadband pump-probe spectra as a function of temperature. The temperatures vary from 0° C (blue) to 40° C (red) in steps of 10° C. The band areas are obtained by the fits illustrated in Fig. 12.8. For comparison, the signal intensities are scaled by the scaling factor obtained in the fit. Assuming equal transition dipole moments for A_1 and A_3, the scaled intensities correspond directly to the populations.*
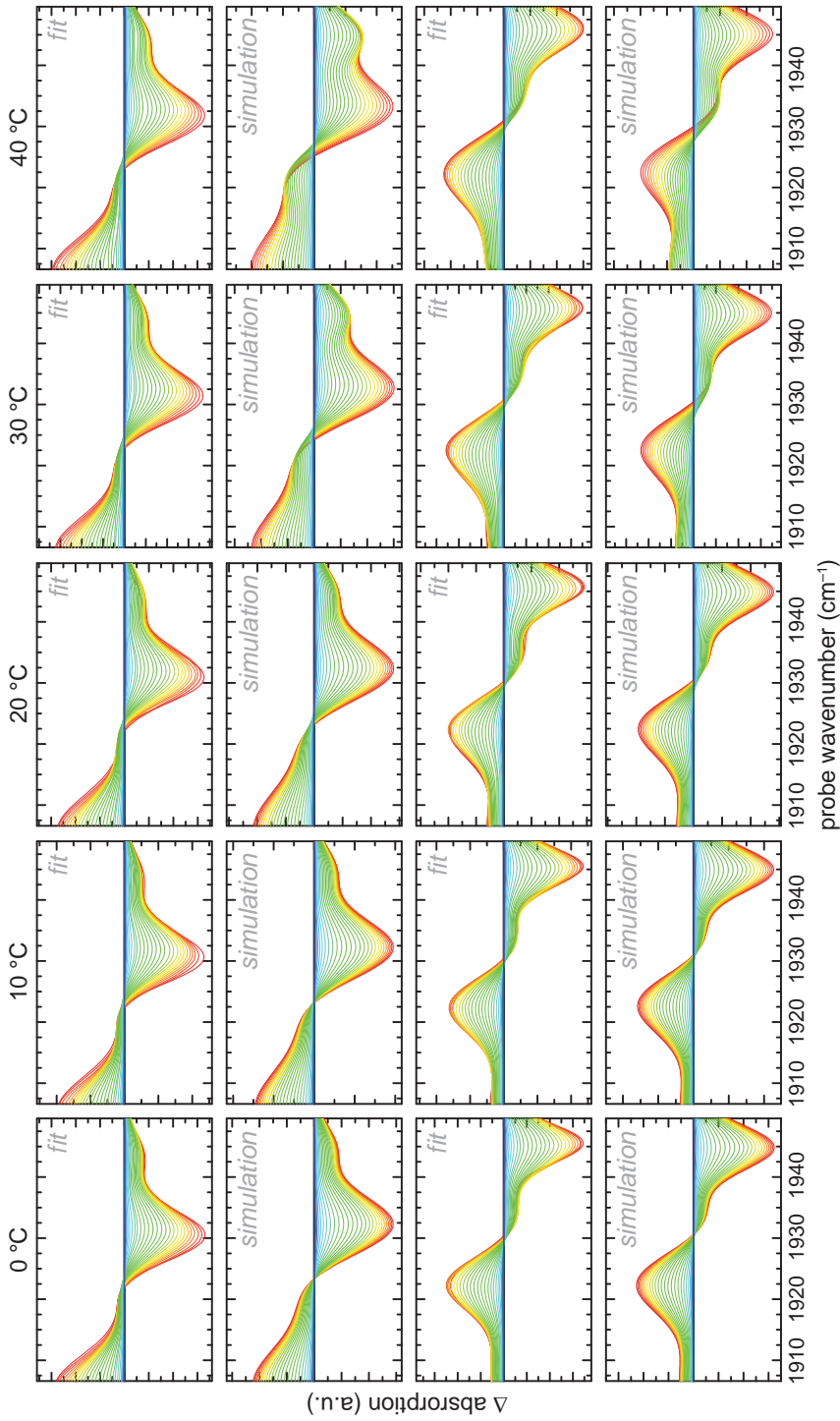
Figure 19.7: *Comparison between fitted and simulated EXSY-2D-IR cuts for the various temperatures. The simulations are based on the simulated population dynamics shown in Fig. 12.12 assuming the same temperature dependence as observed for low temperatures in wild type MbCO and the exchange rate measured at 20° C. The scaled spectra are shown in Fig. 12.13).*

Chapter 20

Additional Myoglobin Spectra

20.1 Wild Type Myoglobin
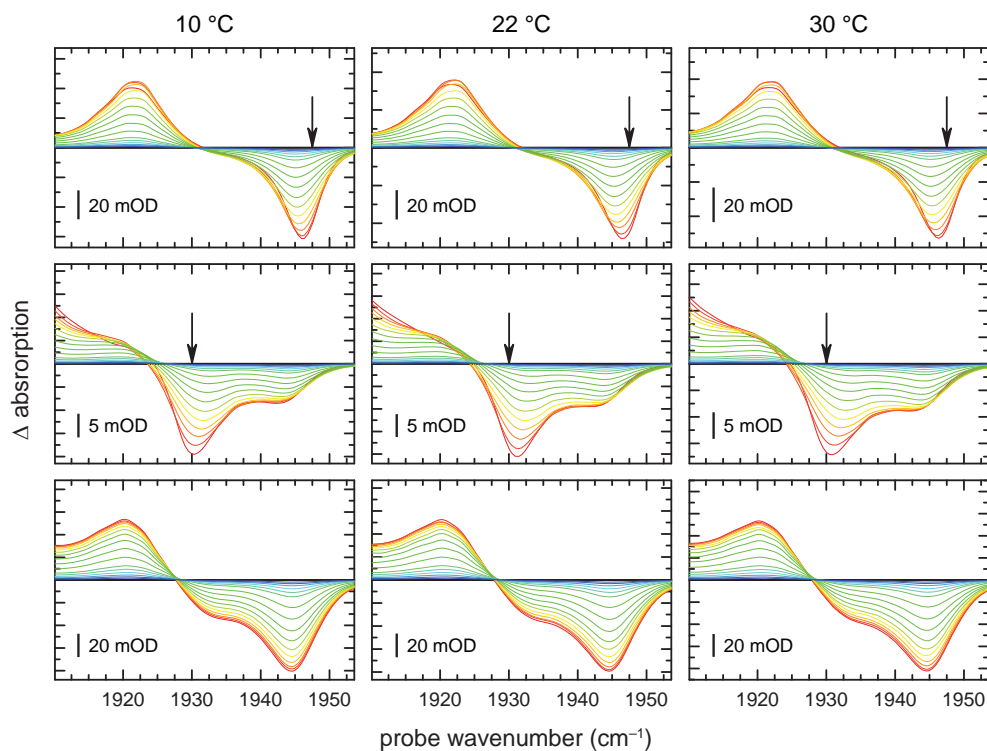
Figure 20.1: *Temperature dependent EXSY-2D-IR cuts (top and middle) and broadband pump-probe spectra (bottom) of MbCO (wild type). The arrows indicate the positions of the narrowband pump pulses. The delays between pump and probe pulses were varied from 2 ps (red) to 75 ps (blue). Background: –5 ps.*
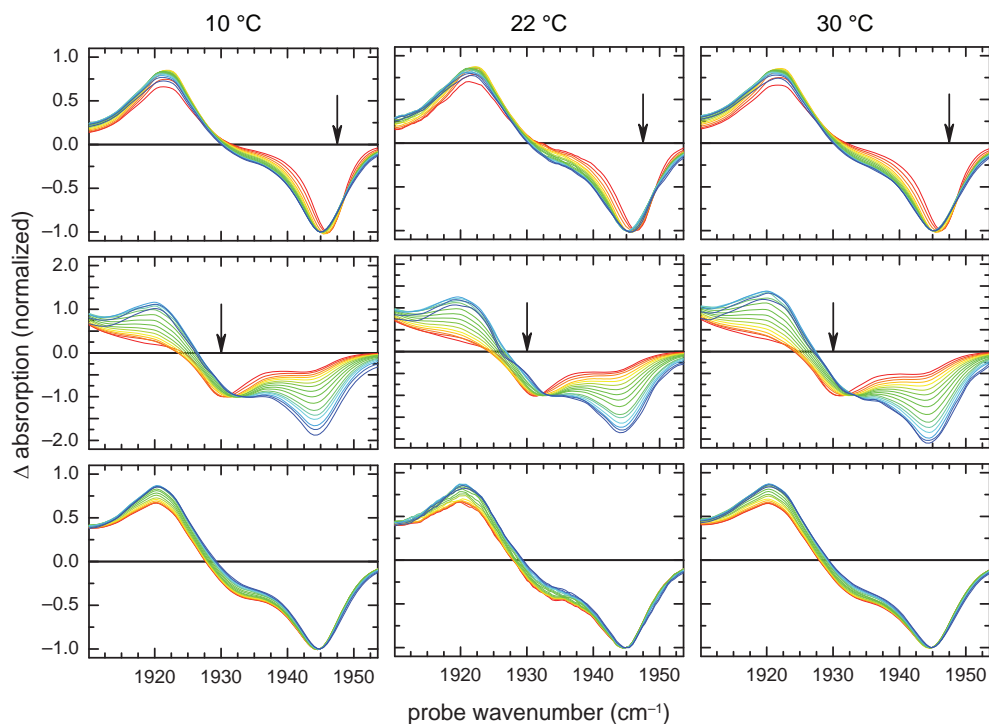
Figure 20.2: *Temperature dependent EXSY-2D-IR cuts (top and middle) and broadband pump-probe spectra (bottom) of MbCO (wild type). The arrows indicate the positions of the narrowband pump pulses. The delays between pump and probe pulses were varied from 2 ps (red) to 75 ps (blue). Background: –5 ps. The spectra are scaled to the intensity of a specific band.*

20.2   L29I Myoglobin
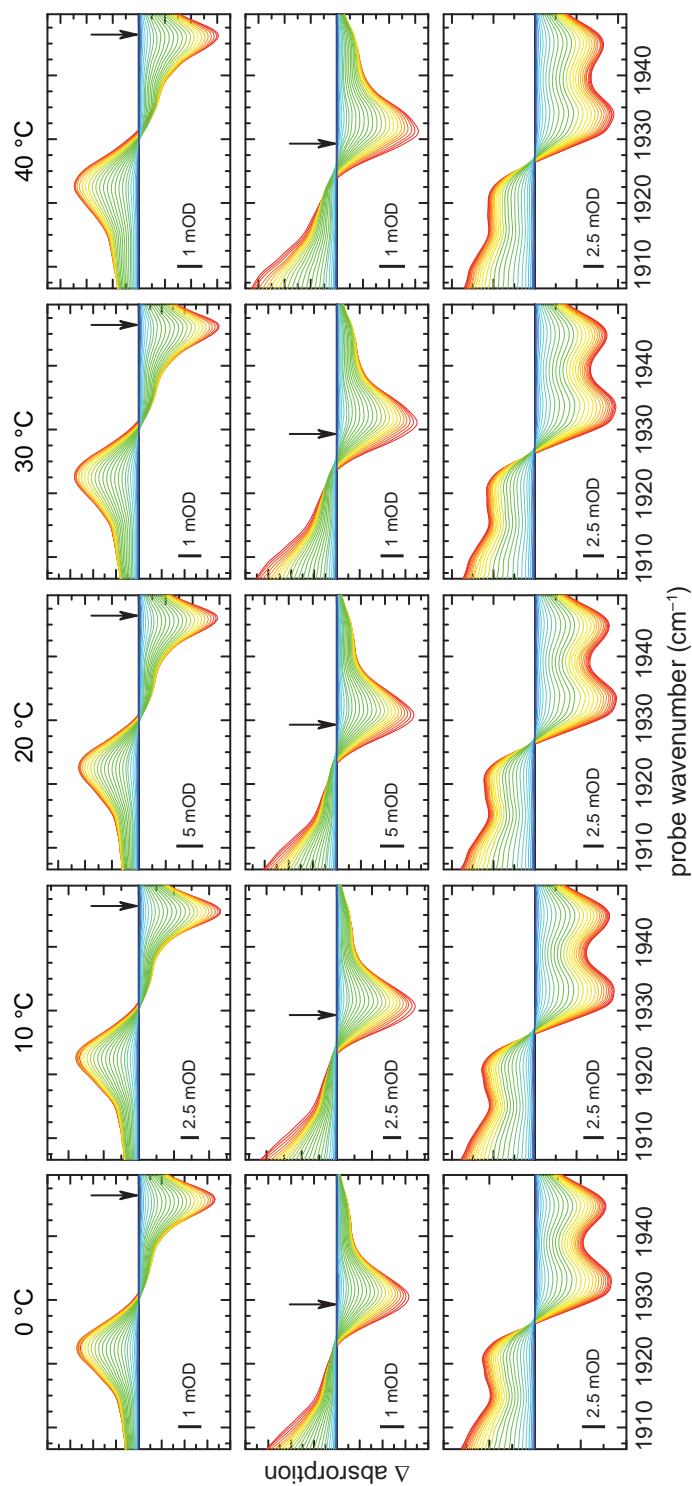
Figure 20.3: *Temperature dependent EXSY-2D-IR cuts (top and middle) and broadband pump-probe spectra (bottom) of L29I MbCO. The arrows indicate the positions of the narrowband pump pulses. The delays between pump and probe pulses were varied from 2 ps (red) to 100 ps (blue). Background: 300 ps.*
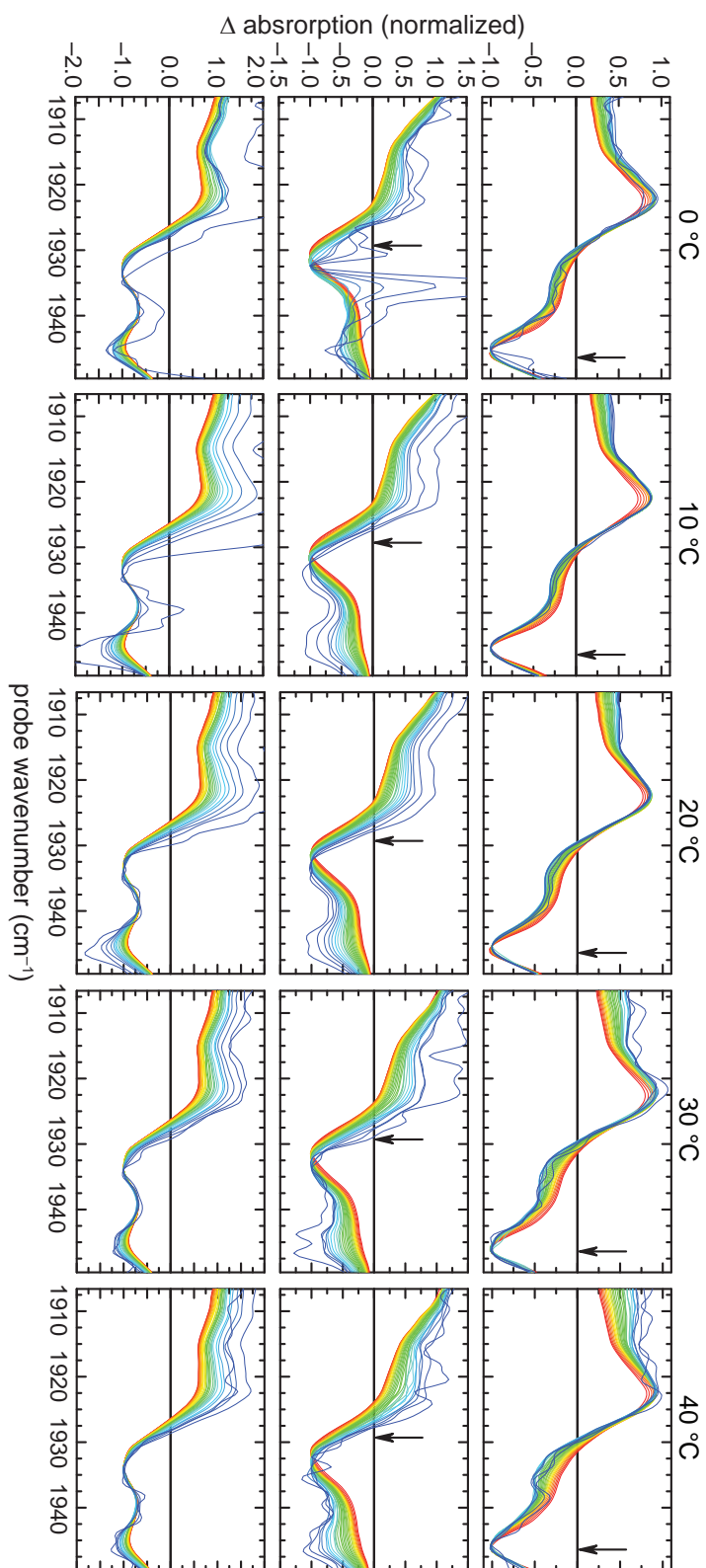
Figure 20.4: *Temperature dependent EXSY-2D-IR cuts (top and middle) and broadband pump-probe spectra (bottom) of L29I MbCO. The arrows indicate the positions of the narrowband pump pulses. The delays between pump and probe pulses were varied from 2 ps (red) to 100 ps (blue). Background: 300 ps. The spectra are scaled to the intensity of a specific band.*

20.3 L29W Myoglobin
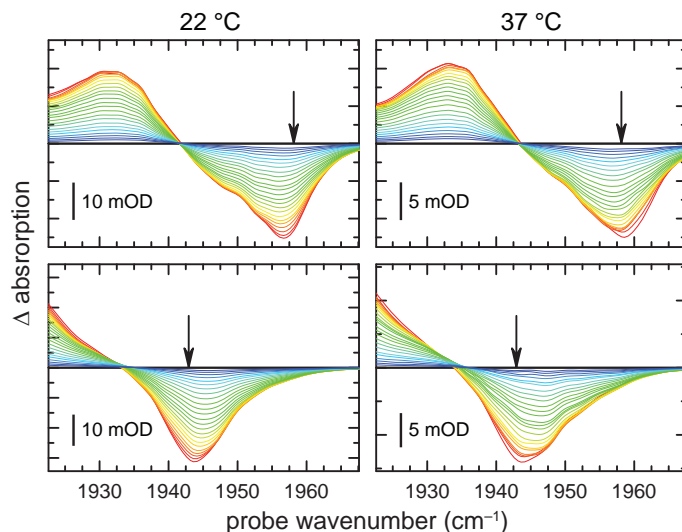
Figure 20.5: *Temperature dependent EXSY-2D-IR cuts (top and middle) and broadband pump-probe spectra (bottom) of L29W MbCO. The arrows indicate the positions of the narrowband pump pulses. The delays between pump and probe pulses were varied from 2 ps (red) to 56 ps (blue). Background: –5 ps.*
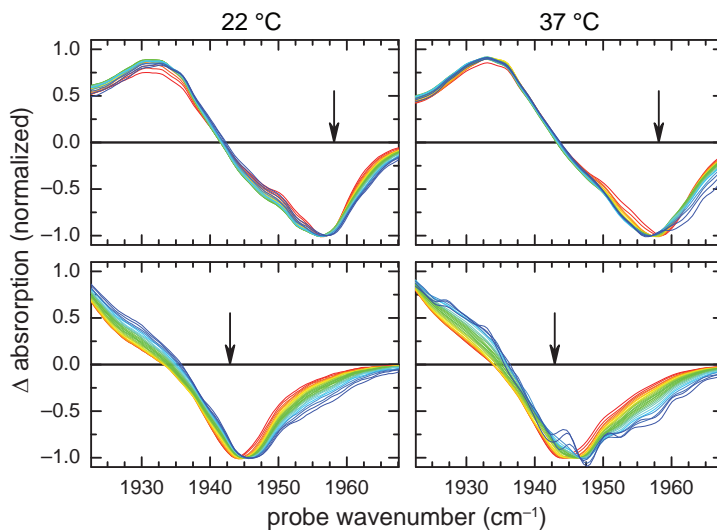
Figure 20.6: *Temperature dependent EXSY-2D-IR cuts (top and middle) and broadband pump-probe spectra (bottom) of L29W MbCO. The arrows indicate the positions of the narrowband pump pulses. The delays between pump and probe pulses were varied from 2 ps (red) to 56 ps (blue). Background: –5 ps. The spectra are scaled to the intensity of the pumped band.*

20.4   V68W Myoglobin
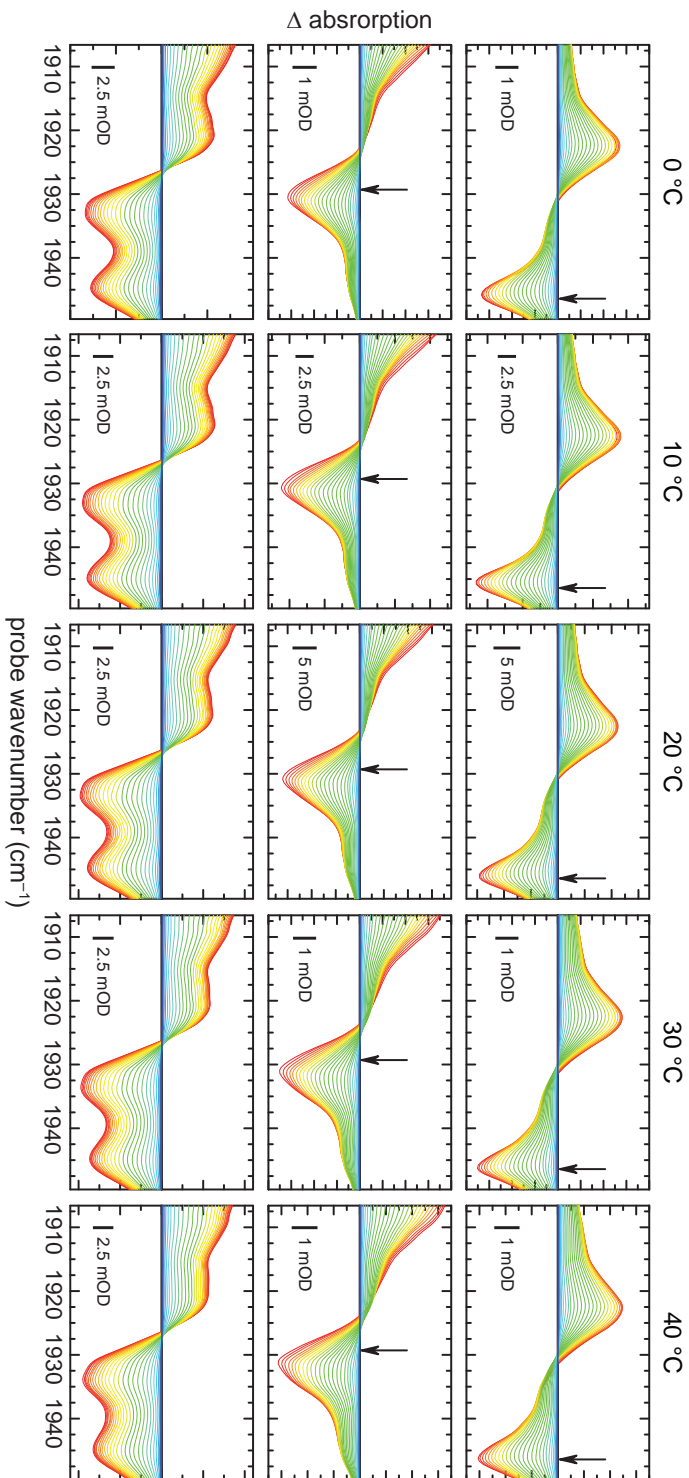
Figure 20.7: *Temperature dependent EXSY-2D-IR cuts (top and middle) and broadband pump-probe spectra (bottom) of V68W MbCO. The arrows indicate the positions of the narrowband pump pulses. The delays between pump and probe pulses were varied from 2 ps (red) to 87 ps (blue). Background: 100 ps.*
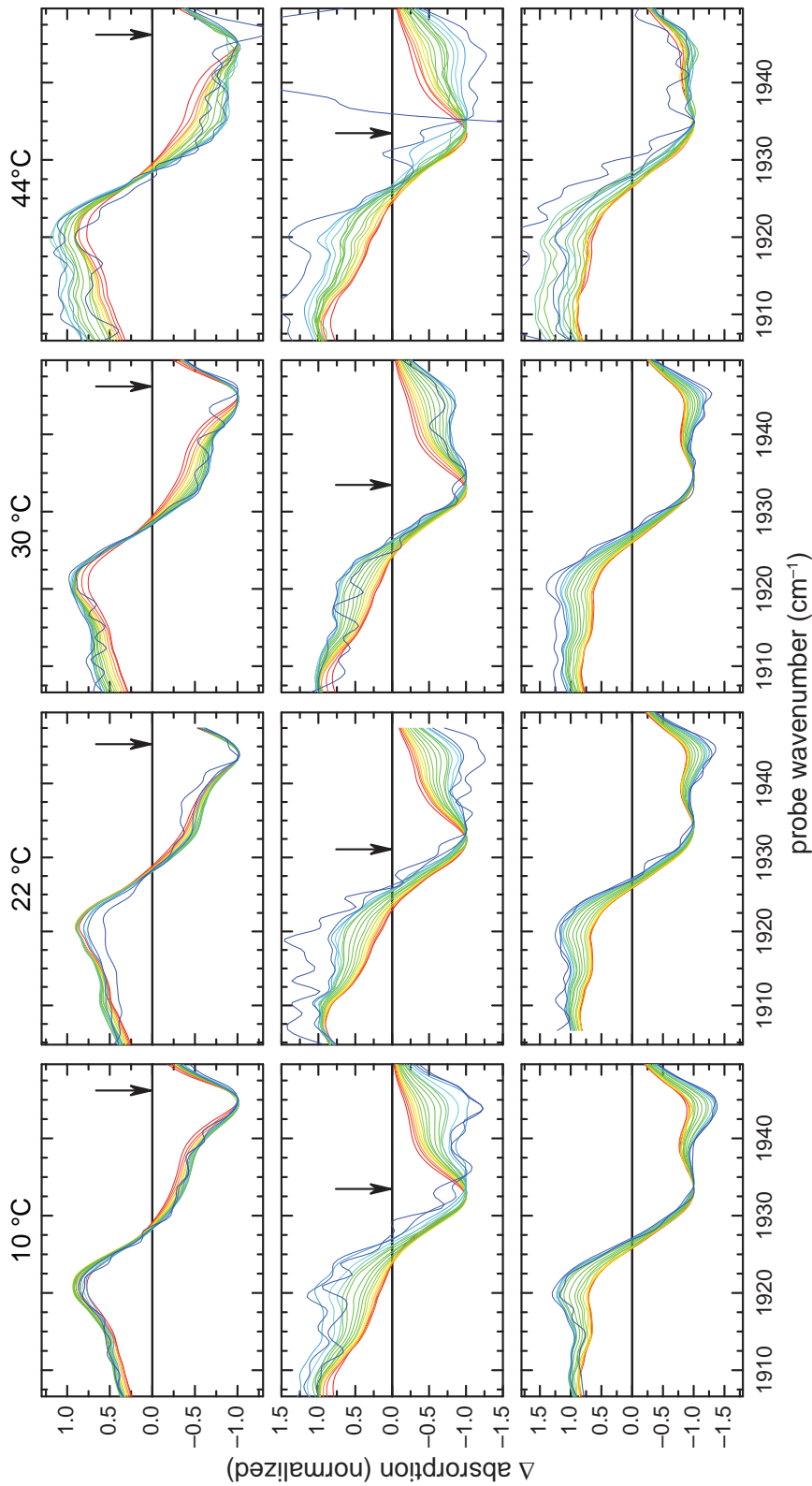
Figure 20.8: *Temperature dependent EXSY-2D-IR cuts (top and middle) and broadband pump-probe spectra (bottom) of V68W MbCO. The arrows indicate the positions of the narrowband pump pulses. The delays between pump and probe pulses were varied from 2 ps (red) to 87 ps (blue). Background: 100 ps. The spectra are scaled to the intensity of a specific band.*

20.5   YLT Myoglobin
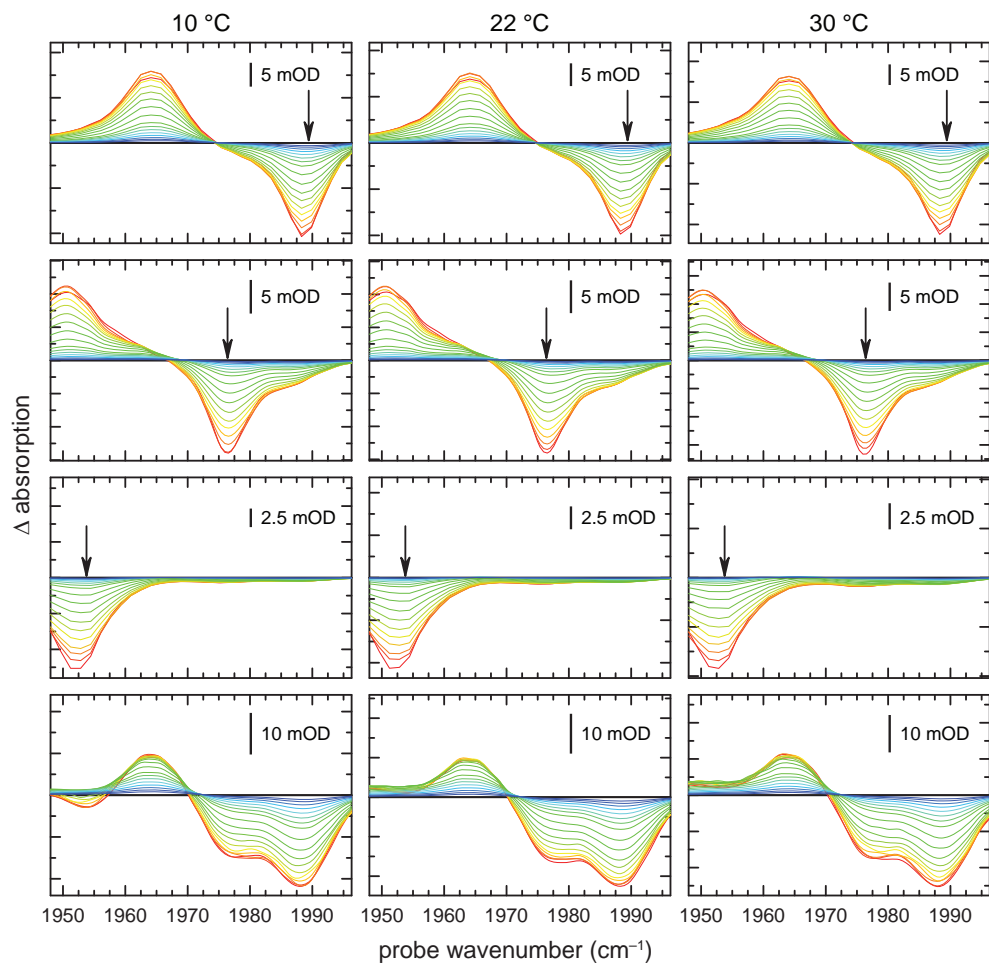
Figure 20.9: *Temperature dependent EXSY-2D-IR cuts (top and middle) and broadband pump-probe spectra (bottom) of YLT MbCO. The arrows indicate the positions of the narrowband pump pulses. The delays between pump and probe pulses were varied from 2 ps (red) to 100 ps (blue). Background: 300 ps.*
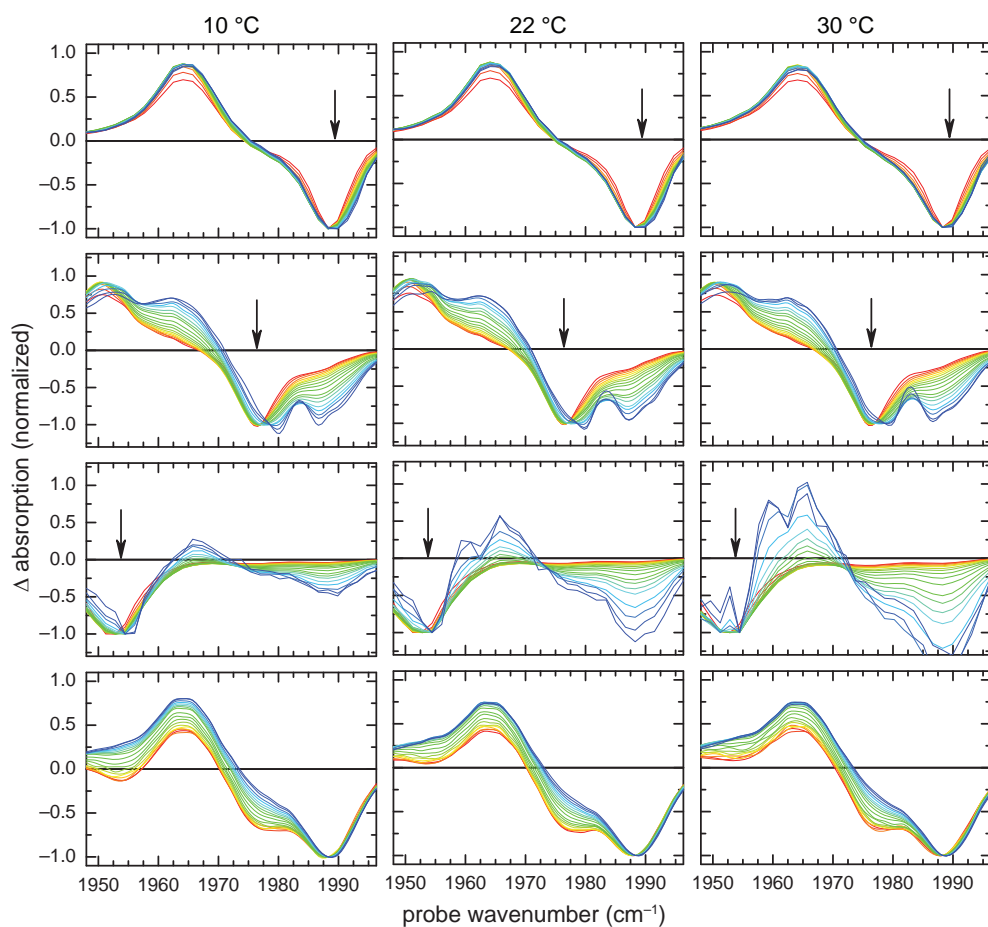
Figure 20.10: *Temperature dependent EXSY-2D-IR cuts (top and middle) and broadband pump-probe spectra (bottom) of YLT MbCO. The arrows indicate the positions of the narrowband pump pulses. The delays between pump and probe pulses were varied from 2 ps (red) to 100 ps (blue). Background: 300 ps. The spectra are scaled to the intensity of a specific band.*

References

[1] Lukas Gallmann, Claudio Cirelli, and Ursula Keller. Attosecond Science: Recent Highlights and Future Trends. *Annu. Rev. Phys. Chem.*, 63(1):447–469, 2012.

[2] Jens Bredenbeck. (Bio)molecular dynamics. Lecture notes of The 20th Jyväskylä Summer School. 2010.

[3] Minhaeng Cho. Ultrafast vibrational spectroscopy in condensed phases. *PhysChemComm*, 5(7):40–58, 2002.

[4] Peter Hamm and Janne Savolainen. Two-dimensional-Raman-terahertz spectroscopy of water: Theory. *J. Chem. Phys.*, 136(9):094516, 2012.

[5] Peter Hamm, Janne Savolainen, Junichi Ono, and Yoshitaka Tanimura. Note: Inverted time-ordering in two-dimensional-Raman-terahertz spectroscopy of water. *J. Chem. Phys.*, 136(23):236101, 2012.

[6] Tobias Brixner, Jens Stenger, Harsha M. Vaswani, Minhaeng Cho, Robert E. Blankenship, and Graham R. Fleming. Two-dimensional spectroscopy of electronic couplings in photosynthesis. *Nature*, 434:625–628, 2005.

[7] Minhaeng Cho. Coherent Two-Dimensional Optical Spectroscopy. *Chem. Rev.*, 108(4):1331–1418, 2008.

[8] Franz Milota, Jaroslaw Sperling, Alexandra Nemeth, Tomáš Mančal, and Harald F. Kauffmann. Two-Dimensional Electronic Spectroscopy of Molecular Excitons. *Acc. Chem. Res.*, 42(9):1364–1374, 2009.

[9] Alexandra Nemeth, Vladimr Luke, Jaroslaw Sperling, Franz Milota, Harald F. Kauffmann, and Tomáš Mančal. Two-dimensional electronic spectra of an aggregating dye: simultaneous measurement of monomeric and dimeric line-shapes. *Phys. Chem. Chem. Phys.*, 11(28):5986–5997, 2009.

[10] Peter Hamm, Manho Lim, and Robin M. Hochstrasser. Structure of the Amide I Band of Peptides Measured by Femtosecond Nonlinear-Infrared Spectroscopy. *J. Phys. Chem. B*, 102(31):6123–6138, 1998.

[11] Ellen H. G. Backus, Robbert Bloem, Rolf Pfister, Alessandro Moretto, Marco Crisma, Claudio Toniolo, and Peter Hamm. Dynamical Transition in a Small Helical Peptide and Its Implication for Vibrational Energy Transport. *J. Phys. Chem. B*, 113(40):13405–13409, 2009.

[12] Chong Fang, Alessandro Senes, Lidia Cristian, William F. DeGrado, and Robin M. Hochstrasser. Amide vibrations are delocalized across the hydrophobic interface of a transmembrane helix dimer. *Proc. Nat. Acad. Sci. U.S.A.*, 103(45):16740–16745, 2006.

[13] Yung Sam Kim, Jianping Wang, and Robin M. Hochstrasser. Two-Dimensional Infrared Spectroscopy of the Alanine Dipeptide in Aqueous Solution. *J. Phys. Chem. B*, 109(15):7511–7521, 2005.

[14] Amber T. Krummel and Martin T. Zanni. DNA Vibrational Coupling Revealed with Two-Dimensional Infrared Spectroscopy: Insight into Why Vibrational Spectroscopy Is Sensitive to DNA Structure. *J. Phys. Chem. B*, 110(28):13991–14000, 2006.

[15] Sander Woutersen and Peter Hamm. Nonlinear two-dimensional vibrational spectroscopy of peptides. *J. Phys.: Condens. Matter*, 14(39):R1035–R1062, 2002.

[16] Martin T. Zanni and Robin M. Hochstrasser. Two-dimensional infrared spectroscopy: a promising new method for the time resolution of structures. *Curr. Opin. Struc. Biol.*, 11(5):516–522, 2001.

[17] Nurettin Demirdöven, Christopher M. Cheatum, Hoi Sung Chung, Munira Khalil, Jasper Knoester, and Andrei Tokmakoff. Two-Dimensional Infrared Spectroscopy of Antiparallel β-Sheet Secondary Structure. *J. Am. Chem. Soc.*, 126(25):7981–7990, 2004.

[18] M. Khalil, N. Demirdöven, and A. Tokmakoff. Coherent 2D IR Spectroscopy: Molecular Structure and Dynamics in Solution. *J. Phys. Chem. A*, 107(27):5258–5279, 2003.

[19] Ellen H. G. Backus, Phuong H. Nguyen, Virgiliu Botan, Rolf Pfister, Alessandro Moretto, Marco Crisma, Claudio Toniolo, Gerhard Stock, and Peter Hamm. Energy Transport in Peptide Helices: A Comparison between High- and Low-Energy Excitations. *J. Phys. Chem. B*, 112(30):9091–9099, 2008.

[20] Ellen H. G. Backus, Phuong H. Nguyen, Virgiliu Botan, Alessandro Moretto, Marco Crisma, Claudio Toniolo, Oliver Zerbe, Gerhard Stock, and Peter Hamm. Structural Flexibility of a Helical Peptide Regulates Vibrational Energy Transport Properties. *J. Phys. Chem. B*, 112(48):15487–15492, 2008.

[21] Spyridon Kaziannis, Joseph A. Wright, Marco Candelaresi, Rafal Kania, Gregory M. Greetham, Anthony W. Parker, Christopher J. Pickett, and Neil T. Hunt. The role of CN and CO ligands in the vibrational relaxation dynamics of model compounds of the [FeFe]-hydrogenase enzyme. *Phys. Chem. Chem. Phys.*, 13(21):10295–10305, 2011.

[22] Igor V. Rubtsov. Relaxation-Assisted Two-Dimensional Infrared (RA 2DIR) Method: Accessing Distances over 10 and Measuring Bond Connectivity Patterns. *Acc. Chem. Res.*, 42(9):1385–1394, 2009.

[23] Marco Schade, Alessandro Moretto, Marco Crisma, Claudio Toniolo, and Peter Hamm. Vibrational Energy Transport in Peptide Helices after Excitation of C–D Modes in Leu-$d_1$0. *J. Phys. Chem. B*, 113(40):13393–13397, 2009.

[24] H. J. Bakker and J. L. Skinner. Vibrational Spectroscopy as a Probe of Structure and Dynamics in Liquid Water. *Chem. Rev.*, 110(3):1498–1517, 2010.

[25] John B. Asbury, Tobias Steinel, C. Stromberg, K. J. Gaffney, I. R. Piletic, Alexi Goun, and M. D. Fayer. Hydrogen Bond Dynamics Probed with Ultrafast Infrared Heterodyne-Detected Multidimensional Vibrational Stimulated Echoes. *Phys. Rev. Lett.*, 91(23), 2003.

[26] S. Park, K. Kwak, and M.D. Fayer. Ultrafast 2D-IR vibrational echo spectroscopy: a probe of molecular dynamics. *Laser Phys. Lett.*, 4(10):704–718, 2007.

[27] Kyungwon Kwak, Daniel E. Rosenfeld, Jean K. Chung, and Michael D. Fayer. Solute–Solvent Complex Switching Dynamics of Chloroform between Acetone and DimethylsulfoxideTwo-Dimensional IR Chemical Exchange Spectroscopy. *J. Phys. Chem. B*, 112(44):13906–13915, 2008.

[28] Junrong Zheng, Kyungwon Kwak, John Asbury, Xin Chen, Ivan R. Piletic, and M. D. Fayer. Ultrafast Dynamics of Solute-Solvent Complexation Observed at Thermal Equilibrium in Real Time. *Science*, 309(5739):1338–1343, 2005.

[29] Thomas Elsaesser. Two-Dimensional Infrared Spectroscopy of Intermolecular Hydrogen Bonds in the Condensed Phase. *Acc. Chem. Res.*, 42(9):1220–1228, 2009.

[30] S. Woutersen, Y. Mu, G. Stock, and P. Hamm. Hydrogen-bond lifetime measured by time-resolved 2D-IR spectroscopy: *N*-methylacetamide in methanol. *Chem. Phys*, 266(2-3):137–147, 2001.

[31] Erik T.J. Nibbering, Jens Dreyer, Oliver Kühn, Jens Bredenbeck, Peter Hamm, and Thomas Elsaesser. Vibrational dynamics of hydrogen bonds. In Oliver Kühn, Ludger Wöste, A. W. Castleman, J. P. Toennies, K. Yamanouchi, and W. Zinth, editors, *Analysis and Control of Ultrafast Photoinduced Reactions*, volume 87 of *Springer Series in Chemical Physics*, pages 619–687. Springer, 2007.

[32] Yung Sam Kim and Robin M. Hochstrasser. Comparison of Linear and 2D IR Spectra in the Presence of Fast Exchange. *J. Phys. Chem. B*, 110(17):8531–8534, 2006.

[33] Sungnam Park, Michael Odelius, and Kelly J. Gaffney. Ultrafast Dynamics of Hydrogen Bond Exchange in Aqueous Ionic Solutions. *J. Phys. Chem. B*, 113(22):7825–7835, 2009.

[34] Krupa Ramasesha, Sean T. Roberts, Rebecca A. Nicodemus, Aritra Mandal, and Andrei Tokmakoff. Ultrafast 2D IR anisotropy of water reveals reorientation during hydrogen-bond switching. *J. Chem. Phys.*, 135:054509, 2011.

[35] James F. Cahoon, Karma R. Sawyer, Jacob P. Schlegel, and Charles B. Harris. Determining Transition-State Geometries in Liquids Using 2D-IR. *Science*, 319(5871):1820–1823, 2008.

[36] Hiroaki Maekawa, Matteo De Poli, Alessandro Moretto, Claudio Toniolo, and Nien-Hui Ge. Toward Detecting the Formation of a Single Helical Turn by 2D IR Cross Peaks between the Amide-I and -II Modes. *J. Phys. Chem. B*, 113(34):11775–11786, 2009.

[37] John B. Asbury, Tobias Steinel, and M.D. Fayer. Using ultrafast infrared multi-dimensional correlation spectroscopy to aid in vibrational spectral peak assignments. *Chem. Phys. Lett.*, 381(1-2):139–146, 2003.

[38] Andreas T. Messmer. *Remixing of vibrational eigenstates investigated by Transient 2D-IR Spectroscopy*. Master thesis, ETH Zürich, Zürich, 2007.

[39] Chunte Sam Peng, Kevin C. Jones, and Andrei Tokmakoff. Anharmonic Vibrational Modes of Nucleic Acid Bases Revealed by 2D IR Spectroscopy. *J. Am. Chem. Soc.*, 133(39):15650–15660, 2011.

[40] Haruto Ishikawa, Kyungwon Kwak, Jean K. Chung, Seongheun Kim, and Micheael D. Fayer. Direct observation of fast protein conformational switching. *Proc. Nat. Acad. Sci. U.S.A.*, 105(25):8619–8624, 2008.

[41] Haruto Ishikawa, Ilya J. Finkelstein, Seongheun Kim, Kyungwon Kwak, Jean K. Chung, Keisuke Wakasugi, Aaron M. Massari, and Michael D. Fayer. Neuroglobin dynamics observed with ultrafast 2D-IR vibrational echo spectroscopy. *Proc. Nat. Acad. Sci. U.S.A.*, 104(41):16116–16121, 2007.

[42] M.D. Fayer. Dynamics of Liquids, Molecules, and Proteins Measured with Ultrafast 2D IR Vibrational Echo Chemical Exchange Spectroscopy. *Annu. Rev. Phys. Chem.*, 60(1):21–38, 2009. PMID: 18851709.

[43] Junron Zheng, Kyungwon Kwak, Jia Xie, and Michael D. Fayer. Ultrafast Carbon-Carbon Single-Bond Rotational Isomerization in Room-Temperature Solution. *Science*, 313:1951–1955, 2006.

[44] Sri Ram G. Naraharisetty, Valeriy M. Kasyanenko, and Igor V. Rubtsov. Bond connectivity measured via relaxation-assisted two-dimensional infrared spectroscopy. *J. Chem. Phys.*, 128(10):104502–104502–7, 2008.

[45] Sri Ram G. Naraharisetty, Valeriy M. Kasyanenko, Jörg Zimmermann, Megan C. Thielges, Floyd E. Romesberg, and Igor V. Rubtsov. C–D Modes of Deuterated Side Chain of Leucine as Structural Reporters via Dual-frequency Two-dimensional Infrared Spectroscopy. *J. Phys. Chem. B*, 113(14):4940–4946, 2009.

[46] Peter Hamm and Martin T. Zanni. *Concepts and Methods of 2D Infrared Spectroscopy*. Cambridge University Press, Cambridge; New York, 2011.

[47] Matthew J. Nee, Robert McCanne, Kevin J. Kubarych, and Manuel Joffre. Two-dimensional infrared spectroscopy detected by chriped pulse upconversion. *Opt. Lett.*, 32(6):713–715, 2007.

[48] Matthew F. DeCamp, Lauren P. DeFlores, Kevin C. Jones, and Andrei Tokmakoff. Single-shot two-dimensional infrared spectroscopy. *Opt. Express*, 15(1):233–241, 2007.

[49] Jens Bredenbeck, Avishek Ghosh, Han-Kwang Nienhuys, and Mischa Bonn. Interface-Specific Ultrafast Two-Dimensional Vibrational Spectroscopy. *Acc. Chem. Res.*, 42(9):1332–1342, 2009.

[50] Cho-Shuen Hsieh, R. Kramer Campen, Ana Celia Vila Verde, Peter Bolhuis, Han-Kwang Nienhuys, and Mischa Bonn. Ultrafast Reorientation of Dangling OH Groups at the Air-Water Interface Using Femtosecond Vibrational Spectroscopy. *Phys. Rev. Lett.*, 107(11):116102, 2011.

[51] Wei Xiong, Jennifer E. Laaser, Randy D. Mehlenbacher, and Martin T. Zanni. Adding a dimension to the infrared spectra of interfaces using heterodyne detected 2D sum-frequency generation (HD 2D SFG) spectroscopy. *Proc. Nat. Acad. Sci. U.S.A.*, 108(52):20902–20907, 2011.

[52] Zhen Zhang, Lukasz Piatkowski, Huib J. Bakker, and Mischa Bonn. Ultrafast vibrational energy transfer at the water/air interface revealed by two-dimensional surface vibrational spectroscopy. *Nat. Chem.*, 3(11):888–893, 2011.

[53] Sang-Hee Shim, David B. Strasfeld, Yun L. Ling, and Martin T. Zanni. Automated 2D IR spectroscopy using a mid-IR pulse shaper and application of this technology to the human islet amyloid polypeptide. *Proc. Nat. Acad. Sci. U.S.A.*, 104(36):14197–14202, 2007. PMID: 17502604 PMCID: 1964818.

[54] Chris T. Middleton, Peter Marek, Ping Cao, Chi-cheng Chiu, Sadanand Singh, Ann Marie Woys, Juan J. de Pablo, Daniel P. Raleigh, and Martin T. Zanni. Two-dimensional infrared spectroscopy reveals the complex behaviour of an amyloid fibril inhibitor. *Nat. Chem.*, 4(5):355–360, 2012.

[55] Jens Bredenbeck, Jan Helbing, Christoph Kolano, and Peter Hamm. Ultrafast 2D–IR Spectroscopy of Transient Species. *ChemPhysChem*, 8(12):1747–1756, 2007.

[56] Christoph Kolano, Jan Helbing, Mariusz Kozinski, Wolfram Sander, and Peter Hamm. Watching hydrogen-bond dynamics in a β-turn by transient two-dimensional infrared spectroscopy. *Nature*, 444:469–472, 2006.

[57] Carlos R. Baiz, Porscha L. McRobbie, Jessica M. Anna, Eitan Geva, and Kevin J. Kubarych. Two-Dimensional Infrared Spectroscopy of Metal Carbonyls. *Acc. Chem. Res.*, 42(9):1395–1404, 2009.

[58] Hoi Sung Chung, Ziad Ganim, Kevin C. Jones, and Andrei Tokmakoff. Transient 2D IR spectroscopy of ubiquitin unfolding dynamics. *Proc. Nat. Acad. Sci. U.S.A.*, 104(36):14237–14242, 2007.

[59] Wei Xiong, Jennifer E. Laaser, Peerasak Paoprasert, Ryan A. Franking, Robert J. Hamers, Padma Gopalan, and Martin T. Zanni. Transient 2D IR Spectroscopy of Charge Injection in Dye-Sensitized Nanocrystalline Thin Films. *J. Am. Chem. Soc.*, 131(50):18040–18041, 2009.

[60] Rafal Kania, Andrew I. Stewart, Ian P. Clark, Gregory M. Greetham, Anthony W. Parker, Michael Towrie, and Neil T. Hunt. Investigating the vibrational dynamics of a 17e$^-$ metallocarbonyl intermediate using ultrafast two dimensional infrared spectroscopy. *Phys. Chem. Chem. Phys.*, 12(5):1051–1063, 2009.

[61] Esben Ravn Andresen and Peter Hamm. Site-Specific Difference 2D-IR Spectroscopy of Bacteriorhodopsin. *J. Phys. Chem. B*, 113(18):6520–6527, 2009.

[62] Feng Ding and Martin T. Zanni. Heterodyned 3D IR spectroscopy. *Chem. Phys*, 341(1-3):95–105, 2007.

[63] Sean Garrett-Roe and Peter Hamm. Purely absorptive three-dimensional infrared spectroscopy. *J. Chem. Phys.*, 130(16):164510, 2009.

[64] John C. Wright. Coherent multidimensional vibrational spectroscopy. *Int. Rev. Phys. Chem.*, 21(2):185–255, 2002.

[65] John C. Wright. Multiresonant Coherent Multidimensional Spectroscopy. *Annu. Rev. Phys.Chem.*, 62(1):209–230, 2011.

[66] Andrei V. Pakoulev, Mark A. Rickard, Kathryn M. Kornau, Nathan A. Mathew, Lena A. Yurs, Stephen B. Block, and John C. Wright. Mixed Frequency-/Time-Domain Coherent Multidimensional Spectroscopy: Research Tool or Potential Analytical Method? *Acc. Chem. Res.*, 42(9):1310–1321, 2009.

[67] Rui Guo, Frederic Fournier, Paul M. Donaldson, Elizabeth M. Gardner, Ian R. Gould, and David R. Klug. Detection of complex formation and determination of intermolecular geometry through electrical anharmonic coupling of molecular vibrations using electron-vibration-vibration two-dimensional infrared spectroscopy. *Phys. Chem. Chem. Phys.*, 11(38):8417, 2009.

[68] Frederic Fournier, Rui Guo, Elizabeth M. Gardner, Paul M. Donaldson, Christian Loeffeld, Ian R. Gould, Keith R. Willison, and David R. Klug. Biological and Biomedical Applications of Two-Dimensional Vibrational Spectroscopy: Proteomics, Imaging, and Structural Analysis. *Acc. Chem. Res.*, 42(9):1322–1331, 2009.

[69] David A. Blank, Laura J. Kaufman, and Graham R. Fleming. Direct fifth-order electronically nonresonant Raman scattering from CS2 at room temperature. *J. Chem. Phys.*, 113(2):771–778, 2000.

[70] Y. L. Li, L. Huang, R. J. Dwayne Miller, Taisuke Hasegawa, and Yoshitaka Tanimura. Two-dimensional fifth-order Raman spectroscopy of liquid formamide: Experiment and Theory. *J. Chem. Phys.*, 128(23):234507, 2008.

[71] W. Kuehn, K. Reimann, M. Woerner, T. Elsaesser, and R. Hey. Two-Dimensional Terahertz Correlation Spectra of Electronic Excitations in Semiconductor Quantum Wells. *J. Phys. Chem. B*, 115(18):5448–5455, 2010.

[72] Isao Noda. Two-dimensional infrared spectroscopy. *J. Am. Chem. Soc.*, 111(21):8116–8118, 1989.

[73] I. Noda, A. E. Dowrey, and C. Marcott. Recent Developments in Two-Dimensional Infrared (2D IR) Correlation Spectroscopy. *Appl. Spectrosc.*, 47(9):1317–1323, 1993.

[74] Neil T. Hunt. 2D-IR spectroscopy: ultrafast insights into biomolecule structure and function. *Chem. Soc. Rev.*, 38(7):1837–1848, 2009.

[75] Junrong Zheng, Kyungwon Kwak, and M. D. Fayer. Ultrafast 2D IR Vibrational Echo Spectroscopy. *Acc. Chem. Res.*, 40(1):75–83, 2007.

[76] Steven M. Arrivo and Edwin J. Heilweil. Conservation of Vibrational Excitation During Hydrogen-Bonding Reactions. *J. Phys. Chem.*, 100(29):11975–11983, 1996.

[77] W. Tandy Grubbs, Thomas P. Dougherty, and Edwin J. Heilweil. Vibrational Energy Dynamics of Hydrogen-Bonded Pyrrole Complexes. *J. Phys. Chem.*, 99(27):10716–10722, 1995.

[78] Gerhard Seifert and Heinrich Graener. Time-Resolved Determination of Picosecond Lifetimes of Weak Hydrogen Bonds in Liquids. *J. Phys. Chem.*, 98(46):11827–11831, 1994.

[79] A. Laubereau and W. Kaiser. Vibrational dynamics of liquids and solids investigated by picosecond light pulses. *Rev. Mod. Phys.*, 50(3):607–665, 1978.

[80] H. Graener, R. Dohlus, and A. Laubereau. Infrared double-resonance spectroscopy of bromoform with picosecond pulses. *Chem. Phys. Lett.*, 140(3):306–310, 1987.

[81] M. C. Asplund, M. T. Zanni, and R. M. Hochstrasser. Two-dimensional infrared spectroscopy of peptides by phase-controlled femtosecond vibrational photon echoes. *Proc. Nat. Acad. Sci. U.S.A.*, 97(15):8219–8224, 2000.

[82] C. Scheurer and S. Mukamel. Design strategies for pulse sequences in multidimensional optical spectroscopies. *J. Chem. Phys.*, 115(11):4989–5004, 2001.

[83] C. Scheurer and S. Mukamel. Infrared analogs of heteronuclear nuclear magnetic resonance coherence transfer experiments in peptides. *J. Chem. Phys.*, 116(15):6803–6816, 2002.

[84] Valentina Cervetto, Jan Helbing, Jens Bredenbeck, and Peter Hamm. Double-resonance versus pulsed Fourier transform two-dimensional infrared spectroscopy: An experimental and theoretical comparison. *J. Chem. Phys.*, 121(12):5935–5942, 2004.

[85] Martin T. Zanni, S. Gnanakaran, Jens Stenger, and Robin M. Hochstrasser. Heterodyned Two-Dimensional Infrared Spectroscopy of Solvent-Dependent Conformations of Acetylproline-NH_2. *J. Phys. Chem. B*, 105(28):6520–6535, 2001.

[86] Sean T. Roberts, Joseph J. Loparo, Krupa Ramasesha, and Andrei Tokmakoff. A fast-scanning Fourier transform 2D IR interferometer. *Opt. Comm.*, 284(4):1062–1066, 2011.

[87] Lauren P. DeFlores, Rebecca A. Nicodemus, and Andrei Tokmakoff. Two-dimensional Fourier transform spectroscopy in the pump-probe geometry. *Opt. Lett.*, 32(20):2966–2968, 2007.

[88] Jan Helbing and Peter Hamm. Compact implementation of Fourier transform two-dimensional IR spectroscopy without phase ambiguity. *J. Opt. Soc. Am. B*, 28(1):171–178, 2011.

[89] M. Khalil, N. Demirdöven, and A. Tokmakoff. Obtaining Absorptive Line Shapes in Two-Dimensional Infrared Vibrational Correlation Spectra. *Phys. Rev. Lett.*, 90(4):047401, 2003.

[90] A. I. Stewart, I. P. Clark, M. Towrie, S. K. Ibrahim, A. W. Parker, C. J. Pickett, and N. T. Hunt. Structure and Vibrational Dynamics of Model Compounds of the [FeFe]–Hydrogenase Enzyme System via Ultrafast Two-Dimensional Infrared Spectroscopy. *J. Phys. Chem. B*, 112(32):10023–10032, 2008.

[91] John B. Asbury, Tobias Steinel, C. Stromberg, K.J. Gaffney, I.R. Piletic, Alexi Goun, and M.D. Fayer. Ultrafast heterodyne detected infrared multidimensional vibrational stimulated echo studies of hydrogen bond dynamics. *Chem. Phys. Lett.*, 374(3-4):362–371, 2003.

[92] Ayanjeet Ghosh, Amanda Remorino, Matthew J. Tucker, and Robin M. Hochstrasser. 2D IR photon echo spectroscopy reveals hydrogen bond dynamics of aromatic nitriles. *Chem. Phys. Lett.*, 469(4-6):325–330, 2009. PMID: 20622983 PMCID: PMC2901127.

[93] Yung Sam Kim, Liu Liu, Paul H. Axelsen, and Robin M. Hochstrasser. 2D IR provides evidence for mobile water molecules in β-amyloid fibrils. *Proc. Nat. Acad. Sci. U.S.A.*, 106(42):17751–17756, 2009.

[94] O. Golonzka, M. Khalil, N. Demirdöven, and A. Tokmakoff. Coupling and orientation between anharmonic vibrations characterized with two-dimensional infrared vibrational echo spectroscopy. *J. Chem. Phys.*, 115(23):10814–10828, 2001.

[95] S. Woutersen and P. Hamm. Structure Determination of Trialanine in Water Using Polarization Sensitive Two-Dimensional Vibrational Spectroscopy. *J. Phys. Chem. B*, 104(47):11316–11320, 2000.

[96] Hongtao Bian, Wei Zhao, and Junrong Zheng. Intermolecular vibrational energy exchange directly probed with ultrafast two dimensional infrared spectroscopy. *J. Chem. Phys.*, 131(12):124501, 2009.

[97] Joanna Borek, Fivos Perakis, Felix Kläsi, Sean Garrett-Roe, and Peter Hamm. Azide-water intermolecular coupling measured by two-color two-dimensional infrared spectroscopy. *J. Chem. Phys.*, 136(22):224503, 2012.

[98] Andreas T. Messmer, Katharina M. Lippert, Peter R. Schreiner, and Jens Bredenbeck. Structure Analysis of Molecules in Mixtures with Ultrafast Two-Dimensional Infrared Spectroscopy. *submitted*.

[99] Malcolm H. Levitt. *Spin Dynamics*. John Wiley & Sons, Chichester; New York; Weinheim [etc.], 2001.

[100] James Keeler. *Understanding NMR Spectroscopy*. Wiley, Chichester, 2005.

[101] Sander Woutersen, Rolf Pfister, Peter Hamm, Yuguang Mu, Daniel S. Kosov, and Gerhard Stock. Peptide conformational heterogeneity revealed from non-linear vibrational spectroscopy and molecular-dynamics simulations. *J. Chem. Phys.*, 117(14):6833–6840, 2002.

[102] Marco Schade and Peter Hamm. Vibrational energy transport in the presence of intrasite vibrational energy redistribution. *J. Chem. Phys.*, 131(4):044511, 2009.

[103] Jens Bredenbeck. 2D-IR Spektroskopie. *Nachr. Chem.*, 54:104–108, 2006.

[104] Steven S. Andrews. Using Rotational Averaging To Calculate the Bulk Response of Isotropic and Anisotropic Samples from Molecular Parameters. *J. Chem. Educ.*, 81(6):877–885, 2004.

[105] Kyung-Koo Lee, Kwang-Hee Park, Sungnam Park, Seung-Joon Jeon, and Minhaeng Cho. Polarization-Angle-Scanning 2DIR Spectroscopy of Coupled Anharmonic Oscillators: A Polarization Null Angle Method. *J. Phys. Chem. B*, 115(18):5456–5464, 2010.

[106] Jun-Ho Choi and Minhaeng Cho. Polarization-angle-scanning two-dimensional infrared spectroscopy of antiparallel β-sheet polypeptide: Additional dimensions in two-dimensional optical spectroscopy. *J. Chem. Phys.*, 133(24):241102, 2010.

[107] Jun-Ho Choi and Minhaeng Cho. Polarization-Angle-Scanning Two-Dimensional Spectroscopy: Application to Dipeptide Structure Determination. *J. Phys. Chem. A*, 115(16):3766–3777, 2011.

[108] Martin T. Zanni, Nien-Hui Ge, Yung Sam Kim, and Robin M. Hochstrasser. Two-dimensional IR spectroscopy can be designed to eliminate the diagonal peaks and expose only the crosspeaks needed for structure determination. *Proc. Nat. Acad. Sci. U.S.A.*, 98(20):11265–11270, 2001.

[109] Jens Bredenbeck, Jan Helbing, and Peter Hamm. Transient two-dimensional infrared spectroscopy: Exploring the polarization dependence. *J. Chem. Phys.*, 121(12):5943–5957, 2004.

[110] D. L. Andrews and T. Thirunamachandran. On three-dimensional rotational averages. *J. Chem. Phys.*, 67(11):5026–5033, 1977.

[111] D. A Long. *The Raman Effect : A Unified Treatment of the Theory of Raman Scattering by Molecules*. Wiley, Chichester; New York, 2002.

[112] T. Lian, B. Locke, T. Kitagawa, M. Nagai, and R. M. Hochstrasser. Determination of iron-carbon monoxide geometry in the subunits of carbonmonoxy hemoglobin M Boston using femtosecond infrared spectroscopy. *Biochemistry*, 32(22):5809–5814, 1993.

[113] Manho Lim, Timothy A. Jackson, and Philip A. Anfinrud. Orientational Distribution of CO before and after Photolysis of MbCO and HbCO: A Determination Using Time-Resolved Polarized Mid-IR Spectroscopy. *J. Am. Chem. Soc.*, 126(25):7946–7957, 2004.

[114] B. Locke, T. Lian, and R.M. Hochstrasser. Determination of Fe-CO geometry and heme rigidity in carbonmonoxyhemoglobin using femtosecond IR spectroscopy. *Chem. Phys*, 158(2-3):409–419, 1991.

[115] Luuk J. G. W. van Wilderen, Craig N. Lincoln, and Jasper J. van Thor. Modelling Multi-Pulse Population Dynamics from Ultrafast Spectroscopy. *PLoS ONE*, 6(3):e17373, 2011.

[116] Anjum Ansari and Attila Szabo. Theory of photoselection by intense light pulses. Influence of reorientational dynamics and chemical kinetics on absorbance measurements. *Biophys. J.*, 64(3):838–851, 1993.

[117] Seungsoo Hahn, Hochan Lee, and Minhaeng Cho. Theoretical calculations of infrared absorption, vibrational circular dichroism, and two-dimensional vibrational spectra of acetylproline in liquids water and chloroform. *J. Chem. Phys.*, 121(4):1849–1865, 2004.

[118] Howe-Siang Tan, Ivan R. Piletic, and M. D. Fayer. Polarization selective spectroscopy experiments: methodology and pitfalls. *J. Opt. Soc. Am. B*, 22(9):2009–2017, 2005.

[119] Bruce J. Berne and Robert Pecora. *Dynamic Light Scattering: With Applications to Chemistry, Biology, and Physics*. Dover Publications Inc, Dover edition, 2000.

[120] R. S Hartman, W. M Konitsky, D. H Waldeck, Y. J Chang, and E. W Castner. Probing solute–solvent electrostatic interactions: Rotational diffusion studies of 9,10-disubstituted anthracenes. *J. Chem. Phys.*, 106(19):7920–7930, 1997.

[121] U. S. Raikar, C. G. Renuka, Y. F. Nadaf, B. G. Mulimani, and A. M. Karguppikar. Rotational Diffusion and Solvatochromic Correlation of Coumarin 6 Laser Dye. *J. Fluoresc.*, 16(6):847–854, 2006.

[122] Y. L. A. Rezus and H. J. Bakker. Effect of urea on the structural dynamics of water. *Proc. Nat. Acad. Sci. U.S.A.*, 103(49):18417–18420, 2006.

[123] Spectra Physics. *Spitfire Pro, User Manual, Rev. A.* 2008.

[124] Spectra Physics. *Empower, User's Manual, Rev. B.* 2005.

[125] Spectra Physics. *Millenia Pro s-series, User's Manual, Rev. B.* 2006.

[126] Spectra Physics. *Tsunami, User's Manual, Rev. D.* 2002.

[127] Ute K. Förster. *Untersuchung der Konformation und Dynamik von RNA mit Hilfe fluoreszierender Farbstoffmoleküle*. PhD thesis, Johann Wolfgang Goethe - Universität, Frankfurt am Main, 2010.

[128] Robert W Boyd. *Nonlinear Optics*. Academic Press, San Diego, CA, 2003.

[129] W. Demtröder. *Laserspektroskopie : Grundlagen und Techniken*. Springer, Berlin, 2000.

[130] Dieter Meschede. *Optik, Licht und Laser*. Vieweg + Teubner in GWV Fachverlage, Wiesbaden, 2008.

[131] Giulio Cerullo and Sandro De Silvestri. Ultrafast optical parametric amplifiers. *Rev. Sci. Instrum.*, 74(1):1–18, 2003.

[132] R. R. Alfano and S. L. Shapiro. Emission in the Region 4000 to 7000 ÅVia Four-Photon Coupling in Glass. *Phys. Rev. Lett.*, 24(11):584–587, 1970.

[133] N. Aközbek, A. Becker, and S. L. Chin. Propagation and filamentation of femtosecond laser pulses in optical media. *Laser physics*, 15(4):607–615, 2005.

[134] A. Brodeur and S. L. Chin. Ultrafast white-light continuum generation and self-focusing in transparent condensed media. *J. Opt. Soc. Am. B*, 16(4):637–650, 1999.

[135] M. Kolesik, G. Katona, J. V. Moloney, and E. M. Wright. Physical Factors Limiting the Spectral Extent and Band Gap Dependence of Supercontinuum Generation. *Phys. Rev. Lett.*, 91(4):043905, 2003.

[136] M. Kolesik, G. Katona, J.V. Moloney, and E.M. Wright. Theory and simulation of supercontinuum generation in transparent bulk media. *Appl. Phys. B: Lasers Opt.*, 77(2):185–195, 2003.

[137] R. L. Fork, C. V. Shank, C. Hirlimann, R. Yen, and W. J. Tomlinson. Femtosecond white-light continuum pulses. *Opt. Lett.*, 8(1):1–3, 1983.

[138] A. L. Gaeta. Catastrophic collapse of ultrashort pulses. *Phys. Rev. Lett.*, 84(16):3582–3585, 2000.

[139] M. Bradler, P. Baum, and E. Riedle. Femtosecond continuum generation in bulk laser host materials with sub-μJ pump pulses. *Appl. Phys. B: Lasers Opt.*, 97(3):561–574, 2009.

[140] P. Hamm, R. A Kaindl, and J. Stenger. Noise suppression in femtosecond mid-infrared light sources. *Opt. Lett.*, 25(24):1798–1800, 2000.

[141] Jens Bredenbeck and Peter Hamm. Versatile small volume closed-cycle flow cell system for transient spectroscopy at high repetition rates. *Rev. Sci. Instrum.*, 74(6):3188–3189, 2003.

[142] S. Woutersen and P. Hamm. Isotope-edited two-dimensional vibrational spectroscopy of trialanine in aqueous solution. *J. Chem. Phys.*, 114(6):2727–2737, 2001.

[143] Pavol Bodis, Matthijs R. Panman, Bert H. Bakker, Aurelio Mateo-Alonso, Maurizio Prato, Wybren Jan Buma, Albert M. Brouwer, Euan R. Kay, David A. Leigh, and Sander Woutersen. Two-Dimensional Vibrational Spectroscopy of Rotaxane-Based Molecular Machines. *Acc. Chem. Res.*, 42(9):1462–1469, 2009.

[144] Olaf F. A. Larsen, Pavol Bodis, Wybren Jan Buma, Jeffrey S. Hannam, David A. Leigh, and Sander Woutersen. Probing the structure of a rotaxane with two-dimensional infrared spectroscopy. *Proc. Nat. Acad. Sci. U.S.A.*, 102(38):13378–13382, 2005.

[145] H. Graener, G. Seifert, and A. Laubereau. Direct observation of rotational relaxation times by time-resolved infrared spectroscopy. *Chem. Phys. Lett.*, 172(6):435–439, 1990.

[146] Howe-Siang Tan, Ivan R. Piletic, and M. D. Fayer. Orientational dynamics of water confined on a nanometer length scale in reverse micelles. *J. Chem. Phys.*, 122(17):174501, 2005.

[147] Howard Maskill. *The Investigation of Organic Reactions and Their Mechanisms.* Blackwell Pub., Oxford; Ames, Iowa, 2006.

[148] Edward D. Hughes, Christopher K. Ingold, and Alan D. Scott. 253. Reaction kinetics and the Walden inversion. Part II. Homogeneous hydrolysis, alcoholysis, and ammonolysis of α-phenylethyl halides. *J. Chem. Soc.*, pages 1201–1208, 1937.

[149] Reinhard Brückner. *Reaktionsmechanismen : organische Reaktionen, Stereochemie, moderne Synthesemethoden.* Spektrum, Akad. Verl., Heidelberg; Berlin; Oxford, 1996.

[150] William Clegg. *Crystal Structure Determination.* Oxford University Press, Oxford; New York, 1998.

[151] Peter J Hore. *Nuclear Magnetic Resonance.* Oxford University Press, Oxford [etc.], 1995.

[152] Jeffrey H Simpson. *Organic Structure Determination Using 2-D NMR Spectroscopy : A Problem-Based Approach.* Elsevier/AP, Amsterdam; Boston, 2012.

[153] Horst Friebolin. *Ein- und Zweidimensionale NMR-Spektroskopie : eine Einführung.* Wiley-VCH, Weinheim, 2006.

[154] D. Neuhaus and M.P. Williamson. *The Nuclear Overhauser Effect in Structural and Conformational Analysis.* Wiley-VCH, Weinheim, 2000.

[155] Bernd Wrackmeyer. Application of 119Sn NMR Parameters. In *Annual Reports on NMR Spectroscopy*, volume 38, pages 203–264. Elsevier, 1999.

[156] Martin Karplus. Contact Electron-Spin Coupling of Nuclear Magnetic Moments. *J. Chem. Phys.*, 30(1):11–15, 1959.

[157] Ernö Pretsch, Philippe Buehlmann, Christian Affolter, and Martin Badertscher. *Spektroskopische Daten zur Strukturaufklärung organischer Verbindungen.* Springer, Berlin, 2002.

[158] Christina M. Thiele. Residual Dipolar Couplings (RDCs) in Organic Structure Determination. *Eur. J. Org. Chem.*, 2008(34):5673–5685, 2008.

[159] Benjamin Böttcher, Volker Schmidts, Jevgenij A. Raskatov, and Christina M. Thiele. Bestimmung der Konformation des Schlsselintermediats einer enantioselektiven Palladium-katalysierten allylischen Substitution mithilfe dipolarer Restkopplungen. *Angew. Chem.*, 122(1):210–214, 2010.

[160] Rebecca S. Lipsitz and Nico Tjandra. Residual Dipolar Couplings in NMR Structure Analysis. *Annu. Rev. Bioph. Biom.*, 33(1):387–413, 2004.

[161] J. H. Prestegard, C. M. Bougault, and A. I. Kishore. Residual Dipolar Couplings in Structure Determination of Biomolecules. *Chem. Rev.*, 104(8):3519–3540, 2004.

[162] Andrew E. Derome. *Modern NMR techniques for Chemistry Research*. Pergamon Press, Oxford [Oxfordshire]; New York, 1987.

[163] Peter Spiteller. NMR Übungen. http://www.ia.uni-bremen.de/nmr/uebung/struk2.html.

[164] Armin Geyer. NMR-Spektroskopie: Struktur und Dynamik organischer Moleküle. http://www.staff.uni-marburg.de/~geyer/download/NMR_Skript_Okt05.pdf, 2012.

[165] Beat Vögeli, Takuya F. Segawa, Dominik Leitz, Alexander Sobol, Alexandra Choutko, Daniel Trzesniak, Wilfred van Gunsteren, and Roland Riek. Exact Distances and Internal Dynamics of Perdeuterated Ubiquitin from NOE Buildups. *J. Am. Chem. Soc.*, 131(47):17215–17225, 2009.

[166] Dominik Leitz, Beat Vögeli, Jason Greenwald, and Roland Riek. Temperature Dependence of ^{1}H$_N$-^{1}H$_N$ Distances in Ubiquitin As Studied by Exact Measurements of NOEs. *J. Phys. Chem. B*, 115(23):7648–7660, 2011.

[167] Craig P. Butts, Catharine R. Jones, Emma C. Towers, Jennifer L. Flynn, Lara Appleby, and Nicholas J. Barron. Interproton distance determinations by NOE – surprising accuracy and precision in a rigid organic molecule. *Org. Biomol. Chem.*, 9(1):177–184, 2011.

[168] Craig P. Butts, Catharine R. Jones, Zhongshu Song, and Thomas J. Simpson. Accurate NOE-distance determination enables the stereochemical assignment of a flexible molecule – arugosin C. *Chem. Comm.*, 48(72):9023–9025, 2012.

[169] F. Dong and R. E. Miller. Vibrational Transition Moment Angles in Isolated Biomolecules: A Structural Tool. *Science*, 298(5596):1227–1230, 2002.

[170] M. Y. Choi, F. Dong, and R. E. Miller. Multiple tautomers of cytosine identified and characterized by infrared laser spectroscopy in helium nanodroplets: probing structure using vibrational transition moment angles. *Philos. Trans. Roy. Soc. A*, 363(1827):393–413, 2005.

[171] Yvonne Gnas and Frank Glorius. Chiral Auxiliaries - Principles and Recent Applications. *Synthesis*, 12:1899–1930, 2006.

[172] D. A. Evans, M. D. Ennis, and D. J. Mathre. Asymmetric Alkylation Reactions of Chiral Imide Enolates. A Practical Approach to the Enantioselective Synthesis of α-Substituted Carboxylic Acid Derivatives. *J. Am. Chem. Soc.*, 104(6):1737–1739, 1982.

[173] David A. Evans, K. T. Chapman, and J. Bisaha. Asymmetric Diels-Alder Cycloaddition Reactions with Chiral α,β-Unsaturated *N*-Acyloxazolidinones. *J. Am. Chem. Soc.*, 110(4):1238–1256, 1988.

[174] D. A. Evans, J. Bartroli, and T. L. Shih. Enantioselective Aldol Condensations. 2. Erythro-Selective Chiral Aldol Condensations via Boron Enolates. *J. Am. Chem. Soc.*, 103(8):2127–2129, 1981.

[175] D. A. Evans, J. M. Takacs, L. R. McGee, M. D. Ennis, D. J. Mathre, and J. Bartroli. Chiral enolate design. *Pure Appl. Chem.*, 53(6):1109–1127, 1981.

[176] D. A. Evans, K. T. Chapman, and J. Bisaha. New Asymmetric Diels-Alder Cycloaddition Reactions. Chiral α,β-Unsaturated Carboximides as Practical Chiral Acrylate and Crotonate Dienophile Synthons. *J. Am. Chem. Soc.*, 106(15):4261–4263, 1984.

[177] David J. Ager, Indra Prakash, and David R. Schaad. 1,2-Amino Alcohols and Their Heterocyclic Derivatives as Chiral Auxiliaries in Asymmetric Synthesis. *Chem. Rev.*, 96(2):835–876, 1996.

[178] David J. Ager, Indra Prakash, and David R. Schaad. Chiral Oxazolidinones in Asymmetric Synthesis. *Aldrichimica Acta*, 30(1):3–12, 1997.

[179] Jesse Dambacher, Robert Anness, Patrick Pollock, and Mikael Bergdahl. Highly diastereoselective conjugate additions of monoorganocopper reagents to chiral imides. *Tetrahedron*, 60(9):2097–2110, 2004.

[180] Steven D. Bull, Stephen G. Davies, A. Christopher Garner, Dennis Kruchinin, Min-Suk Key, Paul M. Roberts, Edward D. Savory, Andrew D. Smith, and James E. Thomson. SuperQuat 5,5-dimethyl-4-*iso*-propyloxazolidin-2-one as a mimic of Evans 4-*tert*-butyloxazolidin-2-one. *Org. Biomol. Chem.*, 4:2945–2964, 2006.

[181] Terrence J. Connolly, Zhixian Ding, Yumin Gong, Michael F. MacEwan, Jan Szeliga, and Asaf Alimardanov. Modified Chelation-Controlled Reduction of an *N*-Acryloyloxazolidin-2-one. *Org. Process Res. Dev.*, 14(6):1448–1452, 2012.

[182] Waldemar Adam and Aimin Zhang. High π–Facial Selectivity Through Chelation of Magnesium Ions in the DMD Epoxidation of α,β-Unsaturated Imides with Chiral Pyrrolidinone Auxiliaries. *Eur. J. Org. Chem.*, 2004(1):147–152, 2004.

[183] Elizabeth H. Krenske, K. N. Houk, Andrew G. Lohse, Jennifer E. Antoline, and Richard P. Hsung. Stereoselectivity in oxyallyl-furan (4 + 3) cycloadditions: control of intermediate conformations and dispersive stabilisation in cycloadditions involving oxazolidinone auxiliaries. *Chem. Sci.*, 1(3):387–392, 2010.

[184] Michael A. Walker and Clayton H. Heathcock. Extending the Scope of the Evans Asymmetric Aldol Reaction: Preparation of Anti and "non-Evans" Syn Aldols. *J. Org. Chem.*, 56(20):5747–5750, 1991.

[185] D.A. Evans and J.T. Shaw. Recent advances in asymmetric synthesis with chiral imide auxiliaries. *Actualite Chimique*, 2003(4/5):35–38, 2003.

[186] David A. Evans, Günter Helmchen, and Magnus Rüping. Chiral Auxiliaries in Asymmetric Synthesis. In Mathias Christmann and Stefan Bräse, editors, *Asymmetric Synthesis : The Essentials*. Wiley-VCH, Weinheim, 2008.

[187] Erick M Carreira and Lisbet Kvaerno. *Classics in Stereoselective Synthesis*. Wiley-VCH, Weinheim, 2009.

[188] David A. Evans, Steven L. Bender, and Joel. Morris. Total Synthesis of the Polyether Antibiotic X-206. *J. Am. Chem. Soc.*, 110(8):2506–2526, 1988.

[189] Leo A. Paquette, Ronan Guevel, Shuichi Sakamoto, In Ho Kim, and Jason Crawford. Convergent Enantioselective Synthesis of Vinigrol, an Architecturally Novel Diterpenoid with Potent Platelet Aggregation Inhibitory and Antihypertensive Properties. 1. Application of Anionic Sigmatropy to Construction of the Octalin Substructure. *J. Org. Chem.*, 68(16):6096–6107, 2003.

[190] David A. Evans, Jason S. Tedrow, Jared T. Shaw, and C. Wade Downey. Diastereoselective Magnesium Halide-Catalyzed *anti*-Aldol Reactions of Chiral *N*-Acyloxazolidinones. *J. Am. Chem. Soc.*, 124(3):392–393, 2002.

[191] Waldemar Adam, Sara G. Bosio, and Nicholas J. Turro. Highly Diastereoselective Dioxetane Formation in the Photooxygenation of Enecarbamates with an Oxazolidinone Chiral Auxiliary: Steric Control in the [2+2] Cycloaddition of Singlet Oxygen through Conformational Alignment. *J. Am. Chem. Soc.*, 124(30):8814–8815, 2002.

[192] Mahavir Prashad, Yugang Liu, Hong-Yong Kim, Oljan Repic, and Thomas J Blacklock. Enantioselective synthesis of (2*S*,2'*R*)-erythro-methylphenidate. *Tetrahedron: Asymmetry*, 10(18):3479–3482, 1999.

[193] Ahmed Abdel-Magid, Lendon N. Pridgen, Drake S. Eggleston, and Ivan. Lantos. Metal-Assisted Aldol Condensation of Chiral α-Halogenated Imide Enolates: A Stereocontrolled Chiral Epoxide Synthesis. *J. Am. Chem. Soc.*, 108(15):4595–4602, 1986.

[194] Michael T. Crimmins, Bryan W. King, Elie A. Tabet, and Kleem Chaudhary. Asymmetric Aldol Additions: Use of Titanium Tetrachloride and (–)-Sparteine for the Soft Enolization of *N*-Acyl Oxazolidinones, Oxazolidinethiones, and Thiazolidinethiones. *J. Org. Chem.*, 66(3):894–902, 2001.

[195] Luiz C. Dias. Chiral Lewis Acid Catalysts in Diels-Alder Cycloadditions: Mechanistic Aspects and Synthetic Applications of Recent Systems. *J. Braz. Chem. Soc.*, 8(4):289–332, 1997.

[196] Henri B. Kagan and Olivier Riant. Catalytic Asymmetric Diels Alder Reactions. *Chem. Rev.*, 92(5):1007–1019, 1992.

[197] Taeboem Oh and Michael Rally. Reagent-Controlled Asymmetric Diels-Alder Reactions. A Review. *Org. Prep. Proced. Int.*, 26(2):129–158, 1994.

[198] Francis A Carey and Richard J Sundberg. *Advanced Organic Chemistry*. Springer, New York, 2007.

[199] Jonathan Clayden, Nick Greeves, Stuart Warren, and Peter Wothers. *Organic Chemistry*. Oxford University Press, Oxford, 2001.

[200] K. C Nicolaou, Scott A Snyder, Tamsyn Montagnon, and Georgios Vassilikogiannakis. The Diels–Alder Reaction in Total Synthesis. *Angew. Chem. Int. Ed.*, 41(10):1668–1698, 2002.

[201] David A. Evans, Brett D. Allison, and Michael G. Yang. Chelate-controlled carbonyl addition reactions. The exceptional chelating ability of dimethylaluminum chloride and methylaluminum dichloride. *Tetrahedron Lett.*, 40(24):4457–4460, 1999.

[202] David A. Evans, Brett D. Allison, Michael G. Yang, and Craig E. Masse. The Exceptional Chelating Ability of Dimethylaluminum Chloride and Methylaluminum Dichloride. The Merged Stereochemical Impact of α- and β-Stereocenters in Chelate-Controlled Carbonyl Addition Reactions with Enolsilane and Hydride Nucleophiles. *J. Am. Chem. Soc.*, 123(44):10840–10852, 2001.

[203] Snezhana M. Bakalova, Filipe J. S. Duarte, Miglena K. Georgieva, Eurico J. Cabrita, and A. Gil Santos. An Alternative Mechanism for Diels-Alder Reactions of Evans Auxiliary Derivatives. *Chem. Eur. J.*, 15(31):7665–7677, 2009.

[204] Stephen Castellino and Wesley J. Dwight. Diethylaluminum chloride complexes of an *N*-acyloxazolidinone: NMR investigation. *J. Am. Chem. Soc.*, 115(7):2986–2987, 1993.

[205] Stephen Castellino. Tin tetrachloride chelation of an *N*-acyloxazolidinone: an NMR investigation. *J. Org. Chem.*, 55(18):5197–5200, 1990.

[206] Peter R. Schreiner and Alexander Wittkopp. H-Bonding Additives Act Like Lewis Acid Catalysts. *Org. Lett.*, 4(2):217–220, 2002.

[207] Giovanni Desimoni, Giuseppe Faita, Anna Gamba Invernizzi, and Pierpaolo Righetti. Can a Chiral Catalyst Containing the Same Ligand/Metal Components Promote the Formation of Both Enantiomers Enantioselectively? The Bis(Oxazoline)-Magnesium Perchlorate-Catalyzed Asymmetric Diels-Alder Reaction. *Tetrahedron*, 53:7671–7688, 1997.

[208] Hisashi Yamamoto and Kentaro Futatsugi. "Designer Acids": Combined Acid Catalysis for Asymmetric Synthesis. *Angew. Chem. Int. Ed.*, 44(13):1924–1942, 2005.

[209] Claude Agami and Franois Couty. The Use of *N*-Boc-1,3-Oxazolidines as Chiral Auxiliaries in Asymmetric Synthesis. *Eur. J. Org. Chem.*, 2004(4):677–685, 2004.

[210] Branislav Dugovič, Lubor Fišera, and Christian Hametner. Reversal of Regioselectivity of Nitrone 1,3-Dipolar Cycloadditions by Lewis Acids. *Synlett*, 9:1569–1572, 2004.

[211] Kiyoshi Tomioka, Aki Muraoka, and Motomu Kanai. Diastereoselective Thiophenol Addition to (S)-N-α,β-Unsaturated carbonyl-γ-[(trityloxy)methyl]-γ-butyrolactams. *J. Org. Chem.*, 60(19):6188–6190, 1995.

[212] David Benoit, Elliot Coulbeck, Jason Eames, and Majid Motevalli. On the structure and chiroptical properties of (S)-4-isopropyl-oxazolidin-2-one. *Tetrahedron: Asymmetry*, 19(9):1068–1077, 2008.

[213] Motomu Kanai, Aki Muraoka, Takanori Tanaka, Masami Sawada, Nobuo Ikota, and Kiyoshi Tomioka. Conformational preference and diastereoselectivity of (S)-*N*-(α,β-unsaturated carbonyl)-γ-trityloxymethyl-γ-butyrolactam. *Tetrahedron Lett.*, 36:9349–9352, 1995.

[214] Eric A. Noe and Morton Raban. Stereochemistry in Trivalent Nitrogen Compounds. XXVIII. Conformational Analysis and Torsional Barriers of Imides and Triamides. *J. Am. Chem. Soc.*, 97(20):5811–5820, 1975.

[215] Y. L. A Rezus and H. J Bakker. On the orientational relaxation of HDO in liquid water. *J. Chem. Phys.*, 123(11):114502, 2005.

[216] Christopher J Cramer. *Essentials of Computational Chemistry*. Wiley, Chichester, 2004.

[217] A. A. El-Azhary and H. U. Suter. Comparison between Optimized Geometries and Vibrational Frequencies Calculated by the DFT Methods. *J. Phys. Chem.*, 100(37):15056–15063, 1996.

[218] Jeffrey P. Merrick, Damian Moran, and Leo Radom. An Evaluation of Harmonic Vibrational Frequency Scale Factors. *J. Phys. Chem. A*, 111(45):11683–11700, 2007.

[219] Neil G. Connelly, Richard M. Hartshorn, Ture Damhus, and Alan T. Hutton. *Nomenclature of Inorganic Chemistry*. RSC Publishing, Cambridge, 2005.

[220] A. Salzer. Nomenclature of Organometallic Compounds of the Transition Elements. *Pure Appl. Chem.*, 71:1557–1585, 1999.

[221] Nils Wiberg, Arnold Fr. Hollemann, and Egon Wiberg. *Lehrbuch der anorganischen Chemie*. De Gruyter, Berlin, 101. edition, 1995.

[222] Robbert Bloem, Sean Garrett-Roe, Halina Strzalka, Peter Hamm, and Paul Donaldson. Enhancing signal detection and completely eliminating scattering using quasi-phase-cycling in 2D IR experiments. *Opt. Express*, 18(26):27067–27078, 2010.

[223] Jae-Nam Cha, Byeong-Seo Cheong, and Han-Gook Cho. Solvation of $Mg(ClO_4)_2$ in Deuterated Acetonitrile Studied by Means of Vibrational Spectroscopy. *J. Phys. Chem. A*, 105(10):1789–1796, 2011.

[224] K. D. Rector, A. S. Kwok, C. Ferrante, A. Tokmakoff, C. W. Rella, and M. D. Fayer. Vibrational anharmonicity and multilevel vibrational dephasing from vibrational echo beats. *J. Chem. Phys.*, 106:10027–10036, 1997.

[225] M. Khalil, N. Demirdöven, and A. Tokmakoff. Vibrational coherence transfer characterized with Fourier-transform 2D IR spectroscopy. *J. Chem. Phys.*, 121(1):362–373, 2004.

[226] Giuliana Cardillo, Luca Gentilucci, Massimo Gianotti, and Alessandra Tolomelli. NMR Investigations on Boron Complexes in the Conjugate Addition on α,β-Unsaturated Imides. *Org. Lett.*, 3(8):1165–1167, 2001.

[227] Tsubasa Inokuma, Yasutaka Hoashi, and Yoshiji Takemoto. Thiourea-Catalyzed Asymmetric Michael Addition of Activated Methylene Compounds to α,β-Unsaturated Imides: Dual Activation of Imide by Intra- and Intermolecular Hydrogen Bonding. *J. Am. Chem. Soc.*, 128(29):9413–9419, 2006.

[228] Le Dai, Hongjun Yang, and Fener Chen. Chiral SquaramideCatalyzed Enantioselective Conjugate Michael Addition of Various Thiols to α,β–Unsaturated N-Acylated Oxazolidin-2-ones. *Eur. J. Org. Chem.*, 2011(26):5071–5076, 2011.

[229] Jeremiah P. Malerich, Koji Hagihara, and Viresh H. Rawal. Chiral Squaramide Derivatives are Excellent Hydrogen Bond Donor Catalysts. *J. Am. Chem. Soc.*, 130(44):14416–14417, 2008.

[230] Wen Yang, Yang Jia, and Da-Ming Du. Squaramide-catalyzed enantioselective Michael addition of malononitrile to chalcones. *Org. Biomol. Chem.*, 10(2):332–338, 2012.

[231] Ye Zhu, Jeremiah P. Malerich, and Viresh H. Rawal. Squaramide–Catalyzed Enantioselective Michael Addition of Diphenyl Phosphite to Nitroalkenes. *Angew. Chem.*, 122(1):157–160, 2010.

[232] Peter R. Schreiner. Metal-free organocatalysis through explicit hydrogen bonding interactions. *Chem. Soc. Rev.*, 32(5):289–296, 2003.

[233] Mark S. Taylor and Eric N. Jacobsen. Asymmetrische Katalyse durch chirale Wasserstoffbrückendonoren. *Angew. Chem.*, 118(10):1550–1573, 2006.

[234] Abigail G. Doyle and Eric N. Jacobsen. Small-Molecule H-Bond Donors in Asymmetric Catalysis. *Chem. Rev.*, 107(12):5713–5743, 2007.

[235] Alexander Wittkopp and Peter R Schreiner. Metal–Free, Noncovalent Catalysis of Diels–Alder Reactions by Neutral Hydrogen Bond Donors in Organic Solvents and in Water. *Chem. Eur. J.*, 9(2):407–414, 2003.

[236] Norbert Hoffmann. Photochemical Reactions as Key Steps in Organic Synthesis. *Chem. Rev.*, 108(3):1052–1103, 2008.

[237] Huw M. L. Davies, Ø ystein Loe, and Douglas G. Stafford. Sequential Cycloaddition Approach to the Tricyclic Core of Vibsanin E. Total Synthesis of (±)-5-epi-10-epi-Vibsanin E. *Org. Lett.*, 7(25):5561–5563, 2005.

[238] Sophie Faure, Sylvie Piva-Le-Blanc, Cyrille Bertrand, Jean-Pierre Pete, Ren Faure, and Olivier Piva. Asymmetric Intramolecular [2+2] Photocycloadditions: α- and β-Hydroxy Acids as Chiral Tether Groups. *J. Org. Chem.*, 67(4):1061–1070, 2002.

[239] Peter Hamm, Jan Helbing, and Jens Bredenbeck. Two-Dimensional Infrared Spectroscopy of Photoswitchable Peptides. *Annu. Rev. Phys. Chem.*, 59(1):291–317, 2008.

[240] Jens Bredenbeck, Jan Helbing, Raymond Behrendt, Christian Renner, Luis Moroder, Josef Wachtveitl, and Peter Hamm. Transient 2D-IR Spectroscopy: Snapshots of the Nonequilibrium Ensemble during the Picosecond Conformational Transition of a Small Peptide. *J. Phys. Chem. B*, 107(33):8654–8660, 2003.

[241] Hoi Sung Chung, Munira Khalil, Adam W Smith, and Andrei Tokmakoff. Transient two-dimensional IR spectrometer for probing nanosecond temperature-jump kinetics. *Rev. Sci. Instrum.*, 78(6):063101, 2007.

[242] AdamW Smith and Andrei Tokmakoff. Probing Local Structural Events in β-Hairpin Unfolding with Transient Nonlinear Infrared Spectroscopy. *Angew. Chem. Int. Ed.*, 46(42):7984–7987, 2007.

[243] Hairong Ma, Chaozhi Wan, and Ahmed H. Zewail. Ultrafast T-Jump in Water: Studies of Conformation and Reaction Dynamics at the Thermal Limit. *J. Am. Chem. Soc.*, 128(19):6338–6340, 2006.

[244] T. Dahinten, J. Baier, and A. Seilmeier. Vibrational energy transfer processes in dye molecules after ultrafast excitation of skeletal modes. *Chem. Phys*, 232(1):239–245, 1998.

[245] F. Emmerling, M. Lettenberger, and A. Laubereau. Vibrational Dynamics of Anthracene in Liquid Solution Studied by Picosecond IR/UV Spectroscopy with Polarization Resolution. *J. Phys. Chem.*, 100(50):19251–19256, 1996.

[246] Luuk J. G. W. van Wilderen, Andreas T. Messmer, and Jens Bredenbeck. Electronically-enhanced 2D-IR exchange spectroscoopy beyond the vibrational T1 time. *in preparation.*

[247] Katherine Henzler-Wildman and Dorothee Kern. Dynamic personalities of proteins. *Nature*, 450:964–972, 2007.

[248] H. Frauenfelder, B. H. McMahon, and P. W. Fenimore. Myoglobin: The hydrogen atom of biology and a paradigm of complexity. *Proc. Nat. Acad. Sci. U.S.A.*, 100(15):8615–8617, 2003. PMID: 12861080 PMCID: PMC166357.

[249] A.M. Nagy, V. Raicu, and R.J.D. Miller. Nonlinear optical studies of heme protein dynamics: Implications for proteins as hybrid states of matter. *Biochim. Biophys. Acta, Proteins Proteomics*, 1749(2):148–172, 2005.

[250] J. C. Kendrew. Myoglobin und die Struktur der Proteine. Nobel-Vortrag am 11. Dezember 1962. *Angew. Chem.*, 75(13):595–603, 1963.

[251] Marius Schmidt, Karin Nienhaus, Reinhard Pahl, Angela Krasselt, Spencer Anderson, Fritz Parak, G. Ulrich Nienhaus, and Vukica Šrajer. Ligand migration pathway and protein dynamics in myoglobin: A time-resolved crystallographic study on L29W MbCO. *Proc. Nat. Acad. Sci. U.S.A.*, 102(33):11704–11709, 2005.

[252] Hans Frauenfelder, Paul W. Fenimore, and Robert D. Young. Protein dynamics and function: Insights from the energy landscape and solvent slaving. *IUBMB Life*, 59(8-9):506–512, 2007.

[253] Hans Frauenfelder, Guo Chen, Joel Berendzen, Paul W. Fenimore, Heln Jansson, Benjamin H. McMahon, Izabela R. Stroe, Jan Swenson, and Robert D. Young. A unified model of protein dynamics. *Proc. Nat. Acad. Sci. U.S.A.*, 106(13):5129–5134, 2009.

[254] P. W. Fenimore, H. Frauenfelder, B. H. McMahon, and F. G. Parak. Slaving: Solvent fluctuations dominate protein dynamics and functions. *Proc. Nat. Acad. Sci. U.S.A.*, 99(25):16047–16051, 2002.

[255] H. Frauenfelder, P. W. Fenimore, G. Chen, and B. H. McMahon. Protein folding is slaved to solvent motions. *Proc. Nat. Acad. Sci. U.S.A.*, 103(42):15469–15472, 2006.

[256] Hans Frauenfelder. Protein Dynamics – Concepts and Experimental Tools. In Hendrik G. Bohr, editor, *Handbook of Molecular Biophysics. Methods and Apllications*, pages 215–229. Wiley-VCH, Weinheim, 2009.

[257] P. W Atkins and Julio De Paula. *Atkins' Physical Chemistry*. Oxford University Press, Oxford; New York, 2006.

[258] Gerold Adam, , Peter Läuger, and Günther Stark. *Physikalische Chemie und Biophysik*. Springer, Berlin, 2003.

[259] Donald J. Winzor and Craig M. Jackson. Interpretation of the temperature dependence of equilibrium and rate constants. *J. Mol. Recognit.*, 19(5):389–407, 2006.

[260] Peter Hänggi, Peter Talkner, and Michal Borkovec. Reaction-rate theory: fifty years after Kramers. *Rev. Mod. Phys.*, 62(2):251–341, 1990.

[261] I. E. T. Iben, D. Braunstein, W. Doster, H. Frauenfelder, M. K. Hong, J. B. Johnson, S. Luck, P. Ormos, A. Schulte, P. J. Steinbach, A. H. Xie, and R. D. Young. Glassy behavior of a protein. *Phys. Rev. Lett.*, 62(16):1916–1919, 1989.

[262] John D. Ferry, Lester D. Grandine, and Edwin R. Fitzgerald. The Relaxation Distribution Function of Polyisobutylene in the Transition from RubberLike to GlassLike Behavior. *J. Appl. Phys.*, 24(7):911–916, 1953.

[263] J. B. Johnson, D. C. Lamb, H. Frauenfelder, J. D. Müller, B. McMahon, G. U. Nienhaus, and R. D. Young. Ligand Binding to Heme Proteins. VI. Interconversion of Taxonomic Substates in Carbonmonoxymyoglobin. *Biophys. J.*, 71(3):1563–1573, 1996.

[264] H. Bässler. Viscous Flow in Supercooled Liquids Analyzed in Terms of Transport Theory for Random Media with Energetic Disorder. *Phys. Rev. Lett.*, 58(8):767–770, 1987.

[265] M. Grünewald, B. Pohlmann, B. Movaghar, and D. Würtz. Theory of non-equilibrium diffusive transport in disordered materials. *Philos. Mag. Part B*, 49(4):341–356, 1984.

[266] R. Zwanzig. Diffusion in a rough potential. *Proc. Nat. Acad. Sci. U.S.A.*, 85(7):2029–2030, 1988.

[267] Stephen J Hagen, Linlin Qiu, and Suzette A Pabit. Diffusional limits to the speed of protein folding: fact or friction? *J. Phys.: Condens. Matter*, 17(18):S1503–S1514, 2005.

[268] Stephen J Hagen. Solvent Viscosity and Friction in Protein Folding Dynamics. *Curr. Protein Pept. Sci.*, 11(5):385–395, 2010. PMID: 20426733.

[269] Jaroslav Vojtěchovský, Kelvin Chu, Joel Berendzen, Robert M. Sweet, and Ilme Schlichting. Crystal Structures of Myoglobin-Ligand Complexes at Near-Atomic Resolution. *Biophys. J.*, 77(4):2153–2174, 1999.

[270] J. C. Kendrew, G. Bodo, H. M. Dintzis, R. G. Parrish, H. Wyckoff, and D. C. Phillips. A Three-Dimensional Model of the Myoglobin Molecule Obtained by X-Ray Analysis. *Nature*, 181:662–666, 1958.

[271] Friedrich Schotte, Jayashree Soman, John S. Olson, Michael Wulff, and Philip A. Anfinrud. Picosecond time-resolved X-ray crystallography: probing protein function in real time. *J. Struc. Biol.*, 147(3):235–246, 2004.

[272] J. O. Alben, D. Beece, S. F. Bowne, W. Doster, L. Eisenstein, H. Frauenfelder, D. Good, J. D. McDonald, M. C. Marden, P. P. Moh, L. Reinisch, A. H. Reynolds, E. Shyamsunder, and K. T. Yue. Infrared spectroscopy of photodissociated carboxymyoglobin at low temperatures. *Proc. Nat. Acad. Sci. U.S.A.*, 79(12):3744–3748, 1982.

[273] Kusai A. Merchant, W. G. Noid, David E. Thompson, Ryo Akiyama, Roger F. Loring, and M. D. Fayer. Structural Assignments and Dynamics of the A Substates of MbCO: Spectrally Resolved Vibrational Echo Experiments and Molecular Dynamics Simulations. *J. Phys. Chem. B*, 107(1):4–7, 2003.

[274] Michael Devereux and Markus Meuwly. Structural Assignment of Spectra by Characterization of Conformational Substates in Bound MbCO. *Biophys. J.*, 96(11):4363–4375, 2009.

[275] C Rovira. Influence of the Heme Pocket Conformation on the Structure and Vibrations of the Fe-CO Bond in Myoglobin: A QM/MM Density Functional Study. *Biophys. J.*, 81(1):435–445, 2001.

[276] Tiansheng Li, Michael L. Quillin, George N. Phillips, and John S. Olson. Structural Determinants of the Stretching Frequency of CO Bound to Myoglobin. *Biochemistry*, 33(6):1433–1446, 1994.

[277] Robert F. Tilton, Irwin D. Kuntz, and Gregory A. Petsko. Cavities in proteins: structure of a metmyoglobin xenon complex solved to 1.9 Å. *Biochemistry*, 23(13):2849–2857, 1984.

[278] Andreas Ostermann, Robert Waschipky, Fritz G. Parak, and G. Ulrich Nienhaus. Ligand binding and conformational motions in myoglobin. *Nature*, 404:205–208, 2000.

[279] Kusai A. Merchant, W. G. Noid, Ryo Akiyama, Ilya J. Finkelstein, Alexei Goun, Brian L. McClain, Roger F. Loring, and M. D. Fayer. Myoglobin-CO Substate Structures and Dynamics: Multidimensional Vibrational Echoes and Molecular Dynamics Simulations. *J. Am. Chem. Soc.*, 125(45):13804–13818, 2003.

[280] Lauren P. DeFlores, Ziad Ganim, Rebecca A. Nicodemus, and Andrei Tokmakoff. Amide I'-II' 2D IR Spectroscopy Provides Enhanced Protein Secondary Structural Sensitivity. *J. Am. Chem. Soc.*, 131(9):3385–3391, 2009.

[281] Lauren P. DeFlores and Andrei Tokmakoff. Water Penetration into Protein Secondary Structure Revealed by Hydrogen–Deuterium Exchange Two-Dimensional Infrared Spectroscopy. *J. Am. Chem. Soc.*, 128(51):16520–16521, 2006.

[282] Ziad Ganim, Hoi Sung Chung, Adam W. Smith, Lauren P. DeFlores, Kevin C. Jones, and Andrei Tokmakoff. Amide I Two-Dimensional Infrared Spectroscopy of Proteins. *Acc. Chem. Res.*, 41(3):432–441, 2008.

[283] Jens Bredenbeck, Jan Helbing, Karin Nienhaus, G. Ulrich Nienhaus, and Peter Hamm. Protein ligand migration mapped by nonequilibrium 2D-IR exchange spectroscopy. *Proc. Nat. Acad. Sci. U.S.A.*, 104(36):14243–14248, 2007.

[284] Sayan Bagchi, Dayton G. Thorpe, Ian F. Thorpe, Gregory A. Voth, and M. D. Fayer. Conformational Switching between Protein Substates Studied with 2D IR Vibrational Echo Spectroscopy and Molecular Dynamics Simulations. *J. Phys. Chem. B*, 114(51):17187–17193, 2010.

[285] Karin Nienhaus, Pengchi Deng, John S. Olson, Joshua J. Warren, and G. Ulrich Nienhaus. Structural Dynamics of Myoglobin: Ligand Migration and Binding in Valine 68 Mutants. *J. Biol. Chem.*, 278(43):42532–42544, 2003.

[286] Karin Nienhaus, Pengchi Deng, Jan M. Kriegl, and G. Ulrich Nienhaus. Structural Dynamics of Myoglobin: Spectroscopic and Structural Characterization of Ligand Docking Sites in Myoglobin Mutant L29W. *Biochemistry*, 42(32):9633–9646, 2003.

[287] José A. Trejo González, M. Paula Longinotti, and Horacio R. Corti. The Viscosity of Glycerol–Water Mixtures Including the Supercooled Region. *J. Chem. Eng. Data*, 56(4):1397–1406, 2011.

[288] Jaroslav Pátek, Jan Hrubý, Jaroslav Klomfar, Monika Součková, and Allan H. Harvey. Reference Correlations for Thermophysical Properties of Liquid Water at 0.1MPa. *J. Phys. Chem. Ref. Data*, 38(1):21–29, 2009.

[289] C. H. Cho, J. Urquidi, S. Singh, and G. Wilse Robinson. Thermal Offset Viscosities of Liquid H_2O, D_2O, and T_2O. *J. Phys. Chem. B*, 103(11):1991–1994, 1999.

[290] Dimitrios Morikis, Paul M. Champion, Barry A. Springer, and Stephen G. Sligar. Resonance Raman investigations of site-directed mutants of myoglobin: effects of distal histidine replacement. *Biochemistry*, 28(11):4791–4800, 1989.

[291] Motonari Tsubaki, Raja B. Srivastava, and Nai Teng Yu. Resonance Raman investigation of carbon monoxide bonding in (carbon monoxy)hemoglobin and -myoglobin: detection of iron-carbon monoxide stretching and iron-carbon-oxygen bending vibrations and influence of the quaternary structure change. *Biochemistry*, 21(6):1132–1140, 1982.

[292] M. J. Frisch, G. W. Trucks, J. R. Cheeseman, G. Scalmani, M. Caricato, H. P. Hratchian, X. Li, V. Barone, J. Bloino, G. Zheng, T. Vreven, J. A. Montgomery, G. A. Petersson, G. E. Scuseria, H. B. Schlegel, H. Nakatsuji, A. F. Izmaylov, R. L. Martin, J. L. Sonnenberg, J. E. Peralta, J. J. Heyd, E. Brothers, F. Ogliaro, M. Bearpark, M. A. Robb, B. Mennucci, K. N. Kudin, V. N. Staroverov, R. Kobayashi, J. Normand, A. Rendell, R. Gomperts, V. G. Zakrzewski, M. Hada, M. Ehara, K. Toyota, R. Fukuda, J. Hasegawa, M. Ishida, T. Nakajima, Y. Honda, O. Kitao, H. Nakai, T. Vreven, J. A. Montgomery, Jr., J. E. Peralta, F. Ogliaro, M. Bearpark, J. J. Heyd, E. Brothers, K. N. Kudin, V. N. Staroverov, R. Kobayashi, J. Normand, K. Raghavachari, A. Rendell, J. C. Burant, S. S. Iyengar, J. Tomasi, M. Cossi, N. Rega, J. M. Millam, M. Klene, J. E. Knox, J. B. Cross, V. Bakken, C. Adamo, J. Jaramillo, R. Gomperts, R. E. Stratmann, O. Yazyev, A. J. Austin, R. Cammi, C. Pomelli, J. W. Ochterski,

R. L. Martin, K. Morokuma, V. G. Zakrzewski, G. A. Voth, P. Salvador, J. J. Dannenberg, S. Dapprich, A. D. Daniels, . Farkas, J. B. Foresman, J. V. Ortiz, J. Cioslowski, and D. J. Fox. Gaussian 09 Revision B.01, 2009.

[293] Yan Zhao and Donald G. Truhlar. The M06 suite of density functionals for main group thermochemistry, thermochemical kinetics, noncovalent interactions, excited states, and transition elements: two new functionals and systematic testing of four M06-class functionals and 12 other functionals. *Theor. Chem. Acc.*, 120(1-3):215–241, 2008.

[294] Andreas Bergner, Michael Dolg, Wolfgang Küchle, Hermann Stoll, and Heinzwerner Preuß. Ab initio energy-adjusted pseudopotentials for elements of groups 13-17. *Mol. Phys.*, 80(6):1431–1441, 1993.

[295] Jacopo Tomasi, Benedetta Mennucci, and Roberto Cammi. Quantum Mechanical Continuum Solvation Models. *Chem. Rev.*, 105(8):2999–3093, 2005.

[296] A. Bondi. van der Waals Volumes and Radii. *J. Phys. Chem.*, 68(3):441–451, 1964.

[297] Andreas T. Messmer, Katharina M. Lippert, Sabrina Steinwand, Eliza-Beth W. Lerch, Kira Hof, David Ley, Dennis Gerbig, Heike Hausmann, Peter R. Schreiner, and Jens Bredenbeck. Two-dimensional Infrared Spectroscopy Reveals Structural Details of an Evans Auxiliary Derivate and its $SnCl_4$ Lewis Acid Complex. *Chem. Eur. J.*, page DOI: 10.1002/chem.201201583, 2012.

[298] Gregory R. Fulmer, Alexander J. M. Miller, Nathaniel H. Sherden, Hugo E. Gottlieb, Abraham Nudelman, Brian M. Stoltz, John E. Bercaw, and Karen I. Goldberg. NMR Chemical Shifts of Trace Impurities: Common Laboratory Solvents, Organics, and Gases in Deuterated Solvents Relevant to the Organometallic Chemist. *Organometallics*, 29(9):2176–2179, 2010.

[299] Oleg V. Dolomanov, Luc J. Bourhis, Richard J. Gildea, Judith A. K. Howard, and Horst Puschmann. OLEX2: a complete structure solution, refinement and analysis program. *J. Appl. Crystallogr.*, 42:339–341, 2009.

[300] George M. Sheldrick. A short history of SHELX. *Acta Crystallogr., Sect. A*, 64:112–122, 2008.

[301] Dong Wang, Ulrike Kreutzer, Youngran Chung, and Thomas Jue. Myoglobin and hemoglobin rotational diffusion in the cell. *Biophys. J.*, 73(5):2764–2770, 1997. PMID: 9370470 PMCID: PMC1181178.

[302] Pál Ormos, David Braunstein, Hans Frauenfelder, Mi Kyung Hong, Shuo/Liang Lin, Todd B. Sauke, and Robert D. Young. Orientation of carbon monoxide and structure-function relationship in carbonmonoxymyoglobin. *Proc. Nat. Acad. Sci. U.S.A.*, 85(22):8492–8496, 1988. PMID: 3186739 PMCID: PMC282484.

[303] Eun Sun Park, Steven S. Andrews, Robert B. Hu, and Steven G. Boxer. Vibrational Stark Spectroscopy in Proteins: A Probe and Calibration for Electrostatic Fields. *J. Phys. Chem. B*, 103(45):9813–9817, 1999.

Abbreviations

1	(4S)-3-((E)-2-Butenoyl)-4(1-methylethyl)2-oxazolidinone
2D-EXSY	two-dimensional exchange spectroscopy
2D-IR	two-dimensional infrared
2D-NMR	two-dimensional nuclear magnetic resonance
2D-THz	two-dimenional Terahertz
2D-VIS	two-dimensional visible
3D-IR	three-dimensional infrared
AAS	atomic absorption spectroscopy
AGS	silver thiogallate
AOM	acousto optic modulator
ap	antiperiplanar
ar	anti-reflective
Au	gold
BBO	β-barium borate
c	cis
COSY	correlation spectroscopy
CPA	chirped pulse amplification
CS	conformational substate
cw	continuous wave
DFG	difference frequency generation
DFT	density functional theory
DOVE-FWM	doubly vibrationally enhanced four wave mixing
EPR	electron paramagnetic resonance
EtOAc	ethyl acetate
EVV-2D-IR	electron-vibration-vibration two-dimensional infrared
EXSY	exchange spectroscopy
EXSY-2D-IR	exchange two-dimensional infrared
FID	free induction decay
FP	Fabry–Perot
FTIR	Fourier tranform infrared
FWHM	full-width at half-maximum
GaAs	gallium arsenide
GVD	group velocity dispersion
HMBC	heteronuclear multiple bond correlation spectroscopy
HSQC	heteronuclear single quantum correlation spectroscopy
IR	infrared
IVR	intramolecular vibrational energy redistribution
LBO	lithium triborate
LDA	lithium diisopropylamine

Mb	myoglobin
MbCO	carbonmonoxy myoglobin
MCT	mercury cadmium telluride
MD	molecular dynamics
MeCN	acetonitrile
ν	vibrations of **1**
ν'	vibrations of **1**·$SnCl_4$, main species
ν^A	vibrations of **1**·$SnCl_4$, species A
ν^B	vibrations of **1**·$SnCl_4$, species B
ν^C	vibrations of **1**·$SnCl_4$, species C
ν^*	vibrations of **1**·$Mg(MeCN)_x$
Nd:YLF	neodymium(III) doped lithium yttrium fluoride
Nd:YVO	neodymium(III) doped yttrium vanadate
NMR	nuclear magnetic resonance
NOE	nuclear Overhauser effect
NOESY	nuclear Overhauser effect spectroscopy
OPA	optical parametric amplification
p	protective
P2D-IR	polarization-dependent two-dimensional infrared
PAS 2D-IR	polarization angle scanning two-dimensional infrared
PCM	polariyable continuum model
Ph	phenyl
RA-2D-IR	relaxation-assisted two-dimensional infrared
RDC	dicarbonylacetylacetonato rhodium
ROESY	rotation frame Overhauser effect spectroscopy
rpm	revolutions per minute
SDD	Stuttgart Dresden effective core potential
SFG	sum frequency generation
SFG-2D-IR	sum frequency two-dimensional infrared
SHG	second harmonic generation
sp	synperiplanar
t	trans
Tf	triflate
TFA	trifluoroacetic acid
THF	tetrahydrofuran
Ti:Sa	titanium(III) doped sapphire
TMSCl	trimethylsilyl cloride
TOCSY	total correlation spectroscopy
TPFPP	5,10,15,20-tetrakis(pentafluorophenyl)porphyrin
UV	ultraviolet
VIS	visible
v/v	volume/volume
w	weight proportion
wt	wild type
YLT	L29Y H64L V68T

List of Figures

List of Tables

Danksagung

und die wissenschaftliche Genauigkeit. Danke auch für die motivierenden Worte und die Unterstützung (damit meine ich nicht nur das Korrekturlesen meiner englischen Texte) selbst nachdem du zu Wiley gegangen bist. Ich hoffe, dass die Freundschaft noch lange halten wird.

Wie würde der Lasertisch noch heute aussehen, ohne die Arbeit von *Ernst Winter*? Wie häufig kam ich kurz vor Feierabend in der Werkstatt vorbei und habe noch ganz dringend etwas gebraucht? Danke für deine Zuverlässigkeit, deine Geduld und auch dafür, dass du immer mitgedacht hast und mir damit die Arbeit manches Mal erleichtert hast. Danke auch an *Viktor Schäfer*, ohne dessen Elektronik kein Spektrum gemessen worden wäre und den *Mitarbeitern der Feinmechanikwerkstätten* unter der Leitung von *Herrn Jäger* und *Herrn Ott*. Allen *Mitarbeitern* des Instituts danke ich für die Atmosphäre und die vielen, vielen Kuchen während meiner Zeit am IfB; *Frau Lill* für die administrative Arbeit im Hintergrund, *Georg Wille* für seinen Input zur Röntgenstrukturaufklärung, *Hans-Werner Müller* für das fröhliche Guten Morgen jeden Tag, *Carsten Krejtschi* für die kurze, aber sehr schöne gemeinsame Zeit im Labor und nicht zuletzt *Maxi Frei*: Manchmal kann die Heimat so nah sein...

Besonderer Dank gilt auch dem *AK Wachtveitl*. Bei euch habe ich mich immer sehr wohl gefühlt. Zudem wäre ohne euch der Lasertisch nur halb so voll und viele Experimente nicht möglich gewesen. Danke, dass wir so viel ausleihen durften und ihr mich mit Rat und Tat unterstützt habt: Karsten Neumann hatte fast jedes Problem selbst schon gehabt und kannte oft eine Lösung. *Nina Gildenhoff*, *Ute Förster* und *Peter Trojanovski* haben das Labor mit uns geteilt und ich habe die Zeit und Gespräche mit euch wirklich sehr genossen. Nicht vergessen werde ich den ganz speziellen und schönen Skitag an der Kanzelwand mit Ute :-).

Das Leben hier in Frankfurt bestand nicht nur aus dem Labor. Daher auch ein ganz spezieller Dank an die *Kajakgruppe* des Hochschulsports. Ihr habt mir ein geniales Hobby beigebracht, das ich nicht mehr missen möchte. Ich hoffe, dass es noch ganz viele tolle gemeinsame Touren geben wird. Jetzt habe ich auch endlich wieder ein bisschen mehr Zeit. *Matthias Pfeiffer* und *Thomas Plöttner* möchte ich auch dafür danken, dass ich mit euch so manches Mal die Wand hochgehen durfte.

Zu besonderem Dank bin ich *meinen Freunden* verpflichtet, die immer ein offenes Ohr für mich gehabt haben, mich ermutigt haben, und mich auf die ein oder andere Weise auch mal abgelenkt haben. Stellvertretend für alle möchte ich hier *Debbie Riedi*, *Birgit Thiel*, *Dominik Leitz* (danke auch für die NMR Insider Informationen), *Anna Evans*, *Gaby Blatter*, *Denise Steiner* und *Katrin Niedermann* nennen. Ich möchte an dieser Stelle auch all denjenigen danken, die ich während meiner wissenschaftlichen Karriere und auf Konferenzen kennen lernen durfte und mit denen mich immer noch eine Freundschaft verbindet.

Auch die Unterstützung durch *meine immer grösser werdende Familie* war von unschätzbarem Wert. Danke für die Ermutigungen, die Ratschläge und das Interesse an meiner Arbeit, die soweit weg ist von dem, was ihr kennt. *Meinen Eltern* und *meinem Bruder* gilt hier ein ganz besonderes Dankeschön.

Den größten Anteil an dieser Arbeit hat meine Frau *Elke*. Vielen Dank, dass du mit mir nach Frankfurt gezogen bist, mich immer bedingungslos unterstützt hast und auch immer Verständnis hattest, wenn ich z.B. die Nacht im Labor verbracht habe, oder, gerade in der Phase des Zusammenschreibens, gedanklich immer woanders war. Ohne dich hätte ich irgendwann zwischendrin bestimmt aufgegeben. Nicht zuletzt möchte ich dir auch dafür danken, dass du mir ein nicht verschiebbares Abgabedatum gesetzt hast. Ich freue mich schon sehr auf die gemeinsame Zeit zu dritt.

Eidesstattliche Versicherung

Ich erkläre hiermit an Eides statt, dass ich die vorgelegte Dissertation über

Shedding Light on Reaction Mechanisms
–
Structure Determination of Reactive Intermediates and Investigation of Protein Structural Dynamics Using 2D-IR Spectroscopy

selbständig angefertigt und mich anderer Hilfsmittel als der in ihr angegebenen nicht bedient habe, insbesondere, dass alle Entlehnungen aus anderen Schriften mit Angabe der betreffenden Schrift gekennzeichnet sind.

Ich versichere, nicht die Hilfe einer kommerziellen Promotionsvermittlung in Anspruch genommen zu haben.

Frankfurt am Main, den ....
(Unterschrift)

Erklärung

Ich erkläre hiermit, dass ich mich bisher keiner Doktorprüfung unterzogen habe.

Frankfurt am Main, den ....
(Unterschrift)

Lebenslauf

Andreas Thomas Meßmer
Oberurseler Str. 31
61440 Oberursel

Persönliche Daten

Geburtsdatum:	23. Mai 1983
Geburtsort:	Engen/Hegau
Nationalitäten:	D, CH (Bürgerort: Leuggern AG)
Familienstand:	verheiratet

Ausbildung

seit 11/2007	Promotion in der Arbeitsgruppe von Prof. Dr. Jens Bredenbeck, Institut für Biophysik, Johann Wolfgang Goethe-Universität Frankfurt.
	Dissertationsthema: *Shedding Light on Reaction Mechanisms – Structure Determination of Reactive Intermediates and Investigation of Protein Structural Dynamics Using 2D-IR Spectroscopy.*
10/2006 – 09/2007	Masterstudium Chemie, ETH Zürich, Schweiz. Abschluss: Master of Science ETH in Chemie; mit Auszeichnung (Note: 5.85).
	Masterarbeit: *Remixing of Vibrational Eigenstates investigated by Transient 2D-IR Spectroscopy – a theoretical and experimental study.* Betreut durch Prof. Dr. Peter Hamm, Universität Zürich, Schweiz. Ausgezeichnet mit der ETH Medaille.
	Projektarbeit II: *Calciumalginat als Modellsystem für extrazelluläre Polymere – Eine Untersuchung mittels AFM, CLSM und TERS.* Betreut durch Prof. Dr. Renato Zenobi, ETH Zürich, Schweiz.
	Projektarbeit I: *Transient 2D-IR spectroscopy of a light induced process – remixing of vibrational eigenstates.* Betreut durch Prof. Dr. Peter Hamm, Universität Zürich, Schweiz.

10/2003 – 09/2006	Bachelorstudium Chemie, ETH Zürich, Schweiz. Abschluss: Bachelor of Science ETH in Chemie (Note: 5.20).
10/2002 – 07/2003	Zivildienst als Rettungssanitäter bei der DRK Rettungsdienst GmbH Konstanz.
08/1993 – 06/2002	Friedrich-Wöhler-Gymnasium, Singen am Hohentwiel. Abschluss: Abitur (Note: 1.1).
08/1989 – 07/1993	Grundschule GHS Tengen.

Lehrerfahrung

2010 – 2012	Praktikumsbetreuung *Physik für Mediziner*.
2009 – 2012	Praktikumsbetreuung *Biophysikalisches Praktikum für Fortgeschrittene*.
2010 – 2011	Übungsbetreuung *Biophysik Wahlpflicht für Physiker und Chemiker*.
2010	Betreuung des AK Praktikums von Sabrina Steinwand.
2009 – 2010	Praktikumsbetreuung *CEF Explorer*.

Auszeichungen und Stipendien

2011	*Skinner Prize* der Royal Chemical Society.
2009	Teilnahme am *59th Meeting of Nobel Laureates* in Lindau.
2008 – 2010	*Kekulé Stipendium* des FCI.
2008	*ETH Medaille* für eine vorzügliche Masterarbeit.
2006 – 2007	*Stipendium* des Chatelâin Fonds der ETH Zürich.
2006 – 2007	*Stipendium* der Moriz und Elsa von Kuffner-Stiftung.
2004 – 2007	*Stipendium* der Homberger Stiftung.
2002	*NaturEnergie – Schulpreis* für ein hervorragendes Abitur der Naturwissenschaften; gestiftet durch die EnergieDienst GmbH.
2001	Teilnahme an der *Deutschen Schüler Akademie*.

Akademische Lehrer

M. Aebi, D. Alder, N. Amrhein, M. Badertscher, B. Braukmann, J. Bredenbeck, S. Burckhardt-Heroldt, E.M. Carreira, P. Chen, H.-J.W. Dannappel, F. Diederich, R. Eggen, M. Ernst, B. Escher, T. Esslinger, K. Fenner, P. Geimer, D. Günther, P. Hamm, H.-J. Hansen, M. Hippler, W. Höland, K. Hungerbühler, B.M. Jaun, W.H. Koppenol, H.R. Künsch, H.E. Laederach, C. Latkoczy, W.R. Littmann-Wernli, B.H. Meier, E.C. Meister, F. Merkt, F. Merkt, A. Mezzetti, W.E. Morf, R. Nesper, G. Patzke, K.V. Pervushin, P. Pregosin, E. Pretsch, M. Quack, V. Sandoghdar, M. Scheringer, P.H. Seeberger, M. Sommer, R. Sperb, W.J. Stark, G. Stock, D. Stoffer, S. Stoll, C. Thilgen, M. Thomson, A. Togni, W. Uhlig, W.F. van Gunsteren und R. Zenobi.